

AD-A241 859



(1)



DTIC

FLECTE

OCT 28 1991

MODEL IDENTIFICATION AND
CONTROL SYSTEM DESIGN FOR THE
LAMBDA UNMANNED RESEARCH VEHICLE

THESIS

Gerald A. Swift, First Lieutenant, USAF

AFIT/GAE/ENY/91S-4

This document has been approved
for public release and sale; its
distribution is unlimited.

DEPARTMENT OF THE AIR FORCE
AIR UNIVERSITY
AIR FORCE INSTITUTE OF TECHNOLOGY

Wright-Patterson Air Force Base, Ohio

91-14120

91 10 25 040

AFIT/GAE/ENY/91S-4

1

DTIC
ELECTE
OCT 28 1991
S D D

MODEL IDENTIFICATION AND
CONTROL SYSTEM DESIGN FOR THE
LAMBDA UNMANNED RESEARCH VEHICLE

THESIS

Gerald A. Swift, First Lieutenant, USAF

AFIT/GAE/ENY/91S-4

Handwritten notes and stamps on the right side of the page, including a large 'J' and the text 'A-1'.

Approved for public release; distribution unlimited.

INSPECTED
4

MODEL IDENTIFICATION AND CONTROL SYSTEM DESIGN
FOR THE LAMBDA UNMANNED RESEARCH VEHICLE

THESIS

Presented to the Faculty of the School of Engineering
of the Air Force Institute of Technology
Air University
in Partial Fulfillment of the
Requirements for the Degree of
Master of Science in Aeronautical Engineering

Gerald A. Swift, B.S.A.E.

First Lieutenant, USAF

September 1991

Approved for public release; distribution unlimited.

REPORT DOCUMENTATION PAGE

FORM 487-100
10/80 10/80/100

1. AGENCY USE ONLY (Leave blank)		2. REPORT DATE September 1991	3. REPORT TYPE AND DATES COVERED Master's Thesis
4. TITLE AND SUBTITLE Model Identification and Control System Design for the Lambda Unmanned Research Vehicle			5. FUNDING NUMBERS
6. AUTHOR(S) Gerald A. Swift, 1 Lt, USAF			
7. PERFORMING ORGANIZATION NAME(S) AND ADDRESS(ES) Air Force Institute of Technology, WPAFB OH 45433-6583			8. PERFORMING ORGANIZATION REPORT NUMBER AFIT/GAE/ENY/91S-4
9. SPONSORING MONITORING AGENCY NAME(S) AND ADDRESS(ES)			10. SPONSORING MONITORING AGENCY REPORT NUMBER
11. SUPPLEMENTARY NOTES			
12. DISTRIBUTION AVAILABILITY STATEMENT Approved for public release; distribution unlimited			13. DISTRIBUTION CODE
13. ABSTRACT (Maximum 200 words) Research for this thesis centered on the Lambda Unmanned Research Vehicle (URV), an asset of the Flight Dynamics Directorate, Wright Laboratory, at Wright-Patterson AFB. The following tasks were accomplished: (1) a linear, state-space, small perturbation model was developed for both the longitudinal and lateral-directional dynamics of the vehicle, and (2) pitch rate, roll rate, and yaw rate flight controllers were designed using classical and multivariable feedback methods. The parameters of the linear, state-space, small perturbation model were estimated from actual flight test data. Digital Datcom was first used to estimate stability and control derivatives from the vehicle's geometry. Maximum likelihood estimation was then used to adjust the Datcom derivatives so that the estimated state time histories matched the actual state time histories recorded during flight. Pitch rate, roll rate, and yaw rate controller designs were developed using classical feedback methodology characterized by single-input, single-output, open loop transfer function techniques. The controller designs were repeated using the Linear Quadratic Gaussian with Loop Transfer Recovery (LQG/LTR) multivariable feedback approach.			
14. SUBJECT TERMS Unmanned Air Vehicle, Remotely Piloted Vehicle, Maximum Likelihood Estimation, Aircraft Models, Flight Testing, Flight Control Systems, Multivariable Feedback Control			15. NUMBER OF PAGES 242 16. PRICE CODE
17. SECURITY CLASSIFICATION OF REPORT Unclassified	18. SECURITY CLASSIFICATION OF THIS PAGE Unclassified	19. SECURITY CLASSIFICATION OF ABSTRACT Unclassified	20. LIMITATION OF ABSTRACT UL

Acknowledgments

The emerging world of unmanned air vehicles (UAVs) is producing an environment that challenges the engineer to address problems in a unique manner. Conventional constraints are relaxed and ingenuity is emphasized. Low cost, unmanned research testbeds, such as the Lambda Unmanned Research Vehicle, are the laboratories for tomorrow's UAV technologies. I want to thank the Flight Control Division, especially Dan Thompson and the Lambda crew, for allowing me to be a part of their team. I also want to thank Capt Stuart Sheldon for his support and perspectives on new approaches to old problems.

I am also deeply indebted to my thesis advisor, Major Curtis Mracek. His experience in the field of flight testing and his straightforward approach to addressing flight control problems were invaluable to the success of this thesis. I also want to thank Capt Brett Ridgely for his insight to LQG/LTR theory and Dr Brad Liebst for his guidance in control system design.

The computer generated graphics of the Lambda URV were created by Lt Scott Wells. I think the excellent quality of the graphics speaks for itself. I greatly appreciate his unselfish support.

Finally, I want to express my deepest appreciation to my wife, Lori. Her constant support and alternative perspectives were fundamental to my successful completion of the AFIT program.

Gerald A. Swift

Table of Contents

	<u>Page</u>
Acknowledgments	ii
List of Figures	vi
List of Tables	xiii
List of Symbols	xvi
Abstract	xxviii
1. Introduction	1.1
1.1. Thesis Objectives	1.3
2. The Vehicle	2.1
2.1. Lambda Geometric Characteristics	2.1
2.2. Lambda Mass Properties Data	2.7
2.3. Description of Flight Sensors	2.10
3. Linear State Space Perturbation Model	3.1
3.1. Derivation of the General State Space Model	3.3
3.2. Description of Flight Tests	3.11
3.3. Estimation of the State Space Model Prior to Incorporation of Flight Test Data	3.14
3.4. Inclusion of Flight Test Data in Parameter Estimation	3.25
3.5. Final State Space Model	3.43
3.6. Conclusions and Recommendations	3.49
4. Rate Controller Design Using Classical Techniques	4.1
4.1. Projected Flight Envelope	4.2
4.2. Pitch Rate Controller Design	4.6
4.3. Roll Rate Controller Design	4.16
4.4. Yaw Rate Controller Design	4.22
4.5. Discussion of Rate Controller Designs Using Classical Techniques	4.28

	<u>Page</u>
5. Rate Controller Design Using Multivariable Feedback Techniques	5.1
5.1. LQG/LTR Methodology	5.2
5.1.1. The Linear Quadratic Estimator (LQE)	5.3
5.1.2. The Linear Quadratic Regulator (LQR)	5.4
5.1.3. The LQG Compensator with Loop Transfer Recovery	5.6
5.2. Pitch Rate Controller Design	5.10
5.2.1. Open Loop Model	5.10
5.2.2. Performance and Robustness Specifications	5.11
5.2.3. Augmenting Integrators to the Open Loop Model	5.13
5.2.4. LQE Design	5.16
5.2.5. LQG/LTR	5.18
5.2.6. Final Design	5.22
5.3. Roll Rate Controller Design	5.27
5.4. Yaw Rate Controller Design	5.30
5.4.1. Yaw Rate Controller with Roll Angle Regulated	5.30
5.4.2. Yaw Rate Controller with Sideslip Regulated	5.33
5.5. Discussion of Rate Controller Designs Using LQG/LTR	5.38
6. Comparisons and Discussion	6.1
6.1. Discussion of Rate Controller Performance	6.1
6.2. LQG/LTR Versus Classical Rate Controller Design	6.6
6.2.1. Pitch Rate Controller Comparisons	6.6
6.2.2. Roll Rate Controller Comparisons	6.13
6.2.3. Yaw Rate Controller Comparisons	6.19
6.3. Conclusions and Recommendations	6.24
6.3.1. Conclusions	6.24
6.3.2. Recommendations	6.26

Appendices:

- A. Flight Test Data Example.
- B. Maximum Likelihood Parameter Estimation Examples.
- C. Comparison of Actual Flight Test Data to the State Vector Time Responses Estimated by the Final Small Perturbation Model.
- D. Linear, State Space, Small Perturbation Matlab Model: DERCALC.M.
- E. Wind Dynamics Model.
- F. Rate Controller Matlab Models.

Bibliography

Vita

List of Figures

<u>Figure</u>	<u>Page</u>
1.1. Lambda Unmanned Research Vehicle.	1.1
2.1. Three View Drawing of the Lambda URV.	2.2
2.2. Lambda Wing Planform.	2.4
2.3. Lambda Wing Airfoil Cross Section.	2.4
2.4. Lambda Vertical Tail Planform.	2.5
2.5. Lambda Horizontal Tail Planform.	2.5
2.6. Lambda Internal Arrangement Schematic.	2.6
3.1. Airplane Coordinate System.	3.3
3.2. Airplane Geometry Used for the Airplane Math Model.	3.7
3.3. Change in Short Period Natural Frequency with a Change in Vehicle Center of Gravity Location.	3.39
3.4. Change in Short Period Damping Ratio with a Change in Vehicle Center of Gravity Location.	3.39
3.5. Pitch command and Elevator Deflection Time History for Flight Maneuver PD, HF, FT 11/20/90.	3.44
3.6. Scaling of the Pitch Command Input for the Flight Maneuver PD, HF, FT 11/20/90.	3.44
3.7. Comparison of Estimated and Actual Elevator Surface Deflection for the First Pitch Doublet Maneuver.	3.46
4.1. Avionics Bay Arrangement for the Lambda URV.	4.4
4.2. Center of Gravity Excursion Diagram for the Lambda URV.	4.5
4.3. Projected Flight Envelope for the Lambda URV.	4.5
4.4. Pitch Rate Controller Block Diagram (Negative Feedback with a Gain and a Lead).	4.7
4.5. General Root Locus for Figure 4.4 Block Diagram.	4.8
4.6. Typical Root Locus for Figure 4.4 Block Diagram.	4.9
4.7. Closed Loop Time Response for $K_q = -2.5$, $a_L = 5.0$.	4.10

<u>Figure</u>	<u>Page</u>
4.8. Final Pitch Rate Controller Block Diagram for Flight Condition #1.	4.12
4.9. Root Locus for the Controller Design for Flight Condition #1.	4.12
4.10. Closed Loop Time Response for the Pitch Rate Controller Design for Flight Condition #1.	4.13
4.11. Bode Magnitude and Phase Plot for the Controller Design for Flight Condition #1.	4.13
4.12. Closed Loop Time Responses for the Final Pitch Rate Controller Point Designs.	4.14
4.13. Block Diagram for the Final Pitch Rate Controller Design.	4.15
4.14. Roll Rate Controller Block Diagram (Negative Feedback with a Gain and a Lead).	4.16
4.15. General Root Locus for Figure 4.14 Block Diagram.	4.17
4.16. Root Locus for the Roll Rate Controller for Flight Condition #1 with $K_p=0.15$ and $a_1=3.0$.	4.19
4.17. Closed Loop Time Response for the Roll Rate Controller Design for Flight Condition #1.	4.19
4.18. Bode Magnitude and Phase Plot for the Roll Rate Controller Design for Flight Condition #1.	4.20
4.19. Closed Loop Time Responses for the Final Roll Rate Controller Point Designs.	4.21
4.20. Yaw Rate Controller General Block Diagram (Negative Feedback with a Pure Gain and Two Leads).	4.23
4.21. General Root Locus for Figure 4.20 Block Diagram.	4.24
4.22. Closed Loop Time Response for the Yaw Rate Controller for Flight Condition #1 with $K_r=-2.5$, $a_1=4.0$, $c=0.033$, $d=0.5$.	4.26
4.23. Bode Magnitude and Phase Plot for the Yaw Rate Controller Design for Flight Condition #1.	4.26
4.24. Closed Loop Time Responses for the Final Yaw Rate Controller Point Designs.	4.27

<u>Figure</u>	<u>Page</u>
5.1. Block Diagram of the LQG System.	5.7
5.2. Singular Value Plot of Performance and Robustness Boundaries for Lambda Fate Controller Designs.	5.13
5.3. Unaugmented Open Loop Singular Value Plot.	5.14
5.4. Augmented Open Loop Singular Value Plot.	5.15
5.5. Doubly Augmented Open Loop Singular Value Plot.	5.15
5.6. Singular Value Plot for the Kalman Filter Design Given in Table 5.4.	5.17
5.7. Singular Value Plot for $T_0(s)$ with $q=0$, $p=1$.	5.19
5.8. Singular Value Plot for $T_0(s)$ with $q=1000$, $p=9999$.	5.19
5.9. Closed Loop Time Response for Pitch Rate to a Unit Step Pitch Rate Command.	5.21
5.10. Closed Loop Response for Elevator Deflection to a Unit Step Pitch Rate Command.	5.21
5.11. Closed Loop Sensitivity Singular Value Plot.	5.23
5.12. Closed Loop Time Responses to a Unit Step Pitch Rate Command for the Final Pitch Rate Controller Design.	5.26
5.13. Closed Loop Time Responses to a Unit Step Roll Rate Command for the Final Roll Rate Controller Design.	5.29
5.14. Closed Loop Time Responses to a Unit Step Yaw Rate Command for the Final Yaw Rate Controller (Design #1).	5.32
5.15. Kalman Filter Loop Shape for the Yaw Rate Controller (Design #2).	5.35
5.16. $G(s)K(s)$ Loop Shape for the Yaw Rate Controller (Design #2).	5.35
5.17. Closed Loop Time Responses to a Unit Step Yaw Rate Command for the Final Yaw Rate Controller (Design #2).	5.37

<u>Figure</u>	<u>Page</u>
6.1. Closed Loop Time Response Bounds.	6.2
6.2. Closed Loop Pitch Rate Time Response Comparisons.	6.7
6.3. Comparison of Root Loci for the Pitch Rate Compensators.	6.8
6.4. $G(s)K(s)$ Loop Shape Comparisons for the Pitch Rate Controllers.	6.12
6.5. Closed Loop Roll Rate Time Response Comparisons.	6.14
6.6. $G(s)K(s)$ Loop Shape Comparisons for the Roll Rate Controllers.	6.16
6.7. Comparison of Closed Loop Sideslip Response for the Roll Rate Controllers.	6.18
6.8. Closed Loop Yaw Rate Time Response Comparisons.	6.20
6.9. $G(s)K(s)$ Loop Shape Comparisons for the Yaw Rate Controllers.	6.22
6.10. Comparison of Closed Loop Sideslip Response for the Yaw Rate Controllers.	6.23
6.11. Command Generator Tracker (CCT) Block Diagram.	6.28
A.1. Roll Command.	A.2
A.2. Pitch Command.	A.2
A.3. Yaw Command.	A.3
A.4. Roll Command (RC), Pitch Command (PC), and Yaw Command (YC).	A.3
A.5. Roll Rate.	A.4
A.6. Roll Attitude.	A.4
A.7. Pitch Rate.	A.5
A.8. Pitch Attitude.	A.5
A.9. Yaw Rate.	A.6
A.10. Airspeed.	A.6
A.11. Altitude.	A.7

<u>Figure</u>	<u>Page</u>
A.12. Angle of Attack.	A.7
A.13. Angle of Sideslip.	A.8
A.14. Lateral Acceleration.	A.8
A.15. Longitudinal Acceleration.	A.9
A.16. Vertical Acceleration.	A.9
A.17. Left and Right Aileron Deflection.	A.10
A.18. Roll Command and Right Aileron Deflection.	A.10
A.19. Left and Right Elevator Deflection.	A.11
A.20. Pitch Command and Left Elevator Deflection.	A.11
A.21. Left and Right Rudder Deflection.	A.12
A.22. Left and Right Flap Deflection.	A.12
B.1. Angle of Attack Data Fit for the First Pitch Doublet Maneuver (half flaps, full throttle) on the First Flight Test.	B.2
B.2. Pitch Rate Data Fit for the First Pitch Doublet Maneuver (half flaps, full throttle) on the First Flight Test.	B.2
B.3. Roll Rate Data Fit for the First Roll Doublet Maneuver (zero flaps, full throttle) on the First Flight Test.	B.3
B.4. Angle of Sideslip Data Fit for the First Yaw Doublet Maneuver (zero flaps, full throttle) on the First Flight Test.	B.4
B.5. Yaw Rate Data Fit for the First Yaw Doublet Maneuver (zero flaps, full throttle) on the First Flight Test.	B.4
C.1. Actual and Predicted Speed Time History for the Pitch Doublet Maneuver (zero flaps, full throttle).	C.2
C.2. Actual and Predicted Angle of Attack Time History for the Pitch Doublet Maneuver (zero flaps, full throttle).	C.2

<u>Figure</u>	<u>Page</u>
C.3. Actual and Predicted Pitch Rate Time History for the Pitch Doublet Maneuver (zero flaps, full throttle).	C.3
C.4. Actual and Predicted Pitch Angle Time History for the Pitch Doublet Maneuver (zero flaps, full throttle).	C.3
C.5. Actual and Predicted Angle of Sideslip Time History for the Pitch Doublet Maneuver (zero flaps, full throttle).	C.4
C.6. Actual and Predicted Roll Rate Time History for the Pitch Doublet Maneuver (zero flaps, full throttle).	C.4
C.7. Actual and Predicted Roll Attitude Time History for the Pitch Doublet Maneuver (zero flaps, full throttle).	C.5
C.8. Actual and Predicted Yaw Rate Time History for the Pitch Doublet Maneuver (zero flaps, full throttle).	C.5
C.9. Predicted Heading Angle Time History for the Pitch Doublet Maneuver (zero flaps, full throttle).	C.6
C.10. Actual and Predicted Speed Time History for the Roll Doublet Maneuver (zero flaps, full throttle).	C.7
C.11. Actual and Predicted Angle of Attack Time History for the Roll Doublet Maneuver (zero flaps, full throttle).	C.7
C.12. Actual and Predicted Pitch Rate Time History for the Roll Doublet Maneuver (zero flaps, full throttle).	C.8
C.13. Actual and Predicted Pitch Angle Time History for the Roll Doublet Maneuver (zero flaps, full throttle).	C.8
C.14. Actual and Predicted Angle of Sideslip Time History for the Roll Doublet Maneuver (zero flaps, full throttle).	C.9
C.15. Actual and Predicted Roll Rate Time History for the Roll Doublet Maneuver (zero flaps, full throttle).	C.9

<u>Figure</u>	<u>Page</u>
C.16. Actual and Predicted Roll Attitude Time History for the Roll Doublet Maneuver (zero flaps, full throttle).	C.10
C.17. Actual and Predicted Yaw Rate Time History for the Roll Doublet Maneuver (zero flaps, full throttle).	C.10
C.18. Predicted Heading Angle Time History for the Roll Doublet Maneuver (zero flaps, full throttle).	C.11
C.19. Actual and Predicted Speed Time History for the Yaw Doublet Maneuver (zero flaps, full throttle).	C.12
C.20. Actual and Predicted Angle of Attack Time History for the Yaw Doublet Maneuver (zero flaps, full throttle).	C.12
C.21. Actual and Predicted Pitch Rate Time History for the Yaw Doublet Maneuver (zero flaps, full throttle).	C.13
C.22. Actual and Predicted Pitch Attitude Time History for the Yaw Doublet Maneuver (zero flaps, full throttle).	C.13
C.23. Actual and Predicted Angle of Sideslip Time History for the Yaw Doublet Maneuver (zero flaps, full throttle).	C.14
C.24. Actual and Predicted Roll Rate Time History for the Yaw Doublet Maneuver (zero flaps, full throttle).	C.14
C.25. Actual and Predicted Roll Attitude Time History for the Yaw Doublet Maneuver (zero flaps, full throttle).	C.15
C.26. Actual and Predicted Yaw Rate Time History for the Yaw Doublet Maneuver (zero flaps, full throttle).	C.15
C.27. Predicted Heading Angle Time History for the Yaw Doublet Maneuver (zero flaps, full throttle).	C.16

List of Tables

<u>Table</u>	<u>Page</u>
2.1. Geometric Characteristics of the Lambda Vehicle.	2.3
2.2. Lambda Component Weight and Coordinate Data.	2.8
2.3. Lambda Inertia Estimation.	2.9
2.4. Lambda Sensors.	2.10
3.1. Airplane Equations of Motion.	3.4
3.2. Airplane Steady State Equations of Motion.	3.5
3.3. Airplane Perturbed Equations of Motion.	3.6
3.4. Airplane Small Perturbation Equations of Motion.	3.7
3.5. Airplane State-Space Perturbation Model.	3.8
3.6. Airplane Longitudinal Dimensional Stability Derivatives.	3.9
3.7. Airplane Lateral-Directional Dimensional Stability Derivatives.	3.10
3.8. Flight Test #1 Information.	3.11
3.9. Flight Test #2 Information.	3.12
3.10. Accuracy of Sensors Onboard the Lambda URV.	3.13
3.11. Dimensionless Stability and Control Derivatives for the First Flight Test ($X_{cg}=48.217$ inches, $W=203$ pounds).	3.18
3.12. Average Dimensionless Derivatives for the First Flight Test ($X_{cg}=48.217$ in, $W=203$ pounds).	3.21
3.13. Calculation of Dimensional Derivatives and State Space Model for the First Pitch Doublet, Flight Test #1.	3.22
3.14. Summary of Short Period, Roll, and Dutch Roll Approximation Equations.	3.30
3.15. Comparison of Short Period Approximation Characteristics.	3.35
3.16. Comparison of Roll Approximation Characteristics.	3.36

<u>Table</u>	<u>Page</u>
3.17. Comparison of Dutch Roll Approximation Characteristics.	3.37
3.18. Average Dimensionless Derivatives for the First Flight Test ($X_{cg}=47.2$ inches, $W=203$ pounds).	3.38
3.19. Final Dimensionless Derivatives for the Lambda Vehicle ($X_{cg}=47.2$ inches, $W=203$ pounds).	3.42
3.20. Elevator, Aileron, and Rudder Servo Characteristics for the Lambda URV.	3.45
3.21. Final State Space Model.	3.47
4.1. Pitch Rate Controller Point Designs.	4.11
4.2. Roll Rate Controller Point Designs.	4.20
4.3. Yaw Rate Controller Point Designs.	4.25
5.1. Open Loop Longitudinal Dynamics Model for the Flight Condition at the Center of Lambda's Flight Envelope.	5.12
5.2. Process of Adding an Integrator to the Open Loop Dynamics.	5.14
5.3. Characteristics of the Basic Open Loop (Doubly Augmented) System.	5.16
5.4. Kalman Filter Design.	5.17
5.5. LQG Compensator Design.	5.18
5.6. Summary of the Final Pitch Rate Controller Design.	5.25
5.7. Closed Loop Margins for the Final Pitch Rate Controller Design.	5.25
5.8. Summary of the Final Roll Rate Controller Design.	5.28
5.9. Closed Loop Margins for the Final Roll Rate Controller Design.	5.29
5.10. Summary of the Final Yaw Rate Controller (Design #1).	5.31
5.11. Closed Loop Margins for the Final Yaw Rate Controller (Design #1).	5.32

<u>Table</u>	<u>Page</u>
5.12. Summary of the Final Yaw Rate Controller (Design #2).	5.36
5.13. Closed Loop Margins for the Final Yaw Rate Controller (Design #2).	5.36
6.1. Closed Loop Time Response Performance Objectives.	6.5
6.2. Comparison of Pitch Rate Controller Dynamics.	6.9
6.3. Open Loop System Dynamics for the Roll Rate Controllers.	6.13
6.4. Open Loop System Dynamics for the Yaw Rate Controllers.	6.19

List of Symbols

Regular Symbols

<u>Symbol</u>	<u>Definition</u>	<u>Dimension</u>
A_1	I_{xz}/I_{xx}	
a.c.	aerodynamic center	
b	wing span	ft
B_1	I_{xz}/I_{zz}	
c	chord	ft
\bar{c}	mean aerodynamic chord	ft
C_L	lift coefficient	
C_D	drag coefficient	
C_M	pitching moment coefficient	
C_l	rolling moment coefficient	
C_n	yawing moment coefficient	
C_y	side force coefficient	
$C_{L\alpha}$	airplane lift curve slope	1/rad
$C_{L\delta}$	control surface lift effectiveness	1/rad
C_{D_0}	drag coefficient for zero angle of attack, zero elevator and zero stabilizer angle	
$C_{D\alpha}$	variation of drag coefficient with angle of attack	1/rad
$C_{D\delta e}$	variation of drag coefficient with elevator angle	1/rad
C_{L_0}	lift coefficient for zero angle of attack, zero elevator angle and zero stabilizer angle	
$C_{L\delta e}$	variation of lift coefficient with elevator angle	1/rad
C_{M_0}	pitching moment coefficient for zero angle of attack, zero elevator angle and zero stabilizer angle	

<u>Symbol</u>	<u>Definition</u>	<u>Dimension</u>
$C_{M\alpha}$	variation of pitching moment coefficient with angle of attack	1/rad
$C_{M\delta e}$	variation of pitching moment coefficient with elevator angle	1/rad
C_{l_0}	rolling moment coefficient for zero sideslip, aileron and rudder angles	
$C_{l\beta}$	variation of rolling moment coefficient with sideslip angle	1/rad
$C_{l\delta a}$	variation of rolling moment coefficient with aileron angle	1/rad
$C_{l\delta r}$	variation of rolling moment coefficient with rudder angle	1/rad
C_{y_0}	side force coefficient for zero sideslip, aileron and rudder angle	
$C_{y\beta}$	variation of side force coefficient with sideslip angle	1/rad
$C_{y\delta r}$	variation of side force coefficient with rudder angle	1/rad
$C_{y\delta a}$	variation of side force coefficient with aileron angle	1/rad
C_{n_0}	yawing moment coefficient for zero sideslip, aileron and rudder angle	
$C_{n\beta}$	variation of yawing moment coefficient with sideslip angle	1/rad
$C_{n\delta r}$	variation of yawing moment coefficient with rudder angle	1/rad
$C_{n\delta a}$	variation of yawing moment coefficient with aileron angle	1/rad
C_{D_u}	variation of drag coefficient with speed	
C_{L_u}	variation of lift coefficient with speed	
C_{M_u}	variation of pitching moment coefficient with speed	

<u>Symbol</u>	<u>Definition</u>	<u>Dimension</u>
$C_{D\dot{\alpha}}$	variation of drag coefficient with rate of change of angle of attack	
$C_{L\dot{\alpha}}$	variation of lift coefficient with rate of change of angle of attack	
$C_{M\dot{\alpha}}$	variation of pitching moment coefficient with rate of change of angle of attack	
C_{Dq}	variation of drag coefficient with pitch rate	
C_{Lq}	variation of lift coefficient with pitch rate	
C_{Mq}	variation of pitching moment coefficient with pitch rate	
C_{Yp}	variation of side force coefficient with roll rate	
C_{lp}	variation of rolling moment coefficient with roll rate	
C_{np}	variation of yawing moment coefficient with roll rate	
C_{Yr}	variation of side force coefficient with yaw rate	
C_{lr}	variation of rolling moment coefficient with yaw rate	
C_{nr}	variation of yawing moment coefficient with yaw rate	
D	drag	lbs
e	Oswald's efficiency factor	
e_{ss}	steady state error	
F	applied force	lbs
f	perturbed force	lbs
g	acceleration of gravity	ft/sec ²
$G(s)$	system forward path transfer function	

<u>Symbol</u>	<u>Definition</u>	<u>Dimension</u>
I	moment of inertia	slug ft ²
I _{xx}	moment of inertia about X axis	slug ft ²
I _{yy}	moment of inertia about Y axis	slug ft ²
I _{zz}	moment of inertia about Z axis	slug ft ²
I _{xz}	product of inertia in XYZ system	slug ft ²
K	gain constant	
L	rolling moment (about X)	ft lbs
l	perturbed rolling moment	ft lbs
L	lift	lbs
L _β	dimensional variation of rolling moment about X _s with sideslip angle	1/sec ²
L _p	dimensional variation of rolling moment about X _s with roll rate	1/sec
L _r	dimensional variation of rolling moment about X _s with yaw rate	1/sec
L _{δa}	dimensional variation of rolling moment about X _s with aileron angle	1/sec ²
L _{δr}	dimensional variation of rolling moment about X _s with rudder angle	1/sec ²
m	mass	slugs
M	pitching moment	ft lbs
M	Mach number	
m	perturbed pitching moment	ft lbs
M _u	dimensional variation of pitching moment with speed	1/(ft sec)
M _α	dimensional variation of pitching moment with angle of attack	1/sec ²
M _q	dimensional variation of pitching moment with rate of change of angle of attack	1/sec

<u>Symbol</u>	<u>Definition</u>	<u>Dimension</u>
M_q	dimensional variation of pitching moment with pitch rate	1/sec
$M_{\delta e}$	dimensional variation of pitching moment with elevator angle	1/sec ²
N	yawing moment	ft lbs
n	perturbed yawing moment	ft lbs
N_β	dimensional variation of yawing moment about Z_s with sideslip angle	1/sec ²
N_p	dimensional variation of yawing moment about Z_s with roll rate	1/sec
N_r	dimensional variation of yawing moment about Z_s with yaw rate	1/sec
$N_{\delta a}$	dimensional variation of yawing moment about Z_s with aileron angle	1/sec ²
$N_{\delta r}$	dimensional variation of yawing moment about Z_s with rudder angle	1/sec ²
P	roll rate (about X)	rad/sec
p	perturbed roll rate	rad/sec
Q	pitch rate	rad/sec
q	perturbed pitch rate	rad/sec
\bar{q}	dynamic pressure	lbs/ft ²
\bar{r}'	vector distance between the elementary mass particle and the X'Y'Z' system	ft
\bar{r}	vector distance between the elementary mass particle and the airplane c.g.	ft
\bar{r}_p	vector distance between the airplane c.g. and the X'Y'Z' system	ft
R	yaw rate (about Z)	rad/sec
r	perturbed yaw rate	rad/sec
S	surface area, reference wing area	ft ²

<u>Symbol</u>	<u>Definition</u>	<u>Dimension</u>
s	Laplace variable	1/sec
t	time, thickness	sec, ft
T	thrust	lbs
T_R	roll mode time constant	sec
T_S	spiral mode time constant	sec
U	forward velocity	ft/sec
u	perturbed forward velocity	ft/sec
V	side velocity	ft/sec
V_p	velocity of the c.g.	ft/sec
v	perturbed side velocity	ft/sec
W	downward velocity (along Z)	ft/sec
w	perturbed downward velocity	ft/sec
w_f	fuselage width	ft
X, x	distance along X	ft
X_{ac}	location of aerodynamic center	inches
X_{cg}	location of center of gravity	inches
X_{ac}	location of aerodynamic center in terms of \bar{c}	
X_{cg}	location of center of gravity in terms of \bar{c}	
X_u	dimensional variation of X_s -force with speed	1/sec
X_α	dimensional variation of X_s -force with angle of attack	ft/sec ²
$X_{\delta e}$	dimensional variation of X_s -force with elevator angle	ft/sec ²
Y, y	distance along Y	ft

<u>Symbol</u>	<u>Definition</u>	<u>Dimension</u>
Y_β	dimensional variation of Y_s -force with sideslip angle	ft/sec ²
Y_p	dimensional variation of Y_s -force with roll rate	ft/sec
Y_r	dimensional variation of Y_s -force with yaw rate	ft/sec
$Y_{\delta a}$	dimensional variation of Y_s -force with aileron angle	ft/sec ²
$Y_{\delta r}$	dimensional variation of Y_s -force with rudder angle	ft/sec ²
Z, z	distance along Z	ft
Z_u	dimensional variation of Z_s -force with speed	1/sec
Z_α	dimensional variation of Z_s -force with angle of attack	ft/sec ²
$Z_{\dot{\alpha}}$	dimensional variation of Z_s -force with rate of change of angle of attack	ft/sec
Z_q	dimensional variation of Z_s -force with pitch rate	ft/sec
$Z_{\delta e}$	dimensional variation of Z_s -force with elevator angle	ft/sec ²

State Space Symbols

<u>Symbol</u>	<u>Definition</u>	<u>Dimension</u>
A	nxn time invariant system dynamics matrix	
B	nxm time invariant, deterministic input matrix	
C	rxn measurement matrix	
D	rxm feedforward matrix	
Γ	nxS time invariant, process noise input matrix	
Q_0	process noise intensity	
R_f	measurement noise intensity	

<u>Symbol</u>	<u>Definition</u>	<u>Dimension</u>
Q_c	state weighting matrix	
R_c	control weighting matrix	
I	identity matrix	
0	zero matrix	
$e(t)$	error state time history	
$u(t)$	m-vector control input time history	
$w(t)$	wind state time history	
$x(t)$	n-vector state time history	
$\hat{x}(t)$	state estimate	
$y(t)$	r-vector measurment time history	
$\xi(t)$	s-vector white Gaussian process noise	
$\eta(t)$	r-vector white Gaussian measurement noise	
$G_a(s)$	augmented open loop transfer function	
$G_i(s)$	integrator transfer function	
$G_p(s)$	open loop plant transfer function	
J	quadratic cost function	
K_c	regulator gain matrix	
K_f	Kalman filter gain matrix	
$K_{LOG}(s)$	compensator transfer function	
M	error variance matrix	
M_p	maximum peak overshoot to step input	%
S	system sensitivity	mag, db
t_r	rise time	sec
t_s	settling time	sec
$T_{Kc}(s)$	Kalman filter transfer function	

<u>Symbol</u>	<u>Definition</u>	<u>Dimension</u>
$T_R(s)$	regulator transfer function	
a_a	aileron time lag constant (first order)	
a_e	elevator time lag constant (first order)	
a_f	flap time lag constant (first order)	
a_r	rudder time lag constant (first order)	
E	expectation	

Greek Symbols

<u>Symbol</u>	<u>Definition</u>	<u>Dimension</u>
ρ	air density	slug/ft ³
ρ_A	mass density of airplane	slug/ft ³
ω	rotational velocity,	rad/sec
Ψ, ψ	heading angle (total, perturbed)	rad
Θ, θ	pitch attitude angle (total, perturbed)	rad
Φ, ϕ	bank (roll) angle (total, perturbed)	rad
ϕ	also, phase angle or power spectral density	rad or ft ³
γ	flight path angle	rad
α	angle of attack	rad
λ	taper ratio	
Λ	sweep angle	rad
β	sideslip angle	rad
ϵ	downwash angle	rad
Δ	incremental value	
δ	control surface angle	rad, deg
δ_a	aileron angle	rad, deg
δ_e	elevator angle	rad, deg

<u>Symbol</u>	<u>Definition</u>	<u>Dimension</u>
δ_f	flap angle	rad, deg
δ_r	rudder angle	rad, deg
Γ	geometric dihedral angle	rad
σ	sidewash angle	rad, deg
σ	density ratio	
σ	mean square value of gust velocity	ft/sec
ω	frequency	rad/sec
ω_n	undamped natural frequency	rad/sec
ζ	damping ratio	

Subscripts

A	airplane, aerodynamic
T	thrust
x,y,z	components along X,Y,Z respectively
i	i th item or ideal
l	steady state
max	maximum
b	body
o	output
a.c.	aerodynamic center
c.g.	center of gravity
s	stability axes
com	command
a	aileron
e	elevator
f	flap
r	rudder
dr	dutch roll
p	phugoid
sp	short period
R	roll
S	spiral
ss	steady state
g	gust

Acronyms

CGT	Command Generator Tracker
FT	Full Throttle
HF	Half Flaps
HT	Half Throttle
LQE	Linear Quadratic Estimator
LQG	Linear Quadratic Gaussian
LQR	Linear Quadratic Regulator
LTR	Loop Transfer Recovery
MAC	Mean Aerodynamic Chord
MGC	Mean Geometric Chord
MSL	Mean Sea Level
QFT	Quantitative Feedback Theory
PC	Pitch Command
PD	Pitch Doublet
RC	Roll Command
RD	Roll Doublet
YC	Yaw Command
YD	Yaw Doublet
ZF	Zero Flaps

Abstract

Research for this thesis centered on the Lambda Unmanned Research Vehicle (URV), an asset of the Flight Dynamics Directorate, Wright Laboratory, at Wright-Patterson AFB. The following tasks were accomplished:

(1) a linear, state-space, small perturbation model was developed for both the longitudinal and lateral-directional dynamics of the vehicle, and

(2) pitch rate, roll rate, and yaw rate flight controllers were designed using classical and multivariable feedback methods.

The parameters of the linear, state-space, small perturbation model were estimated from actual flight test data. Digital Datcom was first used to estimate stability and control derivatives from the vehicle's geometry. Maximum likelihood estimation was then used to adjust the Datcom derivatives so that the estimated state time histories matched the actual state time histories recorded during flight. Pitch rate, roll rate, and yaw rate controller designs were developed using classical feedback methodology characterized by single-input, single-output, open loop transfer function techniques. The controller designs were repeated using the Linear Quadratic Gaussian with Loop Transfer Recovery (LQG/LTR) multivariable feedback approach. Closed loop performance, system robustness, and control power usage for the resulting compensator designs were then compared and contrasted.

1. Introduction

In 1987 the Flight Control Division (FIG) of the Flight Dynamics Directorate, Wright Laboratory, began development of a new unmanned research vehicle (URV) named Lambda. At that time, FIG was flying two XBQM-106 strike and harassment drones modified as flight control research vehicles. Although several successful programs were completed using these vehicles, a new URV with the following characteristics was desired:

- low cost,
- modular airframe,
- decoupled control surfaces,
- increased payload capacity, and
- horizontal take-off and landing (no launcher).

Hence, Lambda was acquired to provide FIG with an affordable, flexible research vehicle for testing and demonstrating flight control concepts, devices, and systems. A schematic of the vehicle is provided in Figure 1.1.

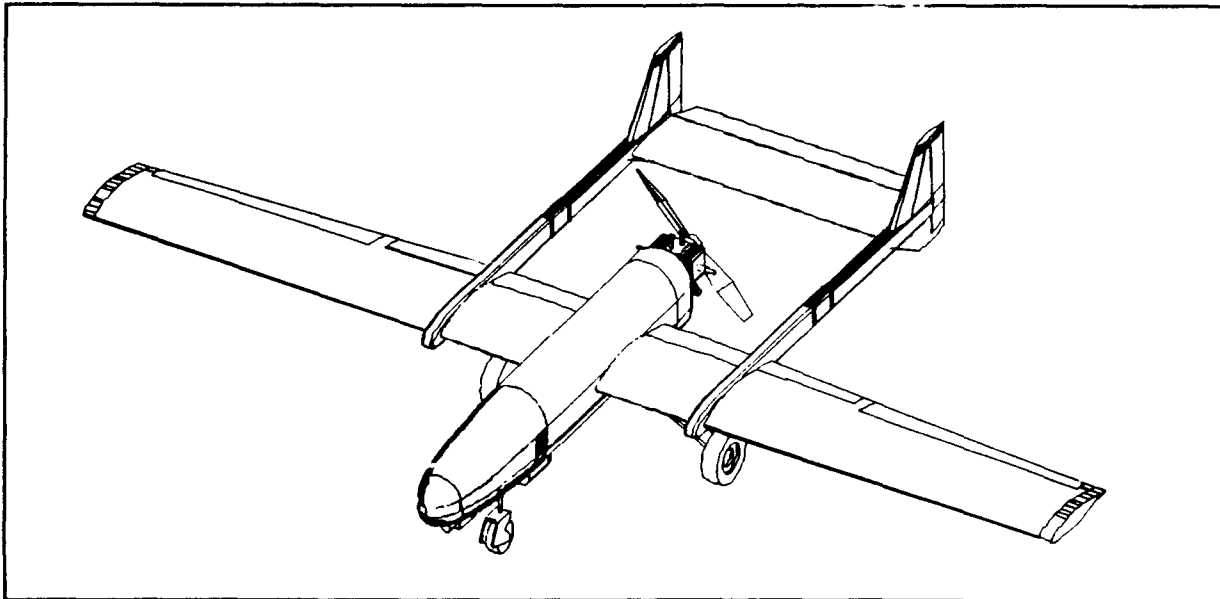


Figure 1.1. Lambda Unmanned Research Vehicle.

Since first flight in 1989, Lambda has flown as a remotely piloted vehicle. Control commands from a ground operator are up-linked to the URV via its telemetry system. Lambda has also been instrumented to measure airplane parameters during flight [1].

These parameters include the following:

- roll, pitch, and yaw commands,
- roll, pitch, and yaw rates,
- roll and pitch attitudes,
- airspeed and altitude,
- angle of attack,
- angle of sideslip,
- longitudinal, lateral, and vertical accelerations, and
- aileron, elevator, rudder, and flap deflections.

A video camera onboard the vehicle transmits a real time picture of the URV's flight.

The avionics system is being developed through supplemental funding through the Unmanned Air Vehicle Joint Program Office (UAV JPO) in Washington, D.C.. Integration of navigation, mission planning, and flight management functions into a low cost avionics system adaptable to a wide range of unmanned air vehicle concepts is the UAV JPO's primary interest. The automatic flight control system will be inserted in the electrical link between the pilot commands and the control surfaces and will include the control laws for vehicle response to pilot commands. The primary functions required will be control augmentation and wings leveling. Additional functions may include functional integration of the navigation/flight management package to include altitude hold, heading hold, control surface reconfiguration, and out-of-sight maneuvering [2].

1.1. Thesis Objectives

Since there is no wind tunnel data available for the Lambda URV, a large degree of uncertainty exists in the stability and control derivative data. The current mathematical model of the aircraft relies on estimates of the aerodynamic derivatives calculated with the Digital Datcom computer program [3]. These derivatives are uncertain; hence, any control system designed with the current model might not perform to FIG's satisfaction. Due to the prohibitive cost of wind tunnel tests, and the fact that Lambda has already been proven airworthy, Phase I of this thesis will be to identify an accurate model of the aircraft from actual flight data gathered in November 1990. Digital Datcom will be the primary tool used to predict the aerodynamic model for Lambda. The model will then be compared to actual flight test data and fine tuned to accurately predict the vehicle's aerodynamic stability and control derivatives. The primary benefit will be an accurate mathematical model of the Lambda URV which can be used for future research projects. Phase I will also validate the use of Digital Datcom for predicting the aerodynamic models of unmanned air vehicles in the 150-250 pound weight class.

Phase II of this thesis project will be to design flight control systems for the Lambda URV that regulate pitch rate, roll rate, and yaw rate. Although the flight control system that will eventually be implemented will probably be one that regulates attitudes (bank angle, heading angle, etc.), Wright Laboratory

has specifically asked for rate controller designs. Rate regulation is usually more difficult than attitude control and tends to exploit the limitations of the methodologies being used. This thesis will specifically look at the classical and multivariable feedback approaches to rate controller design. Other approaches, such as using quantitative feedback theory (QFT) techniques, are also being investigated by the Flight Dynamics Laboratory. The classical rate controller systems will be designed using the methods described primarily in Foskam [4] and McRuer [5]. The multivariable rate controllers will be designed using the Linear Quadratic Gaussian with Loop Transfer Recovery (LQG/LTR) approach. In 1986, Ridgely and Banda [6] wrote an excellent handbook which details the LQG/LTR methodology. Finally, the classical and multivariable feedback rate controllers will be compared and contrasted, thus providing Wright Laboratory with valuable insights into the two design approaches.

2. The Vehicle

A complete description of the geometric characteristics and internal layout is presented in this chapter. The mass properties data obtained from the Flight Dynamics Laboratory is also presented, but proved to be inaccurate. Changes to this data were made during the development of the aerodynamic model and will be presented in the next chapter.

2.1. Lambda Geometric Characteristics

Figure 2.1 presents a complete three view of the Lambda URV; Table 2.1 provides an overview of the vehicle's geometric characteristics. A summary of the overall layout will now be given.

The general wing layout for the Lambda URV is given in Figure 2.2. The wing airfoil section was designed specifically for the Lambda URV and is not a standard NACA airfoil. Figure 2.3 provides a cross section of the Lambda airfoil.

Lambda has a tail boom configuration with twin vertical tails. Both the vertical and horizontal tail cross sections are standard NACA 0012 airfoils. Figures 2.4 and 2.5 provide the layouts for the vertical and horizontal planforms respectively.

Lambda has 10 decoupled flight control surfaces: 2 inboard flaps, 2 outboard flaps, 2 ailerons, 2 rudders, and a split elevator. However, for this phase of the project, all flap deflections were synchronized, all aileron deflections coupled, both rudder deflections synchronized, and both elevator deflections synchronized.

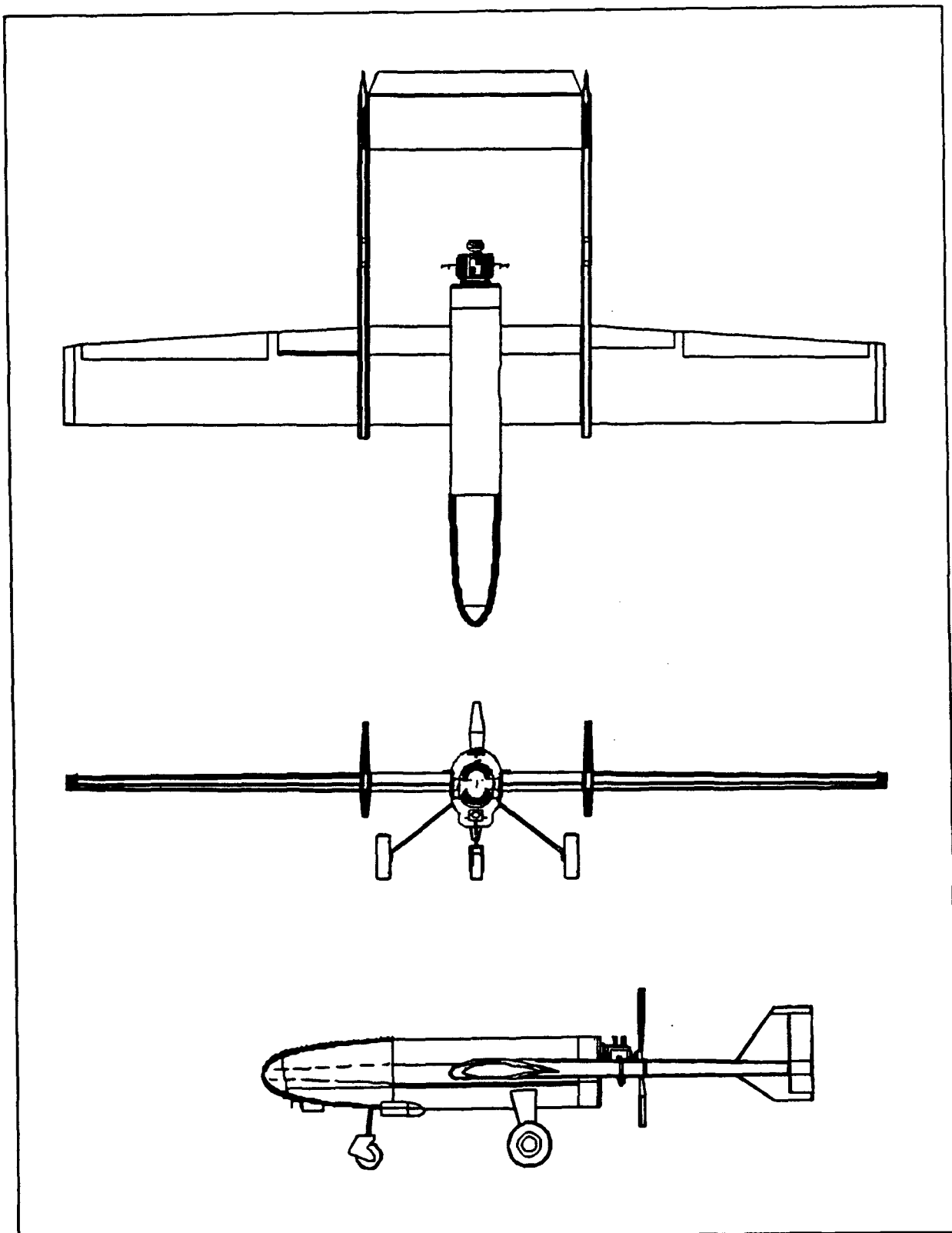


Figure 2.1. Three View Drawing of the Lambda URV.

Table 2.1. Geometric Characteristics of the Lambda Vehicle.

	<u>Wing</u>	<u>Horizontal Tail</u>	<u>Vertical Tail</u>
Area, sq ft	21.10	5.17	1.75
Span, ft	14.07	3.875	1.57
MGC, ft	1.51	1.33	1.125
MGC L.E.: F.S.	41.875	98.0	100.5
Aspect Ratio	9.38	2.90	1.45
Sweep Angle, l.e., deg	0	0	36.0
Taper Ratio	0.80	1.0	0.5
Thickness Ratio	0.182	0.12	0.12
Airfoil	(Fig 2.3)	NACA-0012	NACA-0012
Dihedral Angle, deg	0	0	N/A
Incidence Angle, deg	0	0	0
Aileron chord ratio	inboard: 0.250	outboard: 0.189	
Aileron span ratio	0.505 - 0.978		
Elevator chord ratio	0.305 constant		
Rudder chord ratio	0.250 average		
Flap chord ratio			
inboard flap	0.269 constant		
outboard flap	inboard: 0.269	outboard: 0.250	
Flap span ratio			
inboard flap	0.060 - 0.258		
outboard flap	0.285 - 0.484		
	<u>Fuselage</u>	<u>Overall</u>	
Length, ft	5.90	9.50	
Maximum Height, ft	1.09	2.76	
Maximum Width, ft	0.87	14.07	

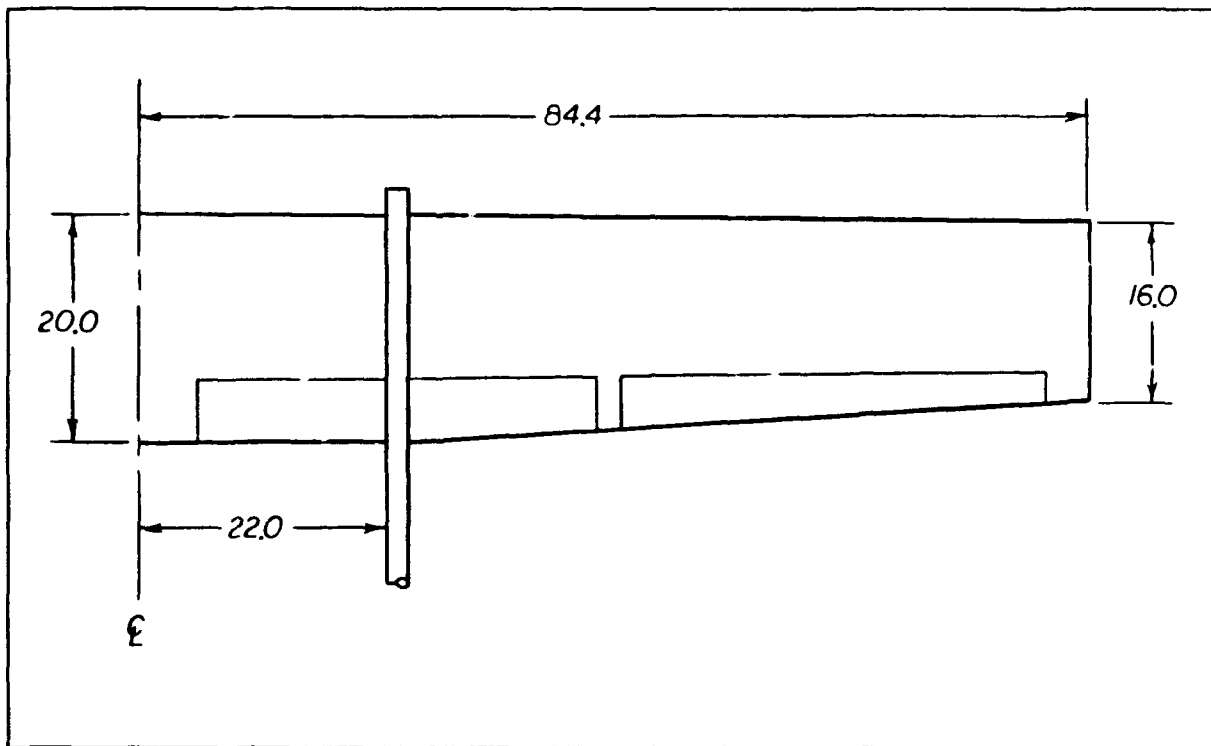


Figure 2.2. Lambda Wing Planform.

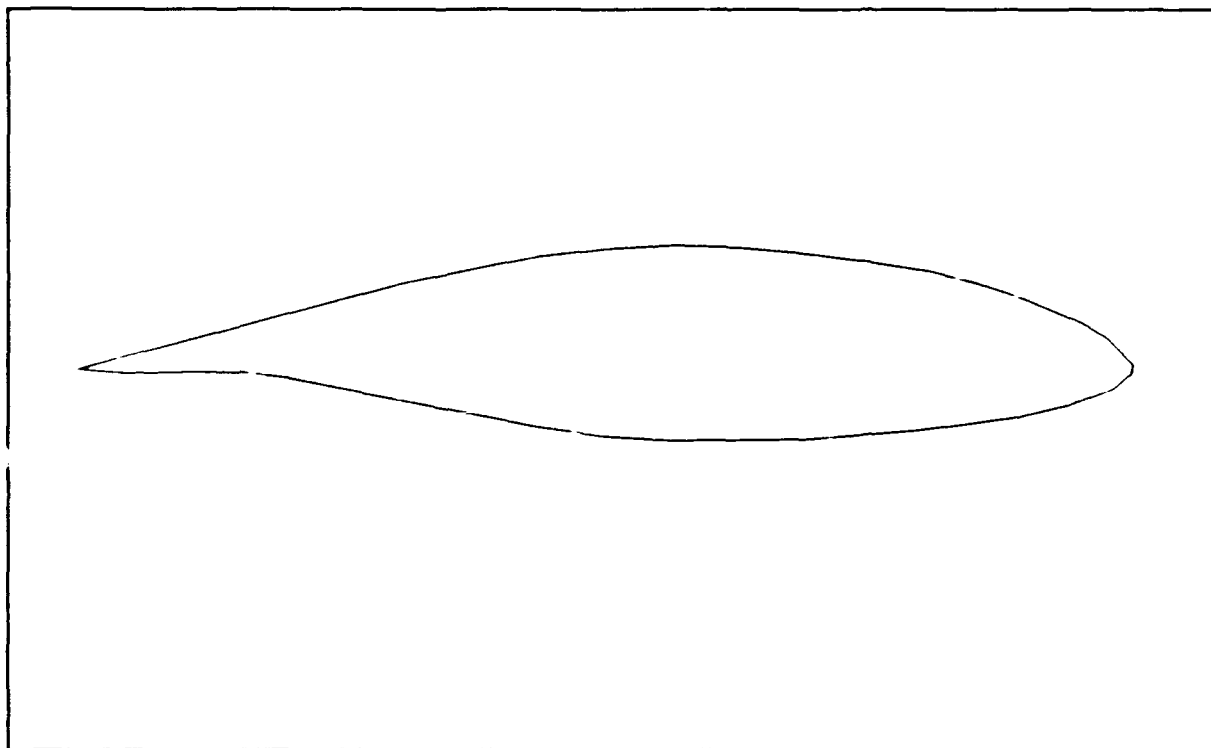


Figure 2.3. Lambda Wing Airfoil Cross Section.

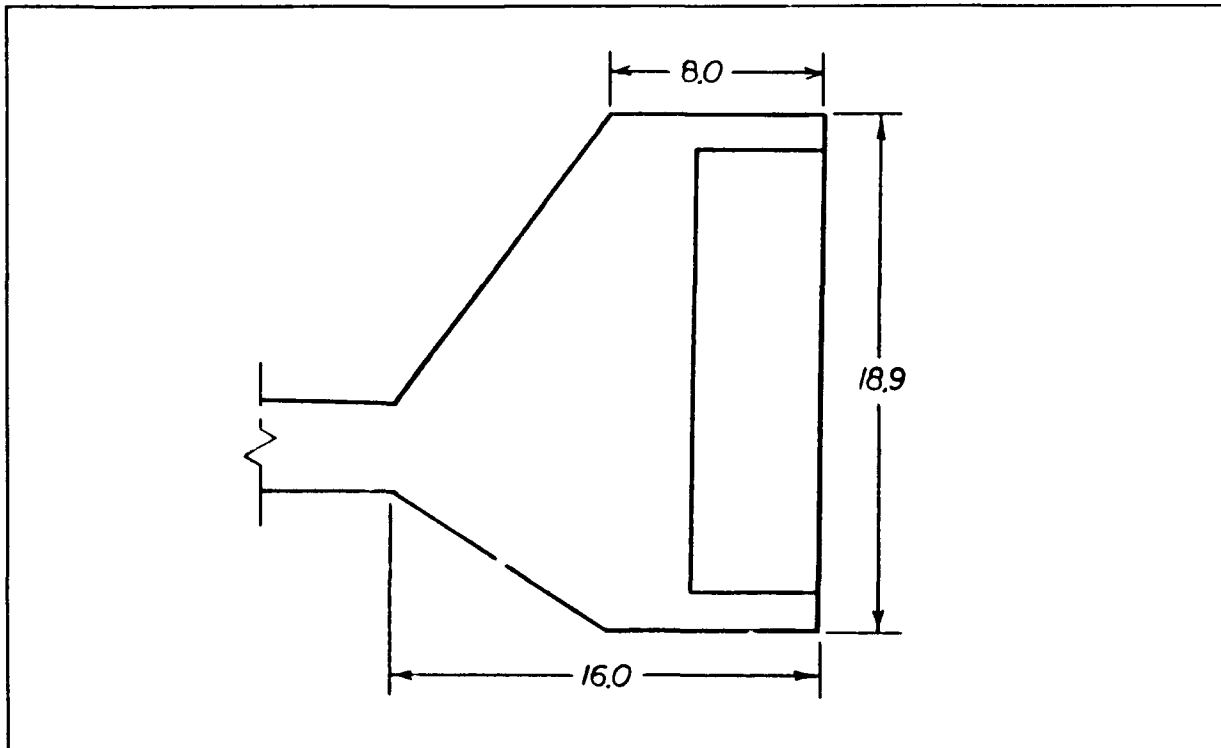


Figure 2.4. Lambda Vertical Tail Planform.

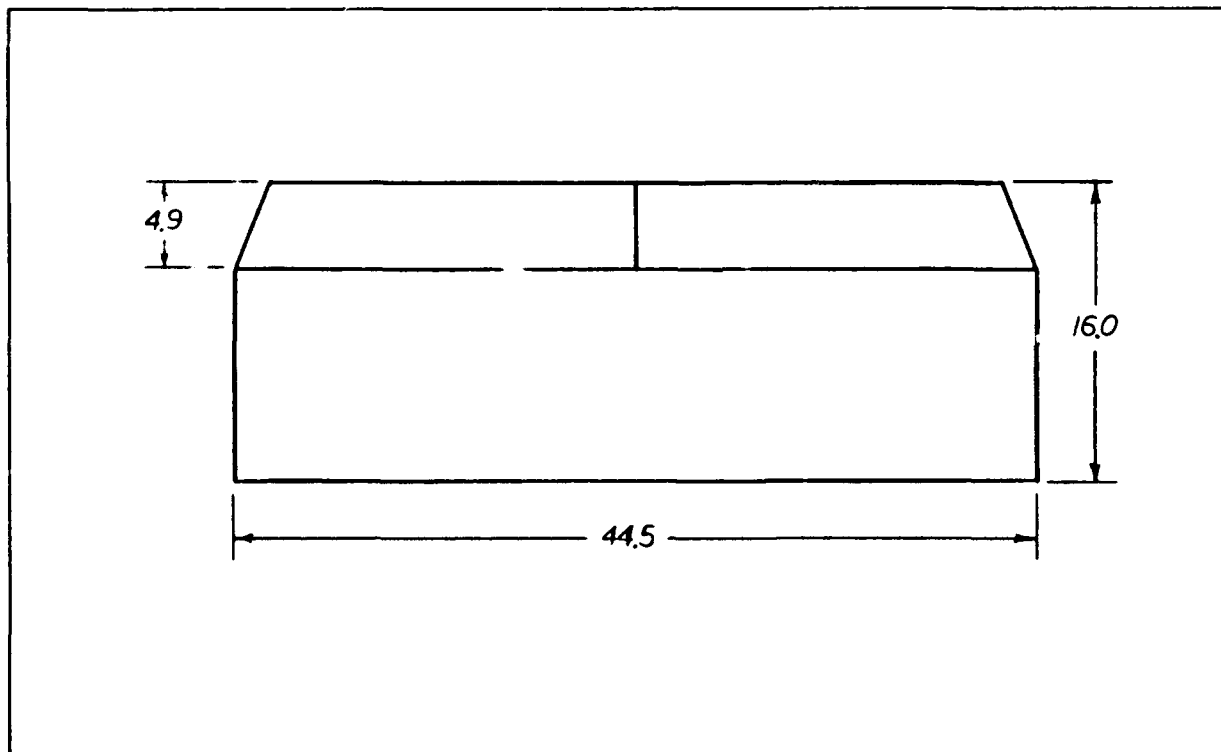


Figure 2.5. Lambda Horizontal Tail Planform.

The internal arrangement of the fuselage is provided in Figure 2.6. Notice the large internal cargo bay dedicated to future research hardware. Lambda is powered by an 18 HP Herbranson engine which sits in the aft section of the fuselage. Lambda has an internal bladder fuel tank that holds approximately 2 1/3 gallons of fuel (14 pounds). The vehicle also has two battery power supplies located in the forward section of the fuselage.

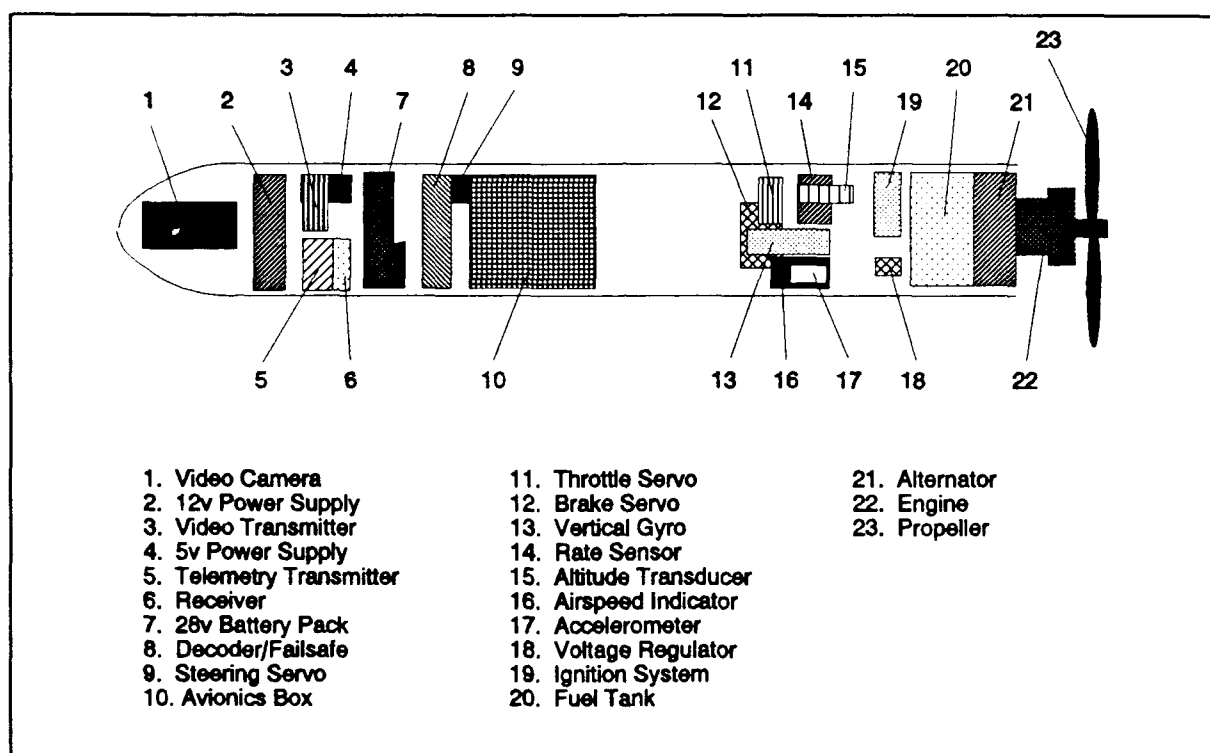


Figure 2.6. Lambda Internal Arrangement Schematic.

2.2. Lambda Mass Properties Data

Very little mass property data was available on the Lambda vehicle. Initially, only an overall weight and estimate of the vehicle center of gravity location were provided by the Flight Control Division for this project. In an effort to correctly estimate the vehicle mass properties, the following was accomplished:

1. obtained measurements of the overall vehicle and established a reference coordinate frame,
2. obtained measurements for the position of individual components and estimated center of gravity locations for each,
3. estimated component weights from the limited data available, and
4. iterated on component weight and center of gravity estimates until overall vehicle weight and center of gravity was appropriate.

Table 2.2 provides the resulting component weight and coordinate data for Lambda. All weights followed by an asterisk are strictly estimates based on known weights from similar components and calculations accomplished by incorporating methods presented in Reference 7. Component weights not followed by an asterisk were later provided by the Flight Control Division. Vehicle inertias, estimated from the weights data, are presented in Table 2.3.

It will be shown later that in order to adequately estimate flight performance, both the c.g. location and inertia data had to be adjusted. Specifically, the overall vehicle c.g. location was moved aft to $X_{cg} = 47.2$ inches for a vehicle weight of 203 pounds, and the roll inertia, I_{xx} , was doubled.

Table 2.2. Lambda Component Weight and Coordinate Data.

COMPONENT	WEIGHT (lbs)	X (in)	Y (in)	Z (in)

Right Wing	11.50	50.000	48.640	21.500
Left Wing	12.00	50.000	-48.640	21.500
Right Wing Root	4.50 *	51.000	14.500	21.500
Left Wing Root	4.50 *	51.000	-14.500	21.500
Fuselage	72.00	35.125	0.000	21.500
Left Tail Boom	5.00 *	69.125	23.250	21.875
Right Tail Boom	5.00 *	69.125	-23.250	21.875
Vertical Tail R	3.00 *	113.250	23.250	25.500
Vertical Tail L	3.00 *	113.250	-23.250	25.500
Horizontal Tail	7.50 *	112.000	0.000	22.250
Main Landing Gear				
Spar	5.25	55.125	0.000	11.850
Left Wheel	4.38	55.125	-14.500	4.313
Right Wheel	4.38	55.125	14.500	4.313
Nose Gear	5.75	25.000	0.000	7.813
** STRUCTURE	147.75			
Engine	11.00	31.375	0.000	25.125
Alternator	7.00	24.500	0.000	25.125
Propeller	1.22	35.875	0.000	25.125
Throttle Servo	2.50	48.625	1.250	24.000
Ignition	0.50 *	59.625	0.625	24.000
Fuel Tank	0.66	63.750	0.000	18.000
** PROPULSION	22.88			
Video Camera	1.00 *	8.500	0.000	15.000
12V Power Supply	1.00 *	14.250	0.000	19.250
5V Power Supply	0.25 *	17.000	1.750	18.000
Receiver	1.15	17.000	-1.500	18.000
Video Transmitter	0.25 *	16.375	1.625	21.750
Telemetry Trans.	0.25 *	16.375	-1.625	21.375
28V Battery Pack	2.00 *	19.750	-1.000	19.000
Decoder/Failsafe	2.00 *	23.250	0.000	24.000
Steering Servo	0.75 *	22.750	2.250	18.500
Avionics Box	12.00	31.500	0.000	16.500
Alt. Transducer	0.25 *	53.625	2.375	23.500
Brake Servo	0.75 *	48.875	-0.750	17.500
Rate Sensor	0.25 *	52.875	1.250	21.500
Accelerometer	0.25 *	52.250	-2.375	23.750
Airspeed Indicator	0.25 *	52.250	-1.875	21.250
Vertical Gyro	0.25 *	50.875	0.000	25.000
Voltage Regulator	1.00	58.875	-2.000	21.750
** FIXED EQUIPMENT	23.65			

EMPTY WEIGHT	194.28	44.986	-0.130	20.222
Fuel	14.00	63.750	0.000	18.000

TAKE-OFF WEIGHT	208.28	46.247	-0.121	20.073

Table 2.3. Lambda Inertia Estimation.

COMPONENT	MASS (slugs)	Xi-Xcg (ft)	Yi-Ycg (ft)	Zi-Zcg (ft)
Right Wing	0.3575	0.1404	4.0638	0.1028
Left Wing	0.3730	0.1404	-4.0429	0.1028
Right Wing Root	0.1399 *	0.2238	1.2188	0.1028
Left Wing Root	0.1399 *	0.2238	-1.1979	0.1028
Fuselage	2.1759	-1.0992	0.0105	0.1028
Left Tail Boom	0.1554 *	1.7342	1.9480	0.1341
Right Tail Boom	0.1554 *	1.7342	-1.9270	0.1341
Vertical Tail R	0.1710 *	5.4738	1.9480	0.4362
Vertical Tail L	0.1710 *	5.4738	-1.9270	0.4362
Horizontal Tail	0.2331 *	5.3071	0.0105	0.1653
MG Spar	0.1632	0.5675	0.0105	-0.7013
MG Left Wheel	0.1360	0.5675	-1.1979	-1.3294
MG Right Wheel	0.1360	0.5675	1.2188	-1.3294
Nose Gear	0.1321	-1.9429	0.0105	-1.0378
Engine	0.3419	-1.4117	0.0105	0.4049
Alternator	0.2176	-1.9846	0.0105	0.4049
Propeller	0.0379	-1.0367	0.0105	0.4049
Throttle Servo	0.0466	0.0258	0.1146	0.3112
Ignition	0.0311 *	0.9425	0.0625	0.3112
Fuel Tank	0.0205	1.2863	0.0105	-0.1888
Video Camera	0.0233 *	-3.3179	0.0105	-0.4388
12V Power Supply	0.0233 *	-2.8387	0.0105	-0.0847
5V Power Supply	0.0078 *	-2.6096	0.1563	-0.1888
Receiver	0.0357	-2.6096	-0.1145	-0.1888
Video Transmitter	0.0078 *	-2.6617	0.1459	0.1237
Telemetry Trans.	0.0078 *	-2.6617	-0.1250	0.0924
28V Battery Pack	0.0622 *	-2.3804	-0.0729	-0.1055
Decoder/Failsafe	0.0466 *	-2.0887	0.0105	0.3112
Steering Servo	0.0233 *	-2.1304	0.1980	-0.1472
Avionics Box	0.3730	-1.4012	0.0105	-0.3138
Alt. Transducer	0.0078 *	0.4425	0.2084	0.2695
Brake Servo	0.0233 *	0.0467	-0.0520	-0.2305
Rate Sensor	0.0078 *	0.3800	0.1146	0.1028
Accelerometer	0.0078 *	0.3279	-0.1875	0.2903
Airspeed Indicator	0.0078 *	0.3279	-0.1458	0.0820
Vertical Gyro	0.0078 *	0.2133	0.0105	0.3945
Voltage Regulator	0.0311	0.8800	-0.1562	0.1237
Fuel	0.44	1.2863	0.0105	-0.1888

INERTIAS: (slugs/sq. ft.)

	Ixx	Iyy	Izz	Ixy	Iyz	Izx
Empty	16.235	25.930	40.218	-0.006	-0.003	0.698
Take-off	16.251	26.666	40.939	-0.001	-0.004	0.592

2.3. Description of Flight Sensors

Table 2.4 lists the sensors (and their accuracies) onboard the Lambda URV. Sensor data is continuously downlinked (sampled every 1/60th second) to a ground station receiver via the telemetry transmitter.

Table 2.4. Lambda Sensors.

<u>Sensor</u>	<u>Maximum Limits</u>	<u>Accuracy</u>
Roll Rate	± 40 deg/sec	± 1% full scale
Pitch Rate	± 40 deg/sec	± 1% full scale
Yaw Rate	± 40 deg/sec	± 1% full scale
Roll Attitude	± 90 deg	± 1% full scale
Pitch Attitude	± 60 deg	± 1% full scale
Angle of Attack	± 25 deg	± 1 deg
Angle of Sideslip	± 45 deg	± 1 deg
Airspeed	0 - 150 knots	± 2% full scale
Altitude	0 - 10,000 ft	± 100 ft
Longitudinal Accel	± 20 g's	± 2% full scale
Lateral Acceleration	± 3 g's	± 2% full scale
Vertical Acceleration	± 2 g's	± 2% full scale
Aileron Deflection	± 20 deg	± 1 deg
Elevator Deflection	± 20 deg	± 1 deg
Flap Deflection	-10 to 30 deg	± 1 deg
Rudder Deflection	± 25 deg	± 1 deg
Roll Command	± 20 deg	
Pitch Command	± 20 deg	
Yaw Command	± 25 deg	

3. Linear State Space Perturbation Model

This chapter describes the methodology and tools used to develop the linear, state space, small perturbation model for the Lambda Unmanned Research Vehicle. There exist several means by which to estimate a model for the Lambda URV, each varying in cost and time to accomplish. The most direct method is to do wind tunnel testing. Since the budget for the Lambda research vehicle is limited, wind tunnel modeling could not be accomplished. Lambda was designed with inherent stability and is flown quite satisfactorily with open loop controls. Therefore, the approach adopted to estimate the vehicle dynamics was as follows:

Step 1. Develop a conventional, analytical math model for Lambda and use empirical methods to estimate the model parameters.

Step 2. Conduct flight tests and collect time history measurements of the state and control variables.

Step 3. Use the flight test data to validate and fine tune the math model developed in Step 1.

Section 3.1 summarizes the development of an analytical, linear, state-space perturbation model for the Lambda URV. Section 3.2 provides a brief description of the flight tests accomplished with the Lambda URV in November 1990. Section 3.3 discusses the empirical methods used to estimate the model parameters, specifically, the vehicle's stability and control derivatives. Given the airplane geometry and mass properties, these methods, based on data from past aircraft of similar performance and configuration, predict the dimensionless airplane

stability and control derivatives. Section 3.4 details the parameter estimation techniques incorporating the flight test data which were used to tune the airplane math model. Section 3.5 then discusses the modeling of the flight control actuators and the addition of their dynamics into the state space model. The end product, therefore, is a linear state space perturbation model for the Lambda URV which estimates the state perturbation variables for a given set of pilot command inputs. Finally, Section 3.6 gives a general discussion of the overall model and outlines approaches that can be considered to improve the accuracy of this model.

3.1. Derivation of the General State Space Model

Consider an airplane whose motion is tracked with respect to an inertial reference frame as in Figure 3.1. Newton's Second Law in terms of conservation of both linear and angular momentum about the vehicle center of gravity can be expressed as follows [4]:

$$\frac{d}{dt} \int_V \rho_A \frac{d\vec{r}'}{dt} dV = \int_V \rho_A \vec{g} dV + \int_S \vec{F} dS \quad (3.1)$$

(linear momentum) (applied forces)

$$\frac{d}{dt} \int_V \vec{r}' \times \rho_A \frac{d\vec{r}'}{dt} dV = \int_V \vec{r}' \times \rho_A \vec{g} dV + \int_S \vec{r}' \times \vec{F} dS \quad (3.2)$$

(angular momentum) (applied moments)

where $\int_V dV$ and $\int_S dS$ represent volume and exterior surface integrations respectively.

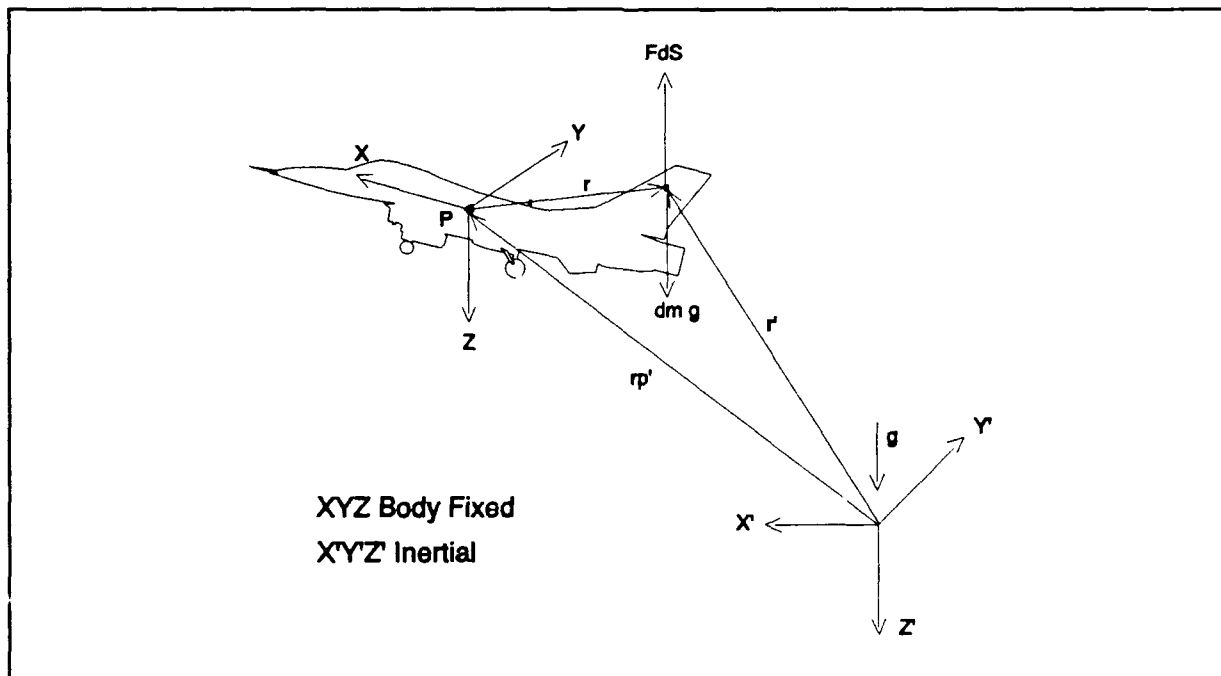


Figure 3.1. Airplane Coordinate System.

The following assumptions are now made [4]:

1. The earth's rotation is negligible, therefore, $X'Y'Z'$ is a fixed coordinate system.
2. The earth's gravitation is uniform and always points in the Z' direction. This is called the "flat earth" assumption.
3. The time span is short, approximately 30 to 60 seconds.
4. The total mass of the airplane is constant with time.
5. The mass distribution of the airplane is constant with time. This is called the "rigid body" assumption.
6. The coordinate system XYZ is a rotating coordinate system and has its origin at the airplane center of mass.
7. The airplane is symmetrical about the $X-Z$ plane; therefore, $I_{xy}=I_{xz}=0$.

From these assumptions, the nine equations of motion for a rigid airplane can be derived and are given in Table 3.1.

Table 3.1. Airplane Equations of Motion.

Force Equations:

$$m(\dot{U} - VR + WQ) = -mg \sin\theta + F_{Ax} + F_{Tx}$$

$$m(\dot{V} + UR - WP) = mg \sin\phi \cos\theta + F_{Ay} + F_{Ty}$$

$$m(\dot{W} - UQ + VP) = mg \cos\phi \cos\theta + F_{Az} + F_{Tz}$$

Moment Equations:

$$I_{xx}\dot{P} - I_{xz}\dot{R} - I_{xz}PQ + (I_{zz} - I_{yy})RQ = L_A + L_T$$

$$I_{yy}\dot{Q} + (I_{xx} - I_{zz})PR + I_{xz}(P^2 - R^2) = M_A + M_T$$

$$I_{zz}\dot{R} - I_{xz}\dot{P} + (I_{yy} - I_{xx})PQ + I_{xz}QR = N_A + N_T$$

Kinematic Equations:

$$P = \dot{\phi} - \dot{\psi} \sin\theta$$

$$Q = \dot{\theta} \cos\phi + \dot{\psi} \cos\theta \sin\phi$$

$$R = \dot{\psi} \cos\theta \cos\phi - \dot{\theta} \sin\phi$$

If steady state flight conditions (accelerations and angular rates equal to zero) are assumed, the general airplane equations of motion reduce to those given in Table 3.2 where the subscript 1 is used to indicate that the flight condition is steady.

Table 3.2. Airplane Steady State Equations of Motion.

Steady State Force Equations:

$$m(-V_1 R_1 + W_1 Q_1) = -mg \sin \theta_1 + F_{Ax1} + F_{Tx1}$$

$$m(U_1 R_1 - W_1 P_1) = mg \sin \phi_1 \cos \theta_1 + F_{Ay1} + F_{Ty1}$$

$$m(-U_1 Q_1 + V_1 P_1) = mg \cos \phi_1 \cos \theta_1 + F_{Az1} + F_{Tz1}$$

Moment Equations:

$$-I_{xz} P_1 Q_1 + (I_{zz} - I_{yy}) R_1 Q_1 = L_{A1} + L_{T1}$$

$$(I_{xx} - I_{zz}) P_1 R_1 + I_{xz} (P_1^2 - R_1^2) = M_{A1} + M_{T1}$$

$$(I_{yy} - I_{xx}) P_1 Q_1 + I_{xz} Q_1 R_1 = N_{A1} + N_{T1}$$

Kinematic Equations:

$$P_1 = \dot{\phi}_1 - \Psi_1 \sin \theta_1$$

$$Q_1 = \dot{\theta}_1 \cos \phi_1 + \Psi_1 \cos \theta_1 \sin \phi_1$$

$$R_1 = \dot{\Psi}_1 \cos \theta_1 \cos \phi_1 - \dot{\theta}_1 \sin \phi_1$$

Now if the motion variables are perturbed from the steady state flight condition, a set of linear perturbation equations about a known steady state condition can be determined. Assuming the initial steady state condition to be rectilinear, level flight, the perturbed state equations of motion relative to this steady state can be extracted (Table 3.3). Steady rectilinear flight is defined as:

- a) no initial side velocity,
- b) no initial bank angle, and
- c) no initial angular velocities.

By perturbing the aerodynamic and thrust force and moment expressions and linearizing about a steady state flight condition, the small perturbation equations of motion as given in Table 3.4 are obtained. Unsubscripted variables are the perturbed quantities.

Table 3.3. Airplane Perturbed Equations of Motion.

Perturbed Force Equations:

$$m(\dot{u} + W_1 q) = -mg\theta \cos\theta_1 + \dot{f}_{Ax} + f_{Tx}$$

$$m(\dot{v} + U_1 r - W_1 p) = mg\phi \cos\theta_1 + \dot{f}_{Ay} + f_{Ty}$$

$$m(\dot{w} - U_1 q) = -mg\theta_1 + \dot{f}_{Az} + f_{Tz}$$

Perturbed Moment Equations:

$$I_{xx}\dot{p} - I_{xz}\dot{r} = \dot{l}_A + l_T$$

$$I_{yy}\dot{q} = \dot{m}_A + m_T$$

$$I_{zz}\dot{r} - I_{xz}\dot{p} = \dot{n}_A + n_T$$

Perturbed Kinematic Equations:

$$p = \dot{\phi} - \psi \sin\theta_1$$

$$q = \dot{\theta}$$

$$r = \dot{\psi} \cos\theta_1$$

Finally, these equations can readily be rearranged into the state space format given in Table 3.5 with the new dimensional stability derivatives defined in Tables 3.6 and 3.7. Tables 3.5, 3.6, and 3.7 form the basis of the airplane math models to be used henceforth. Figure 3.2 defines the geometry used for the math models.

Table 3.4. Airplane Small Perturbation Equations of Motion.

Longitudinal Small Perturbation Equations:

$$\dot{u} = -g\theta\cos\theta_1 + X_u u + X_{T_u} u + X_\alpha \alpha + X_{\delta_e} \delta_e$$

$$\dot{w} - U_1 q = -g\theta\sin\theta_1 + Z_u u + Z_\alpha \alpha + Z_{\dot{\alpha}} \dot{\alpha} + Z_q q + Z_{\delta_e} \delta_e$$

$$\dot{q} = M_u u + M_{T_u} u + M_\alpha \alpha + M_{T_\alpha} \alpha + M_{\dot{\alpha}} \dot{\alpha} + M_q q + M_{\delta_e} \delta_e$$

Lateral-Directional Small Perturbation Equations:

$$\dot{v} + U_1 r = g\phi\cos\theta_1 + Y_\beta \beta + Y_p p + Y_r r + Y_{\delta_a} \delta_a + Y_{\delta_r} \delta_r$$

$$\dot{p} - A_1 \dot{r} = L_\beta \beta + L_p p + L_r r + L_{\delta_a} \delta_a + L_{\delta_r} \delta_r$$

$$\dot{r} - B_1 \dot{p} = N_\beta \beta + N_{T_\beta} \beta + N_p p + N_r r + N_{\delta_a} \delta_a + N_{\delta_r} \delta_r$$

$$A_1 = I_{xz}/I_{xx}$$

$$B_1 = I_{xz}/I_{zz}$$

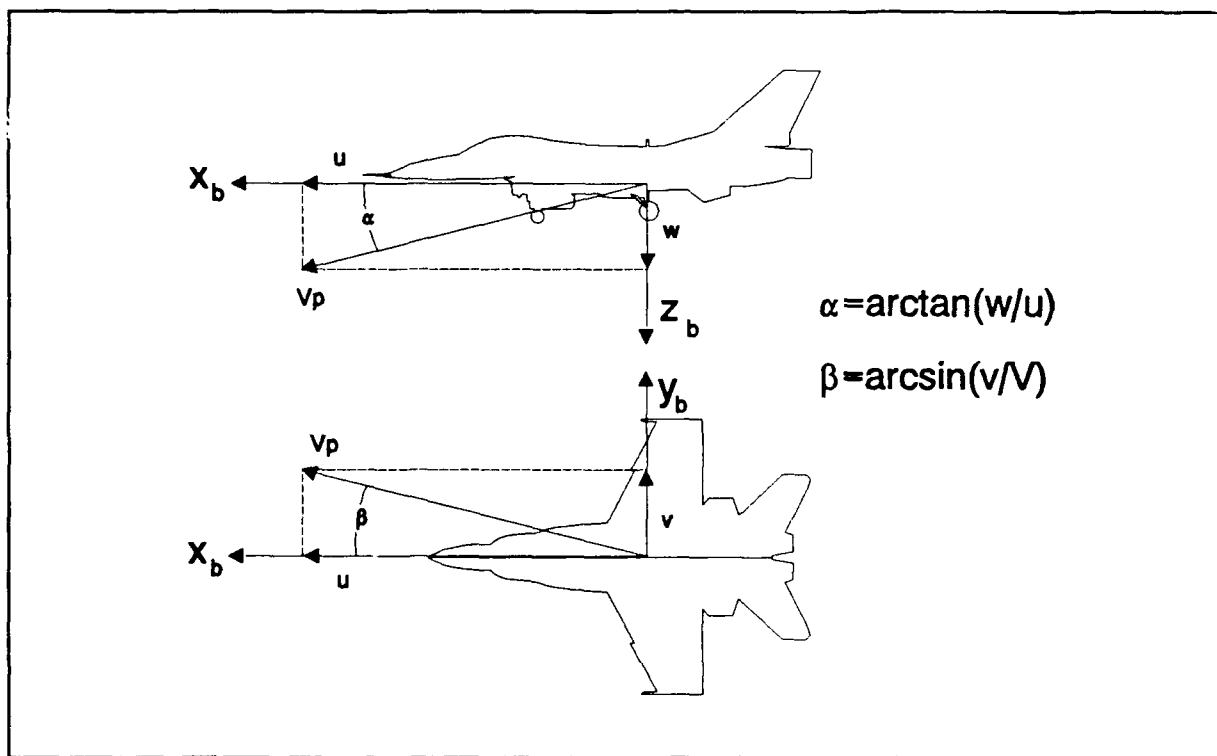


Figure 3.2. Airplane Geometry Used for the Airplane Math Model.

Table 3.5. Airplane State Space Perturbation Model.

Longitudinal Equations of Motion:

$$\begin{Bmatrix} \dot{u} \\ \dot{\alpha} \\ \dot{q} \\ \dot{\theta} \end{Bmatrix} = \begin{bmatrix} X_u & X_\alpha & 0 & -g \cos \theta_1 \\ \frac{Z_u}{U_1 - Z_\alpha} & \frac{Z_\alpha}{U_1 - Z_\alpha} & \frac{U_1 + Z_q}{U_1 - Z_\alpha} & -g \sin \theta_1 \\ M_u + \frac{M_\alpha Z_u}{U_1 - Z_\alpha} & M_\alpha + \frac{M_\alpha Z_\alpha}{U_1 - Z_\alpha} & M_q + \frac{M_\alpha (U_1 + Z_q)}{U_1 - Z_\alpha} & -M_\alpha g \sin \theta_1 \\ 0 & 0 & 1 & 0 \end{bmatrix} \begin{Bmatrix} u \\ \alpha \\ q \\ \theta \end{Bmatrix} + \begin{bmatrix} X_{\delta e} & X_{\delta f} \\ \frac{Z_{\delta e}}{U_1 - Z_\alpha} & \frac{Z_{\delta f}}{U_1 - Z_\alpha} \\ M_{\delta e} + \frac{M_\alpha Z_{\delta e}}{U_1 - Z_\alpha} & M_{\delta f} + \frac{M_\alpha Z_{\delta f}}{U_1 - Z_\alpha} \\ 0 & 0 \end{bmatrix} \begin{Bmatrix} \delta_e \\ \delta_f \end{Bmatrix}$$

Lateral-Directional Equations of Motion:

$$\begin{Bmatrix} \dot{\beta} \\ \dot{p} \\ \dot{\phi} \\ \dot{r} \\ \dot{\psi} \end{Bmatrix} = \begin{bmatrix} \frac{Y_\beta}{U_1} & \frac{Y_p}{U_1} & \frac{g \cos \theta_1}{U_1} & \frac{Y_r}{U_1} - 1 & 0 \\ \frac{L_\beta + A_1 N_\beta}{1 - B_1 A_1} & \frac{L_p + A_1 N_p}{1 - B_1 A_1} & 0 & \frac{L_r + A_1 N_r}{1 - B_1 A_1} & 0 \\ 0 & 1 & 0 & 0 & 0 \\ \frac{N_\beta + B_1 L_\beta}{1 - B_1 A_1} & \frac{N_p + B_1 L_p}{1 - B_1 A_1} & 0 & \frac{N_r + B_1 L_r}{1 - B_1 A_1} & 0 \\ 0 & 0 & 0 & 1 & 0 \end{bmatrix} \begin{Bmatrix} \beta \\ p \\ \phi \\ r \\ \psi \end{Bmatrix} + \begin{bmatrix} \frac{Y_{\delta a}}{U_1} & \frac{Y_{\delta r}}{U_1} \\ \frac{L_{\delta a} + A_1 N_{\delta a}}{1 - B_1 A_1} & \frac{L_{\delta r} + A_1 N_{\delta r}}{1 - B_1 A_1} \\ 0 & 0 \\ \frac{N_{\delta a} + B_1 L_{\delta a}}{1 - B_1 A_1} & \frac{N_{\delta r} + B_1 L_{\delta r}}{1 - B_1 A_1} \\ 0 & 0 \end{bmatrix} \begin{Bmatrix} \delta_a \\ \delta_r \end{Bmatrix}$$

Table 3.6. Airplane Longitudinal Dimensional Stability Derivatives.

$$X_u = - \frac{q_1 S (C_{Du} + 2C_{D1})}{m U_1} \quad (1/\text{sec})$$

$$M_\alpha = \frac{q_1 S c C_{M\alpha}}{I_{yy}} \quad (1/\text{sec}^2)$$

$$X_\alpha = - \frac{q_1 S (C_{D\alpha} - C_{L1})}{m} \quad (\text{ft}/\text{sec}^2)$$

$$M_\dot{\alpha} = \frac{q_1 S c^2 C_{M\dot{\alpha}}}{2 I_{yy} U_1} \quad (1/\text{sec})$$

$$X_{\delta e} = - \frac{q_1 S C_{D\delta e}}{m} \quad (\text{ft}/\text{sec}^2)$$

$$M_q = \frac{q_1 S c^2 C_{Mq}}{2 I_{yy} U_1} \quad (1/\text{sec})$$

$$Z_u = - \frac{q_1 S (C_{Lu} + 2C_{L1})}{m U_1} \quad (1/\text{sec})$$

$$M_{\delta e} = \frac{q_1 S c C_{M\delta e}}{I_{yy}} \quad (1/\text{sec}^2)$$

$$Z_\alpha = - \frac{q_1 S (C_{L\alpha} + C_{D1})}{m} \quad (\text{ft}/\text{sec}^2)$$

$$M_u = \frac{q_1 S c (C_{Mu} + 2C_{M1})}{I_{yy} U_1} \quad (1/\text{ft-sec})$$

$$Z_\dot{\alpha} = - \frac{q_1 S c C_{L\dot{\alpha}}}{2 m U_1} \quad (\text{ft}/\text{sec})$$

$$Z_q = - \frac{q_1 S c C_{Lq}}{2 m U_1} \quad (\text{ft}/\text{sec})$$

$$Z_{\delta e} = - \frac{q_1 S C_{L\delta e}}{m} \quad (\text{ft}/\text{sec}^2)$$

Table 3.7. Airplane Lateral-Directional Dimensional Stability Derivatives.

$Y_{\beta} = \frac{q_1 S C_{Y\beta}}{m} \quad (\text{ft/sec}^2)$	$L_{\delta a} = \frac{q_1 S b C_{l\delta a}}{I_{xx}} \quad (1/\text{sec}^2)$
$Y_p = \frac{q_1 S b C_{Yp}}{2mU_1} \quad (\text{ft/sec})$	$L_{\delta r} = \frac{q_1 S b C_{l\delta r}}{I_{xx}} \quad (1/\text{sec}^2)$
$Y_r = \frac{q_1 S b C_{Yr}}{2mU_1} \quad (\text{ft/sec})$	$N_{\beta} = \frac{q_1 S b C_{n\beta}}{I_{zz}} \quad (1/\text{sec}^2)$
$Y_{\delta a} = \frac{q_1 S C_{Y\delta a}}{m} \quad (\text{ft/sec}^2)$	$N_p = \frac{q_1 S b^2 C_{np}}{2I_{zz}U_1} \quad (1/\text{sec})$
$Y_{\delta r} = \frac{q_1 S C_{Y\delta r}}{m} \quad (\text{ft/sec}^2)$	$N_r = \frac{q_1 S b^2 C_{nr}}{2I_{zz}U_1} \quad (1/\text{sec})$
$L_{\beta} = \frac{q_1 S b C_{l\beta}}{I_{xx}} \quad (1/\text{sec}^2)$	$N_{\delta a} = \frac{q_1 S b C_{n\delta a}}{I_{zz}} \quad (1/\text{sec}^2)$
$L_p = \frac{q_1 S b^2 C_{lp}}{2I_{xx}U_1} \quad (1/\text{sec})$	$N_{\delta r} = \frac{q_1 S b C_{n\delta r}}{I_{zz}} \quad (1/\text{sec}^2)$
$L_r = \frac{q_1 S b^2 C_{lr}}{2I_{xx}U_1} \quad (1/\text{sec})$	

3.2. Description of Flight Tests

Flight testing of the Lambda URV for the Flight Dynamics Laboratory was performed by the contractor Lear-Siegler. Flights were conducted at Jefferson Proving Grounds in southern Indiana. The two flight tests conducted for gathering the data used for this thesis occurred on 20 and 21 November, 1990. Tables 3.8 and 3.9 give a summary of the maneuvers and pertinent conditions during each of those tests. During both tests neither stability augmentation nor feedback control was implemented in the flight control system. Pilot commands were directly uplinked to the vehicle and relayed to the actuators.

Table 3.8. Flight Test #1 Information.

Date: 20 November 1990
Location: Jefferson Proving Grounds, Indiana
Field Elevation: 850 MSL
Temperature: \approx 60 degrees Fahrenheit

Vehicle Weight: 203 lbs (9 lbs fuel)
Approximate Center of Gravity Location: 0.35 MAC

<u>Maneuver</u>	<u>Flaps</u>	<u>Throttle</u>	<u>Speed</u> kts
Pitch Doublet	Half	Full	61
Pitch Doublet	Zero	Full	90
Pitch Doublet	Zero	Half	81
Pitch Doublet	Half	Half	64
Roll Doublet	Zero	Full	92
Roll Doublet	Zero	Half	75
Roll Doublet	Half	Full	76
Roll Doublet	Half	Half	66
Yaw Doublet	Zero	Full	85
Yaw Doublet	Zero	Half	71
Yaw Doublet	Half	Full	66
Yaw Doublet	Half	Half	58

Table 3.9. Flight Test #2 Information.

Date: 21 November 1990
Location: Jefferson Proving Grounds, Indiana
Field Elevation: 850 MSL
Temperature: \approx 60 degrees Farenheit

Vehicle Weight: 203 lbs (9 lbs fuel)
Approximate Center of Gravity Location: 0.35 MAC

<u>Maneuver</u>	<u>Flaps</u>	<u>Throttle</u>	<u>Speed</u> kts
Pitch Doublet	Zero	Full	97
Pitch Doublet	Zero	Half	78
Pitch Doublet	Half	Half	71
Roll Doublet	Zero	Full	98
Roll Doublet	Zero	Half	75
Roll Doublet	Half	Half	69
Yaw Doublet	Zero	Full	94
Yaw Doublet	Zero	Half	79
Yaw Doublet	Half	Half	70

The actual flight test data consisted of 25 parameters continuously sampled during the flight. The sampling rate on the data was 60 hertz. The Flight Dynamics Laboratory truncated the entire set of data collected during a flight into files that consist of 10 seconds of actual flight test data for each maneuver. Each data set usually begins 1-2 seconds before the onset of a maneuver. Table 3.10 lists the sensors used on the Lambda URV and their corresponding accuracy. The throttle setting sensor failed on both flight tests.

Table 3.10. Accuracy of Sensors Onboard the Lambda URV.

<u>Sensor</u>	<u>Maximum Limits</u>	<u>Accuracy</u>
Roll Rate	± 40 deg/sec	± 1% full scale
Pitch Rate	± 40 deg/sec	± 1% full scale
Yaw Rate	± 40 deg/sec	± 1% full scale
Roll Attitude	± 90 deg	± 1% full scale
Pitch Attitude	± 60 deg	± 1% full scale
Angle of Attack	± 25 deg	± 1 deg
Angle of Sideslip	± 45 deg	± 1 deg
Airspeed	0 - 150 knots	± 2% full scale
Altitude	0 - 10,000 ft	± 100 ft
Longitudinal Accel	± 20 g's	± 2% full scale
Lateral Acceleration	± 3 g's	± 2% full scale
Vertical Acceleration	± 2 g's	± 2% full scale
Aileron Deflection	± 20 deg	± 1 deg
Elevator Deflection	± 20 deg	± 1 deg
Flap Deflection	-10 to 30 deg	± 1 deg
Rudder Deflection	± 25 deg	± 1 deg
Roll Command	± 20 deg	
Pitch Command	± 20 deg	
Yaw Command	± 25 deg	

3.3. Estimation of the State Space Model Prior to Incorporation of Flight Test Data

Once the vehicle geometry is known and the mass properties estimated, the first step in deriving the state space model (Table 3.5) is to estimate the dimensionless stability derivatives. Since most airplanes have wide flight envelopes, the dimensionless stability derivatives are not constant. They typically vary throughout the flight envelope, mainly as a function of Mach and Reynold's number. However, the flight envelope for the Lambda URV is very limited:

stall speed \approx 54 knots, no flaps

\approx 45 knots, with flaps

take-off speed \approx 60-70 knots

landing speed \approx 50-70 knots

maximum speed \approx 100 knots

ceiling $<$ 10,000 feet

Therefore, it is reasonable to assure that for a given set of mass properties, the change in dimensionless stability coefficients throughout the flight envelope will be insignificant.

One method of estimating dimensionless stability derivatives is through the use of the USAF Stability and Control Datcom [3]. The fundamental purpose of the USAF Stability and Control Datcom is to provide a systematic summary of methods for estimating stability and control characteristics in preliminary design applications. Datcom is somewhat voluminous and contains various levels of estimation depending on the level of complexity the

engineer is willing to attempt. Part VI of the Roskam Design Texts [8] is an excellent rework of the Datcom manuals condensed in a form which can be easily used by the engineer.

The bulk of the estimation of the dimensionless stability and control derivatives, however, was accomplished through the use of Digital Datcom [9]. Digital Datcom is a computer program developed by the McDonnell Douglas Corporation for the Flight Dynamics Laboratory that calculates static stability, high-lift and control device, and dynamic-derivative characteristics using the methods contained in Sections 4 through 7 of the USAF Stability and Control Datcom. The computer program also offers a trim option that computes control deflections and aerodynamic data for vehicle trim at subsonic Mach numbers. The program requires the user to construct input decks that completely describe the vehicle geometry, center of gravity location, airfoil data, flight conditions, and range of control surface deflections.

A complete set of stability and control derivative estimations using the Datcom program was accomplished for the 12 flight conditions corresponding to the first day of flight tests. All estimations were made with the vehicle weight at 203 pounds and center of gravity location at 48.217 inches (35% of the mean aerodynamic chord). Since Datcom calculates stability and control derivatives over a range of angle of attacks, the trim condition for each flight maneuver had to be determined; the corresponding true angle of attack calculated; and the respective stability and control derivatives obtained from the Datcom

output.

Table 3.11 lists the entire set of estimated dimensionless stability and control derivatives for each of the 12 flight maneuvers from the first day of flight testing. These were obtained by using Datcom and the methods outlined above. A final value for each derivative was selected by taking an average of the derivatives from the 12 different flight conditions. These final dimensionless derivatives are given in Table 3.12.

Using the dimensionless derivatives in Table 3.12, the dimensionless stability and control derivatives can be calculated for each flight condition by using the equations given in Tables 3.6 and 3.7. The vehicle geometric characteristics and inertia values required for these calculations were presented in Tables 2.1 and 2.3 respectively. Once these dimensional derivatives are calculated, the perturbation equations of motion presented in Table 3.5 can be constructed. An example of the resulting perturbation equations for the first pitch doublet on the first flight test is presented in Table 3.13.

Two state space models, one for the longitudinal equations of motion and one for the lateral-directional equations of motion, can be constructed as follows:

Longitudinal:

$$\dot{\underline{x}} = \underline{A} \underline{x} + \underline{B} \delta$$

$$\underline{y} = \underline{C} \underline{x} + \underline{D} \delta$$

Lateral-Directional:

$$\dot{\underline{x}} = \underline{A} \underline{x} + \underline{B} \delta$$

$$\underline{y} = \underline{C} \underline{x} + \underline{D} \delta$$

(3.3)

where,

$\underline{x} \equiv n$ vector of state variables

$\underline{\delta} \equiv m$ vector of control inputs

$\underline{A} \equiv n \times n$ systems dynamics matrix

$\underline{B} \equiv n \times m$ input matrix

$\underline{y} \equiv$ full state measurement vector

$\underline{C} \equiv n \times n$ identity matrix

$\underline{D} \equiv n \times m$ zero matrix

\underline{x} , $\underline{\delta}$, \underline{A} , and \underline{B} were defined in Table 3.5 for both the longitudinal and lateral-directional cases. By choosing \underline{C} to be the identity matrix, the output of the state model will simply be the states themselves.

Table 3.11. Dimensionless Stability and Control Derivatives for the First Flight Test ($X_{cg}=48.217$ inches, $W=203$ pounds).

	F1P1 PDHFFT	F1P2 PDZFFT	F1P3 PDZFHT	F1P4 PDHFHT
W, lbs	203	203	203	203
S, in ²	3038.4	3038.4	3038.4	3038.4
b, in	168	168	168	168
l_v , in	60	60	60	60
z_v , in	2	2	2	2
X_{cg} , % chord	0.35	0.35	0.35	0.35
V, fps	104	152	136	108
ρ , slug/ft ³	0.002240	0.002240	0.002240	0.002240
q, psf	12.11878	25.88687	20.72384	13.06892
M	0.094	0.137	0.123	0.097
RN/ft	628595	921394	825159	652142
CL ₁	0.793879	0.371649	0.464240	0.736162
α , deg	1.14	-0.15	0.82	0.53
(all dimensionless derivatives in per degree)				
C _{Lα}	0.1015	0.102	0.1027	0.101
C _{Mα}	-0.01373	-0.01312	-0.01369	-0.01371
C _{Dα}	0	0	0	0
C _{Lu}	0.000123	0.000124	0.000124	0.000122
C _{Mu}	0	0	0	0
C _{Dq}	0	0	0	0
C _{Lq}	0.1113	0.1132	0.1127	0.1115
C _{Mq}	-0.2549	-0.2584	-0.2574	-0.2553
C _{D$\dot{\alpha}$}	0	0	0	0
C _{L$\dot{\alpha}$}	0.03499	0.03665	0.03551	0.03493
C _{M$\dot{\alpha}$}	-0.1048	-0.1098	-0.1064	-0.1046
C _{Yβ_v}	-0.00625	-0.00625	-0.00625	-0.00625
C _{Yβ}	-0.00763	-0.00763	-0.00763	-0.00763
C _{Lβ}	-0.00026	-0.00023	-0.00025	-0.00024
C _{Nβ}	0.001696	0.001672	0.001679	0.001693
C _{Yp}	-0.00003	-0.00002	-0.00002	-0.00002
C _{Lp}	-0.00917	-0.00933	-0.00935	-0.00913
C _{Np}	-0.00069	-0.00518	-0.00065	-0.00060
C _{Yr}	0.004464	0.004468	0.004465	0.004466
C _{Lr}	0.001689	0.001239	0.001602	0.001461
C _{Nr}	-0.00159	-0.00159	-0.00159	-0.00159
C _{Lδ_e}	0.009	0.0089	0.0089	0.009
C _{Mδ_e}	-0.02484	-0.02439	-0.0245	-0.02478
C _{Yδ_a}	0	0	0	0
C _{Lδ_a}	0.004552	0.004552	0.004552	0.004552
C _{Nδ_a}	-0.00026	-0.00019	-0.00024	-0.00022
C _{Yδ_r}	0.005	0.005	0.005	0.005
C _{Lδ_r}	0.000023	0.000064	0.000033	0.000043
C _{Nδ_r}	-0.00167	-0.00163	-0.00164	-0.00167
C _{Dδ_f}	0.00159	0.00142	0.00154	0.00151
C _{Lδ_f}	0.0245	0.0248	0.0247	0.0245
C _{Mδ_f}	-0.00422	-0.00438	-0.00439	-0.00361

Table 3.11. Continued.

	F1R1 RDZFFT	F1R2 RDZFHT	F1R3 RDHFFT	F1R4 RDHFHT
W, lbs	203	203	203	203
S, in ²	3038.4	3038.4	3038.4	3038.4
b, in	168	168	168	168
l _v , in	60	60	60	60
z _v , in	2	2	2	2
X _{cg} , % chord	0.35	0.35	0.35	0.35
V, fps	156	127	129	111
ρ, slug/ft ³	0.002240	0.002240	0.002240	0.002240
q, psf	27.26727	18.07173	18.64540	13.80506
M	0.141	0.114	0.116	0.1
RN/ft	945964	768852	781137	673641
CL ₁	0.352835	0.532370	0.515990	0.696907
α, deg	-0.35	1.53	-1.85	0.12
(all dimensionless derivatives in per degree)				
C _{Lα}	0.1024	0.1021	0.09901	0.1006
C _{Mα}	-0.01451	-0.01123	-0.01323	-0.0132
C _{Du}	0	0	0	0
C _{Lu}	0.000124	0.000122	0.000122	0.000122
C _{Mu}	0	0	0	0
C _{Dq}	0	0	0	0
C _{Lq}	0.1125	0.1114	0.1124	0.1117
C _{Mq}	-0.2563	-0.2541	-0.2571	-0.2557
C _{Dδ}	0	0	0	0
C _{Lδ}	0.0344	0.03174	0.03568	0.03592
C _{Mδ}	-0.103	-0.09506	-0.1069	-0.1076
C _{Yβv}	-0.00625	-0.00625	-0.00625	-0.00625
C _{Yβ}	-0.00763	-0.00763	-0.00763	-0.00763
C _{lβ}	-0.00022	-0.00027	-0.00018	-0.00023
C _{nβ}	0.001671	0.001683	0.001682	0.001691
C _{Yp}	-0.00002	-0.00003	-0.00001	-0.00002
C _{lp}	-0.00932	-0.00937	-0.00897	-0.00911
C _{np}	-0.00048	-0.00075	-0.00026	-0.00054
C _{Yr}	0.004468	0.004462	0.004470	0.004467
C _{lr}	0.001164	0.001868	0.000579	0.001309
C _{nr}	-0.00159	-0.00159	-0.00159	-0.00159
C _{Lδe}	0.0089	0.0089	0.0089	0.009
C _{Mδe}	-0.02437	-0.02456	-0.02449	-0.02432
C _{Yδa}	0	0	0	0
C _{lδa}	0.004552	0.004552	0.004552	0.004552
C _{nδa}	-0.00022	-0.00021	-0.00009	-0.00020
C _{Yδr}	0.005	0.005	0.005	0.005
C _{lδr}	0.000070	0.000011	0.000117	0.000055
C _{nδr}	-0.00163	-0.00165	-0.00165	-0.00164
C _{Dδf}	0.0014	0.00164	0.00118	0.00146
C _{Lδf}	0.0248	0.0247	0.0247	0.0246
C _{Mδf}	-0.00312	-0.00358	-0.00423	-0.00436

Table 3.11. Continued.

	F1Y1 YDZFFT	F1Y2 YDZFHT	F1Y3 YDHFFT	F1Y4 YDHFHT
W, lbs	203	203	203	203
S, in ²	3038.4	3038.4	3038.4	3038.4
b, in	168	168	168	168
l _v , in	60	60	60	60
z _v , in	2	2	2	2
X _{cg} , % chord	0.35	0.35	0.35	0.35
V, fps	144	119	111	99
ρ, slug/ft ³	0.002240	0.002240	0.002240	0.002240
q, psf	23.23365	15.86669	13.80506	10.98153
M	0.13	0.108	0.1	0.089
RN/ft	874300	722782	672617	597882
CL ₁	0.414091	0.606355	0.696907	0.876094
α, deg	0.3	2.3	0.12	2.01
(all dimensionless derivatives in per degree)				
C _{Lα}	0.1023	0.1033	0.1006	0.1011
C _{Mα}	-0.01333	-0.01388	-0.01332	-0.01118
C _{Du}	0	0	0	0
C _{Lu}	0.000124	0.000124	0.000122	0.000122
C _{Mu}	0	0	0	0
C _{Dq}	0	0	0	0
C _{Lq}	0.1129	0.112	0.1106	0.1099
C _{Mq}	-0.2581	-0.2564	-0.2527	-0.2512
C _{Dδ}	0	0	0	0
C _{Lδ}	0.03622	0.03506	0.03293	0.03101
C _{Mδ}	-0.1085	-0.105	-0.09864	-0.09288
C _{Yβv}	-0.00625	-0.00625	-0.00625	-0.00625
C _{Yβ}	-0.00763	-0.00763	-0.00763	-0.00763
C _{lβ}	-0.00024	-0.00029	-0.00023	-0.00028
C _{nβ}	0.001675	0.001687	0.001692	0.001699
C _{Yp}	-0.00002	-0.00003	-0.00002	-0.00003
C _{lp}	-0.00934	-0.00939	-0.00911	-0.00921
C _{np}	-0.00058	-0.00086	-0.00054	-0.00081
C _{Yr}	0.004467	0.004458	0.004467	0.004459
C _{lr}	0.001407	0.002159	0.001309	0.002015
C _{nr}	-0.00159	-0.00158	-0.00159	-0.00158
C _{Lδe}	0.0089	0.0089	0.009	0.009
C _{Mδe}	-0.02444	-0.02463	-0.02467	-0.02449
C _{Yδa}	0	0	0	0
C _{lδa}	0.004552	0.004552	0.004552	0.004552
C _{nδa}	-0.00022	-0.00033	-0.00020	-0.00031
C _{Yδr}	0.005	0.005	0.005	0.005
C _{lδr}	0.000050	-0.00001	0.000055	-0.00000
C _{nδr}	-0.00164	-0.00166	-0.00166	-0.00166
C _{Dδf}	0.00148	0.00174	0.00146	0.00171
C _{Lδf}	0.0247	0.0246	0.0246	0.0245
C _{Mδf}	-0.0044	-0.00361	-0.0031	-0.00357

Table 3.12. Average Dimensionless Derivatives for the First Flight Test ($X_{cg}=48.217$ inches, $W=203$ pounds).

AVERAGE DIMENSIONLESS COEFFICIENTS OVER 12 FLIGHT CONDITIONS.

	1/deg	1/rad		1/deg	1/rad
$C_{L\alpha}$	0.1016	5.8184	$C_{L\delta e}$	0.0089	0.5123
$C_{M\alpha}$	-0.0132	-0.7550	$C_{M\delta e}$	-0.0245	-1.4060
C_{Du}	0.0	0.0	$C_{Y\delta a}$	0.0	0.0
C_{Lu}	0.0001	0.0071	$C_{l\delta a}$	0.0045	0.2608
C_{Mu}	0.0	0.0	$C_{n\delta a}$	-0.0002	-0.0131
C_{Dq}	0.0	0.0	$C_{Y\delta r}$	0.0050	0.2865
C_{Lq}	0.1118	6.4081	$C_{l\delta r}$	0.0001	0.0024
C_{Mq}	-0.2556	-14.647	$C_{n\delta r}$	-0.0017	-0.0945
$C_{D\dot{\alpha}}$	0.0	0.0	$C_{D\delta f}$	0.0015	0.0866
$C_{L\dot{\alpha}}$	0.0346	1.9817	$C_{L\delta f}$	0.0246	1.4119
$C_{M\dot{\alpha}}$	-0.1036	-5.9357	$C_{M\delta f}$	-0.0039	-0.2224
$C_{Y\beta v}$	-0.0063	-0.3584			
$C_{Y\beta}$	-0.0076	-0.4372			
$C_{l\beta}$	-0.0002	-0.0143			
$C_{n\beta}$	0.0017	0.0965			
C_{Yp}	-0.0001	-0.0016			
C_{lp}	-0.0092	-0.5292			
C_{np}	-0.0010	-0.0574			
C_{Yr}	0.0045	0.2559			
C_{lr}	0.0015	0.0850			
C_{nr}	-0.0016	-0.0913			

Table 3.13. Calculation of Dimensional Derivatives and State Space Model for the First Pitch Doublet, Flight Test #1.

weight	W	203 lbs
wing area	S	21.1 sq ft
wing span	b	14.07 ft
mean aerodynamic chord	c	1.51 ft
airspeed	U	104 fps
density	ρ	0.002240 slugs/ft ³
inertias	Ixx	16.251 slugs-ft ²
	Iyy	26.666 slugs-ft ²
	Izz	40.939 slugs-ft ²
	Ixz	0.5922 slugs-ft ²
trimmed lift coefficient	C _{L1}	0.793879
trimmed drag coefficient	C _{D1}	0.029
trimmed moment coefficient	C _{M1}	0
trimmed thrust coefficient	C _{Tx1}	0
trimmed thrust moment coefficient	C _{Mx1}	0

Nondimensional Derivatives:

Dimensional Derivatives:

Longitudinal Derivatives:

C _{Mu}	0	M _u	0 rad/ft sec
C _{Mα}	-0.75501	M _α	-10.9323 1/sec ²
C _{Mδ}	-5.93574	M _δ	-0.62394 1/sec
C _{Mq}	-14.6467	M _q	-1.53962 1/sec
C _{MTu}	0	M _{Tu}	0 rad/ft sec
C _{MTα}	0	M _{Tα}	0 1/sec ²
C _{Lu}	0.007071	Z _u	-0.62140 1/sec ²
C _{Lα}	5.818434	Z _α	-236.952 ft/sec ²
C _{Lδ}	1.98167	Z _δ	-0.58296 ft/sec
C _{Lq}	6.408055	Z _q	-1.88510 ft/sec
C _{Da}	0	X _α	32.17 ft/sec ²
C _{Du}	0	X _u	-0.02259 1/sec
C _{Txu}	0	X _{Tu}	0 1/sec
C _{Lδe}	0.512319	Z _{δe}	-20.7604 ft/sec ²
C _{Dδe}	0	X _{δe}	0 ft/sec ²
C _{Mδe}	-1.40603	M _{δe}	-20.3589 1/sec ²
C _{Lδf}	1.411863	Z _{δf}	-57.2122 ft/sec ²
C _{Dδf}	0.086564	X _{δf}	-3.50779 ft/sec ²
C _{Mδf}	-0.22235	M _{δf}	-3.21956 1/sec ²

Table 3.13. Continued.

Nondimensional Derivatives:

Dimensional Derivatives:

Lateral-Directional Derivatives:

$C_{l\beta}$	-0.01431	L_{β}	-3.16807 1/sec ²
C_{lp}	-0.52922	L_p	-7.92542 1/sec
C_{lr}	0.084997	L_r	1.272887 1/sec ²
$C_{l\delta a}$	0.260844	$L_{\delta a}$	57.74793 1/sec ²
$C_{l\delta r}$	0.002439	$L_{\delta r}$	0.539967 1/sec ²
$C_{n\beta}$	0.096543	N_{β}	8.484363 1/sec ²
C_{np}	-0.05738	N_p	-0.34110 1/sec
C_{nr}	-0.09132	N_r	-0.54286 1/sec ²
$C_{n\delta a}$	-0.01311	$N_{\delta a}$	-1.15212 1/sec ²
$C_{n\delta r}$	-0.09453	$N_{\delta r}$	-8.30745 1/sec ²
$C_{y\beta}$	-0.43716	Y_{β}	-17.7148 ft/sec ²
C_{yp}	-0.00155	Y_p	-0.00424 ft/sec
C_{yr}	0.25585	Y_r	0.701317 ft/sec ²
$C_{y\delta a}$	0	$Y_{\delta a}$	0 ft/sec ²
$C_{y\delta r}$	0.286478	$Y_{\delta r}$	11.60881 ft/sec ²
		A_1	0.03644
		B_1	0.01446

Table 3.13. Continued.

STATE SPACE COEFFICIENTS:

Longitudinal: $\theta_1 = 0 \text{ rad}$

$$\begin{bmatrix} \dot{u} \\ \dot{\alpha} \\ \dot{q} \\ \dot{\theta} \end{bmatrix} = \begin{bmatrix} -0.02259 & 32.17 & 0 & -32.174 \\ -0.00594 & -2.26569 & 0.976400 & 0 \\ 0.003707 & -9.51866 & -2.14884 & 0 \\ 0 & 0 & 1 & 0 \end{bmatrix} \begin{bmatrix} u \\ \alpha \\ q \\ \theta \end{bmatrix}$$

$$+ \begin{bmatrix} 0 & -3.50779 \\ -0.19850 & -0.54705 \\ -20.2350 & -2.87823 \\ 0 & 0 \end{bmatrix} \begin{bmatrix} \delta_e \\ \delta_f \end{bmatrix}$$

Lateral-Directional:

$$\begin{bmatrix} \dot{\beta} \\ \dot{p} \\ \dot{\phi} \\ \dot{r} \\ \dot{\psi} \end{bmatrix} = \begin{bmatrix} -0.17033 & -0.00004 & 0.309365 & -0.99325 & 0 \\ -2.86040 & -7.94204 & 0 & 1.25377 & 0 \\ 0 & 1 & 0 & 0 & 0 \\ 8.44299 & -0.45599 & 0 & -0.52473 & 0 \\ 0 & 0 & 0 & 1 & 0 \end{bmatrix} \begin{bmatrix} \beta \\ p \\ \phi \\ r \\ \psi \end{bmatrix}$$

$$+ \begin{bmatrix} 0 & 0.11162 \\ 57.7364 & 0.23736 \\ 0 & 0 \\ -0.31694 & -8.30402 \\ 0 & 0 \end{bmatrix} \begin{bmatrix} \delta_a \\ \delta_r \end{bmatrix}$$

3.4. Inclusion of Flight Test Data in Parameter Estimation

The state time responses using the perturbation model derived in Section 3.3 can now be plotted against the actual perturbation time responses from the flight test data by using the following approach:

1. For the input time history vector \underline{U} , the actual control surface deflection time histories (specifically, the perturbation deflections from an initial steady state value) will be used. The perturbation deflection values are obtained by assuming the airplane is at a steady state value at the beginning of the time history; therefore, the first value in the control deflection time history vector is subtracted from all the rest of the values in the vector.
2. The actual perturbation time responses are calculated from the flight test data by subtracting from the entire response time history vector the steady state value for the parameter before the maneuver.

Plots of the time histories of each of the data parameters for every flight maneuver were generated. Appendix A contains a complete set of plots for the first pitch doublet on the first day of flight testing. Inspection of the flight test data for all 21 maneuvers reveals the following:

1. The measurement data is corrupted by noise.
2. The longitudinal and lateral acceleration data is heavily noise corrupted and possibly unusable.

3. Some of the rate data is incomplete due to the sensors reaching their maximum limits.
4. The angle of attack, pitch attitude, and angle of sideslip data provided by the Flight Control Division had sign inversions. These were corrected for the plots presented in Appendix A.
5. The longitudinal time responses are characterized by two modes: the short period mode time response and the phugoid mode time response. It was observed from the angle of attack and pitch rate time response plots that the frequency, damping ratio, and magnitude of the short period time responses are not accurately modeled. It appears that the output magnitude needs to be decreased, frequency increased, and damping ratio reduced. Observing the speed and pitch attitude time responses indicates that the phugoid mode is not modeled correctly.
6. The lateral-directional time responses are characterized by three modes: the roll mode, spiral mode, and dutch roll time responses. The roll rate and roll attitude time responses show that the roll mode time constant is inaccurately modeled. The angle of sideslip and yaw rate time responses indicate that the magnitude, frequency, and damping of the dutch roll time responses are not modeled accurately. It is difficult (if not impossible) to tell from the plots how accurately the spiral mode is modeled.
7. Overall, the general shapes and trends of the time responses of the perturbation model resemble the actual time responses from the flight test data.

Therefore, by focusing on the short period and phugoid approximations for the longitudinal equations of motion and the roll and dutch roll approximations for the lateral-directional equations of motion, the appropriate dimensionless derivatives were systematically varied to obtain appropriate overall time response characteristics. The procedure for accomplishing this systematic variation in dimensionless derivatives will now be discussed.

Many different approaches exist for identifying stability and control derivatives from flight test data. The more successful approaches involve maximum likelihood estimation techniques which incorporate Kalman filters in the routines to provide state and measurement estimates [10, 11, 12, 13]. These methods often include techniques such as constrained parameter optimization and a priori parameter weighting (often based on wind tunnel data) [10]. Good parameter estimates can be directly obtained from maximum likelihood techniques, especially if the following are accomplished prior to flight testing:

1. Compilation of a thorough description of the data acquisition system [12]. Sensor noise should be completely characterized (through power spectral density analysis) and any biases identified. The effects of data sampling rates and record lengths should also be researched.
2. Turbulence during flight testing needs to be addressed [12]. The parameter estimation techniques to be used should account for the effect of added measurement noise due to atmospheric turbulence.

3. A structural mode analysis should be conducted. In general, if the structural frequencies are higher than the highest aerodynamic frequency by more than a factor of 5 to 10, structural modes can be neglected [12].

4. Characterization of servo dynamics should be accomplished prior to flight testing. The order of the servo dynamics model can seriously impact the efficiency of the parameter identification techniques used.

The main theme from most of the literature in this field of study is that if the above are not thoroughly investigated prior to flight testing, direct parameter identification from maximum likelihood techniques is questionable. What occurs most often when the above are not taken into account is that the maximum likelihood techniques "fit" the flight test data very well but the corresponding parameter estimates may make no physical sense. In these cases, it is not at all unlikely that the stability and control derivatives estimated may have the wrong sign and/or unrealistic magnitudes.

Unfortunately, none of the above considerations were made prior to flight tests of the Lambda vehicle. Sensor noise was not characterized (estimates of sensor accuracy were made), servo dynamics were not characterized, turbulence levels during flight testing were not recorded, and no structural analysis was performed on the vehicle. Consequently, the use of maximum likelihood techniques to directly estimate Lambda's stability and control derivatives led to parameter estimates that fit the

flight test data well but made no physical sense. Therefore, the following ad hoc approach was formulated:

Step 1. Maximum likelihood estimation was used on the data for each pitch doublet maneuver (pitch rate and angle of attack time histories) to derive a second order linear model that fit the flight test data well. Perfect measurements were assumed and the measurements of actual control surface deflection were used (in lieu of pilot command inputs). The eigenvalues of the corresponding estimated state dynamics matrix were then used to calculate the natural frequency and damping ratio of the second order model. These modes correspond to the natural frequency and damping ratio of the standard airplane short period approximation.

Step 2. Step 1 was repeated for each yaw doublet maneuver using the yaw rate and angle of sideslip time histories. Therefore, the result of this step was an estimation of the natural frequency and damping ratio of the standard airplane dutch roll approximation.

Step 3. Maximum likelihood estimation was then used on the data for each roll doublet (roll rate time history) to develop a first order model for the roll mode time constant.

Step 4. Using Digital Datcom, the stability and control derivatives for each flight test maneuver were estimated, and the standard approximations for short period natural frequency and damping ratio, roll mode time constant, and dutch roll natural frequency and damping ratio were calculated. Table 3.14 provides a brief summary of the equations used for these approximations.

Table 3.14. Summary of Short Period, Roll, and Dutch Roll Approximation Equations.

SHORT PERIOD APPROXIMATION:

- α - and θ - degrees of freedom only

$$\omega_{nsp} = \sqrt{\frac{Z_{\alpha}M_q}{U_1} - M_{\alpha}} \quad \zeta_{sp} = -\frac{(M_q + M_{\dot{\alpha}} + Z_{\alpha}/U_1)}{2\omega_{nsp}}$$

PHUGOID APPROXIMATION:

- u - and θ - degrees of freedom only

$$\omega_{np} = \sqrt{-\frac{Z_u \dot{\alpha}}{U_1}} \quad \zeta_p = -\frac{X_u}{2\omega_{np}}$$

ROLL APPROXIMATION:

- ϕ - degree of freedom only

$$T_R = -1/L_p$$

SPIRAL APPROXIMATION:

- β - and r - degrees of freedom only

$$T_S = -\frac{(L_{\beta} + N_{\beta}A_1)}{L_{\beta}N_r - N_{\beta}L_r}$$

DUTCH ROLL APPROXIMATION:

- β - and ψ - degrees of freedom only

$$\omega_{ndr} = \sqrt{(Y_{\beta}N_r + N_{\beta}U_1 - N_{\beta}Y_r)/U_1} \quad \zeta_{dr} = -\frac{N_r + Y_{\beta}/U_1}{2\omega_{ndr}}$$

Step 5. The results of Step 4 were compared to the maximum likelihood estimates in Steps 1 through 3. The Datcom derivative estimates were adjusted until an acceptable overall constant value of each stability and control derivative was found that fit the overall second or first order characteristics of the flight

test data well. For example, iteration on $C_{M\alpha}$ led to value that estimated the short period natural frequency for each pitch doublet maneuver reasonably well.

Admittedly, this ad hoc approach was not able to derive parameter estimates for the "weaker" phugoid and spiral modes. However, as will be shown, this approach was able to accurately model all rate time responses and α , β time responses. θ and ϕ time responses were less accurately modeled and speed time response modeling often varied significantly from flight test data. Also, some roll and pitch mode coupling was observed in the flight test data which, again, this approach was not able to address. In general, linear small perturbation theory will not be able to adequately model pitch/roll mode coupling. Nonlinear techniques should be used if this phenomenon is to be accurately studied. A discussion of the actual implementation and results of accomplishing Steps 1 through 5 will now be given.

A fourth order longitudinal state space model was developed in Section 3.2 to estimate the u , α , q , and θ time responses to elevator and flap deflections; and a fifth order lateral-directional state space model was constructed to estimate the β , p , ϕ , r , and Ψ time responses to aileron and rudder deflections. To estimate the appropriate frequencies, damping ratios, and time constants for the actual time responses, these fourth and fifth order models were reduced to either first or second order models using the short period, roll, and dutch roll approximations (Table 3.14). The short period approximation used a two state

model and focused on the α - and q - degrees of freedom. The roll approximation used a single state model and focused on the p - degree of freedom. The dutch roll approximation used a two state model and focused on the β - and r - degrees of freedom.

The second order state space model used for the maximum likelihood estimations was as follows:

$$\begin{bmatrix} \dot{x}_1 \\ \dot{x}_2 \end{bmatrix} = \begin{bmatrix} P(1) & P(2) \\ P(4) & P(5) \end{bmatrix} \begin{bmatrix} x_1 \\ x_2 \end{bmatrix} + \begin{bmatrix} P(3) \\ P(6) \end{bmatrix} \delta \quad (3.4)$$

$$\hat{y} = [C_1 \ C_2] \begin{bmatrix} x_1 \\ x_2 \end{bmatrix}$$

where the values C_1 and C_2 are known constants, parameters $P(1)$ through $P(6)$ are to be estimated, and \hat{y} is the estimated sensor measurement to be compared to the actual measurement y . It was assumed there was no process or measurement noise, and the actual surface deflection time histories for the control input were used. It was also assumed that the system started from rest (zero initial conditions). The objective, then, was to vary the parameters $P(1)$ through $P(6)$ until the error between y and \hat{y} over the entire time history was made as small as possible. Therefore, the maximum likelihood approach used minimized the quadratic cost function:

$$RSS = \sqrt{\sum (y - \hat{y})^2} \quad (3.5)$$

where RSS is the root sum square of the error between y and \hat{y} at each sample in the time history. A similar set-up can be shown for a simple first order model. The maximum likelihood routine in the program MATRIXx developed by Integrated Systems, Inc. of Palo Alto, California, was used to perform all maximum likelihood estimates presented in this thesis.

A two state maximum likelihood model was estimated for each pitch doublet from the first day of flight testing; a single state maximum likelihood model was estimated for each roll doublet; and a two state maximum likelihood model was estimated for each yaw doublet. Appendix B contains an example for each type of maneuver of the data fit achieved from the maximum likelihood iterations.

The results from the maximum likelihood iterations were as follows:

1. The maximum likelihood calculations arrived at parameters for the state models that fit the actual time responses fairly well. In theory, direct back-calculation of the dimensional derivatives from the parameters converged upon by the maximum likelihood iterations should yield the "ideal" stability and control derivatives. Unfortunately, this only comes close to being true for the roll mode approximation. The dimensional derivatives back-calculated for both the short period and dutch roll approximations lead to unrealistic values. Some derivatives even had incorrect signs.

2. The eigenvalues of the maximum likelihood state dynamics matrix approximate the characteristic natural frequency and damping ratio of the actual time responses for the two state models or the time constant of the actual time response for the one state model.

3. The estimated maximum likelihood models for the pitch doublets revealed that the short period natural frequency from the Datcom estimates needed to be increased and damping ratio needed to be decreased. Table 3.15 compares the values of the natural frequency and damping ratio between the maximum likelihood results and the initial Datcom estimations. From the short period approximation equations, increasing the magnitude of M_a will directly increase the short period natural frequency and decreasing the magnitude of M_a will directly decrease the short period damping ratio. There is really only one effective way to increase the magnitude of M_a -- increase $C_{M\alpha}$. Recall that $C_{M\alpha}$ is approximated by:

$$C_{M\alpha} = C_{L\alpha}(X_{cg} - X_{ac}) \quad (3.6)$$

Since the Datcom methods for estimating the value for $C_{L\alpha}$ and the location of the airplane aerodynamic center are usually quite accurate, the center of gravity location should be the variable to change to increase $C_{M\alpha}$. Recall that the mass property data received from the Flight Dynamics Laboratory was suspect and the value given for the c.g. location highly questionable. Using Datcom, plots of short period frequency and damping ratio as a function of c.g. location were constructed. From these, an

appropriate value of X_{cg} was selected that provided appropriate values of short period natural frequency and damping ratio.

Table 3.15. Comparison of Short Period Approximation Characteristics.

$$X_{cg} = 48.217 \text{ inches}$$

<u>Flight Maneuver</u>	DATCOM		MAXLIKE	
	ω_{nsp} (rad/sec)	ζ_{sp}	ω_{nsp} (rad/sec)	ζ_{sp}
F1P1	3.800	0.4203	4.667	0.2218
F1P2	5.554	0.4203	6.359	0.3334
F1P3	4.969	0.4203	5.871	0.3050
F1P4	3.946	0.4203	4.529	0.2517

where, (First Day Flight Test)

F1P1 - Pitch Doublet, Half Flaps, Full Throttle
 F1P2 - Pitch Doublet, Zero Flaps, Full Throttle
 F1P3 - Pitch Doublet, Zero Flaps, Half Throttle
 F1P4 - Pitch Doublet, Half Flaps, Half Throttle

4. The roll maximum likelihood estimation revealed that the initial roll mode time constant needed to be decreased by almost a factor of two. Table 3.16 compares the values of the roll mode time constants between the maximum likelihood results and the initial Datcom estimations. Again, the methods used by Datcom to estimate C_{lp} have been proven through experience to be quite accurate, which again points to the questionability of the mass property, I_{xx} . A quick estimation of the roll inertia, I_{xx} , based on inertia data of airplanes with a similar configuration to Lambda ("radius of gyration" method [7]) revealed that indeed the initial value of 16.25 slugs-sq. ft. appeared to be low. Doubling the initial value of I_{xx} led to time responses that closely fit the roll rate and roll attitude flight test data.

Table 3.16. Comparison of Roll Approximation Characteristics.

$$X_{cg} = 48.217 \text{ inches}$$

<u>Flight Maneuver</u>	DATCOM		MAXLIKE	
	$\frac{L_p}{1/\text{sec}}$	$\frac{L_{\delta a}}{1/\text{sec}^2}$	$\frac{L_p}{1/\text{sec}}$	$\frac{L_{\delta a}}{1/\text{sec}^2}$
F1R1	-11.91	129.9	-4.580	45.83
F1R2	-9.698	86.10	-4.149	34.03
F1R3	-9.851	88.83	-4.780	38.62
F1R4	-8.476	65.77	-4.579	32.99

where, (First Day Flight Test)

F1R1 - Roll Doublet, Zero Flaps, Full Throttle
 F1R2 - Roll Doublet, Zero Flaps, Half Throttle
 F1R3 - Roll Doublet, Half Flaps, Full Throttle
 F1R4 - Roll Doublet, Half Flaps, Half Throttle

5. The estimated maximum likelihood models for the yaw doublets showed that the dutch roll natural frequency needed to be decreased and dutch roll damping ratio increased. Table 3.17 compares the values of the natural frequency and damping ratio between the maximum likelihood results and the initial Datcom estimations. From the dutch roll approximation equations, it is observed that decreasing N_β will directly decrease the dutch roll natural frequency, and increasing N_r will directly increase the dutch roll damping ratio. Changes in N_β and N_r will be accomplished by adjusting the nondimensional coefficients $C_{n\beta}$ and C_{nr} , respectively.

Table 3.17. Comparison of Dutch Roll Approximation Characteristics.

$$X_{cg} = 48.27 \text{ inches}$$

<u>Flight Maneuver</u>	DATCOM		MAXLIKE	
	ω_{ndr} (rad/sec)	ζ_{dr}	ω_{ndr} (rad/sec)	ζ_{dr}
F1Y1	4.041	0.1222	3.226	0.1646
F1Y2	3.340	0.1222	2.423	0.2491
F1Y3	3.115	0.1222	2.695	0.2029
F1Y4	2.779	0.1222	2.382	0.1818

where, (First Day Flight Test)

F1Y1 - Yaw Doublet, Zero Flaps, Full Throttle
 F1Y2 - Yaw Doublet, Zero Flaps, Half Throttle
 F1Y3 - Yaw Doublet, Half Flaps, Full Throttle
 F1Y4 - Yaw Doublet, Half Flaps, Half Throttle

Two more Datcom runs were accomplished at vehicle center of gravity locations forward of the c.g. location from the initial Datcom run. The c.g. locations chosen were at $X_{cg}=47.311$ inches and 45.311 inches. The c.g. location of 47.311 inches corresponds to the most forward location based on the mass property data provided by the Flight Control Division.

The longitudinal dimensional derivatives for the first two pitch doublet maneuvers on the first flight test were estimated and the corresponding short period natural frequency and damping ratio calculated. Figures 3.3 and 3.4 plot the change in short period natural frequency and damping ratio, respectively, versus vehicle center of gravity location for the two flight conditions. From the maximum likelihood estimations, a short period natural frequency of 4.67 rad/sec is optimum for the first flight condition and a natural frequency of 6.36 rad/sec is optimum for

the second flight condition. From Figure 3.3 it is seen that not one c.g. location will provide both of these natural frequencies but a c.g. location of 47.2 inches comes fairly close (much closer than the original estimate of 48.217 inches). Thus, the value of 47.2 inches was chosen as the best estimate for the center of gravity location for the overall vehicle weight of 203 pounds. A final, complete set of Datcom runs were then accomplished (for all 12 flight conditions on the first day flight test) for this new c.g. location and the dimensionless derivatives correspondingly calculated. Table 3.18 gives the final values for the new set of dimensionless coefficients.

Table 3.18. Average Dimensionless Derivatives for the First Flight Test ($X_{cg}=47.2$ inches, $W=203$ pounds).

AVERAGE DIMENSIONLESS COEFFICIENTS OVER 12 FLIGHT CONDITIONS.

	1/deg	1/rad		1/deg	1/rad
$C_{L\alpha}$	0.1016	5.8203	$C_{L\delta e}$	0.0051	0.2908
$C_{M\alpha}$	-0.0192	-1.1014	$C_{M\delta e}$	-0.0147	-0.8449
C_{Du}	0.0	0.0	$C_{Y\delta a}$	0.0	0.0
C_{Lu}	0.0001	0.0071	$C_{l\delta a}$	0.0046	0.2608
C_{Mu}	0.0	0.0	$C_{n\delta a}$	-0.0002	-0.0137
C_{Dq}	0.0	0.0	$C_{Y\delta r}$	0.0050	0.2865
C_{Lq}	0.1241	7.1128	$C_{l\delta r}$	0.0001	0.0022
C_{Mq}	-0.2687	-15.397	$C_{n\delta r}$	-0.0016	-0.0943
$C_{D\dot{\alpha}}$	0.0	0.0	$C_{D\delta f}$	0.0015	0.0849
$C_{L\dot{\alpha}}$	0.0353	2.0232	$C_{l\delta f}$	0.0246	1.4185
$C_{M\dot{\alpha}}$	-0.1077	-6.1735	$C_{M\delta f}$	-0.0050	-0.2904
$C_{Y\beta v}$	-0.0063	-0.3584	C_{Yr}	0.0045	0.2601
$C_{Y\beta}$	-0.0076	-0.4372	C_{lr}	0.0015	0.0876
$C_{l\beta}$	-0.0003	-0.0145	C_{nr}	-0.0016	-0.0944
$C_{n\beta}$	0.0017	0.0970			
C_{Yp}	-0.0001	-0.0016			
C_{lp}	-0.0097	-0.5538			
C_{np}	-0.0006	-0.0360			

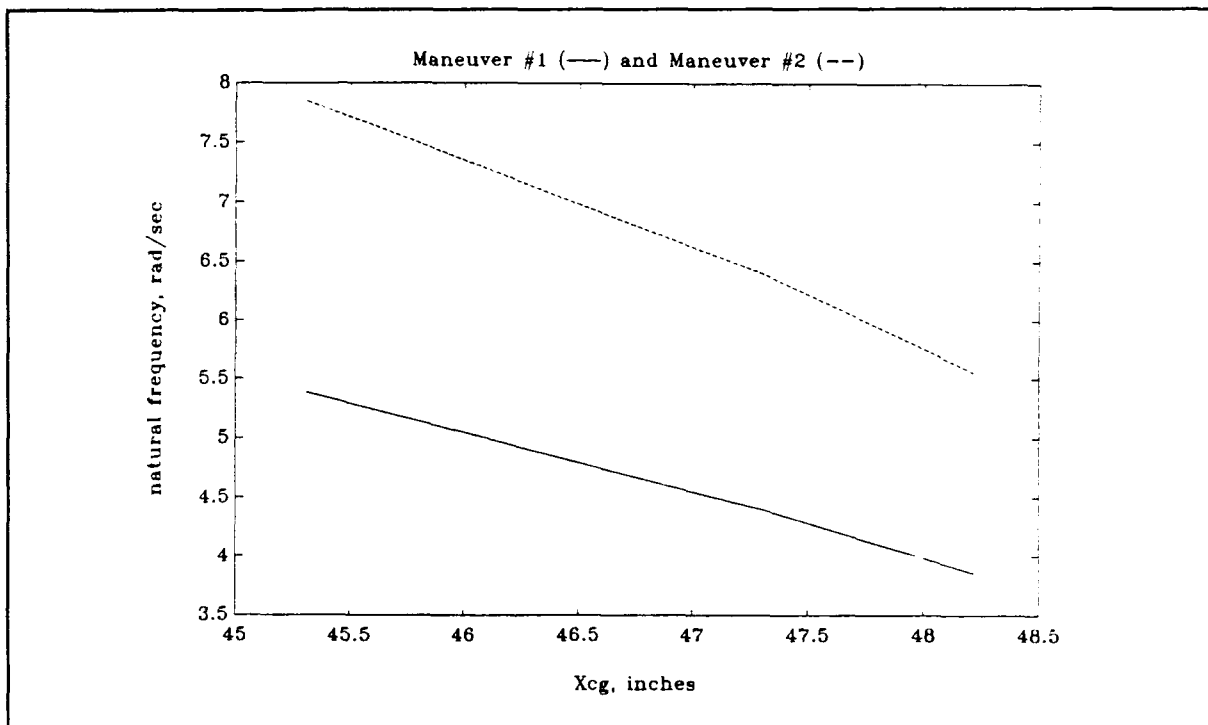


Figure 3.3. Change in Short Period Natural Frequency with a Change in Vehicle Center of Gravity Location.

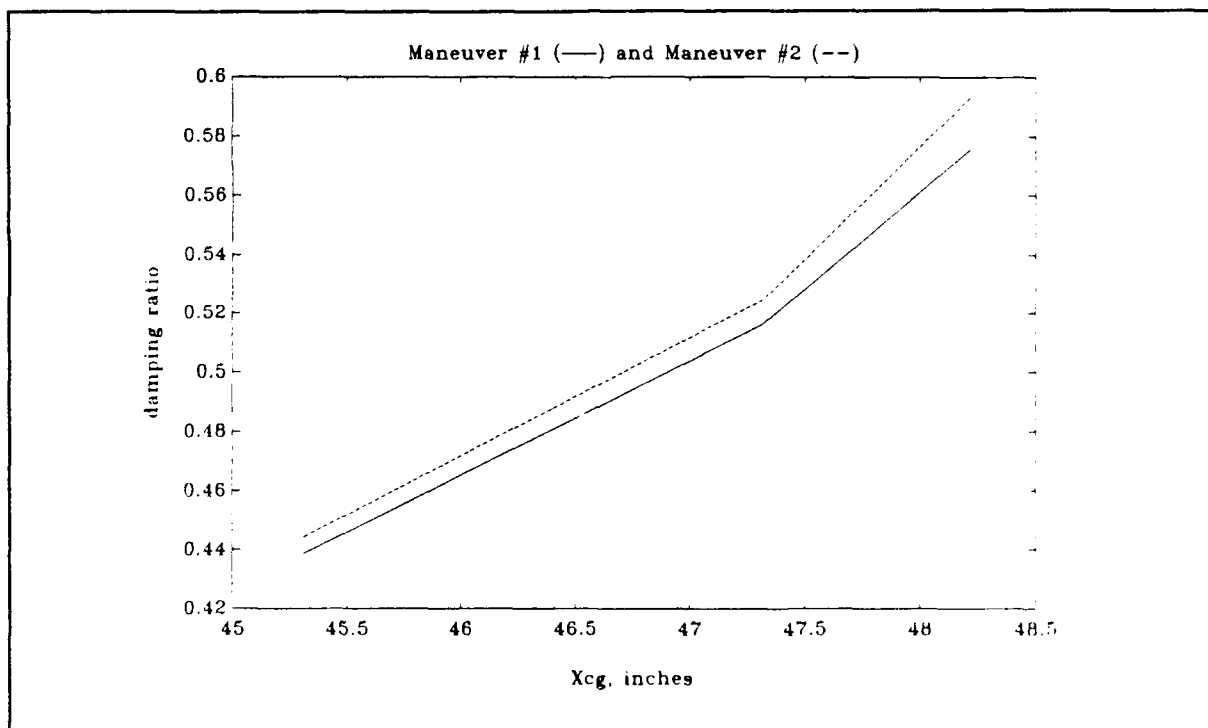


Figure 3.4. Change in Short Period Damping Ratio with a Change in Vehicle Center of Gravity Location.

The state time responses were simulated with the new estimated equations of motion, and the overall state space perturbation model was then fine tuned as follows:

1. By concentrating on the pitch doublet time responses, $C_{M\dot{\alpha}}$ was varied until a short period damping ratio was obtained that appeared to adequately fit the flight test data. The final value of $C_{M\dot{\alpha}}$ arrived at was 3.347 per radian. The magnitude of this value seems reasonable, but for most airplanes this derivative (due to "the lag of downwash" from the wing) has a negative value. The only reasonable explanation for the positive value for $C_{M\dot{\alpha}}$ is that since the horizontal tail lies directly in the flow of the propeller propwash and is well aft of the wing itself, the horizontal tail does not see a lag of downwash effect from the wing. Instead, it experiences a "lag of upwash" effect from the propeller wake. This is only speculation based on the characteristics observed in the time responses of the flight test data.

2. Focusing on the roll doublet time responses, the value of $I_{xx}=32.5$ slugs-sq. ft. produced very adequate results.

3. By concentrating on the yaw doublet time responses, $C_{n\dot{\beta}}$ and C_{nr} were varied to obtain dutch roll frequencies and damping ratios that adequately matched the flight test time responses. The new values iterated upon only required small magnitude changes from the Datcom estimated values. Although a constant value for $C_{n\dot{\beta}}$ matched the frequency for all the yaw doublet time responses, a constant value of C_{nr} resulted in a damping ratio

that appeared correct for only 3 of the 4 yaw doublet time responses. The last yaw doublet maneuver at half flaps and half throttle seemed to require a higher damping ratio than the other yaw doublet maneuvers. Since no good explanation was determined for this observation, a constant value for C_{nr} was used.

Table 3.19 presents the final values for the dimensionless derivatives arrived at for the Lambda vehicle with a c.g. location of 47.2 inches and vehicle weight of 203 pounds. The next section will address the actuator lags and provide the simulated time responses to the pilot command inputs.

Table 3.19. Final Dimensionless Derivatives for the Lambda Vehicle ($X_{cg}=47.2$ inches, $W=203$ pounds).

Longitudinal:
(per radian)

$C_{Mu} = 0.000$
 $C_{Ma} = -1.101$
 $C_{M\dot{a}} = 3.347$
 $C_{Mq} = -15.40$
 $C_{Lu} = 0.007071$
 $C_{La} = 5.820$
 $C_{L\dot{a}} = 2.023$
 $C_{Lq} = 7.113$
 $C_{Da} = 0.000$
 $C_{Du} = 0.000$
 $C_{L\delta e} = 0.2908$
 $C_{D\delta e} = 0.000$
 $C_{M\delta e} = -0.8449$
 $C_{L\delta f} = 1.419$
 $C_{D\delta f} = 0.08489$
 $C_{M\delta f} = -0.2904$

Lateral-Directional:
(per radian)

$C_{l\beta} = -0.01451$
 $C_{lp} = -0.5538$
 $C_{lr} = 0.08763$
 $C_{l\delta a} = 0.2608$
 $C_{l\delta r} = 0.002223$
 $C_{n\beta} = 0.06000$
 $C_{nr} = -0.1650$
 $C_{n\delta a} = -0.01368$
 $C_{n\delta r} = -0.09434$
 $C_{Y\beta} = -0.4372$
 $C_{Yp} = -0.001600$
 $C_{Yr} = 0.2601$
 $C_{Y\delta a} = 0.000$
 $C_{Y\delta r} = 0.2865$
 $C_{np} = -0.03601$

3.5. Final State Space Model

The final hurdle in constructing a full math model for the Lambda URV was the calculation of actuator lags and determination of any scaling required of the pilot command signals. Figure 3.5 shows the pilot pitch command and corresponding elevator deflection time histories for the first pitch doublet for the first flight test. Notice that, indeed, a time lag exists between the input command and the actual control surface deflection due to the actuator lag, and a scaling factor is evident between the magnitudes of the command input and actual deflection. Similar results hold for the aileron and rudder deflections due to pilot roll and yaw commands, respectively.

First, the scale factor for the command inputs were estimated by trial and error. Figure 3.6 shows one such iteration for the first pitch doublet flight maneuver. Notice that a constant scale factor does not quite reduce the command input to coincide with the maximum and minimum elevator deflection values. The same characteristics were observed for the roll and yaw command scalings.

A simple first order lag was used to approximate the servo dynamics. Higher order models were briefly investigated but the minor gain in modeling accuracy did not justify the increased model complexity. A least squares optimization routine which minimized the square of the error between the first order approximation and actual servo deflection was constructed to estimate the best value for the servo lag time constant.

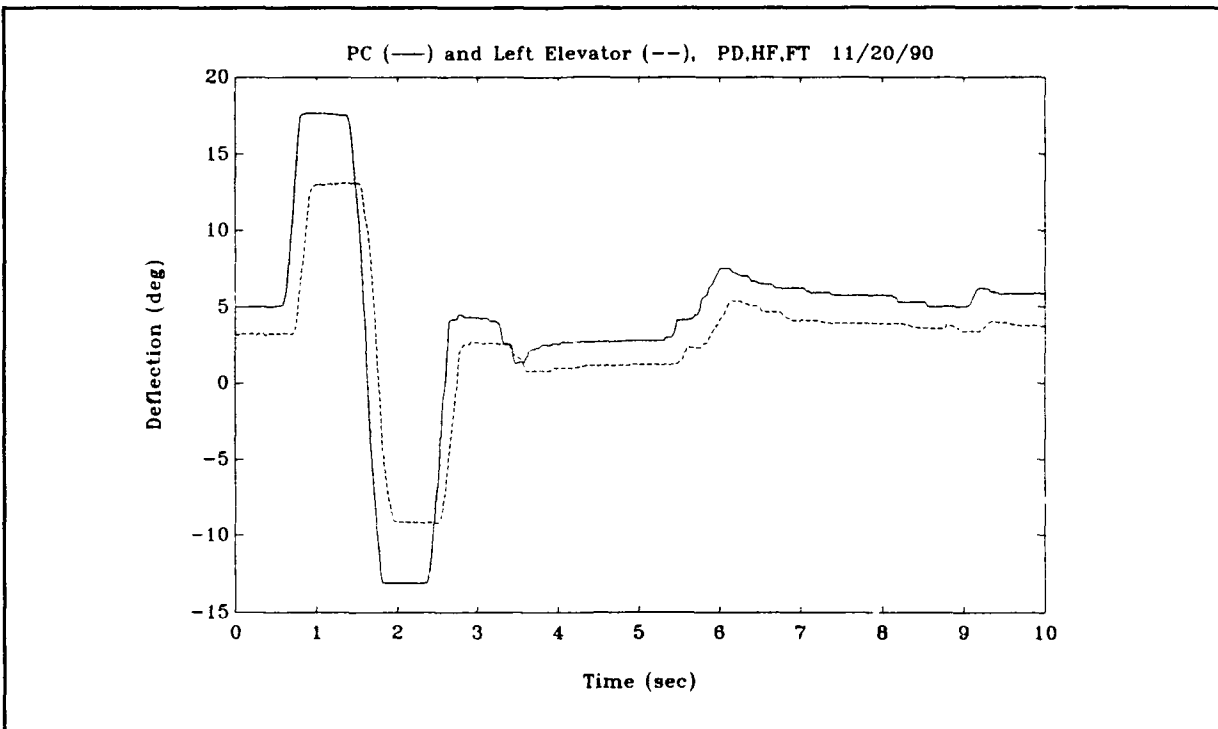


Figure 3.5. Pitch Command and Elevator Deflection Time History for Flight Maneuver PD,HF,FT 11/20/90.

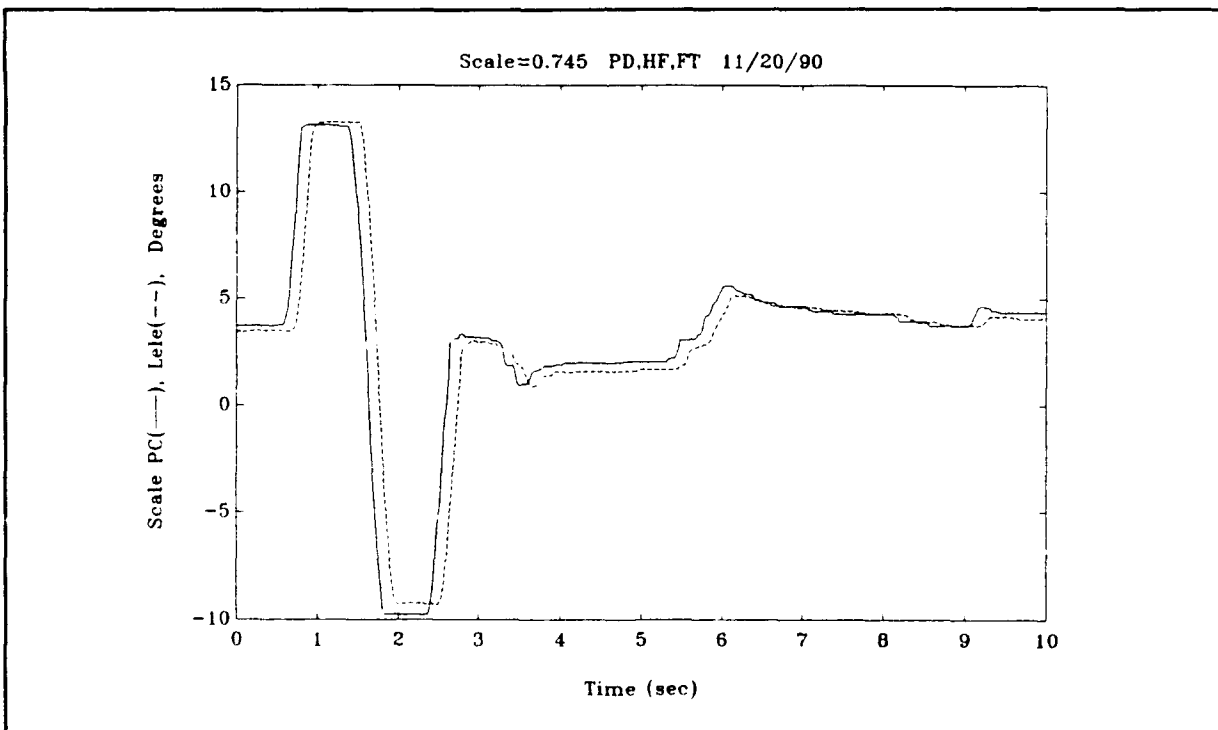


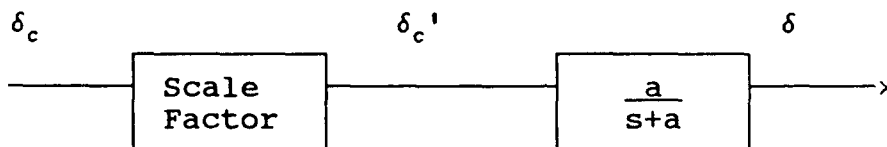
Figure 3.6. Scaling of the Pitch Command Input for the Flight Maneuver PD,HF,FT 11/20/90.

Table 3.20 summarizes the final values for the elevator, aileron, and rudder scalings and time lag constants. Figure 3.7 provides a comparison between the servo model's performance and the actual control surface deflection time histories for one pitch maneuver.

Table 3.20. Elevator, Aileron, and Rudder Servo Characteristics for the Lambda URV.

<u>Actuator</u>	<u>Scaling</u> (output/command)	<u>Lag Constant</u> ($a/[s+a]$)
Elevator	0.725	6.5
Aileron	0.700	5.5
Rudder	0.900	6.2

MODEL:



The final state space model using the pilot commands as the inputs is given by Table 3.31. The total state vector includes the longitudinal perturbation state vector, the lateral-directional perturbation state vector, the longitudinal control surface deflection perturbation state vector, and the lateral-directional control surface deflection perturbation state vector. The control input vector consists of the pilot elevator, flap (usually zero), aileron, and rudder command inputs. Appendix C provides an example of the model's approximation of the state vector time responses compared to the actual flight test data for each type of flight test maneuver conducted.

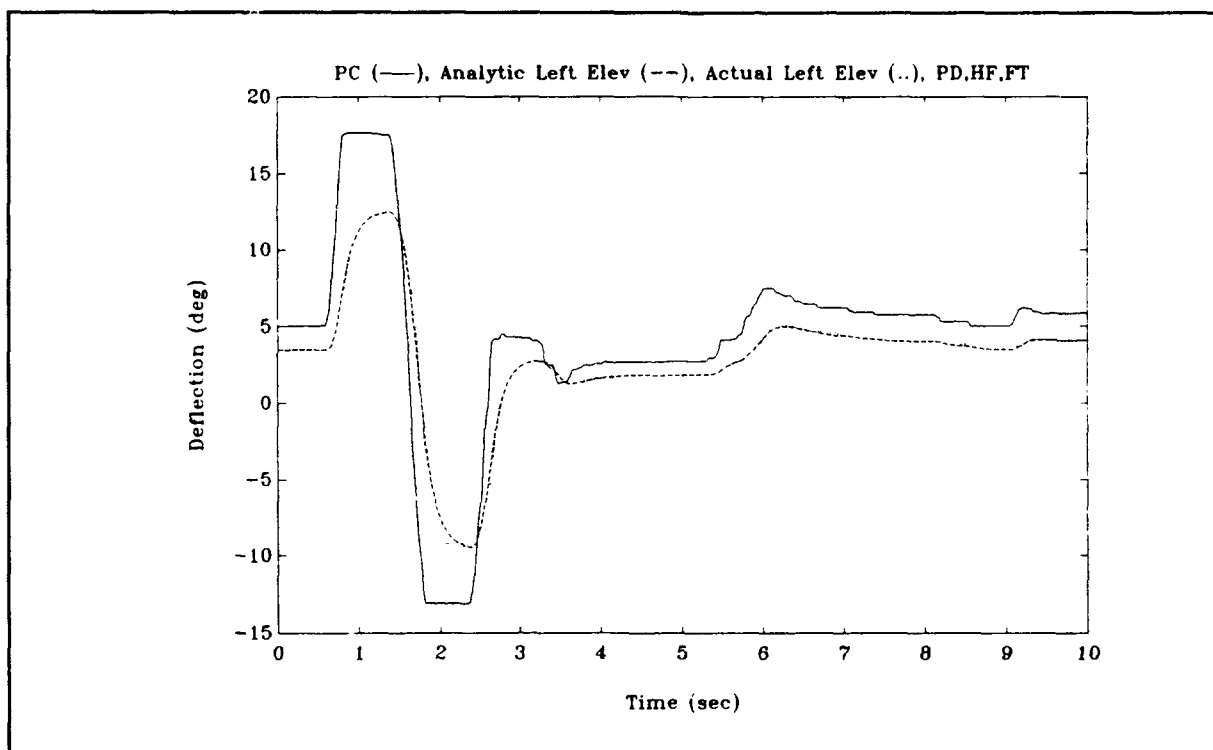


Figure 3.7. Comparison of Estimated and Actual Elevator Surface Deflection for the First Pitch Doublet Maneuver.

Table 3.21. Final State Space Model.

$$\begin{Bmatrix} \dot{x}_1 \\ \dot{x}_2 \\ \dot{x}_{\delta 1} \\ \dot{x}_{\delta 2} \end{Bmatrix} = \begin{bmatrix} \underline{A}_1 & \underline{0} & \underline{b}_1 & \underline{0} \\ \underline{0} & \underline{A}_2 & \underline{0} & \underline{b}_2 \\ \underline{0} & \underline{0} & \underline{A}_{\delta 1} & \underline{0} \\ \underline{0} & \underline{0} & \underline{0} & \underline{A}_{\delta 2} \end{bmatrix} \begin{Bmatrix} x_1 \\ x_2 \\ x_{\delta 1} \\ x_{\delta 2} \end{Bmatrix} + \begin{bmatrix} \underline{0} & \underline{0} \\ \underline{0} & \underline{0} \\ \underline{B}_{\delta 1} & \underline{0} \\ \underline{0} & \underline{B}_{\delta 2} \end{bmatrix} \begin{Bmatrix} \underline{u}_{\delta c 1} \\ \underline{u}_{\delta c 2} \end{Bmatrix}$$

$$\begin{Bmatrix} y_1 \\ y_2 \\ y_{\delta 1} \\ y_{\delta 2} \end{Bmatrix} = \begin{bmatrix} \underline{I} & \underline{0} & \underline{0} & \underline{0} \\ \underline{0} & \underline{I} & \underline{0} & \underline{0} \\ \underline{0} & \underline{0} & \underline{I} & \underline{0} \\ \underline{0} & \underline{0} & \underline{0} & \underline{I} \end{bmatrix} \begin{Bmatrix} x_1 \\ x_2 \\ x_{\delta 1} \\ x_{\delta 2} \end{Bmatrix} + \underline{0} \begin{Bmatrix} \underline{u}_{\delta c 1} \\ \underline{u}_{\delta c 2} \end{Bmatrix}$$

where,

$$\underline{A}_1 = \begin{bmatrix} x_u & x_a & 0 & -g \cos \theta_1 \\ \frac{z_u}{U_1 - z_a} & \frac{z_a}{U_1 - z_a} & \frac{U_1 + z_q}{U_1 - z_a} & -g \sin \theta_1 \\ M_u + \frac{M_a z_u}{U_1 - z_a} & M_a + \frac{M_a z_a}{U_1 - z_a} & M_q + \frac{M_a (U_1 + z_q)}{U_1 - z_a} & -M_a g \sin \theta_1 \\ 0 & 0 & 1 & 0 \end{bmatrix}$$

$$\underline{b}_1 = \begin{bmatrix} x_{\delta e} & x_{\delta f} \\ \frac{z_{\delta e}}{U_1 - z_a} & \frac{z_{\delta f}}{U_1 - z_a} \\ M_{\delta e} + \frac{M_a z_{\delta e}}{U_1 - z_a} & M_{\delta f} + \frac{M_a z_{\delta f}}{U_1 - z_a} \\ 0 & 0 \end{bmatrix}$$

Table 3.21. Continued.

$$\underline{A}_2 = \begin{bmatrix} \frac{Y_\beta}{U_1} & \frac{Y_p}{U_1} & \frac{g \cos \theta_1}{U_1} & \frac{Y_r}{U_1} - 1 & 0 \\ \frac{L_\beta + A_1 N_\beta}{1 - B_1 A_1} & \frac{L_p + A_1 N_p}{1 - B_1 A_1} & 0 & \frac{L_r + A_1 N_r}{1 - B_1 A_1} & 0 \\ 0 & 1 & 0 & 0 & 0 \\ \frac{N_\beta + B_1 L_\beta}{1 - B_1 A_1} & \frac{N_p + B_1 L_p}{1 - B_1 A_1} & 0 & \frac{N_r + B_1 L_r}{1 - B_1 A_1} & 0 \\ 0 & 0 & 0 & 1 & 0 \end{bmatrix}$$

$$\underline{b}_2 = \begin{bmatrix} \frac{Y_{\delta a}}{U_1} & \frac{Y_{\delta r}}{U_1} \\ \frac{L_{\delta a} + A_1 N_{\delta a}}{1 - B_1 A_1} & \frac{L_{\delta r} + A_1 N_{\delta r}}{1 - B_1 A_1} \\ 0 & 0 \\ \frac{N_{\delta a} + B_1 L_{\delta a}}{1 - B_1 A_1} & \frac{N_{\delta r} + B_1 L_{\delta r}}{1 - B_1 A_1} \\ 0 & 0 \end{bmatrix}$$

$$\underline{A}_{\delta 1} = \begin{bmatrix} -a_e & 0 \\ 0 & -a_f \end{bmatrix}$$

$$\underline{B}_{\delta 1} = \begin{bmatrix} a_e & 0 \\ 0 & a_f \end{bmatrix}$$

$$\underline{A}_{\delta 2} = \begin{bmatrix} -a_a & 0 \\ 0 & -a_r \end{bmatrix}$$

$$\underline{B}_{\delta 2} = \begin{bmatrix} a_a & 0 \\ 0 & a_r \end{bmatrix}$$

3.6. Conclusions and Recommendations

The following conclusions should be noted:

1. Digital Datcom was an effective tool for estimating Lambda's dimensionless stability and control derivatives. The main modeling problems stemmed from the lack of accurate mass property data. The accuracy of the mass property data presented in Chapter 2 is highly questionable. The center of gravity location from the weights breakdown model presented did not lead to an accurate estimation of the vehicle c.g. location. For the first flight test, this error in estimating the vehicle c.g. location by using the Chapter 2 model may have been as large as 10% of the mean aerodynamic chord. The roll inertia estimated from the Chapter 2 model may have been off by a factor of two. These estimation errors of mass properties directly led to gross errors in estimating the overall stability and control derivatives.
2. Due to the limited information on sensor noise, servo dynamics, and structural dynamics, direct estimation of the stability and control parameters through maximum likelihood estimation techniques was not possible. Maximum likelihood parameter estimation was, however, an effective tool for estimating the second order characteristics of the short period and dutch roll, and the first order characteristics of the roll mode from the flight test α , q , β , r , and p time histories. Short period frequency, dutch roll frequency, and roll mode time constant were accurately estimated through maximum likelihood estimation. Short period and dutch roll damping ratios, however,

required basic "brute force" variation of the stability derivatives ($C_{M\dot{\alpha}}$, C_{nr}) by trial-and-error to obtain adequate damping characteristics over all the flight maneuvers.

3. The phugoid and spiral mode characteristics of Lambda were not directly determined from the flight test data. This was due, in part, to the limited time histories (less than 10 seconds) for each flight maneuver. However, if process and measurement noise characteristics are added to the maximum likelihood estimation process (through the addition of a Kalman filter to estimate states and measurements), the parameters characterizing these modes could probably be determined from the flight test data [10, 11, 12].

4. The flight test data indicated that Lambda has roll/pitch coupling dynamics. This coupling was most prevalent on the pitch doublet maneuvers. The estimation models used in this thesis, however, were unable to address or characterize the observed coupling.

The following recommendations are given:

1. The mass property data on the Lambda URV needs to be revisited. The following pieces of information need to be accurately determined:

- a center of gravity excursion diagram, and
- the mass moment of inertia about each of the principle body axes.

The above information can be obtained experimentally and would not require the Lambda vehicle to be disassembled [14, 15].

Once the most forward and most aft locations of the vehicle c.g.

have been determined, Datcom runs should be accomplished and the stability and control derivatives estimated at each of these locations. The variation of the stability and control derivatives could then be plotted against c.g. location. Another set of flight tests, conducted at vastly different c.g. locations, could then be used to calibrate the stability and control derivative estimations.

2. If a more accurate math model of the Lambda URV is desired, the following will need to be accomplished:

- sensor noise completely characterized,
- servo dynamics completely characterized, and
- structural dynamics analyzed.

Using the above data, a maximum likelihood parameter estimation approach can be created that implements a Kalman filter to estimate states and measurements (not parameters). This approach could also account for atmospheric turbulence during flight testing. Such methods are currently in use at the major flight test centers [12].

3. The effects of the propeller wash over the horizontal tail should be investigated. Two significant pieces of information that could be obtained experimentally are:

- the dynamic pressure over the horizontal tail surface (through the proper installation of a pitot-static tube or pressure taps on the horizontal tail), and
- thrust level data calibrated to throttle setting and atmospheric conditions.

4. Rate Controller Design Using Classical Techniques

Classical flight control design techniques provide a solid starting point for the engineer who is attempting to design a flight control system for a new vehicle. These methods have been used extensively over the years. Several excellent texts exist which thoroughly describe the mechanics of the classical design process. The methods described in texts by Roskam [4] and McRuer [5] will be primarily used for the designs developed in this chapter.

The chapter begins with a definition of Lambda's projected flight envelope and an algorithm for estimating Lambda's stability and control derivatives at the various flight conditions. Sections 4.2 through 4.4 provide the pitch rate, roll rate, and yaw rate controller designs, respectively. Section 4.5 then provides a discussion of the overall designs and an overview of the information obtained from using classical design techniques.

All rate compensators developed in this chapter were arbitrarily limited to order less than three. All poles and zeros chosen for the compensators were restricted to the real axis.

4.1. Projected Flight Envelope

Lambda's flight envelope was defined as a function of speed and center of gravity location. Since the vehicle routinely flies below 5,000 ft (predicted ceiling of 10,000 ft), altitude was not incorporated into the definition of the envelope. The basis for the flight envelope was the weight model developed in Chapter 2, performance predictions supplied by the Flight Control Division, and loading predictions supplied by the contractor Lear-Siegler.

The weight model developed in Chapter 2 was corrected to yield the proper center of gravity location determined from the flight test data results given in Chapter 3. Therefore, the entire weight model is based on only one known data point. Indeed, this is a precarious foundation after the effects of incorrectly estimating the vehicle's c.g. location were illustrated in Chapter 3. It will be the job of the Flight Dynamics Laboratory to pursue further flight testing to verify the weight model (see recommendations at the end of Chapter 3). Variations in the vehicle's c.g. location result from the following:

- fuel loading and expenditure during flight, and
- loading arrangements in the avionics bay.

The avionics bay on Lambda can contain 2 avionics boxes (see Figure 4.1). The airplane cannot fly without Avionics Box #1. This box currently weights 9 pounds but projected upgrades may increase its weight to 12 pounds. Avionics Box #2 is optional

and is projected to weigh 15 pounds. The fuel tank is housed in the aft of the fuselage and has a maximum capacity of approximately 2 1/3 gallons (14 pounds). Thus, the four extreme possible loading conditions for Lambda are as follows:

- Avionics Box #1, no fuel
- Avionics Box #1, full fuel
- Avionics Boxes #1 and #2, no fuel
- Avionics Boxes #1 and #2, full fuel.

It should be noted that Lambda has landed, on more than one occasion, with no fuel remaining in the tank. Using the above scenarios, a center of gravity excursion diagram was constructed and is presented in Figure 4.2. The estimated c.g. range for Lambda is as follows:

most forward c.g. location:	45.83 inches (21.85% MAC)
most aft c.g. location:	47.75 inches (32.43% MAC)

The in-flight weight can vary from 181 pounds up to 213 pounds.

The Flight Dynamics Laboratory has predicted the following speed ranges for the Lambda URV:

maximum speed	100 knots
stall speed, no flaps	54 knots
stall speed, full flaps	45 knots

Thus, the projected flight envelope is given in Figure 4.3.

Two more sets of Digital Datcom computations were accomplished at the most forward and most aft c.g. locations. These were combined with the Datcom estimations at the flight test condition to provide a linear estimation of the change in

dimensionless stability and control derivatives with center of gravity location. All linear estimations were adjusted to pass through the correct derivative value at the flight test condition ($X_{cg}=48.186$ inches) as determined in Chapter 3. A MATLAB program was then developed that calculates the linear, state space, small perturbation model (both longitudinal and lateral-directional) for Lambda given the center of gravity location, trimmed flight speed, dynamic pressure, vehicle weight, and trimmed pitch angle as inputs. The program, named DERCALC, is presented in Appendix D and was the foundation for all controller design work.

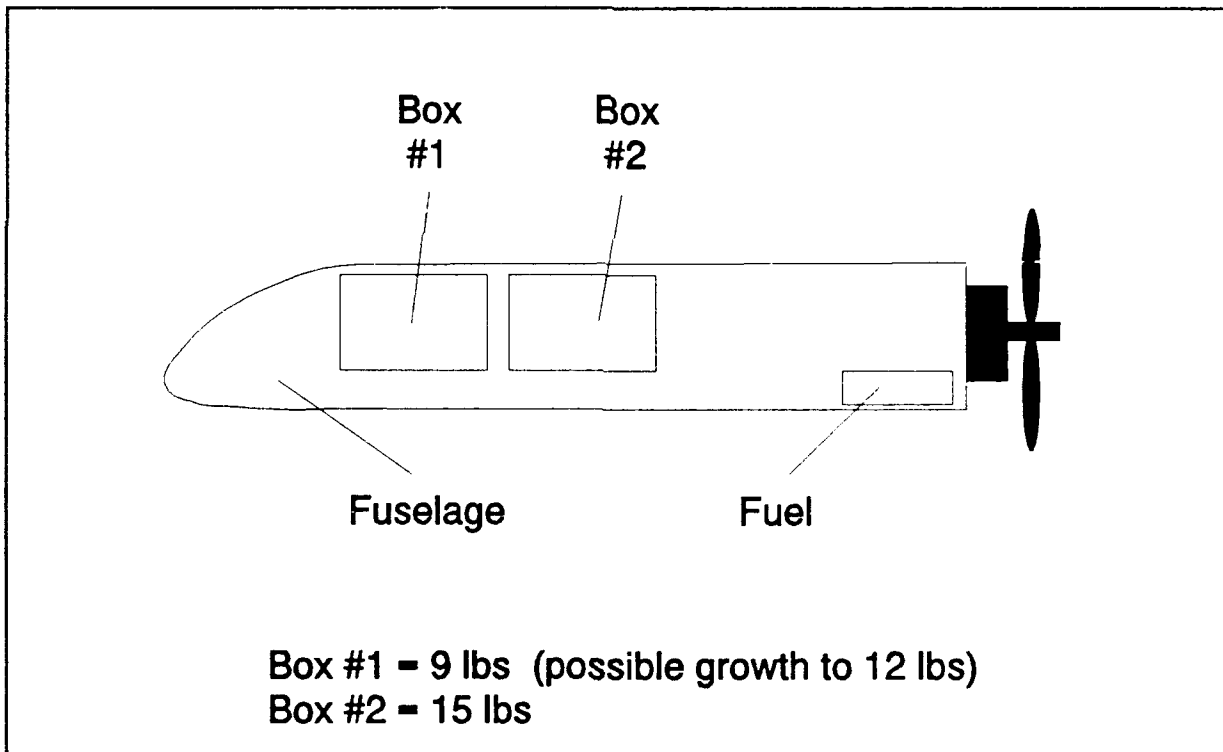


Figure 4.1. Avionics Bay Arrangement for the Lambda URV.

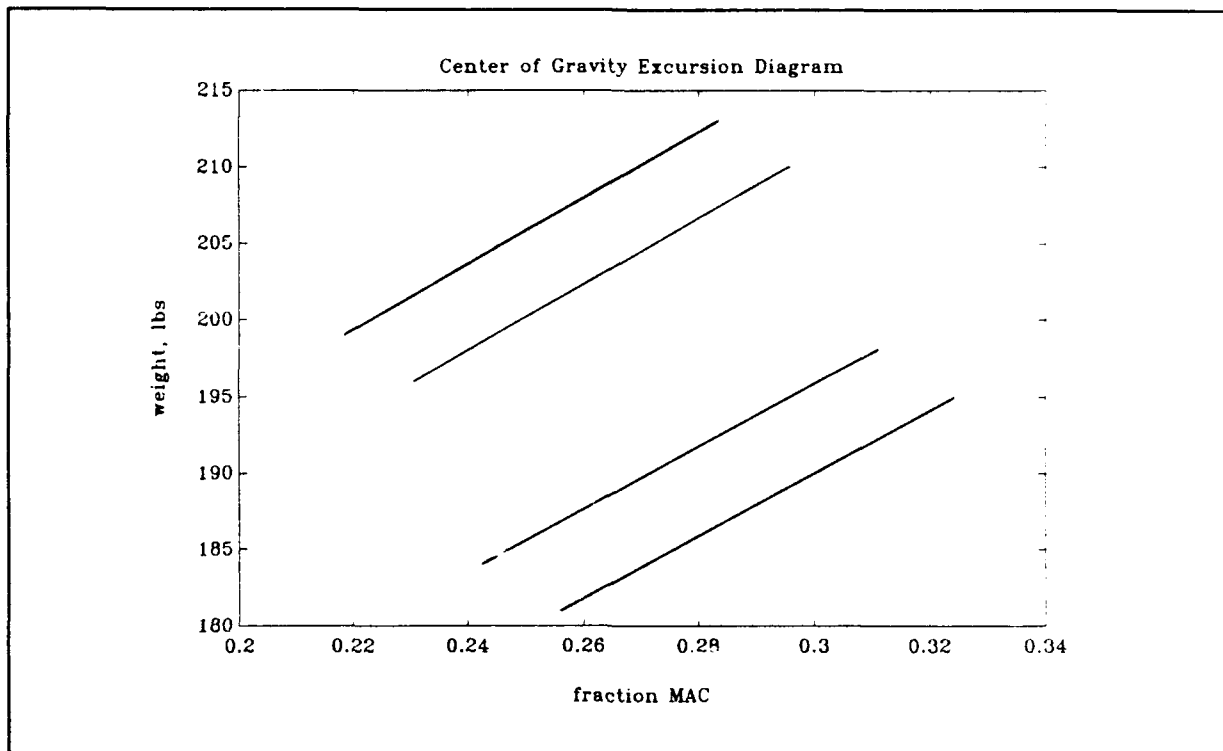


Figure 4.2. Center of Gravity Excursion Diagram for Lambda.

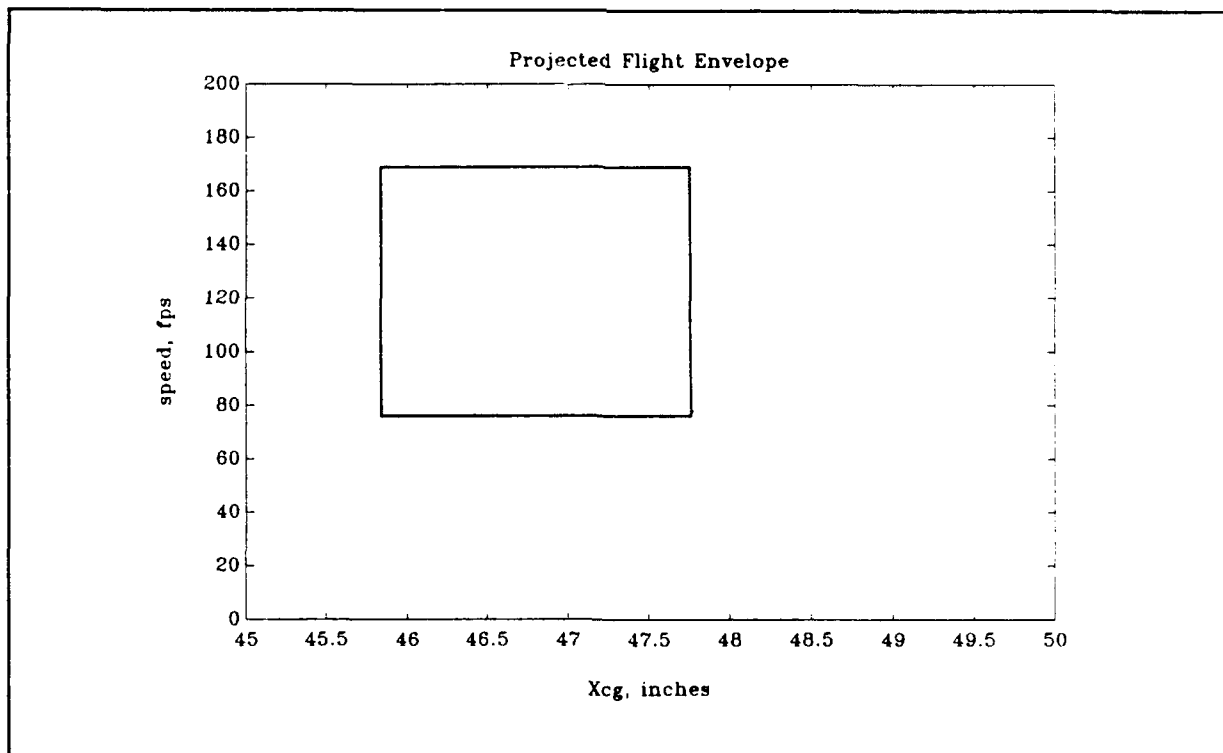


Figure 4.3. Projected Flight Envelope for the Lambda URV.

4.2. Pitch Rate Controller Design

The classical philosophy for a pitch rate controller design is a single input/single output (SISO) transfer function approach that involves the selection of gains, poles, and zeros confined to the real axis for the compensator. The fundamental tools are the block diagram, root locus diagrams, bode magnitude and phase plots, and closed loop time response plots. Four point designs, one for each corner of Lambda's flight envelope, were accomplished. The design for the slow speed, most forward c.g. location will be described in detail.

Flight Condition #1 Point Design.

$$\begin{array}{lll} X_{cg}=45.83 \text{ in} & \bar{q}_1=6.866 \text{ psf} & \theta_1=0 \text{ deg} \\ U_1=76.0 \text{ fps} & W_1=200 \text{ lbs} & \end{array} \quad (4.1)$$

The pitch rate to elevator deflection transfer function for this flight condition is as follows:

$$\frac{q(s)}{\delta_e(s)} = \frac{-7.104s(s+0.283)(s+1.351)}{(s^2+2.901s+14.81)(s^2-0.0175s+0.306)} \quad (4.2)$$

which corresponds to the following characteristic modes:

short period natural frequency:	3.849 rad/sec
short period damping ratio:	0.3769
phugoid natural frequency:	0.553 rad/sec
phugoid damping ratio:	-0.0159

Notice that the phugoid mode is unstable at this flight condition. The elevator servo dynamics are modeled as a pure lag:

$$G_s(s) = \frac{\delta_e(s)}{\delta_e(s)_{com}} = \frac{6.5}{s+6.5} \quad (4.3)$$

Initially, a negative feedback compensator using a pure gain and a lead were designed. The general block diagram for this pitch rate controller design is given in Figure 4.4.

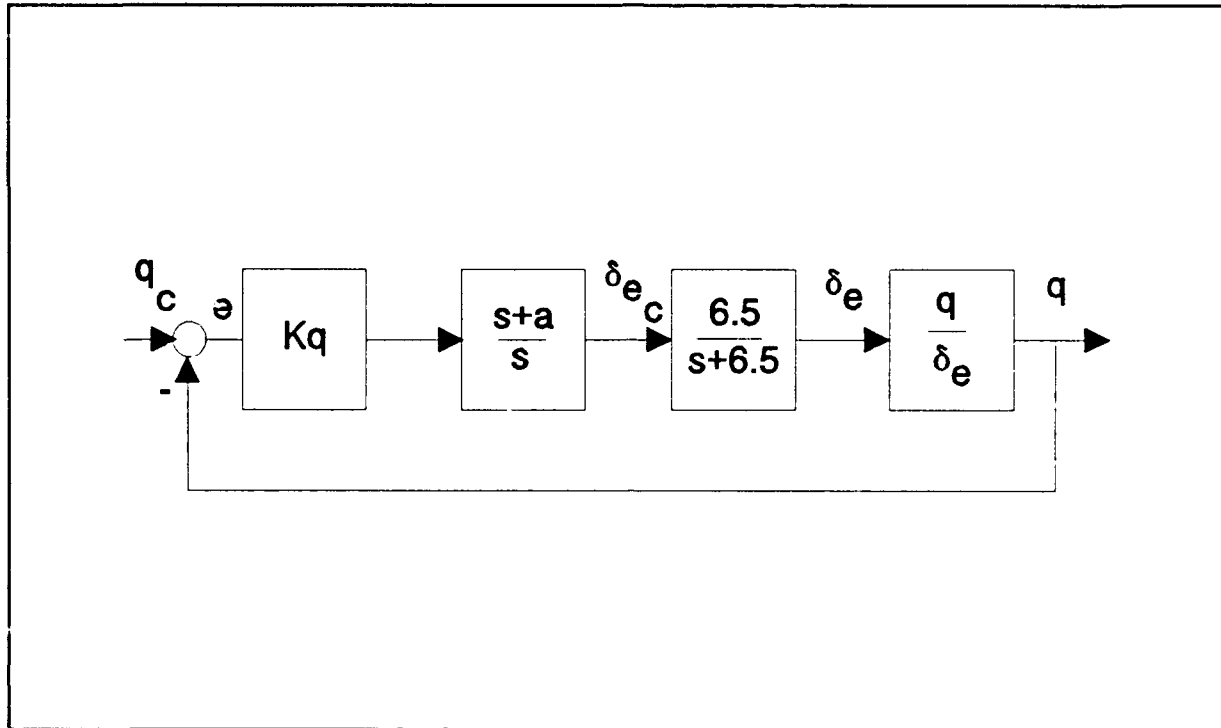


Figure 4.4. Pitch Rate Controller Block Diagram (Negative Feedback with a Gain and a Lead).

The open loop transfer function for this system is:

$$G_{OL}(s) = Kq \frac{(s+a_l)}{s} \frac{6.5}{(s+6.5)} \frac{q(s)}{\delta_e(s)} \quad (4.4)$$

and the steady state error is:

$$e_{ss} = 1 - \frac{Kq(6.5)(a_l)(-2.7195)}{6.5(4.5339) + Kq(6.5)(a_l)(-2.7195)} \quad (4.5)$$

A generic root locus diagram for this system is given in Figure 4.5. Selection of Kq and the lead constant (a_l) requires the following considerations:

1. Steady state error (Eqn. 4.5) decreases as $Kq \cdot a_l$ increases.

2. Increasing a_1 moves the center of the root locus asymptotes towards the imaginary axis. Specifically, this shifts the short period locus towards the imaginary axis.
3. Increasing K_q moves the phugoid roots into the stable region of the s-plane, but also quickly decreases short period damping.

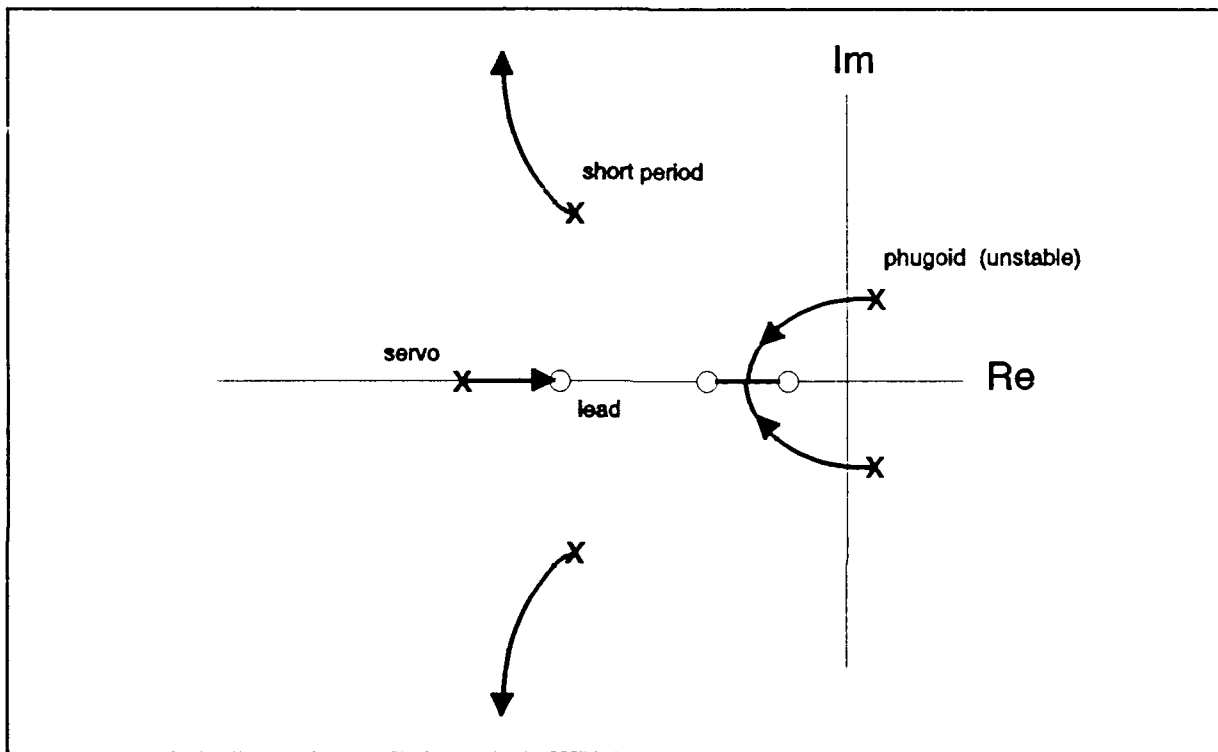


Figure 4.5. General Root Locus for Figure 4.4 Block Diagram.

It should be noted that most conventional airplanes have elevators with faster servos. In such a case, a typical root locus for the same problem set-up is given in Figure 4.6. In this case, increasing K_q would move the phugoid roots to the stable half of the s-plane without sacrificing short period damping. The trade-off in this case would be between steady state error and short period damping.

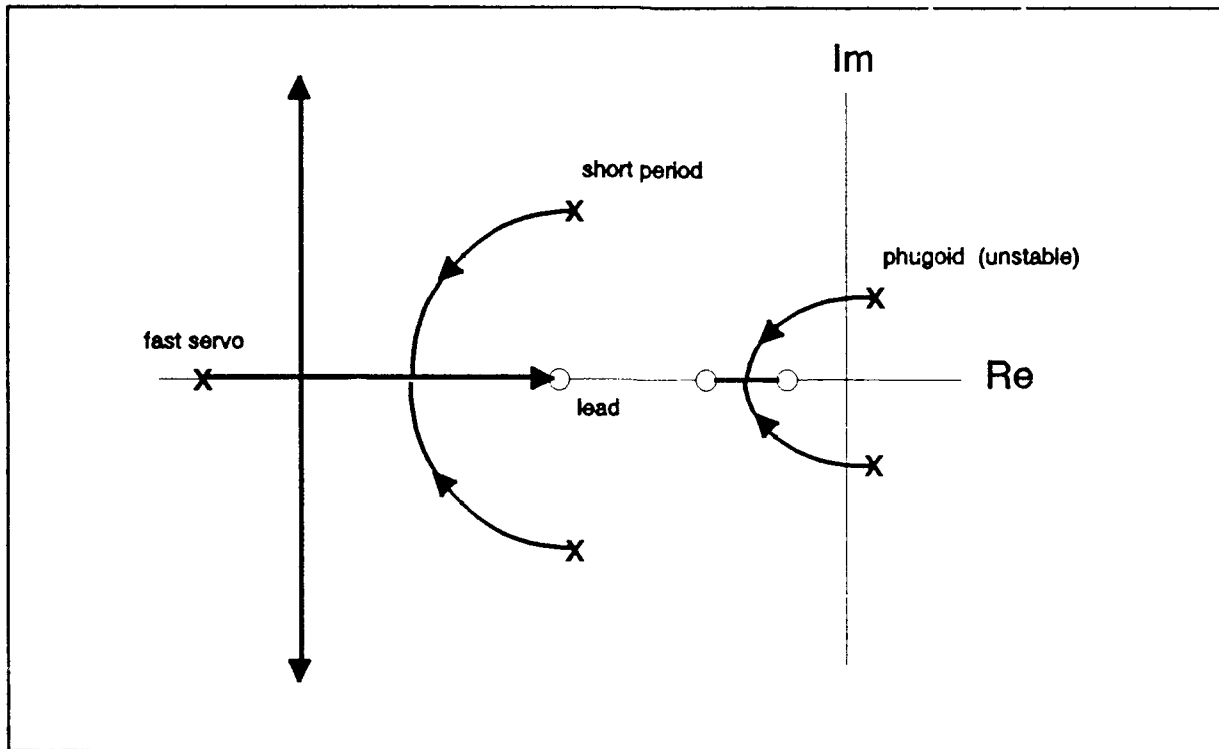


Figure 4.6. Typical Root Locus for Figure 4.4 Block Diagram.

The closed loop time response for $a_l=5.0$ and $K_q=-2.5$ is given in Figure 4.7. Notice that the response is highly oscillatory (low short period damping) and has a steady state error of 11.8%. Increasing K_q would reduce the steady state error but would increase the oscillations.

Adding a lead to the compensator of the form, $G(s)=(s+c)/(s+d)$ where $c < d$, results in slightly lower steady state error and better short period damping at a higher K_q . The added zero, placed on the real axis in the vicinity of the short period poles, tends to slow the reduction of short period damping as K_q is increased.

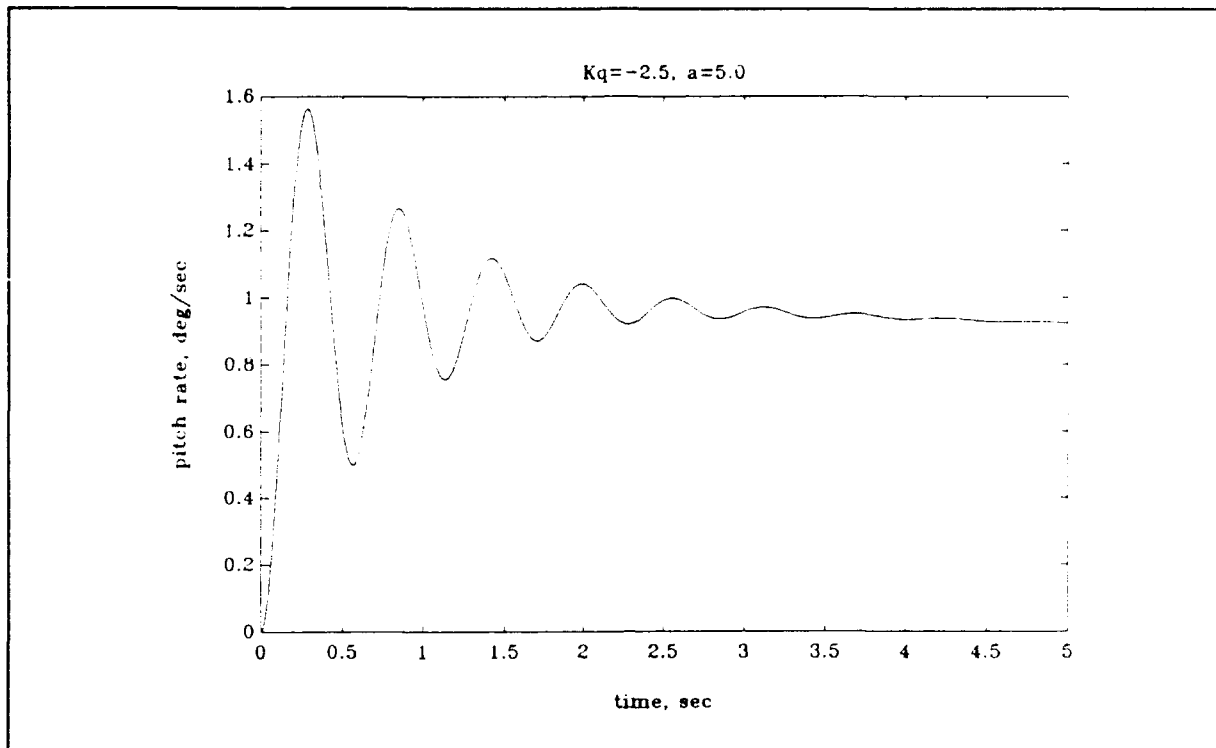


Figure 4.7. Closed Loop Time Response for $K_q=-2.5$, $a_l=5.0$.

The final design selected for this flight condition is summarized in Figure 4.8. The corresponding root locus and closed loop time response are given in Figures 4.9 and 4.10, respectively. The Bode magnitude and phase plot for the open loop transfer function is given in Figure 4.11. Notice that the phase margin for this design is only 13 degrees.

Using the same approach, pitch rate controller point designs were accomplished at the three remaining corners of the flight envelope. Table 4.1 summarizes the point designs. Figure 4.12 provides the closed loop time responses for each of the final designs (at the most aft c.g. location). It should be noted that the main goal in these designs was to keep the steady state error

low (at approximately 5% or less). Another approach could have targeted a standard phase margin (such as 30 degrees) for each point design. In that case, lower gains would have been used which would have resulted in large steady state errors.

Table 4.1. Pitch Rate Controller Point Designs.

FC	X_{cg} (in)	U_1 (fps)	W (lbs)	Kq	a_L	c	d	PM (deg)	e_{ss} (%)
1	45.83	76.0	200	-15	2.75	3.0	4.0	13	5.11
2	45.83	168.9	200	-5	2.75	3.0	4.0	13	5.76
3	47.75	168.9	200	-5	2.75	3.0	4.0	12	3.54
4	47.75	76.0	200	-15	2.75	3.0	4.0	12	3.19

FC \equiv Flight Condition

PM \equiv Phase Margin

The compensator pole and zero placement is constant for all point designs. In order to keep steady state error at approximately 5%, it was absolutely essential to change the compensator gain between the low and high flight speeds. Therefore, gain scheduling as a function of flight speed, U, will be implemented into the controller design as follows:

$$Kq_{low} = -15 \quad (\text{gain at } U=76.0 \text{ fps})$$

$$Kq_{high} = -5 \quad (\text{gain at } U=168.9 \text{ fps})$$

$$Kq = Kq_{low} + (Kq_{low} - Kq_{high})(U-76.0)/(168.9-76.) \quad (4.6)$$

The final design block diagram is presented in Figure 4.13.

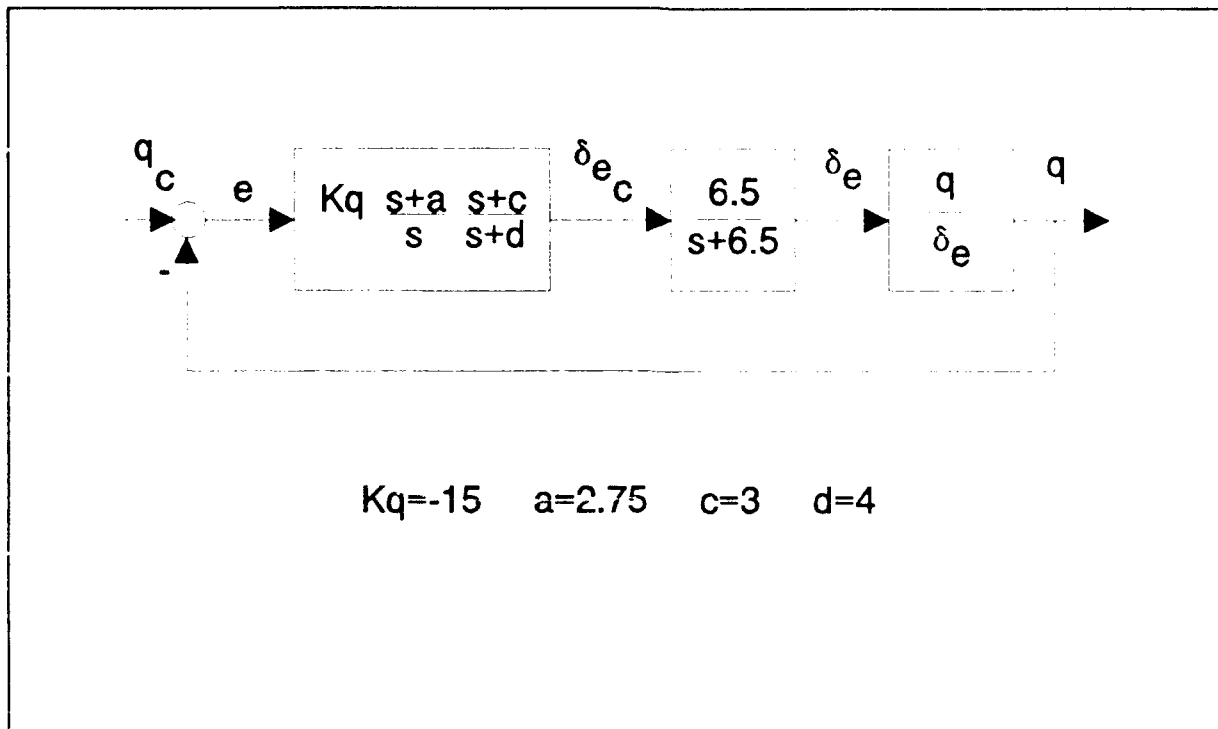


Figure 4.8. Final Pitch Rate Controller Block Diagram for Flight Condition #1.

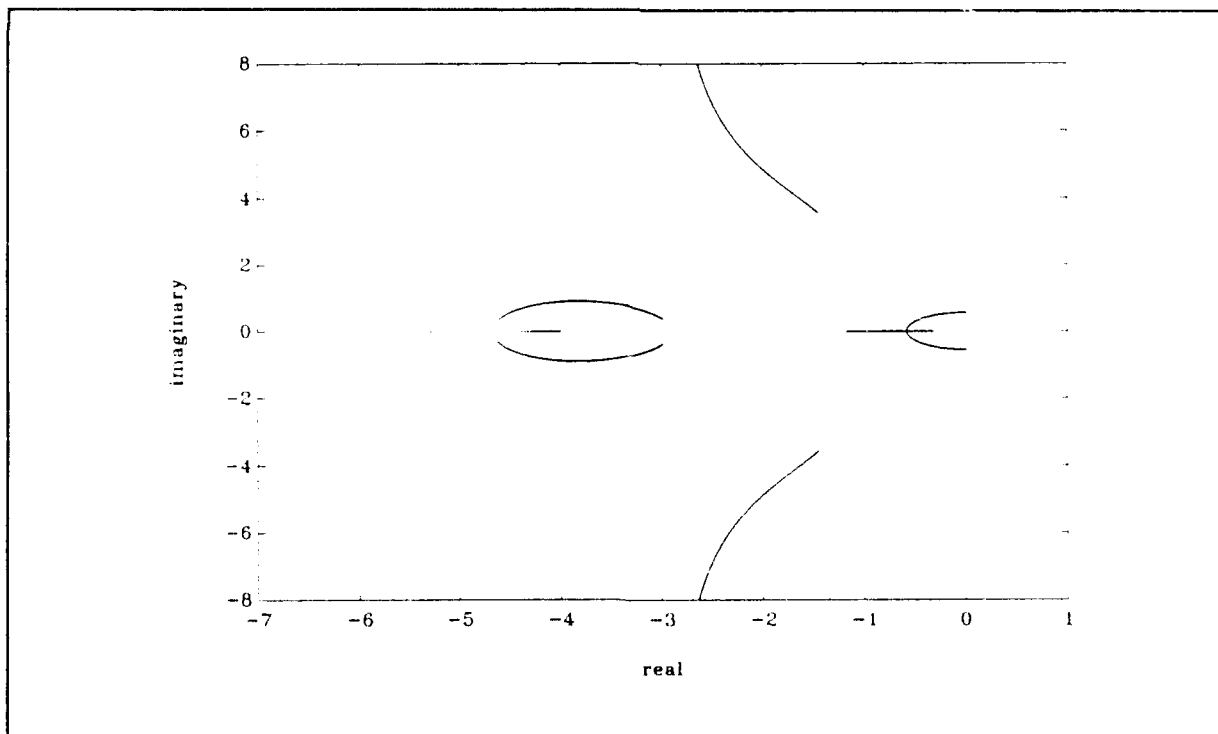


Figure 4.9. Root Locus for the Controller Design for Flight Condition #1.

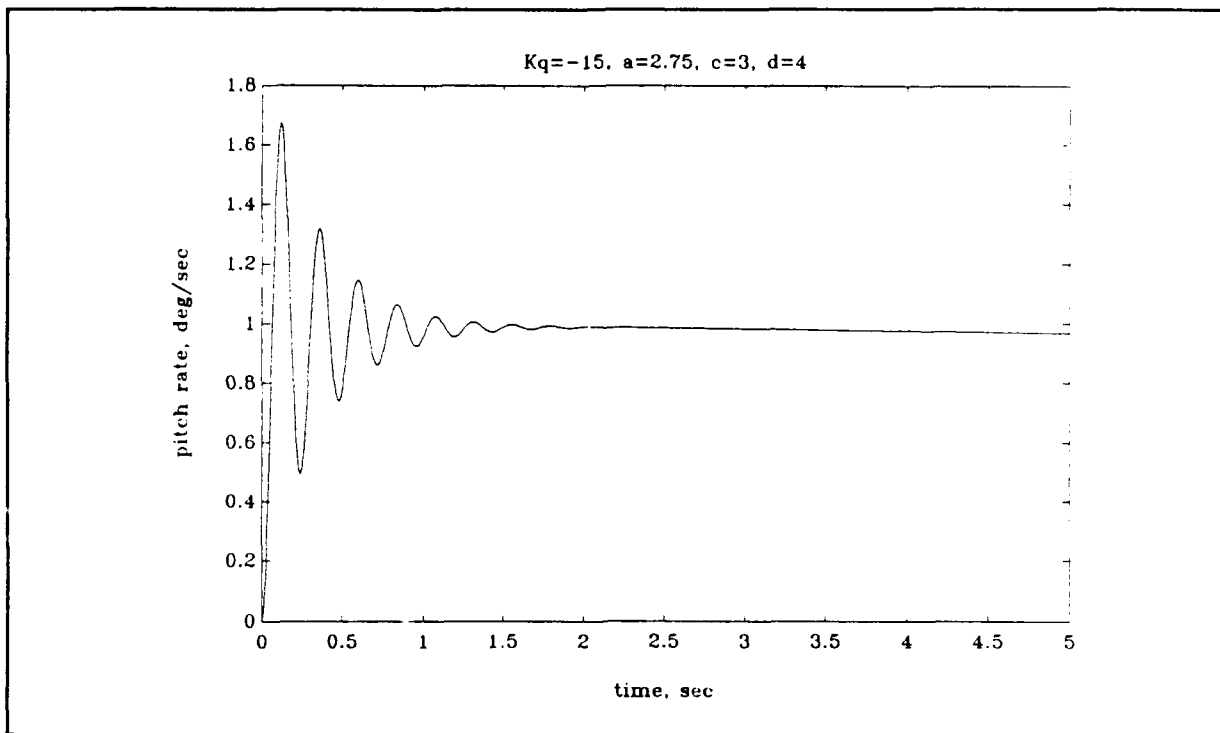


Figure 4.10. Closed Loop Time Response for the Pitch Rate Controller Design for Flight Condition #1.

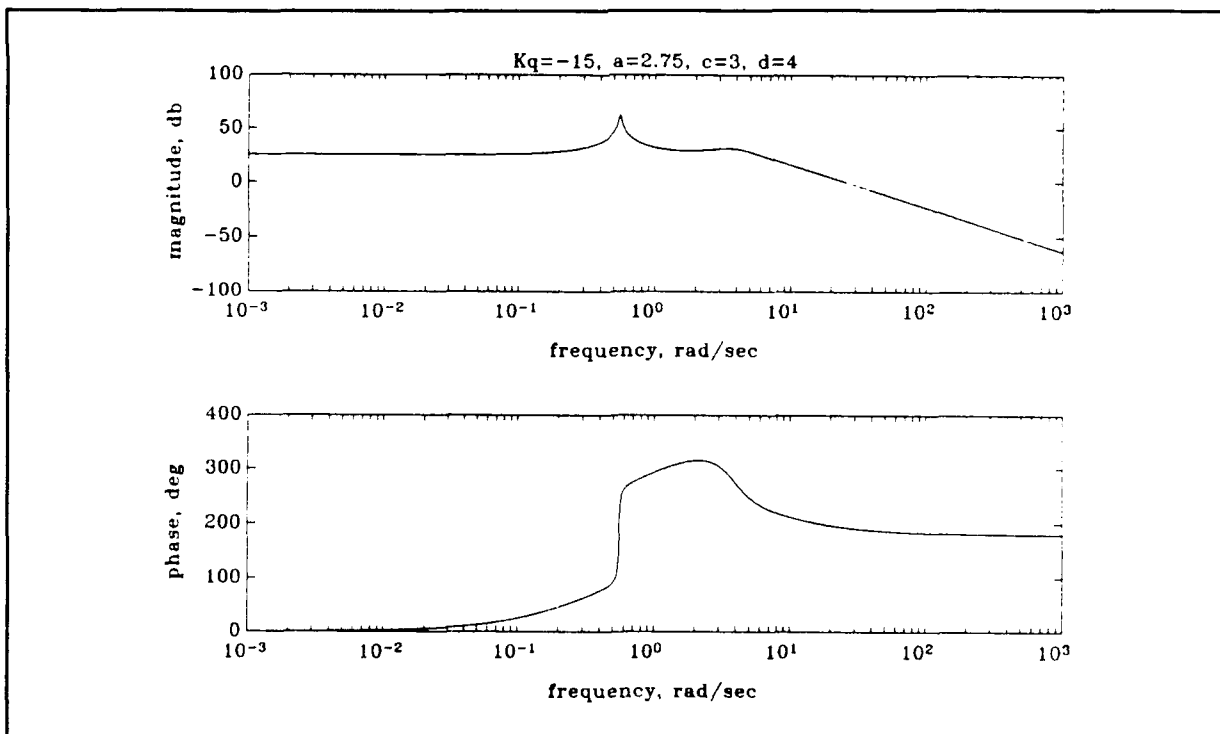


Figure 4.11. Bode Magnitude and Phase Plot for the Controller Design for Flight Condition #1.

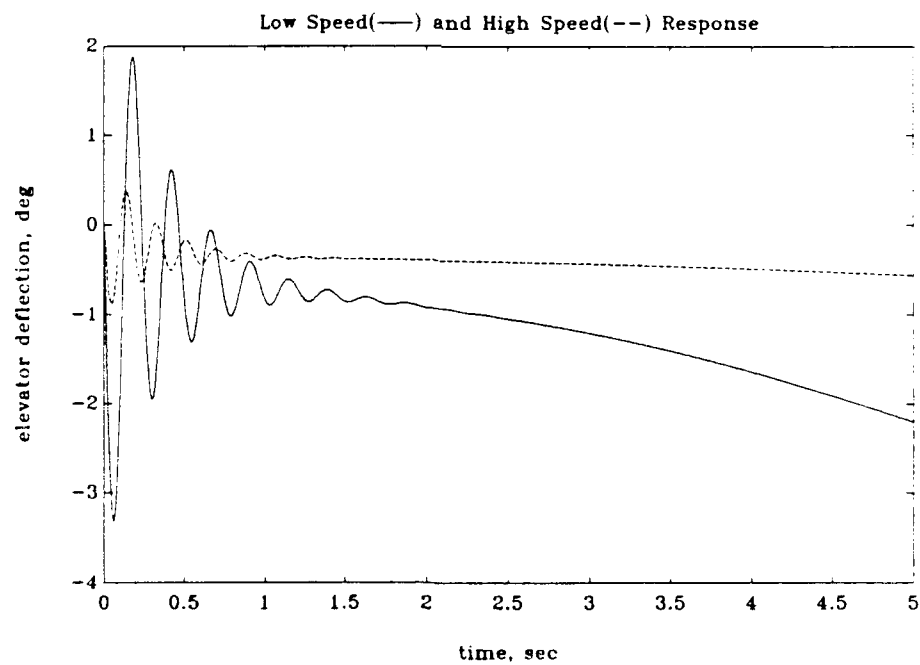
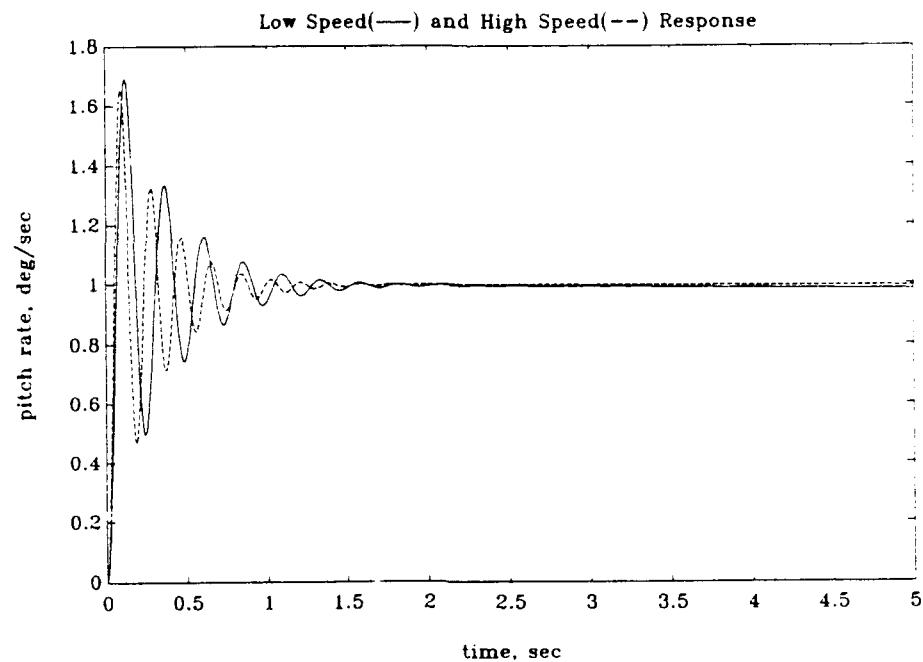


Figure 4.12. Closed Loop Time Responses for the Final Pitch Rate Controller Point Designs.

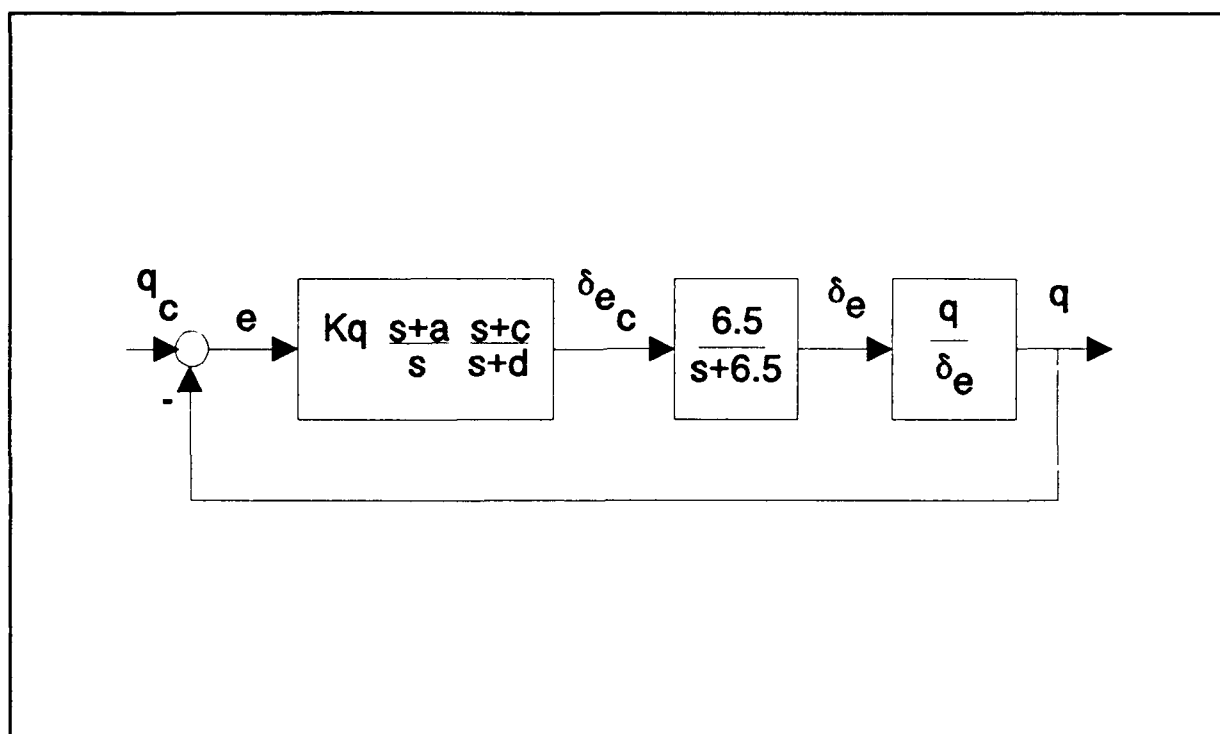


Figure 4.13. Block Diagram for the Final Pitch Rate Controller Design.

4.3. Roll Rate Controller Design

The general block diagram used to design the roll rate controllers is given in Figure 4.14. Four point designs, one for each corner of the flight envelope, were accomplished. The design for the slow speed, most forward c.g. location will be described in detail.

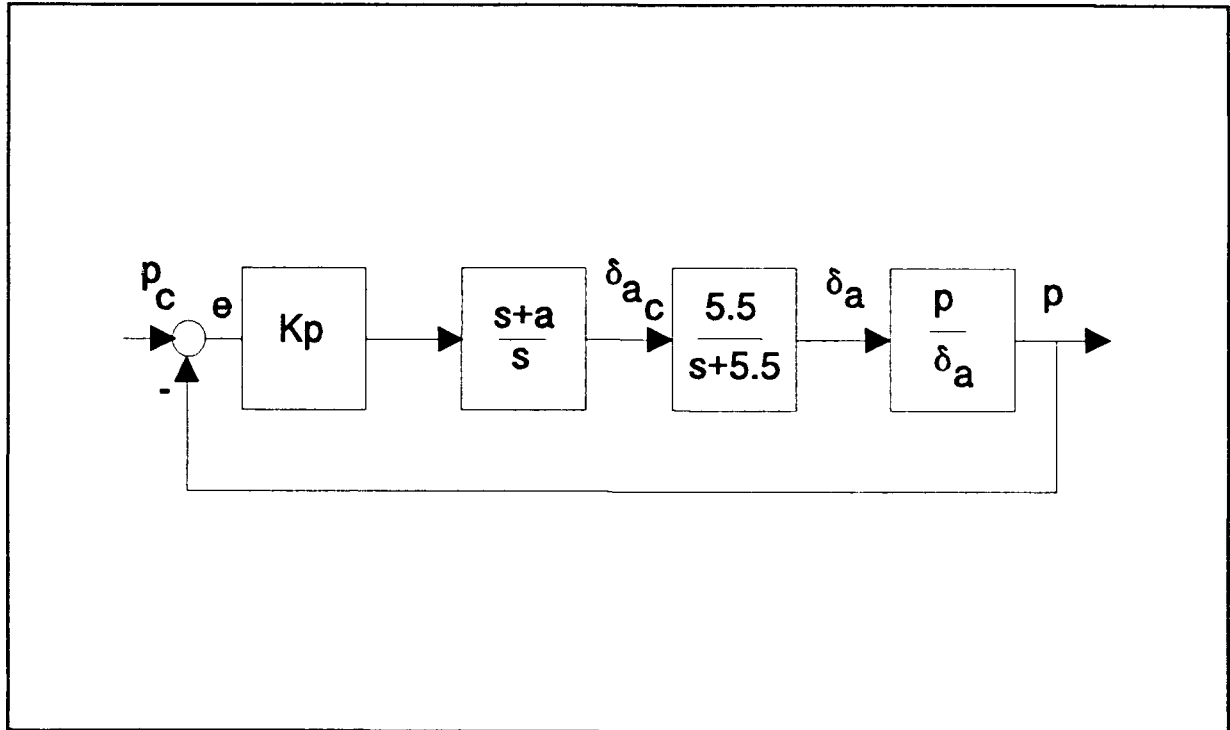


Figure 4.14. Roll Rate Controller Block Diagram
(Negative Feedback with a Gain and a Lead).

Flight Condition #1 Point Design.

$$\begin{array}{lll} X_{cg}=45.83 \text{ in} & \bar{q}_1=6.866 \text{ psf} & \theta_1=0 \text{ deg} \\ U_1=76.0 \text{ fps} & W_1=200 \text{ lbs} & \end{array}$$

The roll rate to aileron deflection transfer function for this flight condition is given below:

$$\frac{p(s)}{\delta_a(s)} = \frac{16.35s(s^2+0.8934s+3.077)}{(s^2+0.9093s+3.307)(s+3.249)(s-0.0328)} \quad (4.7)$$

which corresponds to the following lateral-directional characteristic modes:

dutch roll natural frequency: 1.819 rad/sec
dutch roll damping ratio: 0.2500
roll mode time constant: 0.3078 sec
unstable spiral mode

The aileron servo dynamics are modeled as follows:

$$G_s(s) = \frac{\delta_A(s)}{\delta_A(s)_{com}} = \frac{5.5}{s+5.5} \quad (4.8)$$

A general root locus for the block diagram in Figure 4.14 is given in Figure 4.15. Notice that a gain and a lead will provide an adequate compensator for this control design.

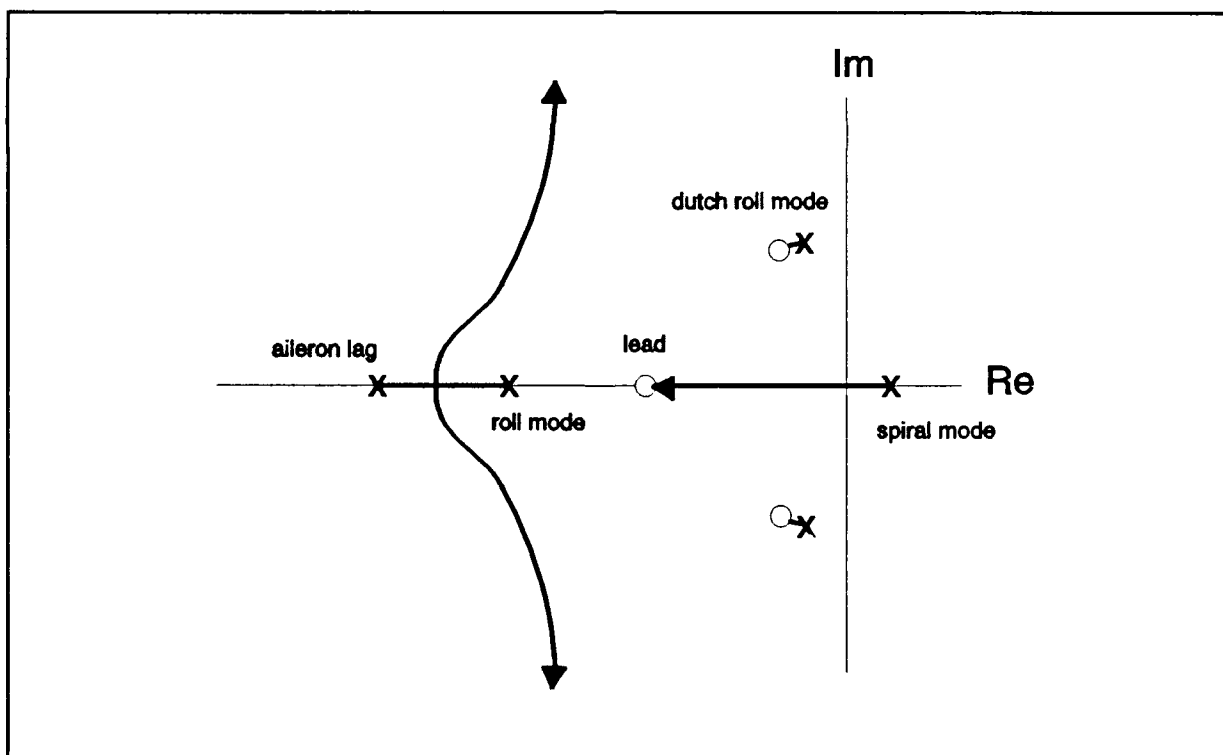


Figure 4.15. General Root Locus for Figure 4.14 Block Diagram.

The open loop transfer function for this system is:

$$G_{OL}(s) = K_p \frac{(s+a_l)}{s} \frac{5.5}{(s+5.5)} \frac{p(s)}{\delta_A(s)} \quad (4.9)$$

and the steady state error is:

$$e_{ss} = 1 - \frac{K_p(a_l)(5.5)(50.31)}{(-0.3524)(5.5) + K_p(a)(5.5)(50.31)} \quad (4.10)$$

The selection of K_p and the lead coefficient (a_l) requires the following considerations:

1. Steady state error (Eqn. 4.10) decreases as $K_p \cdot a_l$ increases.
2. Increasing a_l moves the center of the root locus asymptotes towards the imaginary axis which, in turn, reduces the natural frequency of the closed loop time response.
3. Increasing K_p drives the spiral root stable, reduces the effects of the dutch roll mode, and eventually decreases the damping ratio of the closed loop time response.

The root locus for $K_p=0.15$ and $a_l=3$ is given in Figure 4.16. The corresponding closed loop time response is given in Figure 4.17. The response has a rise time of approximately 0.5 seconds and a settling time of approximately 1 second. The steady state error is 1.6%.

The Bode magnitude and phase plot for the open loop transfer function is given in Figure 4.18. Notice that the phase margin for this design is 73 degrees.

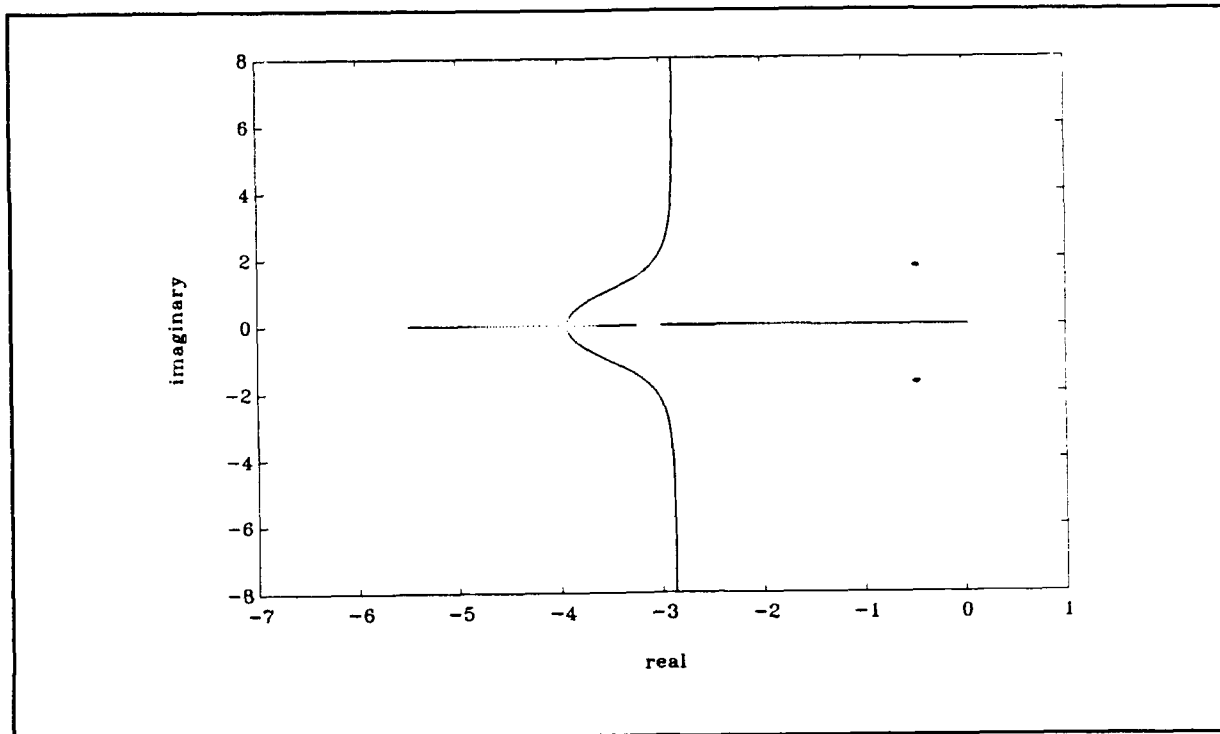


Figure 4.16. Root Locus for the Roll Rate Controller for Flight Condition #1 with $K_p=0.15$ and $a_l=3.0$.

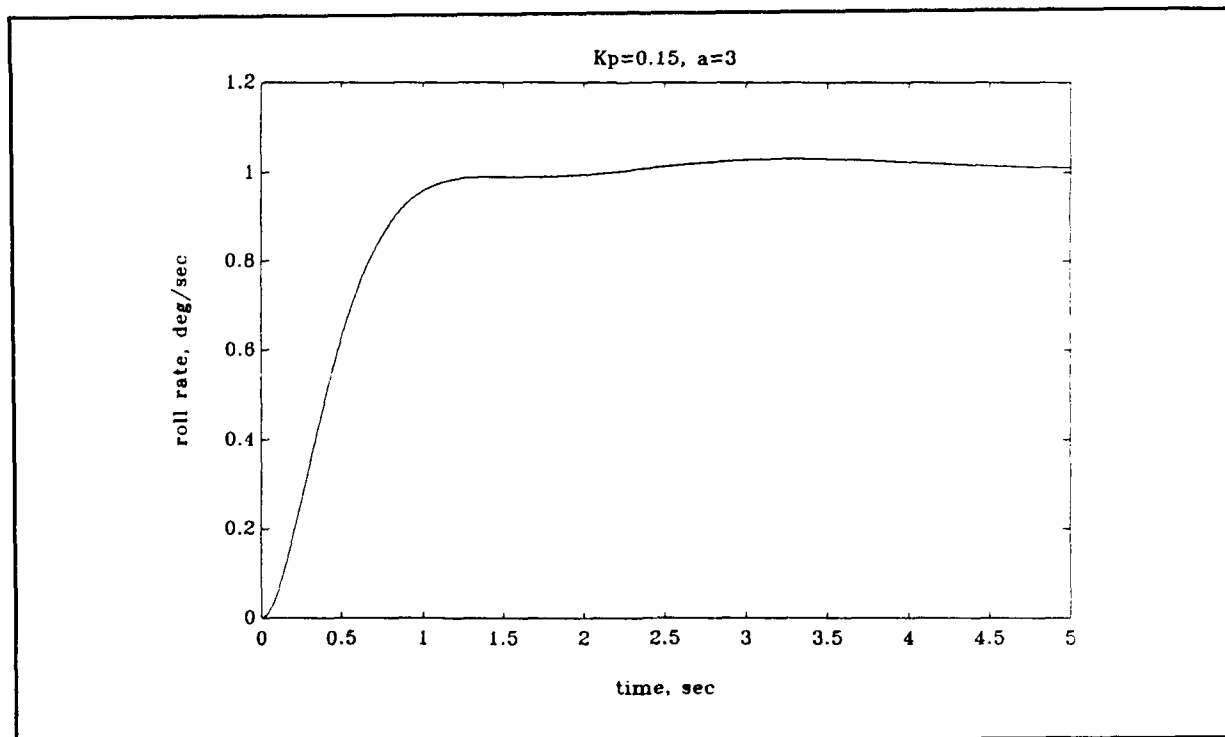


Figure 4.17. Closed Loop Time Response for the Roll Rate Controller Design for Flight Condition #1.

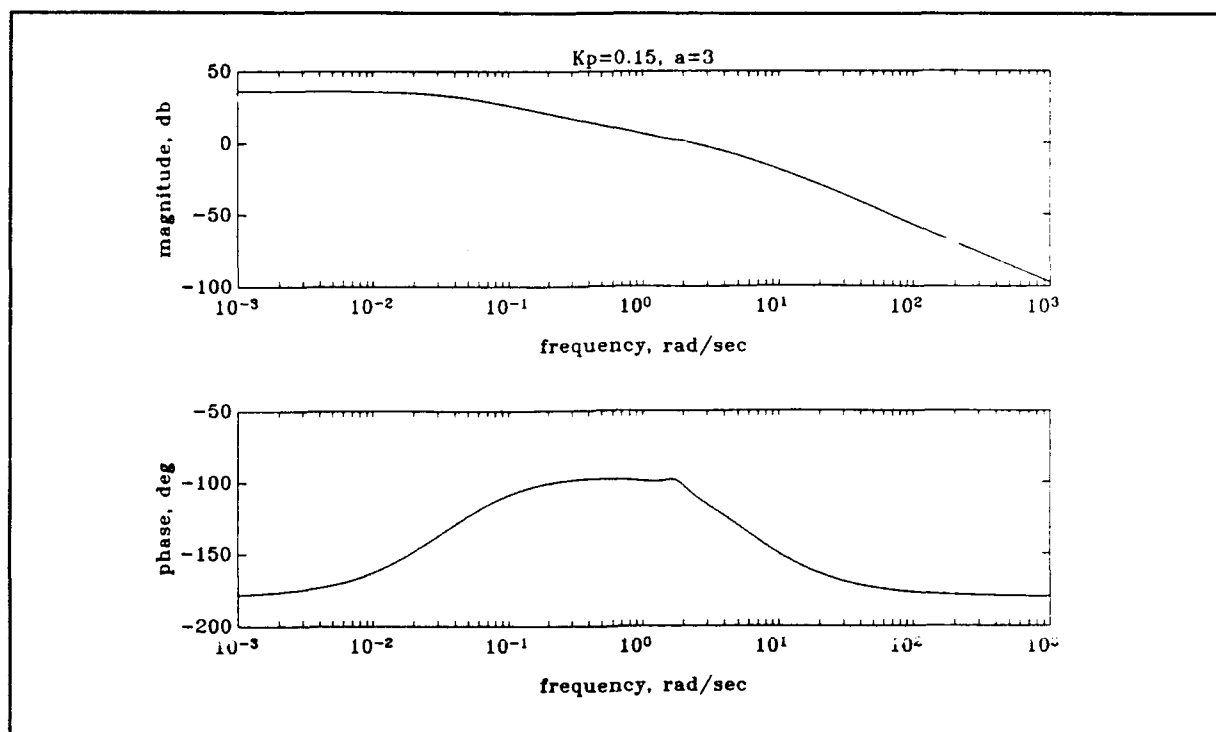


Figure 4.18. Bode Magnitude and Phase Plot for the Roll Rate Controller Design for Flight Condition #1.

The same gain and lead placement produced comparable roll rate controller designs at the other three corners of Lambda's flight envelope. Table 4.2 summarizes the roll rate controller point designs. Figure 4.19 provides the closed loop time responses for each of the final designs (at the most aft c.g. location). These all appear to be very good designs; therefore, gain scheduling will not be required for the roll rate controller.

Table 4.2. Roll Rate Controller Point Designs.

FC	X_{cg} (in)	U_1 (fps)	W (lbs)	Kp	a_L	PM (deg)	e_{ss} (%)	t_s (sec)
1	45.83	76.0	200	0.15	3.0	73	1.6	1.0
2	45.83	168.9	200	0.15	3.0	67	0.4	1.0
3	47.75	168.9	200	0.15	3.0	67	0.3	1.0
4	47.75	76.0	200	0.15	3.0	73	1.6	1.0

FC \equiv Flight Condition
PM \equiv Phase Margin

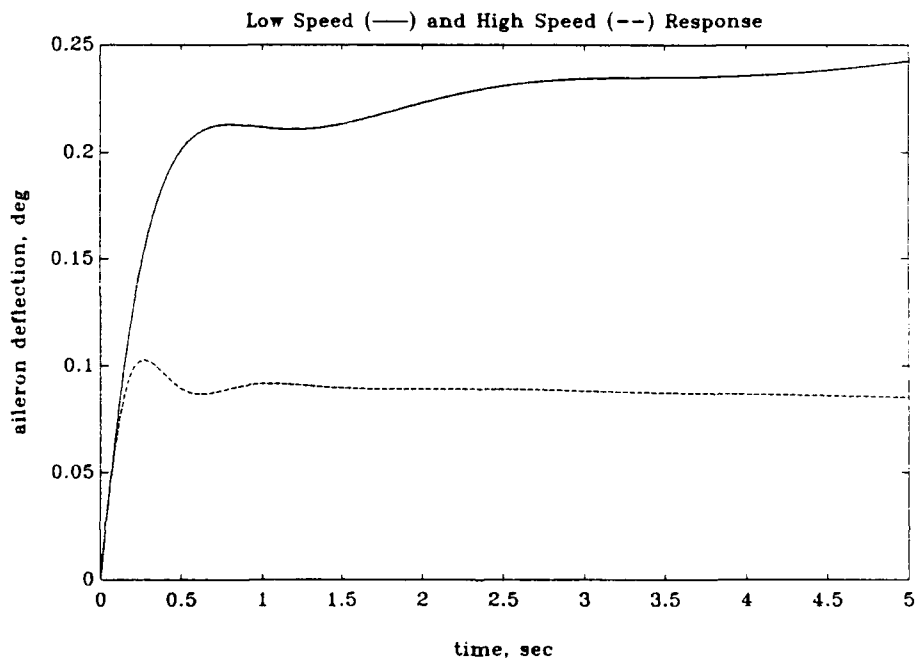
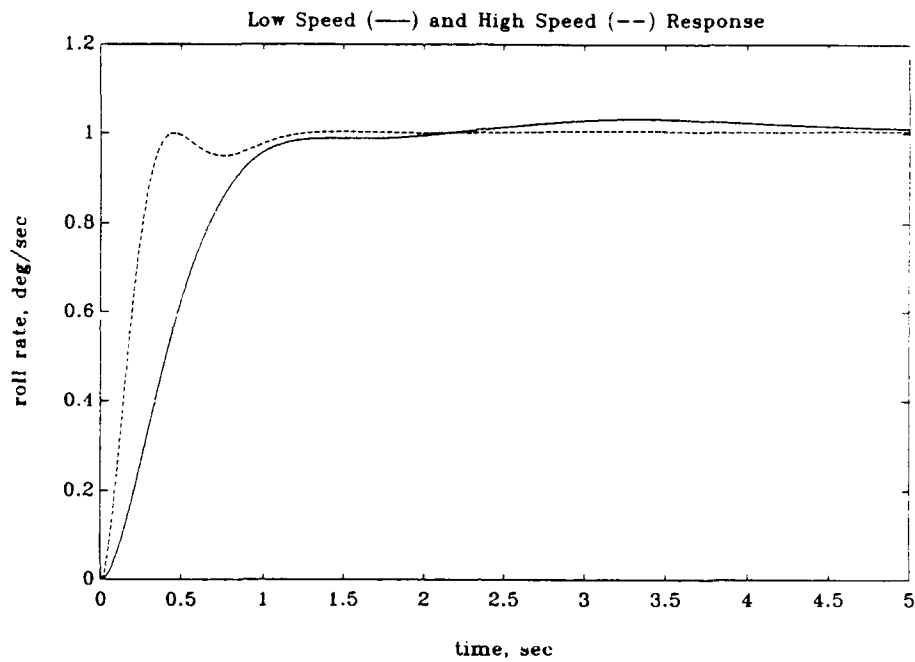


Figure 4.19. Closed Loop Time Responses for the Final Roll Rate Controller Point Designs.

4.4. Yaw Rate Controller Design

The same approach used to design the pitch rate controller was used in the design of the yaw rate controller. Four point designs were again accomplished. The design for the slow speed, most forward c.g. location will be described in detail.

Flight Condition #1 Point Design.

$$\begin{array}{lll} X_{cg}=45.83 \text{ in} & \bar{q}_1=6.866 \text{ psf} & \theta_1=0 \text{ deg} \\ U_1=76.0 \text{ fps} & W_1=200 \text{ lbs} & \end{array}$$

The yaw rate to rudder deflection transfer function is:

$$\frac{r(s)}{\delta_R(s)} = \frac{-3.845(s+3.256)(s^2+0.0306s+0.1060)}{(s^2+0.9093s+3.307)(s+3.249)(s-0.0328)} \quad (4.11)$$

which corresponds to the following lateral-directional characteristic modes:

dutch roll natural frequency: 1.819 rad/sec
dutch roll damping ratio: 0.2500
roll mode time constant: 0.3078 sec
unstable spiral mode

The rudder servo dynamics are modeled as follows:

$$G_s(s) = \frac{\delta_R(s)}{\delta_R(s)_{com}} = \frac{6.2}{s+6.2} \quad (4.12)$$

A negative feedback compensator with a pure gain and two leads produced the best results. The general block diagram for this design is given in Figure 4.19.

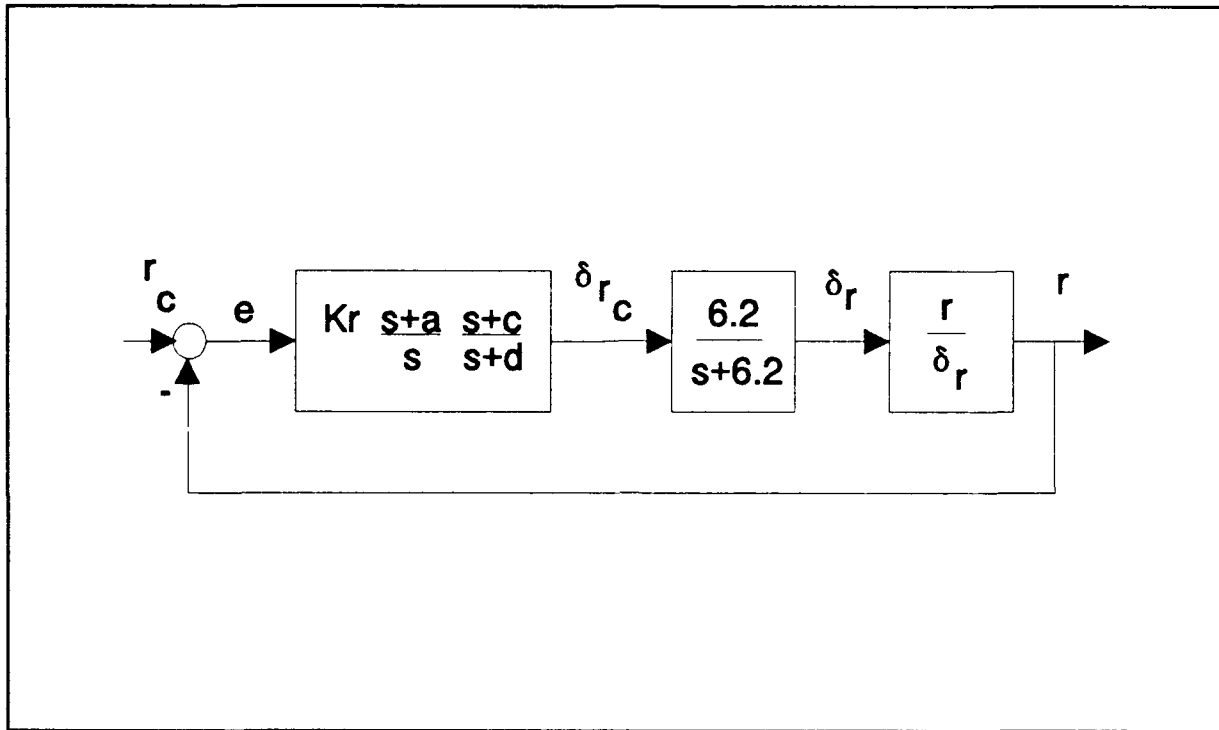


Figure 4.20. Yaw Rate Controller General Block Diagram
(Negative Feedback with a Pure Gain and Two Leads).

The open loop transfer function for this system is as follows:

$$G_{ol}(s) = Kr \frac{(s+a_l)}{s} \frac{(s+c)}{(s+d)} \frac{6.2}{(s+6.2)} \frac{r(s)}{\delta_r(s)} \quad (4.13)$$

The steady state error for this system is zero; therefore, this will be a true Type-1 system. A general root locus for this design is given in Figure 4.21. This is the most complicated root locus yet shown.

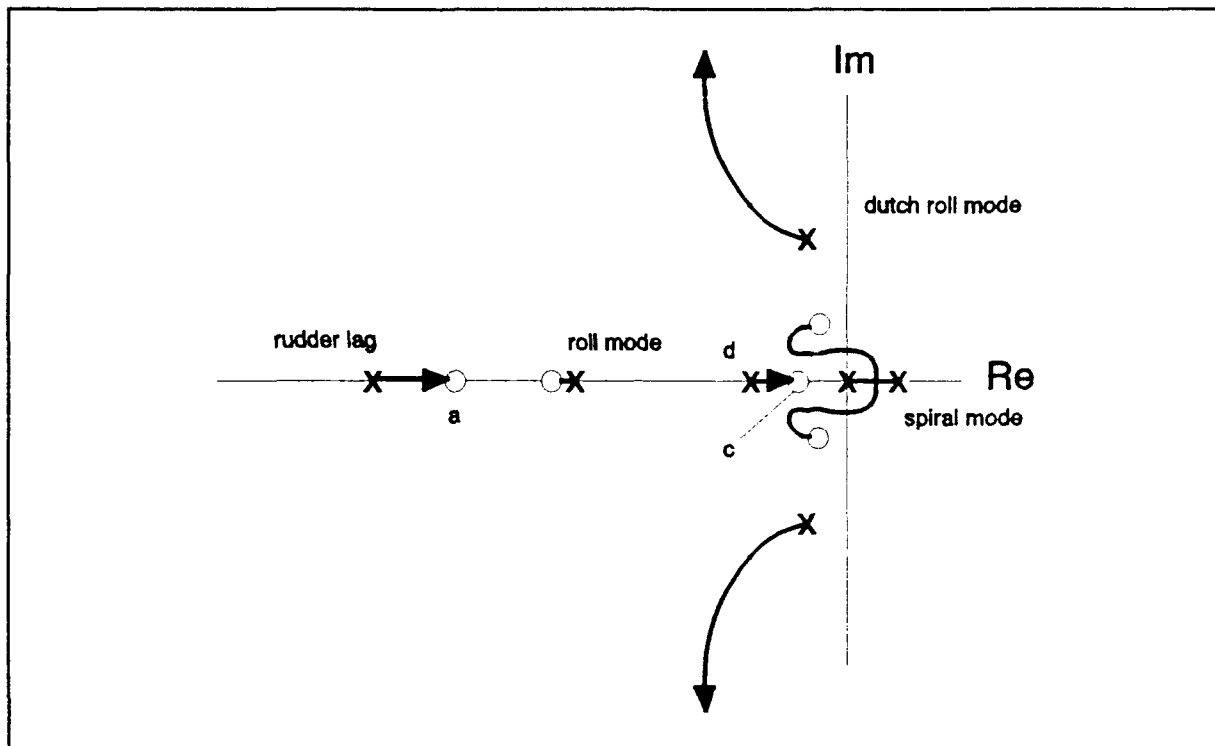


Figure 4.21. General Root Locus for Figure 4.20 Block Diagram.

Selection of K_r , a_l , c , and d requires the following considerations:

1. The best placement for the zero, c , was near the origin so as to mirror the unstable spiral root. This tended accelerate the movement of the locus, formed by the spiral root and pole at the origin, into the stable s -plane and closer to the real axis. Thus, lower gain could be used to drive the spiral locus stable while at the same time maximizing damping ratio.
2. Increasing K_r quickly decreases the damping ratio of the dutch roll mode. This causes large initial oscillation in the closed loop time response. Increasing K_r also drives the spiral locus roots closer to the complex zeros near the origin. If K_r

is large enough, these complex zeros tend to cancel the effect of the spiral locus roots. At the same time, increasing K_r drives the pole originating at d to the zero c which is near the origin. This low frequency pole combined with the near cancellation of the complex pole/zero pair near the origin causes a slowly dying small frequency oscillation in the long term time response.

The closed loop time response for $K_r=-2.5$, $a_l=4.0$, $c=0.033$, and $d=0.5$ is given in Figure 4.22. Several other values for K_r , a_l , c , and d were tried, but this response was actually one of the best. The Bode magnitude and phase plot for the open loop transfer function is given in Figure 4.23. Notice that the phase margin is 22 degrees.

Using the same approach, yaw rate controller point designs were accomplished at the remaining three corners of the flight envelope. Table 4.3 summarizes the point designs and Figure 4.24 provides the corresponding closed loop time responses (at the most aft c.g. location). Gain scheduling of K_r as a function of flight speed is required for all other flight conditions within Lambda's flight envelope.

Table 4.3. Yaw Rate Controller Point Designs.

FC	X_{cg} (in)	U_1 (fps)	W (lbs)	K_r	a_l	c	d	PM (deg)	e_{ss} (%)
1	45.83	76.0	200	-2.5	4.0	0.033	0.5	22	1.50
2	45.83	168.9	200	-1.0	4.0	0.033	0.5	23	1.35
3	47.75	168.9	200	-1.0	4.0	0.033	0.5	23	1.35
4	47.75	76.0	200	-2.5	4.0	0.033	0.5	22	1.50

FC \equiv Flight Condition

PM \equiv Phase Margin

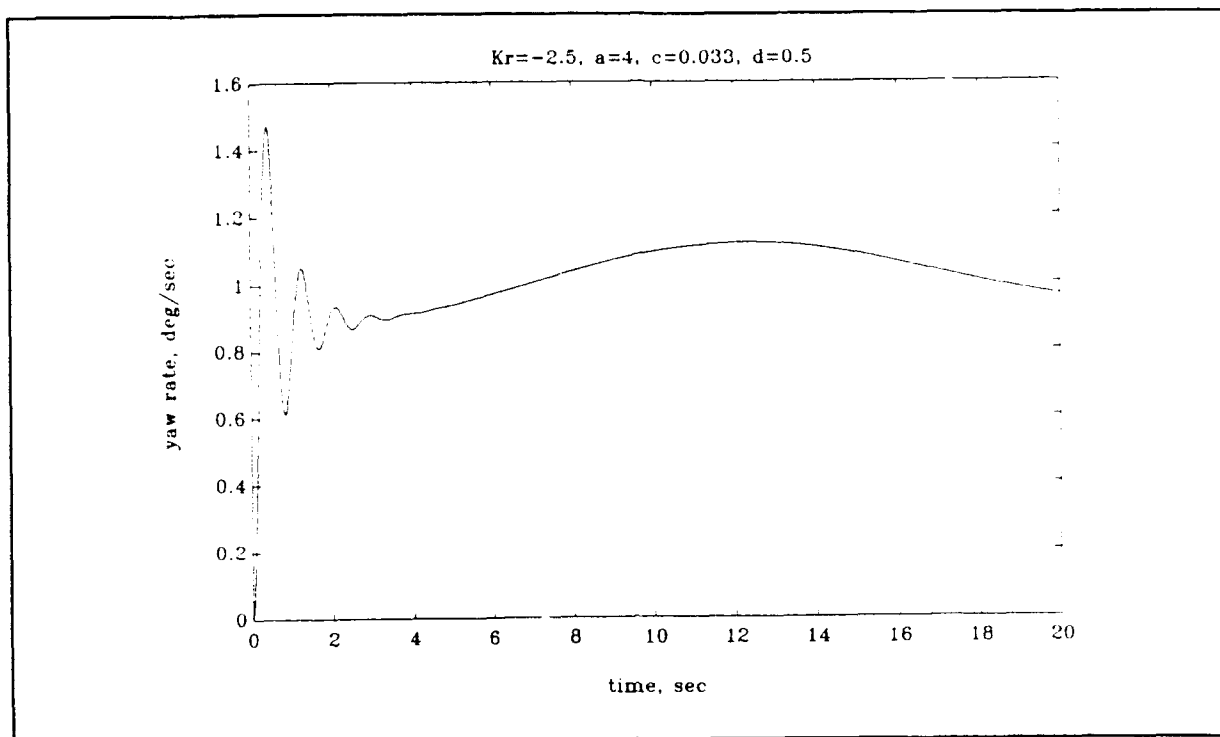


Figure 4.22. Closed Loop Time Response for the Yaw Rate Controller for Flight Condition #1 with $K_r = -2.5$, $a_l = 4$, $c = 0.033$, $d = 0.5$.

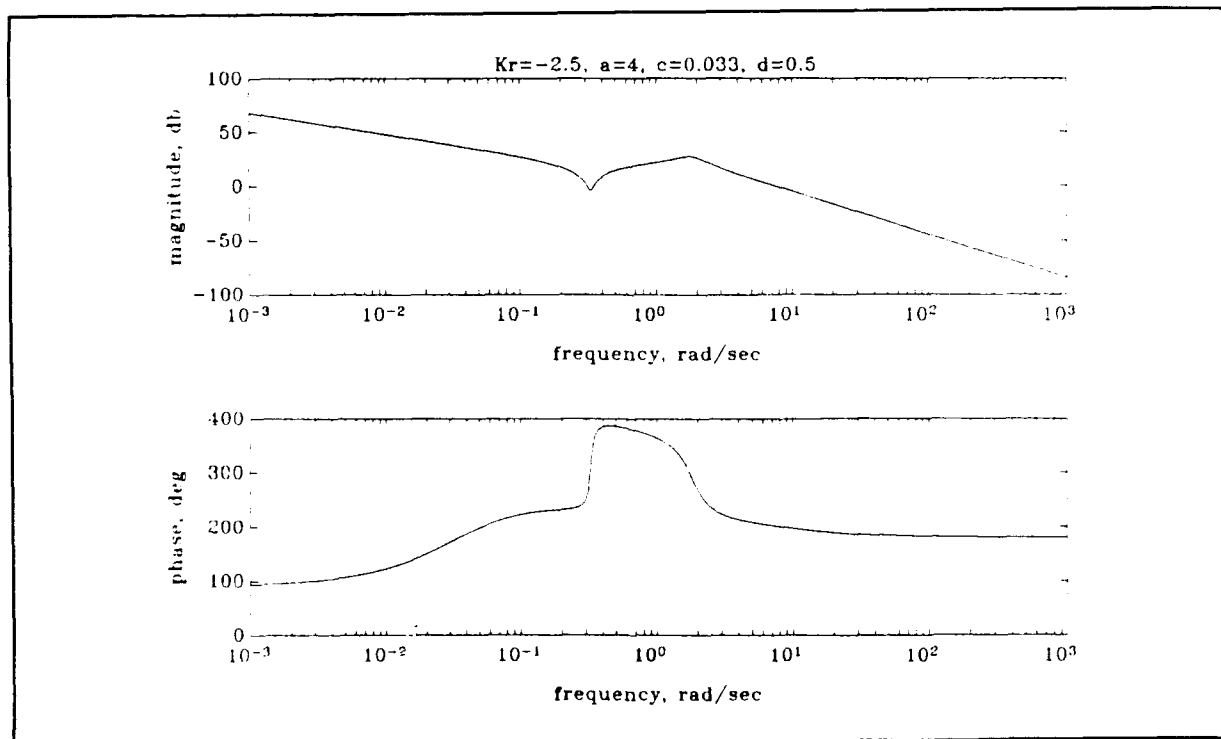


Figure 4.23. Bode Magnitude and Phase Plot for the Yaw Rate Controller Design for Flight Condition #1.

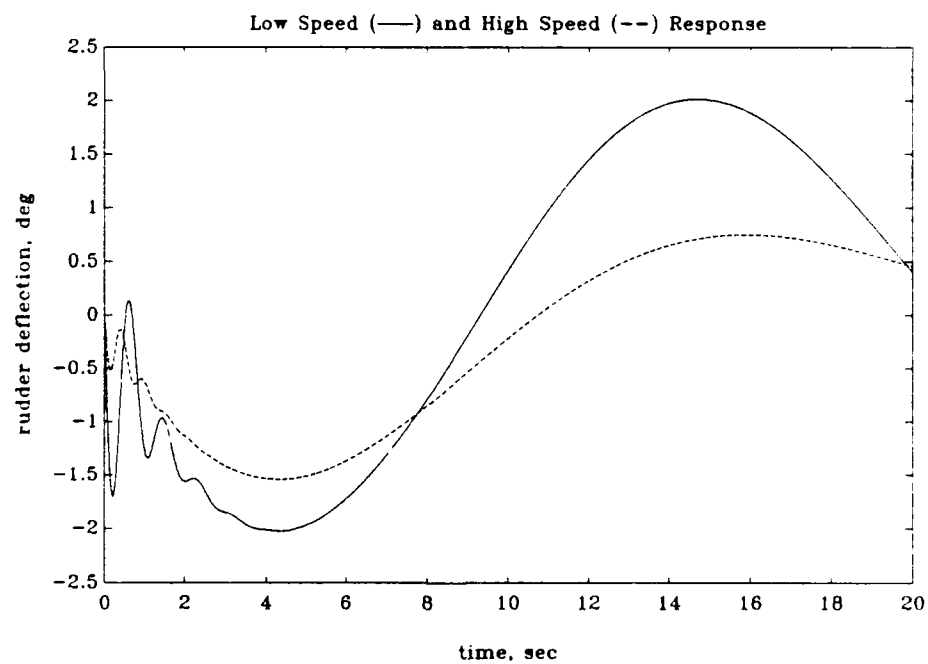
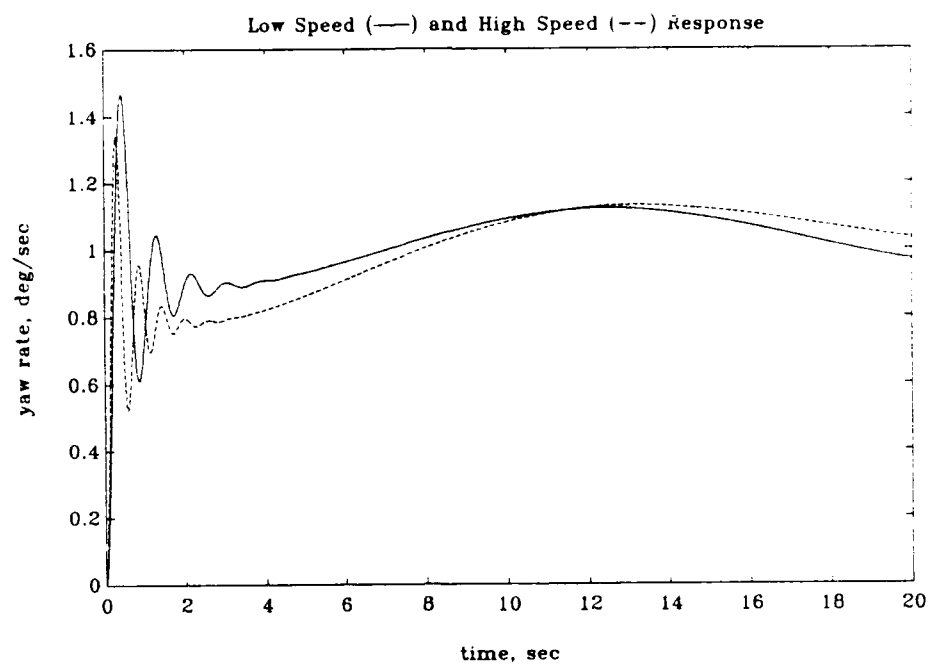


Figure 4.24. Closed Loop Time Responses for the Final Yaw Rate Controller Point Designs.

4.5. Discussion of Rate Controller Designs Using Classical Techniques

The main purpose of this chapter was to create a set of baseline rate controller designs to be compared with the multivariable feedback controller systems to be developed in the next chapter. It should be noted that attention was restricted to only single integrator compensators for the classical rate controller designs. Before proceeding, a discussion of the advantages and disadvantages of the methods used in this chapter are in order.

The main advantage of classical control design is the insight gained of the basic control problem being worked. Root locus techniques clearly show the engineer the characteristic modes of the airplane's open loop system. It emphasizes the strengths and weaknesses of the basic configurational layout. It clearly illustrates the overall control authority the engineer has at his disposal. For example, the slow elevator servo obstructed any attempt to arrive at a good pitch rate controller design for the Lambda URV.

The main disadvantage of classical control design is the lack of structure in choosing pole/zero placement for lag/lead compensation. The designer is forced to iterate between the open loop root locus, open loop Bode plot, and the closed loop time responses in order to select compensator gains, poles, and zeros that produce adequate closed loop performance and system robustness. Furthermore, lead/lag compensation can only be used to a certain extent before the designer begins to seek

compensators that free him from the real axis. The yaw rate controller design is a good example. A technique that would allow near cancellation of undesired modes through complex compensation would provide an opportunity for a better yaw rate controller design.

Finally, classical control techniques do not offer the ability to observe the effects of process or measurement noise on the overall system. The roll rate controller appears to be a successful first design. However, the design still needs to be tested against measurement noise and atmospheric disturbances. If it fails to perform adequately in the presence of noise, classical control techniques offer few alternatives for redesign.

The next chapter re-accomplishes each of the rate controller designs using multivariable feedback techniques. These techniques specifically provide a structure that directly addresses system performance, robustness, and noise.

5. Rate Controller Design Using Multivariable Feedback Techniques

In the last three decades, controller design using state space concepts and techniques have undergone significant research and development. Several multivariable, linear, time-invariant feedback methods for finite dimensional, linear, time-invariant systems exist today. The design methodology that will be used in this chapter is the Linear Quadratic Gaussian with Loop Transfer Recovery (LQG/LTR) approach. The 1981 paper by Doyle and Stein [16] is an excellent introduction to the LQG/LTR approach, with References 17 through 20 providing further development. In 1986, Ridgely and Banda [6] composed a technical report that has since become a handbook for LQG/LTR design. This handbook was used extensively for the controller designs presented in this chapter.

Section 5.1 provides an overview of the LQG/LTR approach used in the design of the rate controllers for Lambda. A basic outline of the methodology and an overview of the tools used is given. The reader is directed to Reference 6 for further development of the LQG/LTR approach used in this chapter. The pitch rate, roll rate, and yaw rate LQG/LTR controller designs for Lambda are presented in Sections 5.2, 5.3, and 5.4, respectively. Finally, Section 5.5 discusses the results of the overall designs and suggests ways to improve the controllers.

5.1. LQG/LTR Methodology

The system model for Lambda is assumed to be of the form:

$$\dot{x}(t) = Ax(t) + Bu(t) + \Gamma\xi(t) \quad (5.1)$$

$$y(t) = Cx(t) + \eta(t) \quad (5.2)$$

where,

$x(t)$ = n-vector state time history
 $u(t)$ = m-vector control input time history
 $y(t)$ = r-vector measurement time history
 $\xi(t)$ = s-vector white Gaussian process noise with statistics

$$E\{\xi(t)\} = 0 \quad (5.3)$$

$$E\{\xi(t)\xi^T(\tau)\} = Q_0\delta(t-\tau) \quad (5.4)$$

with Q_0 a symmetric, positive semidefinite matrix

$\eta(t)$ = r-vector white Gaussian measurement noise with statistics

$$E\{\eta(t)\} = 0 \quad (5.5)$$

$$E\{\eta(t)\eta^T(\tau)\} = R_f\delta(t-\tau) \quad (5.6)$$

with R_f a symmetric, positive definite matrix

A = nxn time invariant system dynamics matrix
 B = nxm time invariant, deterministic input matrix
 C = rxn measurement matrix
 Γ = nxs time invariant, process noise input matrix

It is further assumed that $x(t_0)$, $\xi(t)$ and $\eta(t)$ are independent of each other.

It is now desired to design a Linear Quadratic Gaussian (LQG) compensator for this system. The LQG compensator consists of the following two parts:

- the Linear Quadratic Estimator (LQE), and
- the Linear Quadratic Regulator (LQR).

Furthermore, the LQ estimator and LQ regulator designs will be constructed using the LQG/LTR framework. Specifically, the

approach of breaking the loop at the plant output will be used. The development of this approach is provided in detail in Chapter 9 of Reference 6. Only the mechanics of this approach will be given here.

LQG/LTR design by breaking the loop at the plant output involves the following steps:

1. Design a full-state LQ estimator whose loop shape meets all performance requirements.

2. Design a sequence of LQG compensators by designing a LQ regulator which recovers the properties of the full state estimator.

This procedure will now be described.

5.1.1. The Linear Quadratic Estimator (LQE)

Given the stochastic linear system defined by Equations 5.1 through 5.6, it is desired to produce an estimate, $\hat{x}(T)$, of the state, $x(T)$, at times $T > t_0$, using only the measurement data, $y(t)$, from $t_0 < t < T$. This is done by forming the state error vector,

$$e(t) = x(t) - \hat{x}(t) \quad (5.7)$$

and minimizing the mean square error,

$$e(T) = E\{e^T(t)e(t)\} = E\{\|x(t) - \hat{x}(t)\|^2\} \quad (5.8)$$

The estimator dynamics are then given by

$$\dot{\hat{x}}(t) = A\hat{x}(t) + Bu(t) + K_f[y(t) - C\hat{x}(t)] \quad (5.9)$$

The Kalman filter gain matrix, K_f , which minimizes Equation 5.8 is given by

$$K_f = MC^T R_f^{-1} \quad (5.10)$$

M is the variance of the error and is found by solving the

algebraic Riccati equation,

$$0 = AM + MA^T + \Gamma Q_0 \Gamma^T - MC^T R_f^{-1} CM \quad (5.11)$$

The error dynamics of the estimator are then given by

$$\begin{aligned} \dot{e}(t) &= \dot{x}(t) - \dot{\hat{x}}(t) \\ &= [A - K_f C]e(t) + [\Gamma \quad -K_f][\xi(t) \quad \eta(t)]^T \end{aligned} \quad (5.12)$$

Therefore, the poles of $[A - K_f C]$ are the poles of the filter, and are asymptotically stable iff the pair $[A, \Gamma]$ is stabilizable.

Finally, the estimator loop transfer function is given by

$$T_{KF}(s) = C\Phi K_f \quad (5.13)$$

$$\text{where, } \Phi(s) = (sI - A)^{-1}. \quad (5.14)$$

For the purposes of design, the following assumptions will be made:

1. The process noise is assumed to have unit intensity,

$$Q_0 = I. \quad (5.15)$$

2. The process noise input matrix, Γ , is completely general. The designer can use Γ to help tune the loop shape of the estimator transfer function.

3. The measurement noise is assumed to have the following intensity:

$$R_f = \mu I. \quad (5.16)$$

μ will also be used by the designer to adjust the loop shape of the estimator transfer function.

Thus, the designer has two completely tunable parameters, Γ and μ , to use for shaping the loop of the Kalman filter transfer function.

5.1.2. The Linear Quadratic Regulator (LQR)

For the LQ regulator it is desired to minimize the quadratic

performance index, J , which is given by

$$J = \int_0^\infty [\dot{x}^T(t) Q_c \dot{x}(t) + u^T(t) R_c u(t)] dt \quad (5.17)$$

where,

Q_c = symmetric, positive semidefinite state weighting matrix

R_c = symmetric, positive definite control weight matrix

Assuming $[A, B]$ is stabilizable, the feedback law

$$u(t) = -K_c x(t) \quad (5.18)$$

makes the closed loop system (without noise)

$$\dot{x}(t) = [A - BK_c] x(t) \quad (5.19)$$

asymptotically stable. The matrix, K_c , that minimizes J is

$$K_c = R_c^{-1} B^T P \quad (5.20)$$

where P is the solution to the algebraic Riccati equation

$$0 = A^T P + P A - P B R_c^{-1} B^T P + Q_c \quad (5.21)$$

Defining the system response equation as

$$z(t) = H x(t) \quad (5.22)$$

then,

$$Q_c = H^T H \quad (5.23)$$

Therefore, $z(t)$ is the response that will be regulated. Since the closed loop regulator is given by Equation 5.19, the poles of $[A - BK_c]$ are the poles of the regulator. The regulator loop transfer function is then given by

$$T_R(s) = K_c \Phi B \quad (5.24)$$

Again, for the purposes of design, the following assumptions will be made:

1. The control weighting matrix is

$$R_c = \rho I. \quad (5.25)$$

2. The state weighting matrix is

$$Q_c = H^T H + q^2 C^T C \quad (5.26)$$

where $z(t) = Hx(t)$ is the response to be regulated.

By defining R_c and Q_c in this manner, loop transfer recovery of the Kalman filter design can be realized (if the transmission zeros of the open loop plant are stable). The designer then chooses:

- H based on which states (or combination thereof) are to be regulated,
- ρ based on the amount of control usage willing to be expended, and
- q based on the level of recovery to be achieved.

5.1.3. The LQG Compensator with Loop Transfer Recovery

Combining the LQ estimator with the LQ regulator results in the overall LQG system given in Figure 5.1. The closed loop dynamics are given by:

$$\begin{bmatrix} \dot{x} \\ \dot{\tilde{x}} \end{bmatrix} = \begin{bmatrix} A & -BK_c \\ K_f C & A - BK_c - K_f C \end{bmatrix} \begin{bmatrix} x \\ \tilde{x} \end{bmatrix} + \begin{bmatrix} 0 \\ -K_f \end{bmatrix} r_c + \begin{bmatrix} \Gamma & 0 \\ 0 & K_f \end{bmatrix} \begin{bmatrix} \xi \\ \eta \end{bmatrix} \quad (5.27)$$

$$y = \begin{bmatrix} C & 0 \end{bmatrix} \begin{bmatrix} x \\ \tilde{x} \end{bmatrix} + \begin{bmatrix} 0 & I \end{bmatrix} \begin{bmatrix} \xi \\ \eta \end{bmatrix} \quad (5.28)$$

where,

r_c = system command input.

The poles of the closed loop system are the poles of the regulator and the poles of the estimator combined.

The LQG compensator transfer function is given by

$$K_{LQG}(s) = K_c(sI - A + BK_c + K_f C)^{-1} K_f \quad (5.29)$$

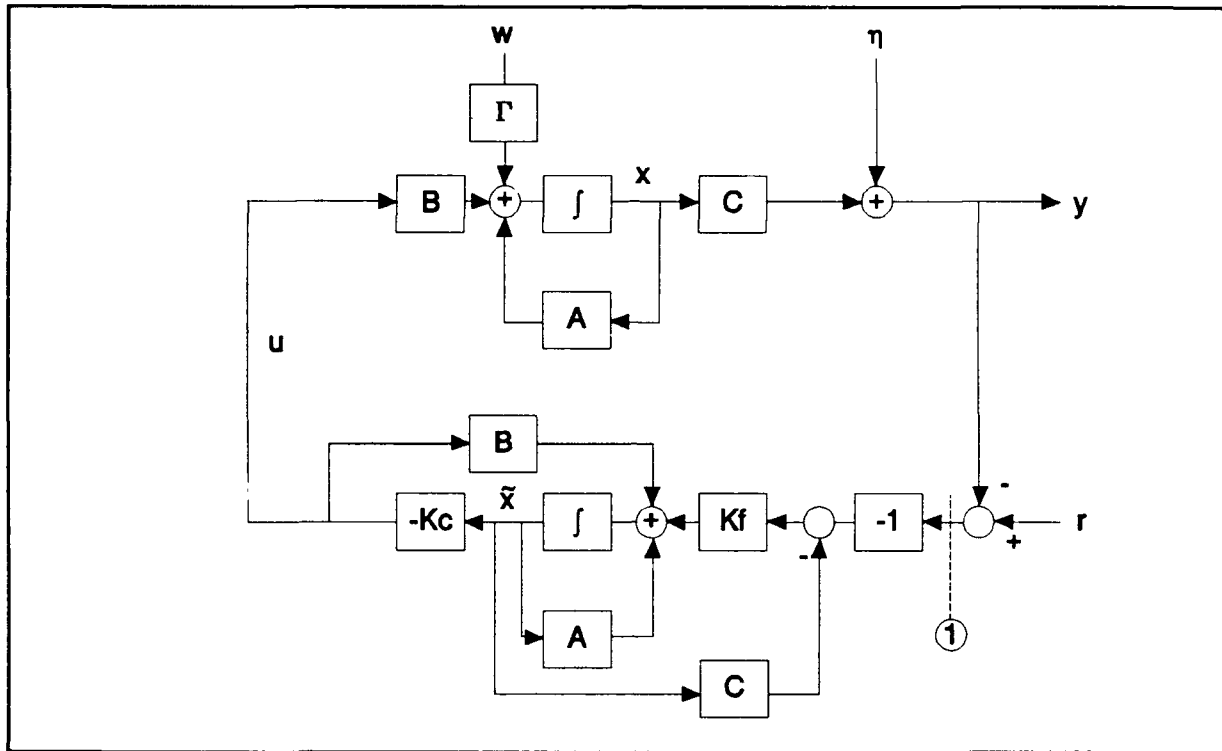


Figure 5.1. Block Diagram of the LQG System.

By breaking the system at point 1 in Figure 5.1 (the plant output), the resulting loop transfer matrix is given by

$$T_o(s) = G(s)K_{LQG}(s) \quad (5.30)$$

where,

$T_o(s)$ = loop transfer matrix for the loop broken at the plant output

$$G(s) = \text{plant transfer function matrix, } G(s) = C\Phi B \quad (5.31)$$

$K_{LQG}(s)$ is given by Equation 5.29.

With the set-up defined, as $q^2 \rightarrow \infty$, the loop transfer matrix $T_o(s)$ of the LQG system approaches the Kalman filter loop transfer function. In other words, the LQG system recovers the

desired performance of the Kalman filter design as q is increased to infinity.

The overall design procedure using the LQG/LTR approach is summarized as follows [6]:

Step 1: Define the design boundaries for system performance and robustness. This requires definition of a multivariable performance profile, $p(\omega)$, and an output multiplicative unstructured uncertainty profile, $l_m(\omega)$. Chapter 4 of Reference 6 is an excellent guide on how to form these profiles. Using $p(\omega)$ and $l_m(\omega)$, the design performance boundaries can be constructed.

Step 2: Select Γ and μ such that $\sigma_i[T_{KF}(s)]$ meets all performance requirements. It is shown in Reference 6 that at low frequency,

$$\mu^{-1/2} \sigma_i[T_{FOL}(s)] \approx \sigma_i[T_{KF}(s)] \quad (5.32)$$

$$\text{where, } T_{FOL}(s) = C\Phi\Gamma. \quad (5.33)$$

Thus, the designer can actively search for the appropriate Γ and μ that provides the desired loop shape by using the approximation of Equation 5.32 without ever having to solve the LQE Riccati equation. Once the proper choice of Γ and μ is determined, the procedure in Section 5.1.1 is used to complete the LQE design.

Step 3: Select H and ρ for the regulator. Choose a value for q and perform the regulator design summarized in Section 5.1.2.

Step 4: Calculate the LQG compensator transfer function, $K_{LQG}(s)$, and the resulting loop transfer matrix, $T_o(s)$.

Step 5: Compare $\sigma_i[T_o(s)]$ with $\sigma_i[T_{KF}(s)]$. If they are significantly different, increase q and repeat Steps 3 and 4. Continue until reasonable agreement between $\sigma_i[T_o]$ and $\sigma_i[T_{KF}]$ is

achieved.

Step 6: Form the closed loop state space model given by Equations 5.27 through 5.28 and evaluate the closed loop time responses. Also evaluate the control usage time histories. These plots will provide insight to whether H and ρ were properly selected. For example, if a regulated state is not forced to zero fast enough, the weighting on this state can be increased through H . Also, if control usage is too extreme, the penalty on control usage can be increased by increasing ρ . Once H or ρ have been changed, repeat Steps 3 through 5 and then re-evaluate the closed loop time histories.

This methodology will be used for all the rate controller designs presented in this chapter.

5.2. Pitch Rate Controller Design

This section presents the pitch rate controller design for Lambda using the LQG/LTR methodology. The design has the following characteristics:

- only the elevator was used for control,
- only pitch rate, q , was regulated,
- a square system was used (number of inputs equal the number of system outputs), thus only q was fed back to the compensator, and
- elevator dynamics and a wind model were added to the open loop plant model.

The pitch rate controller design will be described in detail in order to illustrate the mechanics of LQG/LTR for rate controller design.

5.2.1. Open Loop Model

The basic open loop, longitudinal, linear perturbation model for Lambda was developed in Chapter 3. This model has the following states and control inputs:

$$x(t) = [u(t), \alpha(t), q(t), \theta(t)]^T \quad (5.34)$$

$$u(t) = [\delta_e(t), \delta_f(t)]^T \quad (5.35)$$

with u in feet/second; α , θ , δ_e , and δ_f in radians; and q in radians/second. For the pitch rate controller design, this model was adjusted as follows:

1. All angles were converted from radians to degrees. All rates were converted from radians/second to degrees/second.
2. Flap control input was removed from the model. In actual flight, flaps are not used for control.

3. Wind disturbance dynamics were added to the model. Appendix E provides a description of the wind model used.
4. Control actuator dynamics were added to the model.
5. Process noise, as outlined in Section 5.1.1, was added to the model.
6. Pitch rate was the only state measured.

Table 5.1 summarizes the open loop longitudinal dynamics model, incorporating the above adjustments, for the flight condition at the midpoint of the flight envelope. It should be noted that Γ is still arbitrary at this point (except for the scaling on the wind noise). This model will be used for the development given in Sections 5.2.3 through 5.2.5.

5.2.2. Performance and Robustness Specifications

All of the plant uncertainties and performance requirements were modeled at the output of the plant. The following requirements were chosen [6]:

- at least 26 db gain at $\omega=0.1$ rad/sec,
- at least 60 db gain at $\omega=0.001$ rad/sec, and
- model accuracy within 10% of the true plant up to $\omega=2.0$ rad/sec and then increasing without bound at a rate of 20 db/decade.

A singular value plot of the resulting performance boundaries is given in Figure 5.2. The first two requirements ensure that the controller will be Type-1 over the normal bandwidth of the airplane's dynamics. This should allow for good command following (with zero steady state error) and disturbance rejection at low frequency. The high frequency bound ensures that the system will attenuate high frequency sensor noise. It also characterizes the

stability robustness of the closed loop system. This set of requirements will be used on all rate controller designs developed in this chapter.

Table 5.1. Open Loop Longitudinal Dynamics Model for the Flight Condition at the Center of Lambda's Flight Envelope

The model has the following form:

$$\dot{x}(t) = A_p x(t) + B_p u(t) + \Gamma \xi(t)$$

$$y(t) = C_p x(t) + \eta(t)$$

where,

$$x(t) = [u(t), \alpha(t), q(t), \theta(t), \delta_e(t), w(t)]^T$$

$$u(t) = \delta_{e \text{ com}}(t)$$

and,

$$A_p = \begin{bmatrix} -0.0267 & 0.5615 & 0.000 & -0.5615 & 0.000 & 0.5615 \\ -0.2458 & -2.872 & 0.9715 & 0.000 & -0.1428 & -2.872 \\ -0.1049 & -27.53 & -1.641 & 0.000 & -18.18 & -27.53 \\ 0.000 & 0.000 & 1.000 & 0.000 & 0.000 & 0.000 \\ 0.000 & 0.000 & 0.000 & 0.000 & -6.500 & 0.000 \\ 0.000 & 0.000 & 0.000 & 0.000 & 0.000 & -2.450 \end{bmatrix}$$

$$B_p = \begin{bmatrix} 0.000 \\ 0.000 \\ 0.000 \\ 0.000 \\ 6.500 \\ 0.000 \end{bmatrix} \quad \Gamma = \begin{bmatrix} \Gamma \\ \text{-----} \\ 0.0433 \end{bmatrix}$$

$$C_p = [0.000, 0.000, 1.000, 0.000, 0.000, 0.000]$$

Also, the white Gaussian process and measurement noises have the following characteristics:

$$E[\xi(t)] = 0$$

$$E[\eta(t)] = 0$$

$$E[\xi(t)\xi^T(\tau)] = \delta(t-\tau)$$

$$E[\eta(t)\eta^T(\tau)] = \mu\delta(t-\tau)$$

$$E[\xi(t)\eta^T(\tau)] = 0$$

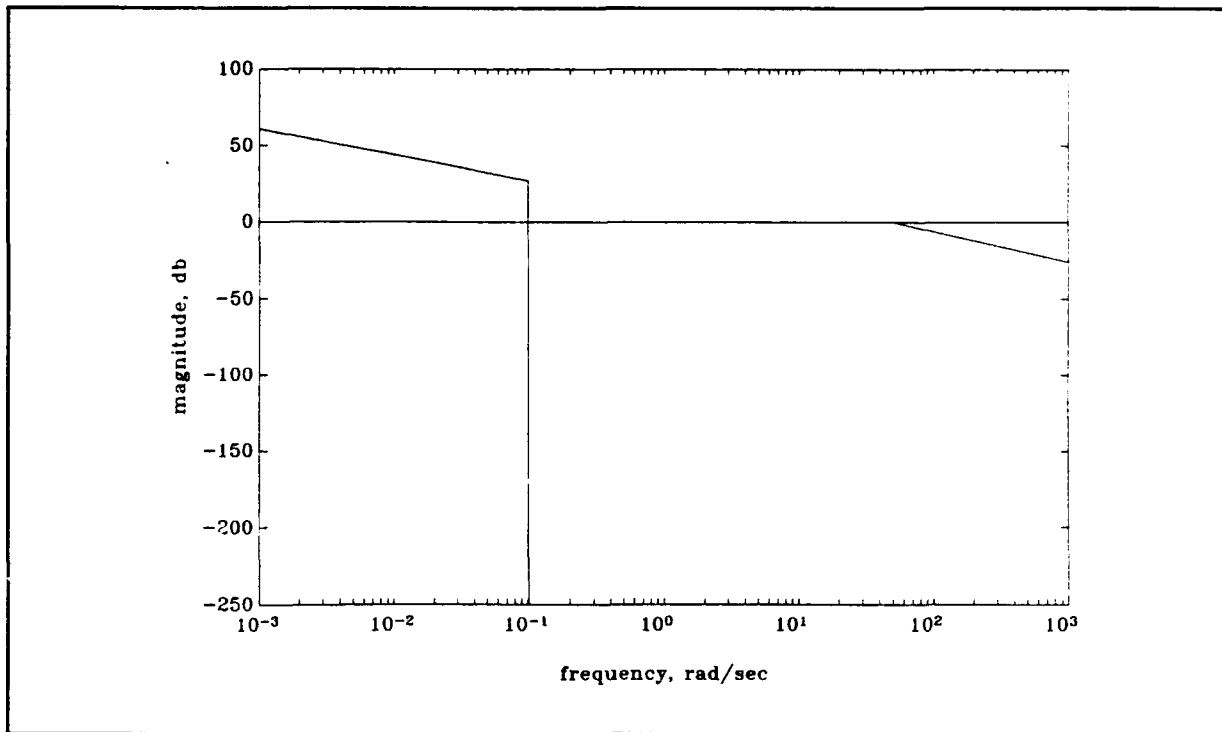


Figure 5.2. Singular Value Plot of Performance and Robustness Boundaries for Lambda Rate Controller Designs.

5.2.3. Augmenting Integrators to the Open Loop Model

A singular value plot (σ -plot) of the unaugmented open loop system is given in Figure 5.3. From this plot it is obvious that integrators need to be augmented to the open loop system.

A single integrator can be added to the open loop dynamics as outlined in Table 5.2. A σ -plot of the augmented open loop system is given in Figure 5.4. Again, the system does not have Type-1 characteristics. After augmenting yet another integrator to the open loop plant, the singular value plot for the doubly augmented system is given in Figure 5.5. The doubly augmented open loop possesses Type-1 characteristics and will be adopted as the basic open loop system for which to begin controller design.

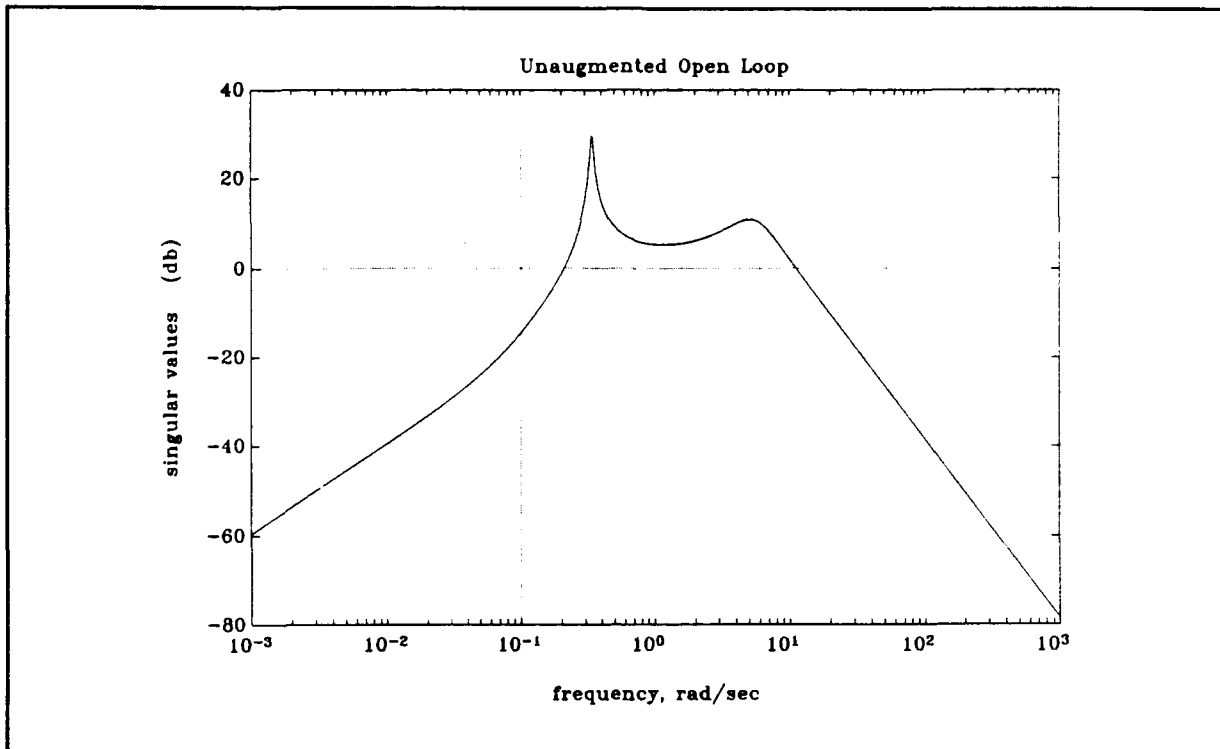
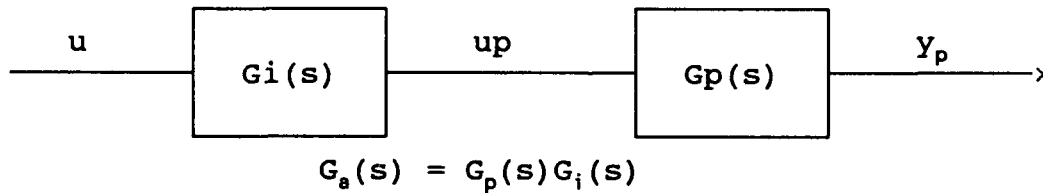


Figure 5.3. Unaugmented Open Loop Singular Value Plot.

Table 5.2. Process of Adding an Integrator to the Open Loop Dynamics



Plant State Space:

$$\dot{x}_p = A_p x_p + B_p u_p$$

$$y_p = C_p x_p + \underline{0} u_p$$

Integrator State Space:

$$\dot{x}_i = \underline{0} x_i + I u$$

$$u_p = I x_i + \underline{0} u$$

Augmented State Space:

$$\dot{x}_a = A_a x_a + B_a u$$

$$y_p = C_a x_a + D_a u$$

where,

$$A_a = \begin{bmatrix} A_p & B_p \\ \underline{0} & \underline{0} \end{bmatrix}$$

$$B_a = \begin{bmatrix} \underline{0} \\ I \end{bmatrix}$$

$$C_a = [C_p \quad \underline{0}]$$

$$D_a = \underline{0}$$

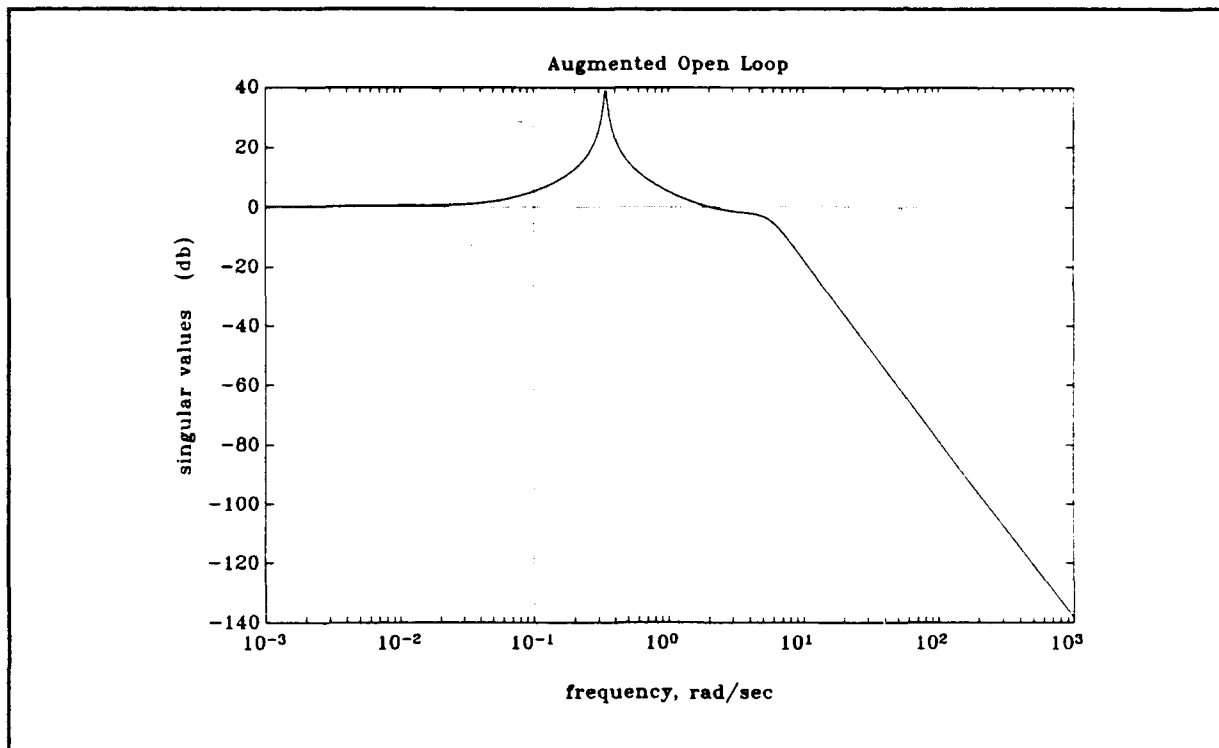


Figure 5.4. Augmented Open Loop Singular Value Plot.

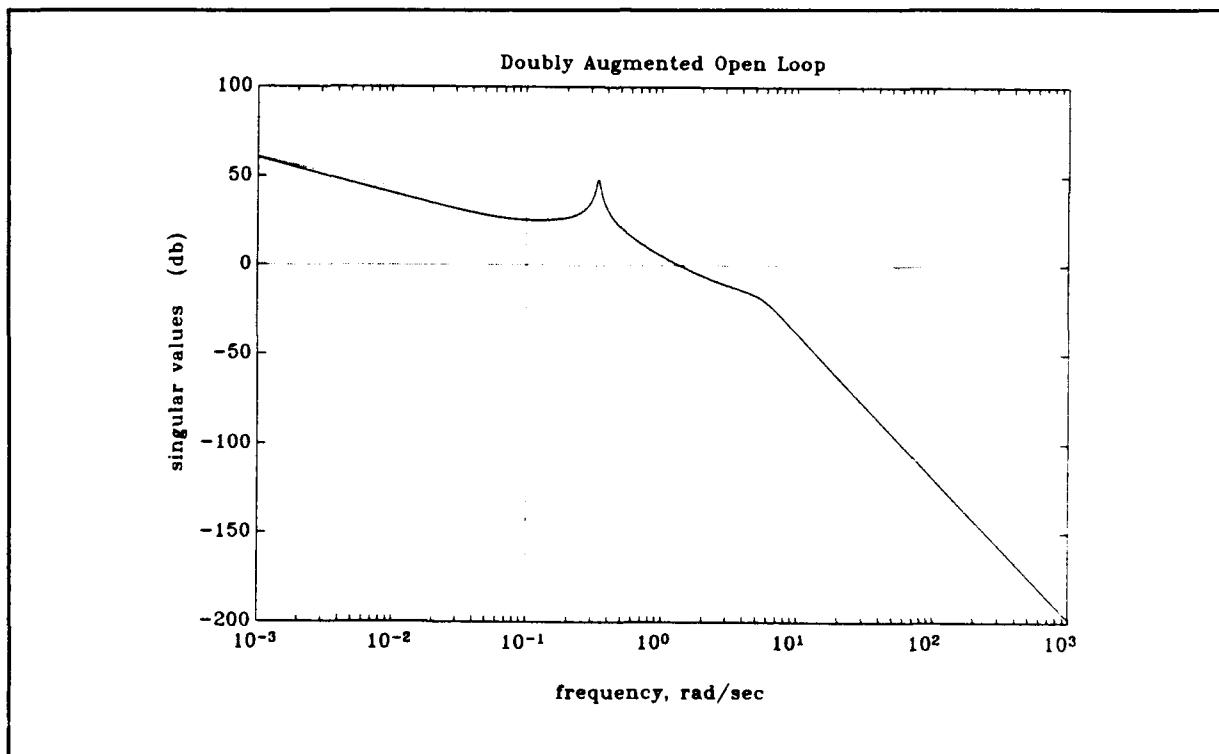


Figure 5.5. Doubly Augmented Open Loop Singular Value Plot.

5.2.4. LOE Design

The poles and zeros of the doubly augmented system are given in Table 5.3. Since the doubly augmented system has a nice loop shape, Γ was set equal to B with the following scaling for the wind model:

$$\Gamma = [0, 0, 0, 0, 0, 0, 0.043254, 0, 1]^T \quad (5.36)$$

↪ wind model noise scaling

Table 5.3. Characteristics of the Basic Open Loop (Doubly Augmented) System

The doubly augmented system has the following form:

$$\dot{x}(t) = Ax(t) + Bu(t) + \Gamma\dot{\xi}(t)$$

$$y(t) = Cx(t) + \eta(t)$$

and the system transfer function is:

$$G(s) = C(sI - A)^{-1}B = C\Phi B$$

The poles of $C\Phi B$ are:

-2.2611 ± 5.1389i
 -0.0086 ± 0.3393i
 -6.500
 -2.450
 0
 0

The zeros of $C\Phi B$ are:

-0.0810
 -2.6020
 -2.450
 0

Using the approximation given in Equation 5.32, $\mu=1/100$ was chosen. Table 5.4 outlines the Kalman filter design that resulted using the methods given in Section 5.1.1. Figure 5.6 is the corresponding singular value plot. This loop shape has a reasonable crossover frequency and provides a good margin for recovery.

Table 5.4. Kalman Filter Design

$$\mu = 1/100$$

$$\Gamma = [0, 0, 0, 0, 0, 0.0433, 0, 1]^T$$

$$K_f = [-0.0190, 0.9973, 6.1292, 1.000, -2.8493, -0.1631, -4.2108, -10.00]^T$$

Poles($C\Phi K_f$):

-1.9883 ± 5.6033i
 -4.0328 ± 1.8232i
 -5.5279
 -1.9684
 -0.0801
 0

Zeros($C\Phi K_f$):

-2.4843 ± 5.4767i
 -6.9359
 -2.8833
 -1.6854
 -0.0808
 0

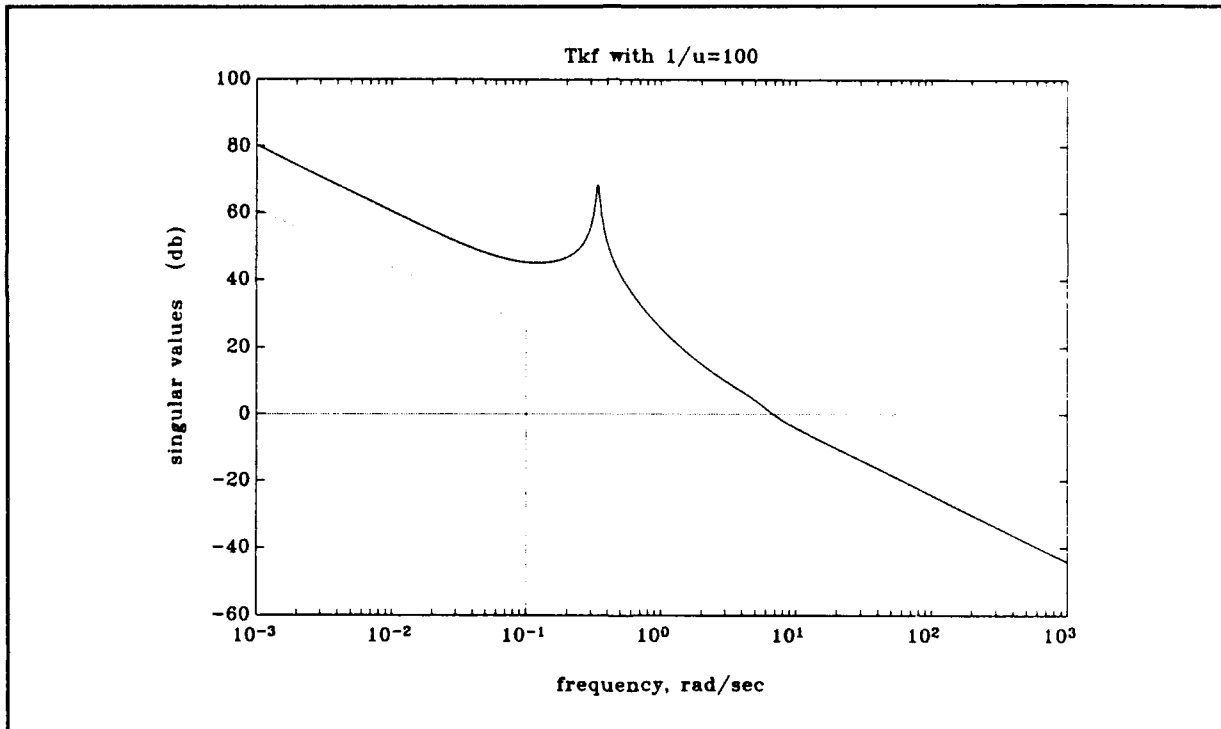


Figure 5.6. Singular Value Plot for the Kalman Filter Design Given in Table 5.4.

5.2.5. LOG/LTR

A sequence of LQG compensators were designed by constructing an LQ regulator which recovered the properties of the LQ estimator. The methodology presented in Sections 5.1.2 and 5.1.3 was used. Table 5.5 presents the final compensator design. Figure 5.7 provides the singular value plot for the loop transfer matrix, $T_o(s)$, for $q=0$, $\rho=1$ and Figure 5.8 is the corresponding plot for $q=1000$, $\rho=9999$. These two plots illustrate the recovery process as q is increased.

Table 5.5. LQG Compensator Design

Regulator:

$$q=1,000 \quad \rho=9,999 \quad H=[0,0,1,0,0,0,0,0]$$

$$K_c=[-2.1148, 10.9746, 1.2673, 0.2844, 1.0982, -1.6828, 22.552, 6.7160]$$

Poles($K_c \Phi B$):

$$\begin{aligned} &-2.3508 \pm 5.9398i \\ &-5.6846 \\ &-3.8031 \\ &-3.4861 \\ &-2.4500 \\ &-0.0801 \\ &0 \end{aligned}$$

Compensator:

Poles(K_{LQG}):

$$\begin{aligned} &-1.6876 \pm 8.1436i \\ &-8.9045 \pm 4.4218i \\ &-2.6658 \\ &-2.4045 \\ &-0.0801 \\ &0 \end{aligned}$$

Zeros(K_{LQG}):

$$\begin{aligned} &-2.2886 \pm 5.1017i \\ &-6.5114 \\ &-2.4905 \\ &-0.9676 \\ &-0.0843 \\ &0 \end{aligned}$$

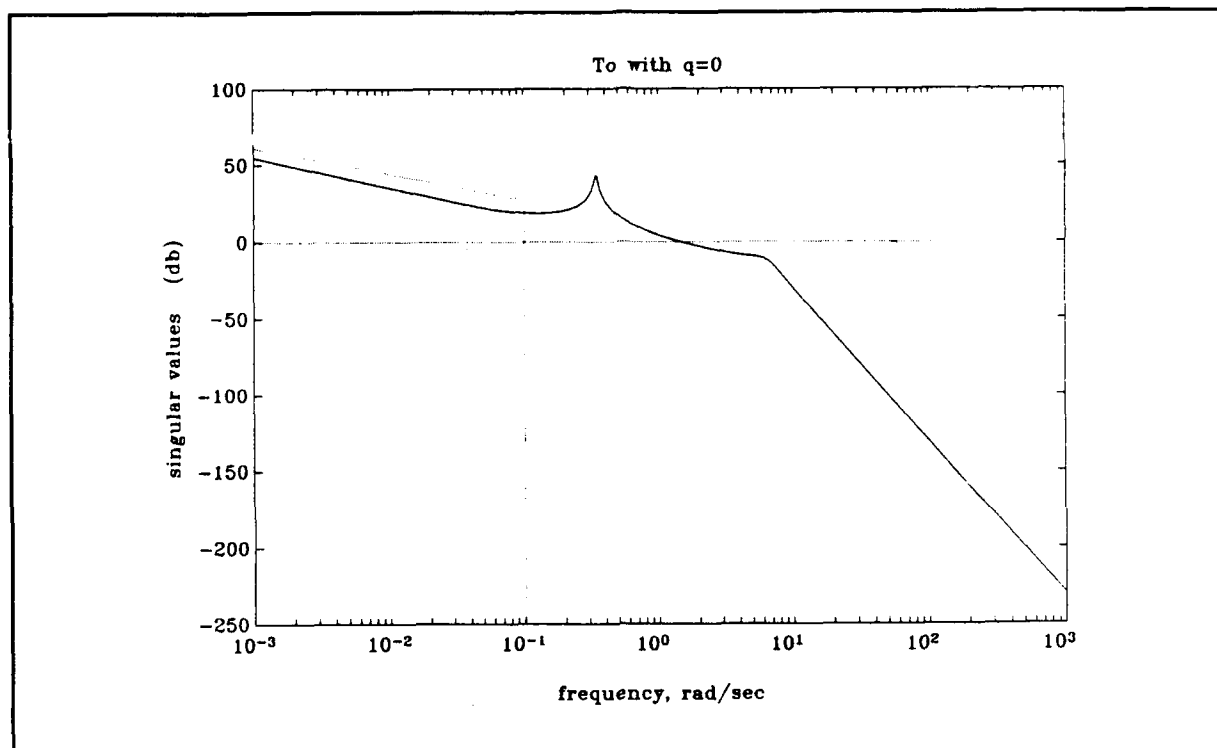


Figure 5.7. Singular Value Plot for $T_o(s)$ with $q=0$, $\rho=1$.

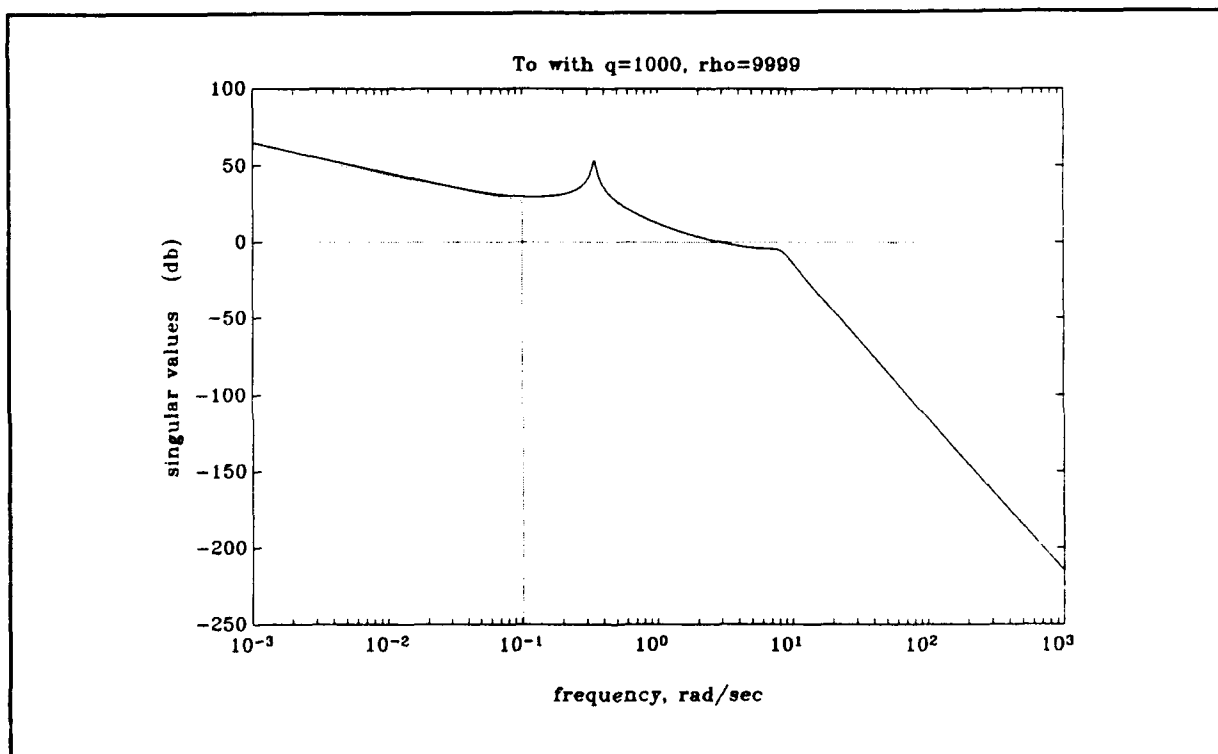


Figure 5.8. Singular Value Plot for $T_o(s)$ with $q=1000$, $\rho=9999$.

The closed loop time response for pitch rate to a unit step pitch rate command is given in Figure 5.9. The corresponding elevator time response is given in Figure 5.10. It should be noted that higher ratios of ρ/q were attempted to reduce the amount of elevator deflection expended. However, the algebraic Riccati software in MATLAB could not solve the LQ regulator algebraic Riccati equations for the higher ρ/q values at this flight condition. The numerical difficulties are due to the fact that as ρ is increased, the regulator algebraic Riccati equation (Equation 5.21) approaches the following Lyapunov equation:

$$A^T P + PA + Q_c = 0 \quad (5.37)$$

This Lyapunov equation has a unique solution if and only if the matrix A is stable. For Λ , the phugoid mode is unstable at slow speed. The numerics are further complicated by the fact that Q_c is an 8x8 matrix of all zeros except for the third position along the diagonal.

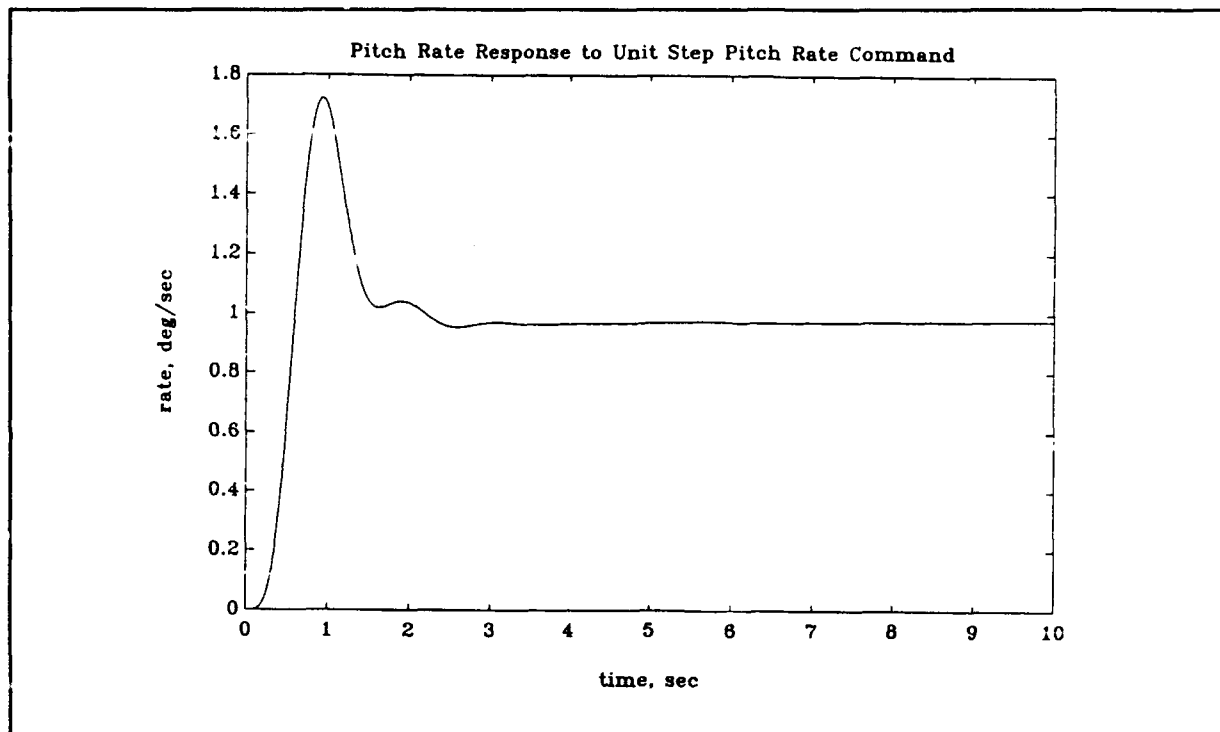


Figure 5.9. Closed Loop Time Response for Pitch Rate to a Unit Step Pitch Rate Command.

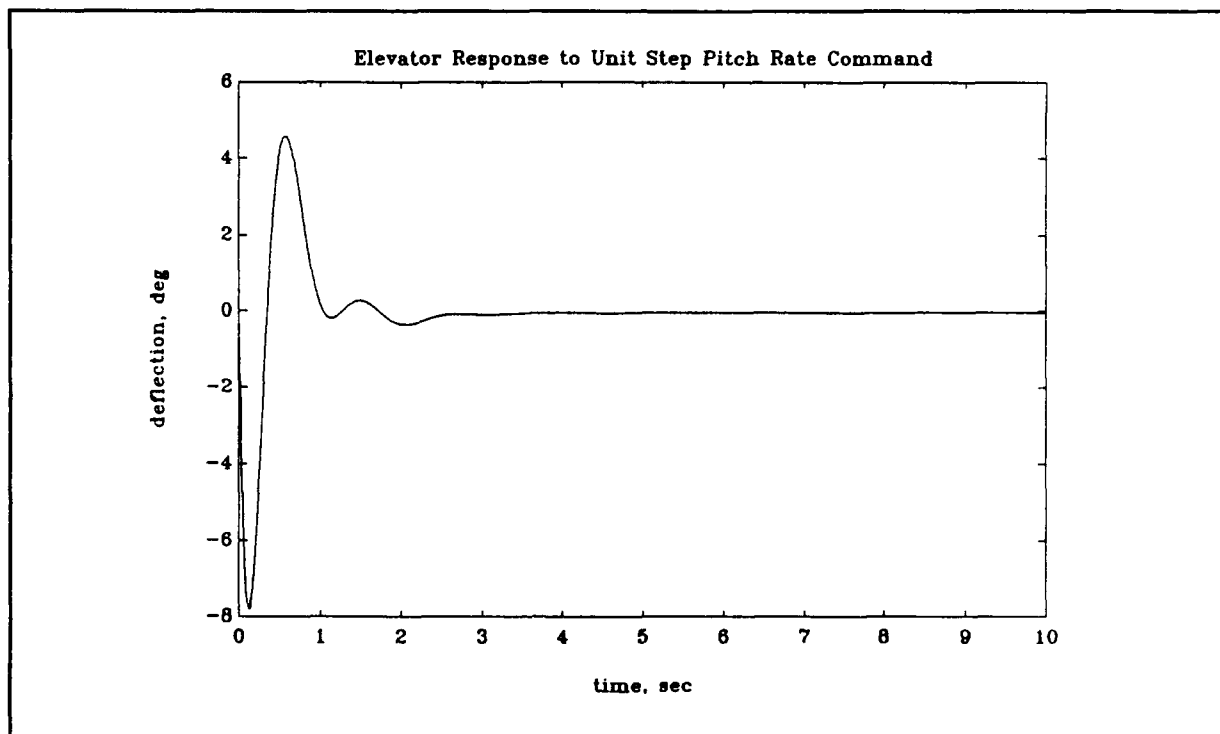


Figure 5.10. Closed Loop Response for Elevator Deflection to a Unit Step Pitch Rate Command.

Finally, the closed loop sensitivity for this point design is given in Figure 5.11. The gain and phase margins for the closed loop system can be obtained from the sensitivity plot by using the following equations:

$$\|S\|_{\infty} = \max \sigma_i\{S\} \quad (5.38)$$

$$GM = [-20*\log(1 + 1/\|S\|_{\infty}), -20*\log(1-1/\|S\|_{\infty})] \quad (5.39)$$

$$PM = \pm 2*\sin^{-1}[1/(2\|S\|_{\infty})] \quad (5.40)$$

where,

S = system sensitivity, magnitude

$\|S\|_{\infty}$ = infinity norm of the system sensitivity, magnitude

GM = independent gain margin, db

PM = independent phase margin, degrees

For this point design, the infinity norm of the system sensitivity, gain margins, and phases margins were as follows:

$$\|S\|_{\infty}=8.801 \quad GM=[-2.690db, 3.918db] \quad PM=\pm 20.92^{\circ}$$

These margins were too low for this to be considered a good design. Thus, complete point designs were repeated at both the high and low speed corners of Lambda's flight envelope. The final design selected is summarized in the next section.

5.2.6. Final Design

The final pitch rate controller design will now be summarized.

The regulator gain, K_c , was chosen from the point design at the high speed flight condition (most aft c.g. location). The ρ/q ratio for this design was 9,090, almost a thousand times

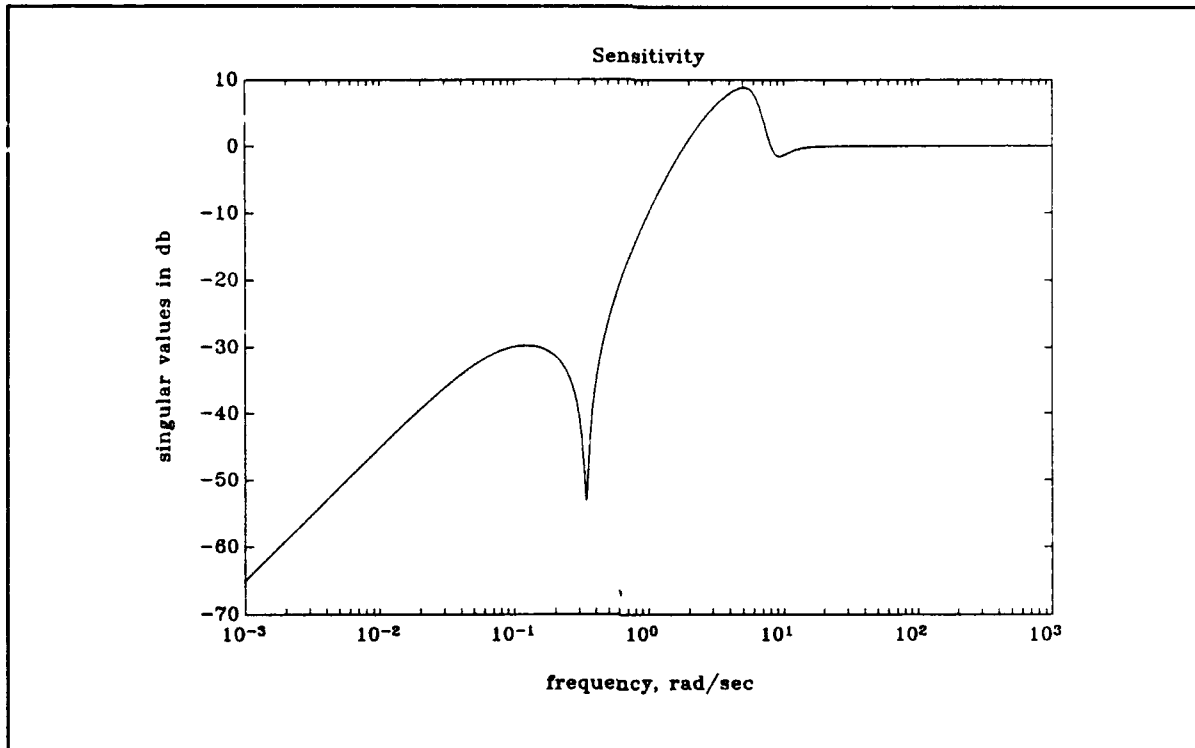


Figure 5.11. Closed Loop Sensitivity Singular Value Plot.

greater than that achieved at the midpoint flight condition. MATLAB could not solve the LQR algebraic Riccati equation for higher values of ρ/q at this flight condition.

Gain scheduling, as a function of flight speed, was accomplished for the Kalman filter gains. The gains were scheduled between the low speed and high speed point designs (aft c.g. location). Thus, the Kalman filter gain, K_f , for any flight speed, U , in Lambda's flight envelope is found as follows:

$$\Delta = (U - 76.0) / (168.9 - 76.0) \quad (5.41)$$

$$K_f = K_{f \text{ low}} + \Delta(K_{f \text{ high}} - K_{f \text{ low}}) \quad (5.42)$$

where,

U = flight speed, feet/sec

$K_{f \text{ low}}$ = low speed filter gain

$K_{f \text{ high}}$ = high speed filter gain

Table 5.6 summarizes the final pitch rate controller design. The MATLAB macro PRATCONV.M is given in Appendix F. This macro calculated the closed loop pitch rate and elevator time responses to a unit step pitch rate command given the trimmed flight condition characteristics as inputs. Using the program, the closed loop time responses to a unit step pitch rate command were generated for all four flight conditions comprising the corners of Lambda's flight envelope and for the flight condition at the center of Lambda's flight envelope. These responses (calculated at the aft c.g. location) are given in Figure 5.12. The closed loop margins at these flight conditions are summarized in Table 5.7.

The overall pitch rate controller design yields reasonable time responses and has satisfactory margins for all flight conditions in Lambda's flight envelope. This is accomplished in spite of the slow elevator servo used on the vehicle. Notice that only one set of regulator gains, that from the high speed point design, was used for all flight conditions. Because of the high ρ/q ratio achievable at the high speed condition, the resulting gain matrix, K_c , produced better closed loop tracking performance while using significantly less elevator deflection than any other set of regulator gains from any other point design. It should also be noted that using gain scheduling for the Kalman filter was not absolutely required. However, the increase in overall compensator tracking performance was significant, thus justifying the added complexity.

Table 5.6. Summary of the Final Pitch Rate Controller Design

Kalman Filter:

$$\mu=1/100 \quad \Gamma=[0,0,0,0,0,0,0.0433,0,1]^T$$

Kalman filter gains at,

	U=76 fps		U=168.9 fps
$K_{f \text{ low}} =$	-0.0211		-0.0024
	1.0498		0.9747
	5.7190		7.7262
	1.0000	$K_{f \text{ high}} =$	1.0000
	-4.2724		-2.3130
	-0.0982		-0.1562
	-5.7255		-3.6393
	-10.000		-10.000

Regulator:

$$\rho=5 \times 10^7 \quad q=5,500 \quad H=[0,0,1,0,0,0,0,0]$$

$$K_c=[-0.0781,0.0072,0.0251,0.0385,-0.0558,-0.2936,2.2065,2.1007]$$

Table 5.7. Closed Loop Margins for the Final Pitch Rate Controller Design

Xcg (in)	flight speed (fps)	lower margin (db)	upper margin (db)	phase margin (deg)
45.8	76.0	-3.2715	5.3101	±26.440
45.8	168.9	-3.8708	7.1605	±32.610
47.8	168.9	-3.9227	7.3479	±33.169
47.8	76.0	-3.2829	5.3409	±26.553
46.8	122.5	-3.7221	6.6507	±31.030

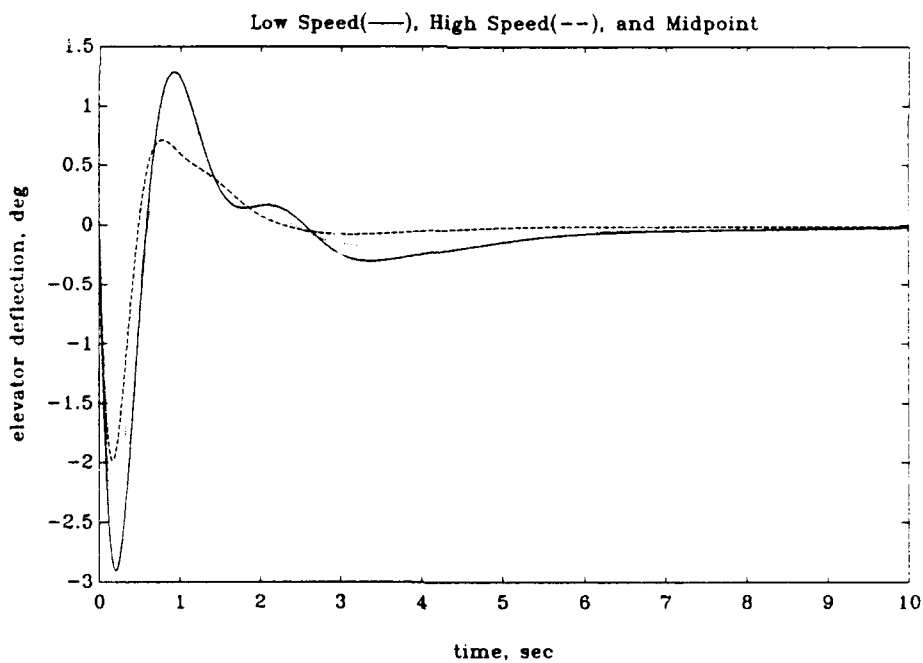
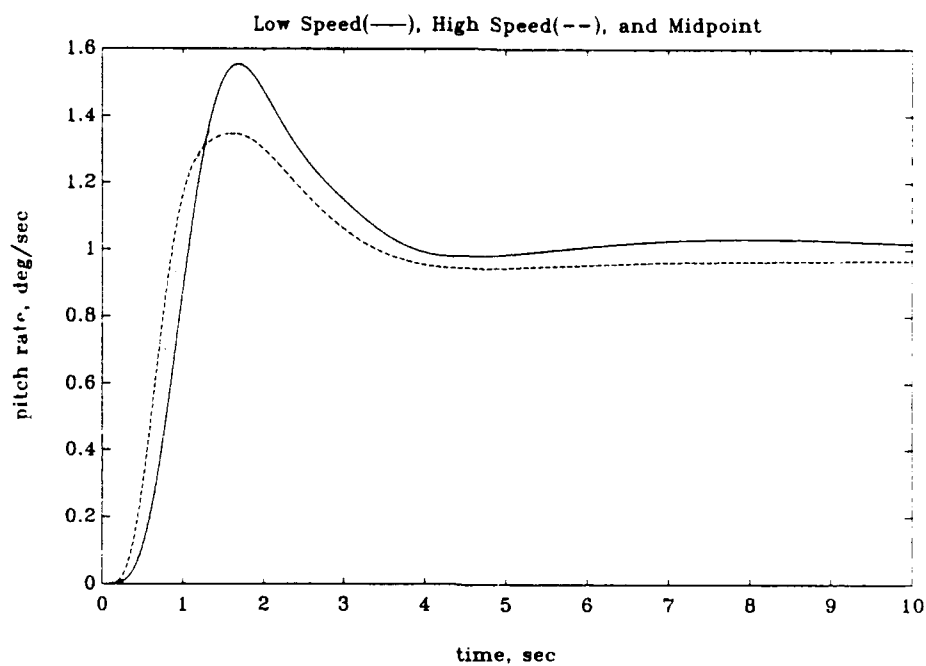


Figure 5.12. Closed Loop Time Responses to a Unit Step Pitch Rate Command for the Fin Pitch Rate Controller Design.

5.3. Roll Rate Controller Design

This section summarizes the final design of the roll rate controller for Lambda using LQG/LTR. This design has the following characteristics:

- the lateral-directional perturbation model developed in Chapter 3 was used with the heading angle state, Ψ , removed (MATLAB could not solve the LQE algebraic Riccati equation with Ψ as a state variable),
- both aileron and rudder were used for control,
- both sideslip and roll rate were regulated and fed back to the compensator (thus producing a square system), and
- aileron dynamics, rudder dynamics, and a wind model were added to the open loop plant model.

The performance and robustness specifications for this design were the same as that used for the pitch rate controller design. The open loop system had to be doubly augmented with integrators to achieve a loop shape with Type-1 characteristics.

As with the pitch rate controller design, the Kalman filter used gain scheduling, as a function of flight speed, to significantly enhance closed loop tracking performance throughout Lambda's flight envelope. The regulator gains resulted from the point design for the flight condition at the middle of Lambda's flight envelope. Table 5.8 summarizes the characteristics of the final roll rate controller design. The roll rate controller macro, RRATCONV.M, is given in Appendix F. The closed loop margins for the final roll rate controller design are given in Table 5.9 and the closed loop time responses (for the aft c.g. location) to a unit step roll rate command are given Figure 5.13.

The overall roll rate controller design produces reasonable

time responses which do not require significant aileron deflection to achieve. The maximum roll rate peak overshoot of approximately 1.4 for roughly all flight conditions offers room for design improvement. The gain and phase margins are all quite satisfactory. It should also be noted that this controller not only tracks roll rate command well, but it also regulates sideslip at the same time.

Table 5.8. Summary of the Final Roll Rate Controller Design

Kalman Filter:

$\mu=1/100$	$\Gamma=B$ with correction for wind			
	4.8762	-0.0339	5.4431	-0.0254
	-0.0339	7.8567	0.9747	11.772
	0	1.0	0	1.0
$K_{f \text{ low}} =$	-11.771	0.0052	$K_{f \text{ high}} =$	-15.306
	0.5145	3.4439		0.4548
	9.9592	-0.3439		6.4415
	0.1227	0.1758		0.0529
	0.6330	5.1064		0.6045
	11.562	-0.4452		8.0256
	0.6455	9.9791		0.8272
	9.9791	-0.6455		9.9657
	(U=76 fps)		(U=168.9 fps)	

Regulator:

	$\rho=5,000$	$q=15$	$H=C$
	0.0128	-0.0042	
	0.0033	0.0014	
	0.0056	0.0079	
	0.0008	0.0023	
	0.0526	0.0101	
$K_c =$	-0.0034	-0.0024	
	-0.0008	-0.0142	
	1.6477	-0.0069	
	-0.0673	0.2667	
	1.8151	-0.0292	
	-0.0292	0.7298	

Table 5.9. Closed Loop Margins for the Final Roll Rate Controller Design

Xcg (in)	flight speed (fps)	lower margin (db)	upper margin (db)	phase margin (deg)
45.8	76.0	-3.1594	5.0161	± 25.342
45.9	168.9	-4.1065	8.0559	± 35.182
47.8	168.9	-4.1203	8.1122	± 35.336
47.8	76.0	-3.1405	4.9677	± 25.158
46.8	122.5	-3.8260	7.0029	± 32.131

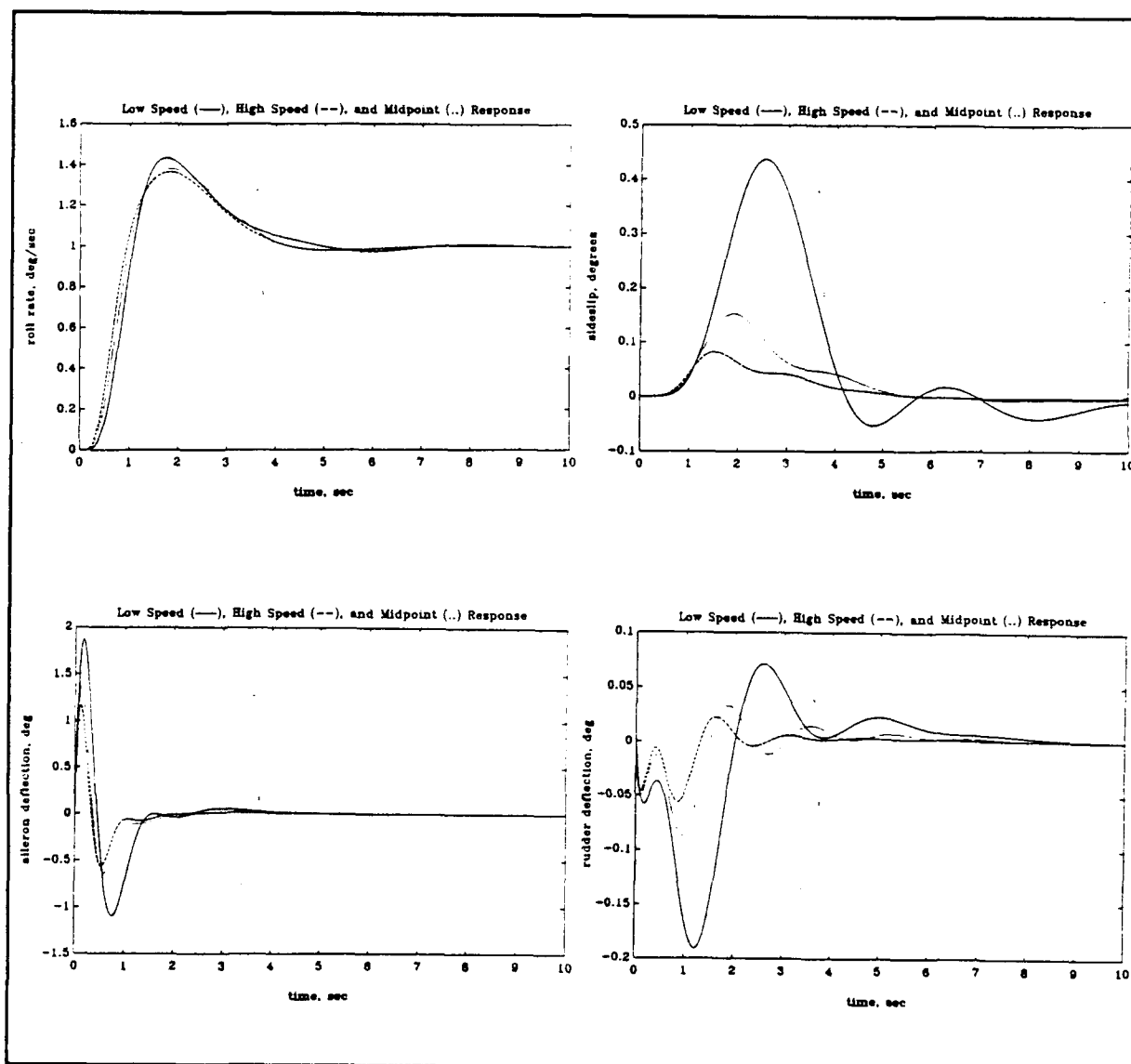


Figure 5.13. Closed Loop Time Responses to a Unit Step Roll Rate Command for the Final Roll Rate Controller Design.

5.4. Yaw Rate Controller Design

This section summarizes the final designs of the yaw rate controllers for Lambda using LQG/LTR. Two yaw rate controllers were designed. The first controller, which regulates roll angle and yaw rate, is presented in Section 5.4.1. The second controller, which regulates sideslip and yaw rate, is discussed in Section 5.4.2.

5.4.1. Yaw Rate Controller with Roll Angle Regulated

This type of yaw rate controller is to be used for scenarios in which a crabbing turn with wings level is required. This situation often arises during final approach for landing in crosswind conditions. This design has the following characteristics:

- the lateral-directional perturbation model developed in Chapter 3 was used with the heading angle state removed,
- both aileron and rudder were used for control,
- both roll angle and yaw rate were regulated and fed back to the compensator (again producing a square system), and
- aileron dynamics, rudder dynamics, and a wind model were added to the open loop system.

The performance and robustness specifications for this design were those given in 5.2.2. Again, the open loop system had to be doubly augmented with integrators to achieve a loop shape with Type-1 characteristics.

The final yaw rate controller design uses gain scheduling, as a function of flight speed, on the Kalman filter gains to improve tracking performance. The regulator gains were selected from the high speed flight condition point design. Table 5.10

controller macro, YRATCONV.M, is given in Appendix F. The closed loop margins for the final yaw rate controller design are given in Table 5.11 and the closed loop time responses (for the aft c.g. location) to a unit step yaw rate command are given in Figure 5.14.

The overall yaw rate controller design produces time responses that look fairly good. The rudder deflections are somewhat high, but are acceptable for a yaw rate controller. The margins for this controller, however, are quite low.

Table 5.10. Summary of the Final Yaw Rate Controller (Design #1)

Kalman Filter:

$\mu=1/1000$ $\Gamma=B$ with correction for wind

$K_{f \text{ low}} =$	0.3134	-1.1759	$K_{f \text{ high}} =$	0.0657	-1.1145
	45.364	-4.6276		79.729	-9.3266
	9.5159	-0.4185		12.614	-0.5844
	-0.4185	8.5273		-0.5844	13.195
	16.280	-2.3618		10.510	-1.7524
	-3.1173	-12.541		-2.7698	-6.7477
	0.4056	-0.6631		0.1756	-0.3826
	21.724	-3.4566		15.634	-3.1244
	-4.0642	-17.325		-4.0222	-11.095
	31.052	-5.9806		30.550	-8.1682
	-5.9806	-31.052		-8.1682	-30.550
	(U=76 fps)			(U=168.9 fps)	

Regulator:

	$\rho=250,000$	$q=1000$	$H=C$
$K_c =$	-0.3534	-1.3977	
	0.2623	-0.1050	
	1.9493	-0.6328	
	0.2312	0.5618	
	3.7852	-1.1872	
	-0.4340	-1.1007	
	-0.0403	0.6506	
	15.242	-1.1797	
	-0.2341	3.3968	
	5.5184	-0.1741	
	-0.1741	2.6006	

Table 5.11. Closed Loop Margins for the Final Yaw Rate Controller (Design #1)

Xcg (in)	flight speed (fps)	lower margin (db)	upper margin (db)	phase margin (deg)
45.8	76.0	-1.6773	2.0807	± 12.228
45.8	168.9	-1.5512	1.8897	± 11.221
47.8	168.9	-1.5395	1.8724	± 11.128
47.8	76.0	-1.6780	2.0817	± 12.233
46.8	122.5	-1.6981	2.1128	± 12.396

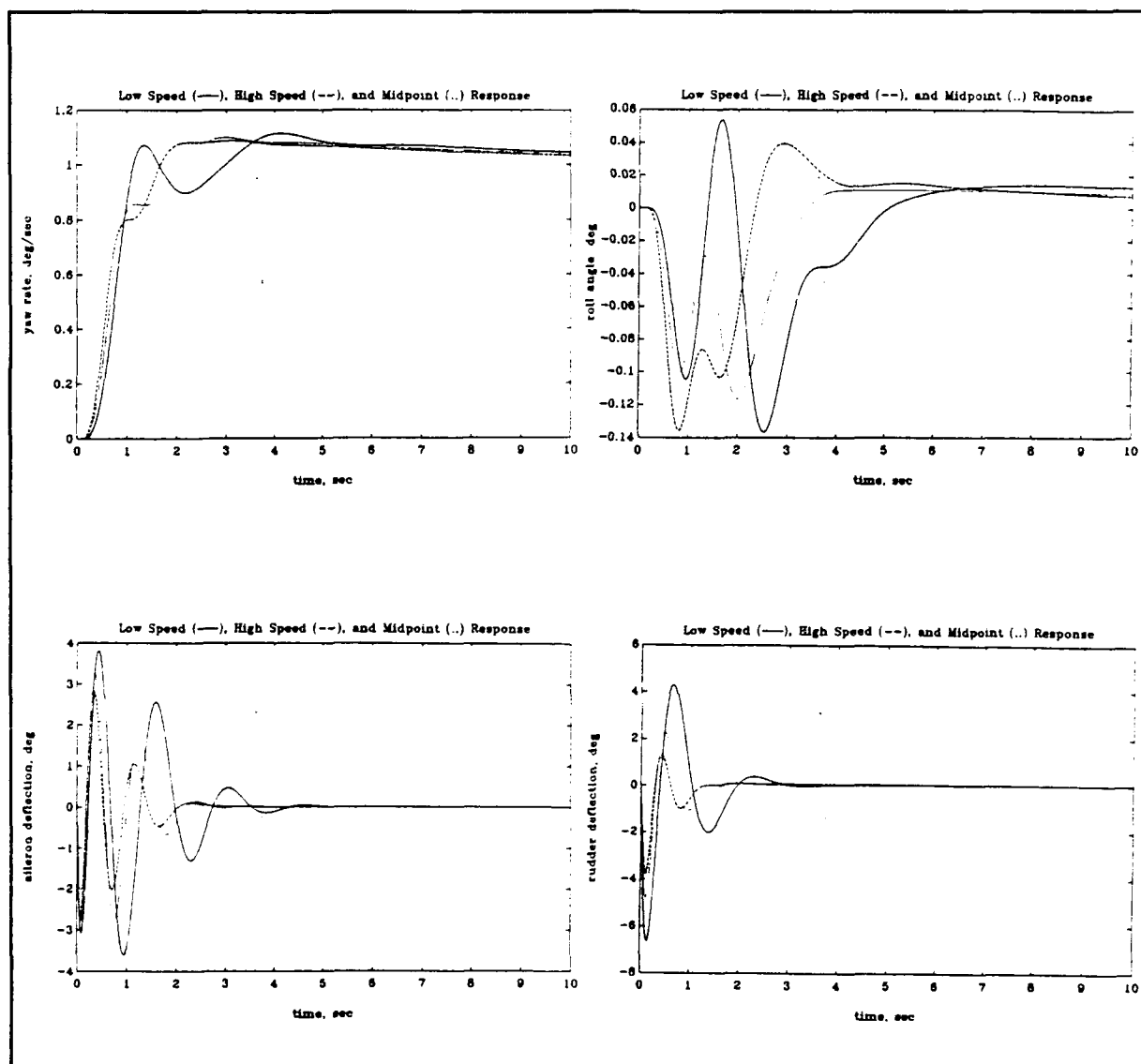


Figure 5.14. Closed Loop Time Responses to a Unit Step Yaw Rate Command for the Final Yaw Rate Controller (Design #1).

5.4.2. Yaw Rate Controller with Sideslip Regulated

The second yaw rate controller design will allow Lambda to perform coordinated turns in response to yaw rate command inputs. The development of this design parallels that of the last yaw rate controller, except that sideslip is regulated and fed back to the compensator instead of roll angle. However, this controller design had to address difficulties not inherent in any of the other rate controllers. Therefore, this design will be described in some detail.

The open loop plant for the high speed flight condition has the following system poles and zeros:

<u>Poles(CΦB):</u>	<u>Zeros(CΦB):</u>
-0.9901 \pm 3.8266i	-40.711
-7.1422	-1.6890
-6.20	16.041
-5.50	
-1.6890	
0.0157	

This system is both unstable and non-minimum phase. This means full recovery of the Kalman filter loop shape with the regulator as $q \rightarrow \infty$ is not possible [6].

Again, the basic plant was doubly augmented with integrators to provide a loop shape with Type-1 characteristics. The Kalman filter design selected targeted a bandwidth of 10 rad/sec and provided plenty of room for whatever recovery was possible by the regulator. Figure 5.15 is the resulting loop shape.

Several combinations of ρ and q were tried, but $\rho=10,000$ and $q=10$ appeared to provide the best recovery while still meeting performance and robustness requirements. Equal penalty weighting

on the regulated states, β and r , did not produce acceptable closed loop time responses. With equal weighting, β was well regulated but r had very large overshoot and extremely long settling time. Thus, the penalty on yaw rate tracking error was increased while the sideslip error penalty was held constant. As the penalty on r increased, both the overshoot and settling time on the yaw rate response were drastically reduced; however, sideslip began to significantly deviate from zero. The H matrix that seemed to produce the best compromise had the penalty on yaw rate 100 times greater than that on sideslip. Figure 5.16 shows the resulting loop shape for $G(s)K(s)$ for the regulator with $\rho=10,000$, $q=10$, and H as just described. Notice that the recovery of the Kalman filter loop shape is really fairly poor. This highlights the impact that an unstable, non-minimum phase system has on recovery. This will be discussed further in the next chapter.

Table 5.12 summarizes the final yaw rate controller design. It was absolutely necessary with this controller to schedule the Kalman filter gains as a function of flight speed in order to improve compensator performance. The controller macro, YRATCONVB.M, is given in Appendix F. The closed loop margins for the final yaw rate controller design are given in Table 5.13, and the closed loop time responses (for the aft c.g. location) to a unit step yaw rate command are given in Figure 5.17.

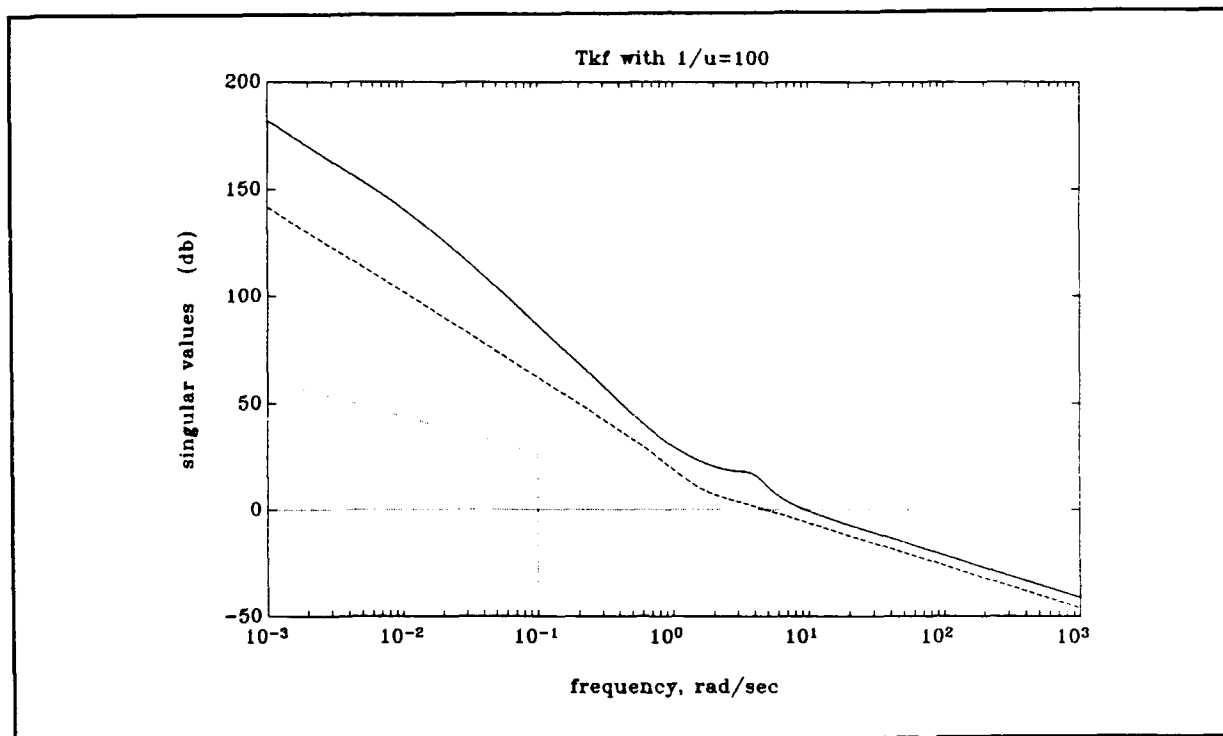


Figure 5.15. Kalman Filter Loop Shape for the Yaw Rate Controller (Design #2).

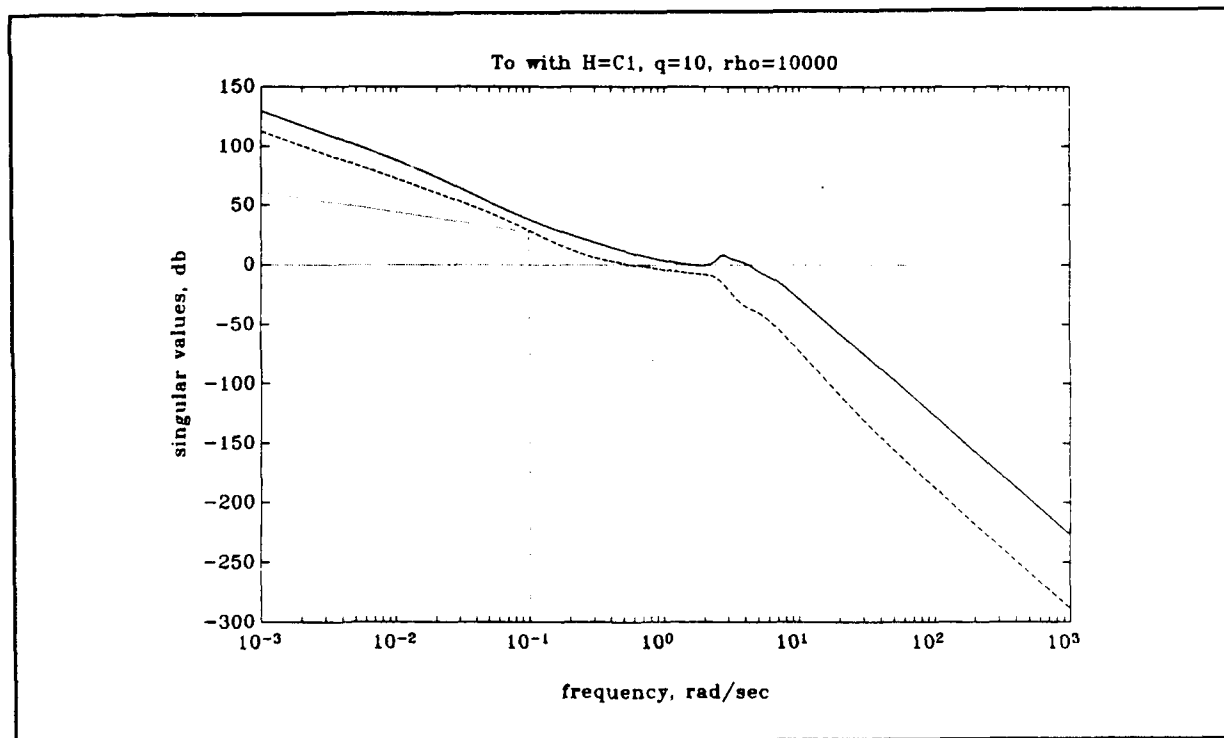


Figure 5.16. $G(s)K(s)$ Loop Shape for the Yaw Rate Controller (Design #2).

Table 5.12. Summary of the Final Yaw Rate Controller (Design #2)

Kalman Filter:

$\mu=1/1000$ $\Gamma=B$ with correction for wind

$K_{f \text{ low}} =$	5.1598	0.1924	$K_{f \text{ high}} =$	4.9195	0.3475
	54.167	16.541		116.71	59.179
	33.939	11.064		74.366	33.031
	0.1924	5.7109		0.3475	8.4798
	13.799	3.6141		11.855	5.6622
	-1.5537	-6.9404		-0.8943	-4.7502
	0.1177	-0.1568		0.0486	-0.0815
	15.606	3.7938		13.594	6.1893
	-1.3997	-8.5124		-0.4654	-6.2006
	9.9511	0.9878		9.6064	2.7779
	0.9878	-9.9511		2.7779	-9.6064

(U=76 fps)

(U=168.9 fps)

Regulator:

$$p=250,000 \quad q=1000 \quad H = \begin{bmatrix} 1 & 0 & 0 & 0 & 0 & 0 & 0 & 0 & 0 & 0 & 0 \\ 0 & 0 & 0 & 100 & 0 & 0 & 0 & 0 & 0 & 0 & 0 \end{bmatrix}$$

$K_c =$	-0.0339	-0.2660
	0.0038	-0.0365
	0.0547	-0.2058
	0.0755	0.1872
	0.0795	-0.4508
	-0.1974	-0.4443
	0.1590	0.4466
	2.3190	-0.5335
	0.1624	1.0663
	2.1511	-0.1029
	-0.1029	1.4567

Table 5.13. Closed Loop Margins for the Final Yaw Rate Controller (Design #2)

Xcg (in)	flight speed (fps)	lower margin (db)	upper margin (db)	phase margin (deg)
45.8	76.0	-1.4104	1.6846	± 10.115
45.8	168.9	-1.4335	1.7178	± 10.295
47.8	168.9	-1.4671	1.7663	± 10.558
47.8	76.0	-1.3794	1.6407	± 9.874
46.8	122.5	-1.7678	2.2220	± 12.960

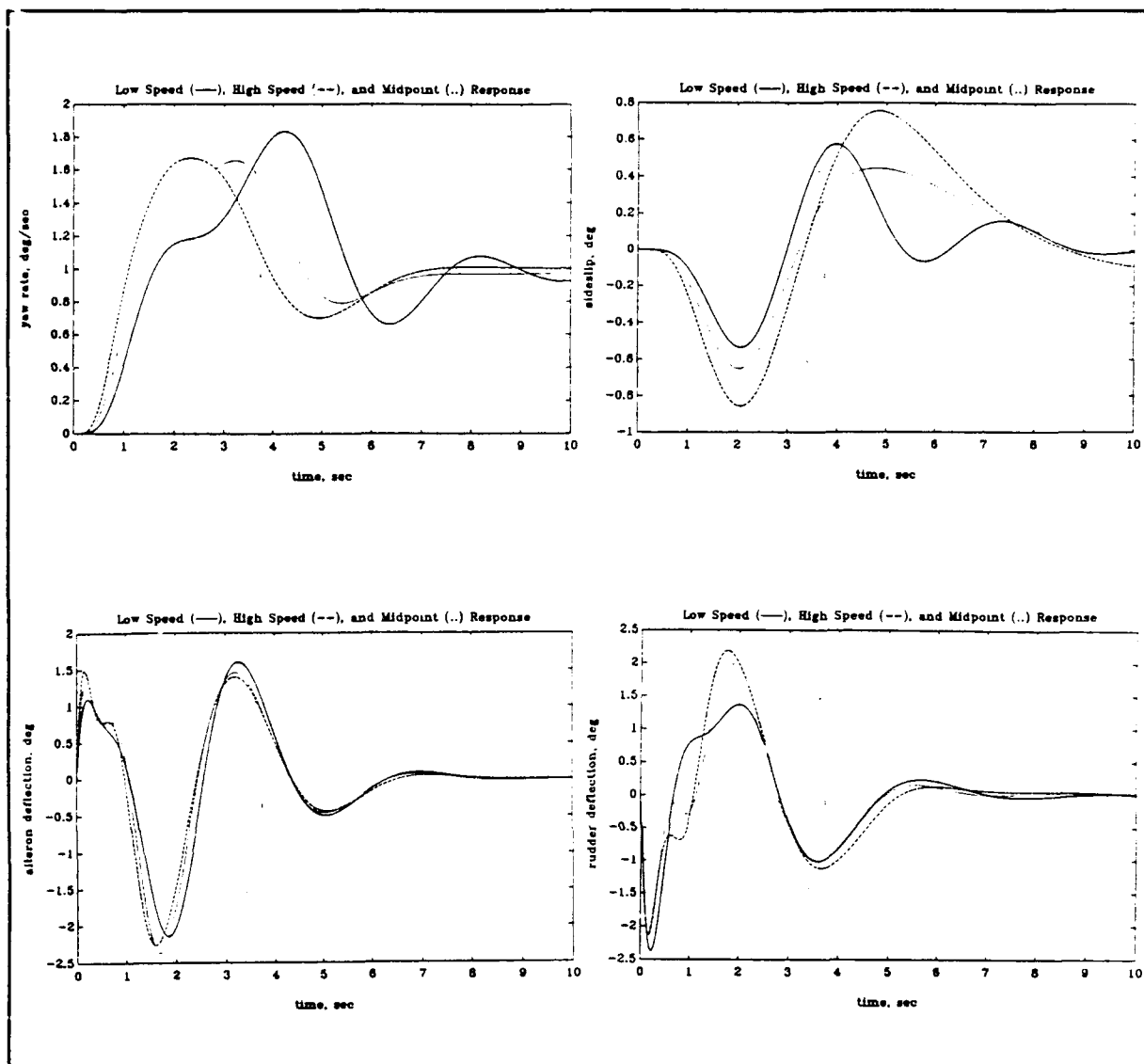


Figure 5.17. Closed Loop Time Responses to a Unit Step Yaw Rate Command for the Final Yaw Rate Controller (Design #2).

Overall, it is immediately obvious that it is difficult to achieve coordinated turns with the Lambda URV. Yaw rate response to a step yaw rate command is characterized by large overshoot and long settling time while sideslip significantly deviates from zero. Closed loop r and β performance could be improved but only if significantly larger control surface deflections are allowed.

5.5. Discussion of Rate Controller Designs Using LQG/LTR

The following discussion highlights the main points of the rate controller designs just presented and offers insight on how the designs could be improved.

It was observed that once a good set of regulator gains were found (no matter what the flight condition they were specifically designed for), these gains provided the same level of performance for all flight conditions in Lambda's envelope. This was not true for the Kalman filter gains. Gain scheduling of the Kalman filter greatly increased the compensator's overall performance.

Lambda has a full array of sensors available. It has the capability to measure u , α , q , and θ in the longitudinal reference frame and β , p , ϕ , and r in the lateral-directional reference frame. However, in the pitch rate controller design, only q was fed back to the compensator; in the roll rate controller, β and p were fed back; and in the yaw rate controller, only r and ϕ or r and β were fed back. Using the same set of regulator gains, the performance of the compensator could be improved by feeding back the additional states available to the Kalman filter.

The main stumbling block encountered in designing the controllers was in solving the LQR algebraic Riccati equation. The software used in MATLAB was highly sensitive to large ρ/q values. Thus, it was somewhat difficult to arrive at a set of LQ regulator gains that did not require large control surface deflections or rates. The level of difficulty encountered varied

from one flight condition to another. For the pitch and yaw rate controllers, the best set of LQR gains were arrived at using the high speed flight conditions. The best regulator gains for the roll rate controller were calculated at the flight condition for the center of the flight envelope. The main point, however, is that in order to obtain good performance, the designer is forced to high ρ/q ratios due to the limited control authority inherent in the Lambda URV. If Lambda had faster control servos, lower values of ρ could be used to achieve the same, or better, levels of closed loop performance. Thus, the numerical problems with the Riccati equations could be side-stepped altogether.

Each rate controller design for Lambda was plagued by unstable dynamics in the open loop plant. At slow speed, the pitch rate controller's open loop plant has unstable phugoid roots. All lateral-directional rate controllers have plants with unstable spiral modes. LQG/LTR is fairly successful at providing compensators with adequate performance when slightly unstable poles in the open loop plant are involved. However, the open loop plant in the second yaw rate controller design (r , β regulated) was also non-minimum phase. Consequently, it was difficult to design an LQG/LTR controller with acceptable performance.

The final pitch and roll rate controller designs had margins adequate to be further considered for actual implementation. Both the final yaw rate controller designs had very marginal performance. Before actual implementation of any of these

controllers, the continuous time designs would need to be discretized and re-tuned. Reference 21 is an excellent source on how to conduct this process.

In the next chapter, the LQG/LTR rate controllers will be compared and contrasted with the controllers developed in Chapter 4. These comparisons will provide further insight into the mechanics of the LQG/LTR methodology.

6. Comparisons and Discussion

This chapter summarizes the controller designs accomplished in Chapters 4 and 5. First, a general discussion of the closed loop time response performance that can be expected from the rate controllers, based on the airplane's stability characteristics and control authority, is given. The rate controllers from Chapters 4 and 5 are then directly compared in Section 6.2. The final results are given in Section 6.3 along with recommendations for future design.

6.1. Discussion of Rate Controller Performance

Closed loop rate response performance is difficult to characterize. Military standards for flying qualities specify levels of performance for basically attitude responses. For example, levels of flying quality are completely characterized for the short period response of angle of attack for piloted aircraft in MIL-STD-1797A. Usually, rate control is part of an overall attitude flight control system whose performance can be judged against military standards. Therefore, there has historically been no reason to pursue performance specifications for rate responses.

The Flight Control Division has attempted to specify closed loop performance on the rate time responses to unit step rate command inputs for Λ . Time response bounds were constructed for the closed loop pitch, roll, and yaw rate time responses. These are shown in Figure 6.1.

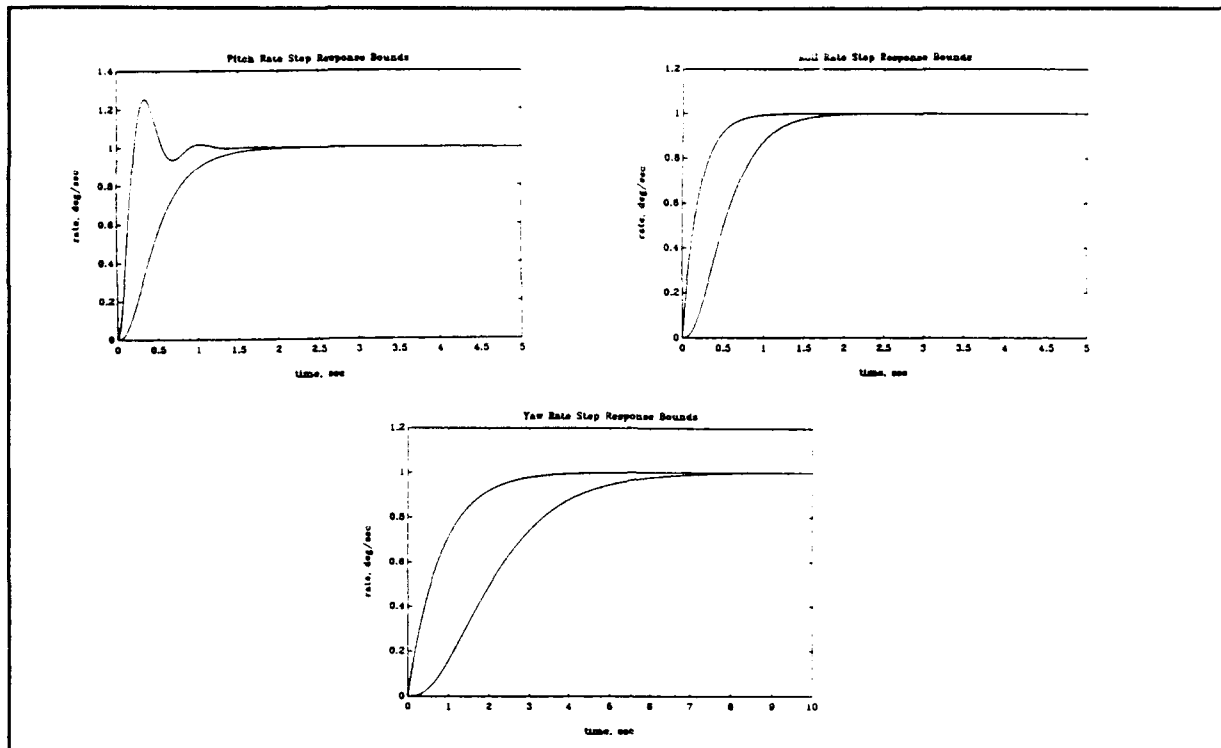


Figure 6.1. Closed Loop Time Response Performance Objectives.

Wheaton [2] summarizes the development of these performance objectives in his thesis. In fact, Wheaton designed rate controllers, using discrete Quantitative Feedback Theory (QFT), whose closed loop rate time responses, for the most part, fell within the performance bounds for all flight conditions in Lambda's flight envelope. Unfortunately, at the time of Wheaton's work, a good model of Lambda's stability and control characteristics did not exist. The key differences between Wheaton's models from those developed in this thesis were in the estimation of the control actuator dynamics. Wheaton used the following model for all actuators:

$$\frac{\delta(s)}{\delta_{com}(s)} = \frac{324}{s^2 + 25.4s + 324} = \frac{324}{s^2 + 2(0.71)(18.0)s + 18^2} \quad (6.1)$$

Whereas, the servo models used in this thesis, which were estimated from actual flight test data, were as follows:

$$\frac{\delta_e}{\delta_{e \text{ com}}} = \frac{6.5}{s+6.5} \quad (6.2)$$

$$\frac{\delta_A}{\delta_{A \text{ com}}} = \frac{5.5}{s+5.5} \quad (6.3)$$

$$\frac{\delta_R}{\delta_{R \text{ com}}} = \frac{6.2}{s+6.2} \quad (6.4)$$

Thus, Wheaton's models used equivalent first order lag constants that were three times faster than that exhibited by the actual airplane.

To meet the upper bound time response on pitch rate from Figure 6.1, the dominant closed loop roots would need to have a natural frequency of 10.0 rad/sec and damping ratio 0.40. Using Wheaton's servo model, this is a realistic objective. However, for the actual airplane this means the dominant closed loop poles will need to be placed beyond the pole of the actuator. A more realistic placement of the dominant closed loop poles would be at a natural frequency of 5.5 rad/sec and a damping ratio of 0.40. Using $\omega_n=5.5$ rad/sec, $\xi=0.40$, and the following approximations, (taken from Reference 22)

$$M_p = (1 - \xi/0.6) * 100 \quad (\%) \quad (6.5)$$

$$t_r = 1.8/\omega_n \quad (\text{sec}) \quad (6.6)$$

$$t_s = 4.6/(\xi\omega_n) \quad (\text{sec}) \quad (6.7)$$

where, $M_p \equiv$ maximum peak overshoot to a unit rate input command

$t_r \equiv$ rise time

$t_s \equiv$ settling time

$\omega_n \equiv$ natural frequency, rad/sec

$\xi \equiv$ damping ratio

would result in a closed loop pitch rate time response to a unit step pitch rate command with the following characteristics:

$$M_p = 33\%$$

$$t_r = 0.327 \text{ sec}$$

$$t_s = 2.09 \text{ sec}$$

This response would not fall within the pitch rate bounds shown in Figure 6.1. Recall from Figure 5.12 for the midpoint flight condition, the closed loop time response from the LQG/LTR controller had the following characteristics:

$$M_p = 40\%$$

$$t_r = 0.5 \text{ sec}$$

$$t_s = 3.0 \text{ sec}$$

which corresponds to a $\omega_n \approx 3.5$ rad/sec and $\xi \approx 0.35$. Thus, LQG/LTR provided a controller design that has reasonable closed loop pole placement with respect to the dynamics of the elevator servo.

Wheaton's upper bounds on roll rate and yaw rate require the closed loop dominant pole to be placed at $s=-5$ and $s=-1.25$, respectively. This corresponds to closed loop time responses with the following characteristics:

<u>Response</u>	<u>M_p (%)</u>	<u>t_r (sec)</u>	<u>t_s (sec)</u>
roll rate	0.0	0.44	0.78
yaw rate	0.0	1.76	3.13

These are reasonable objectives to expect for rise time and settling time; however, it is probably optimistic (due to the

nature of the open loop plant) not to expect oscillatory closed loop response, especially with yaw rate.

Table 6.1 is a summary of closed loop time response characteristics that can be used as a yardstick with which to measure the final controller designs in Chapters 4 and 5. It should be noted that these objectives are arbitrary and are offered to serve more as means of comparison between the closed loop rate responses of this thesis and those of Reference 2.

Table 6.1. Closed Loop Time Response Performance Objectives

<u>Response</u>	<u>M_p (%)</u>	<u>t_r (sec)</u>	<u>t_s (sec)</u>
pitch rate	40	0.50	3.00
roll rate	0.0	0.44	0.78
yaw rate	0.0	1.76	3.13

In the next section, not only will the closed loop time responses of the two design techniques used in this thesis be compared, but the compensator dynamics, loop shapes, and phase margins of the final designs will also be compared.

6.2. LQG/LTR Versus Classical Rate Controller Design

This section provides a direct comparison between LQG/LTR and classical design techniques for each of the final rate controller designs (with gain scheduling implemented). All comparisons will be for the flight condition at the center of Lambda's flight envelope.

6.2.1. Pitch Rate Controller Comparisons

To begin, the open loop system has the following poles and zeros:

Poles(C&B):	Zeros(C&B):
-2.2611 ± 5.1389i	-2.6020
-0.0086 ± 0.3393i	-2.45
-6.5 (servo)	-0.0810
-2.45 (wind)	0

Thus, the open loop plant is stable but has phugoid roots that have low frequency and light damping. Also, the servo dynamics are relatively slow. Such a plant presents a challenge for any controller design.

Figure 6.2 compares the closed loop pitch rate time responses to a unit step pitch rate command for the two final controller designs. The responses exhibit the following characteristics:

Response	M_p (%)	t_r (sec)	t_s (sec)
LQG/LTR	40	0.50	3.00
Classical	70	0.05	1.00

The LQG/LTR approach provided a much better time response with respect to the workload placed on the elevator actuator. In order to lower steady state error, the classical rate controller

was forced to use high gains. This placed the dominant closed loop poles for this design at a high natural frequency at the expense of system damping. By doubly augmenting the open loop system, the LQG approach began with a Type-1 system. Thus, the focus was shifted to closed loop pole placement that did not require an excessive amount of control power to obtain. By increasing the control usage penalty, ρ , closed loop pole placement was kept near the elevator servo root.

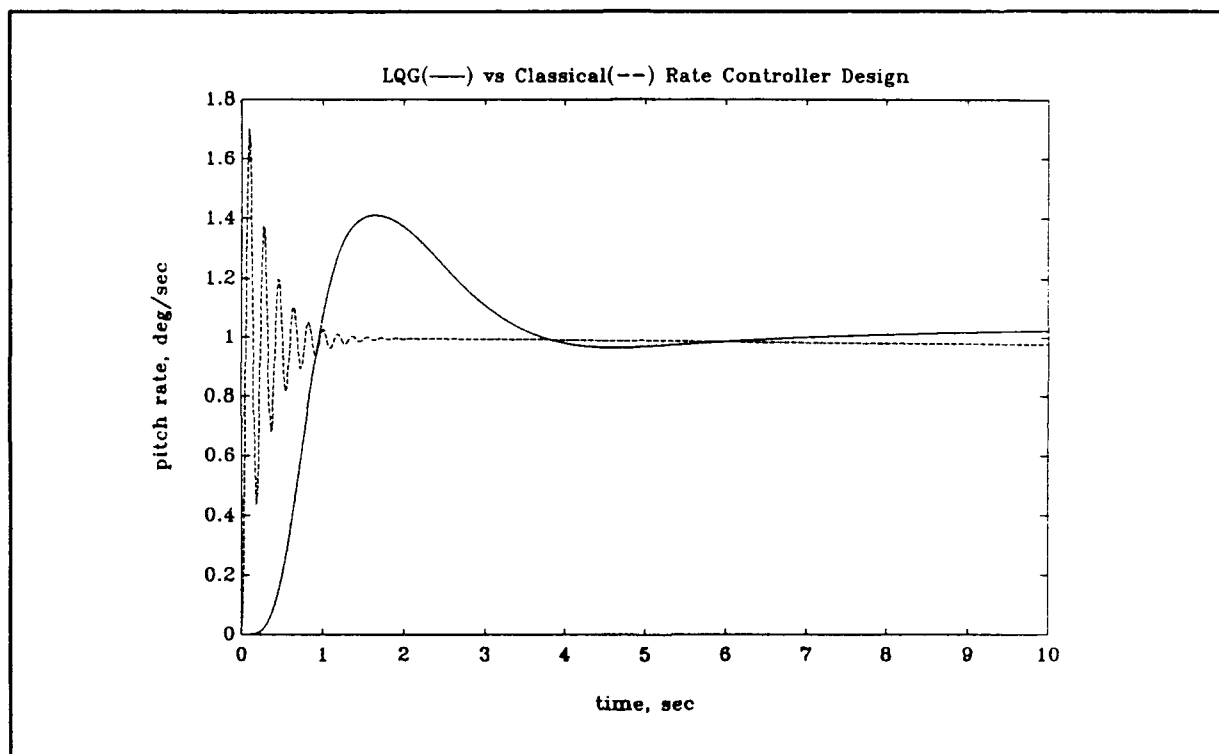


Figure 6.2. Closed Loop Pitch Rate Time Response Comparisons.

The difference in controllers can readily be observed by directly comparing the root locus of the final single-input, single-output compensator designs. This is done in Figure 6.3. Table 6.2 summarizes the pole/zero location for the compensator and closed loop system for the two designs.

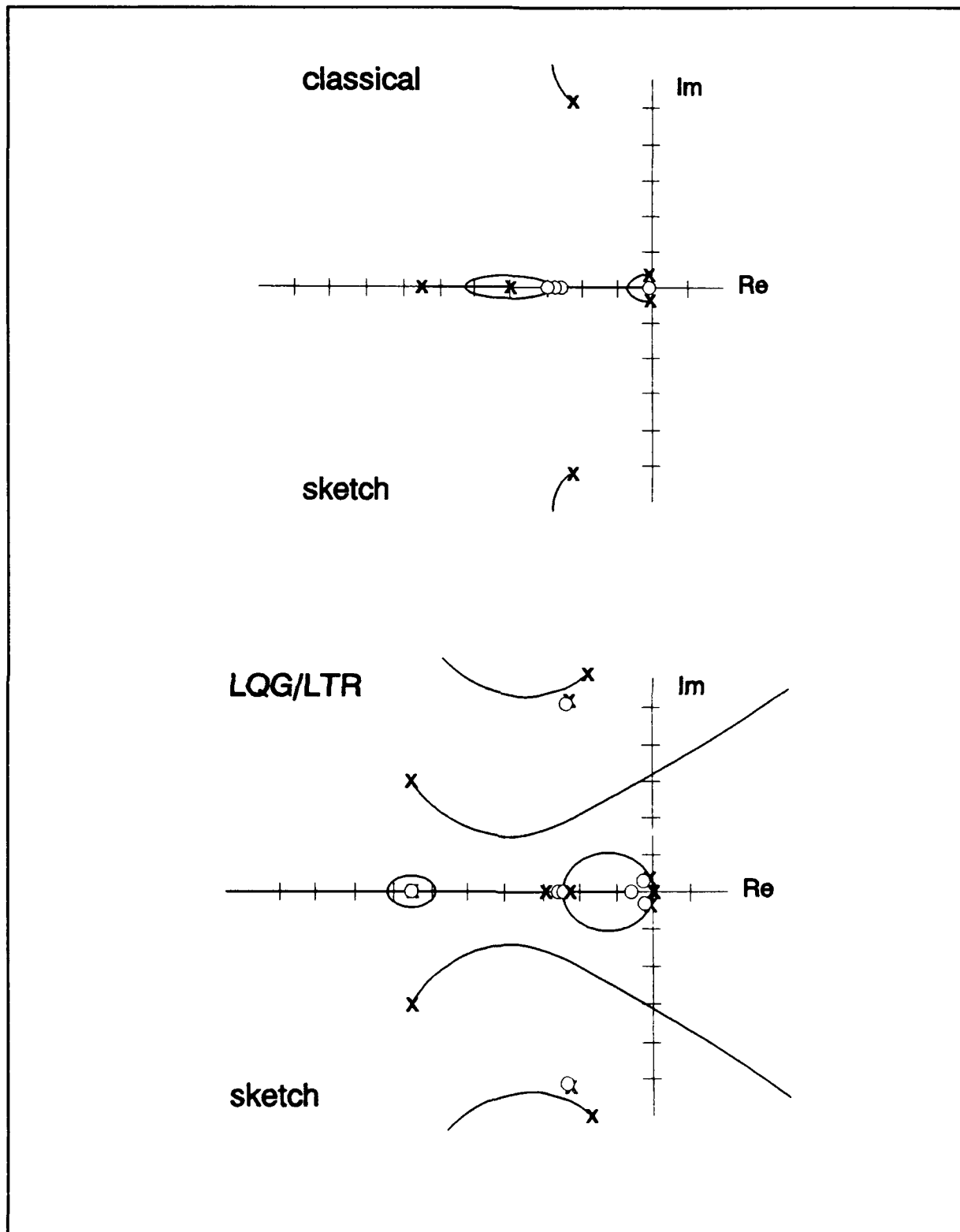


Figure 6.3. Comparison of Root Loci for the Pitch Rate Compensators.

Table 6.2. Comparison of Pitch Rate Controller Dynamics.

Compensator:		Closed Loop:	
<u>LQG/LTR</u>	<u>Classical</u>	<u>LQG/LTR</u>	<u>Classical</u>
Gain: -30.9	-10.0		
Poles:		Poles	
-1.9438 ± 6.5950i	-4.0	-2.5303 ± 5.9182i	-3.2811 ± 34.590i
-6.5769 ± 3.0869i	0	-2.2598 ± 5.1467i	-3.1896 ± 0.4610i
-2.9291		-5.7497	-2.0140
-2.2634		-6.4938	-0.0842
-0.0800		-3.6690 ± 1.5735i	
0		-1.9846	
0		-1.0482 ± 1.0024i	
0		-0.0151 ± 0.2881i	
0		-0.0801	
		-2.45	
		0	
Zeros:		Zeros:	
-2.2587 ± 5.1369	-3.0	-2.2587 ± 5.1369i	-2.75
-0.0136 ± 0.2925i	-2.75	-6.5010	-3.0
-6.5010		-2.6020	-2.6020
-0.6615		-2.4536	-0.0810
-2.4536		-0.6615	
		-0.0136 ± 0.2925i	
		-0.0801	
		-2.45	
		0	

The following comparisons between the two design approaches can be made:

1. No matter how high the gain, the classical system will never be driven unstable (within the accuracy of the linear model); this is not true for the LQG controller. However, this is really a minor point.
2. The LQG/LTR compensator attempts to invert the open loop plant. Compensator zeros are placed on top of the plant poles. Then, LQG/LTR re-defines the system dynamics with the placement

of the compensator poles and remaining zeros. (The order of the compensator is equal to the order of the doubly augmented plant.) Plant inversion is heavily dependent on the quality of the Kalman filter. Obviously, if the filter had not estimated the phugoid roots well, the closed loop time response may have displayed undesirable, slowly dying oscillations. Without scheduling the Kalman filter gains, this is exactly what resulted in the time responses at flight conditions different from the point design. Thus, the LQG/LTR characteristic of plant inversion makes scheduling the Kalman filter gains a necessity.

3. LQG/LTR is a frequency domain methodology. However, the LQG/LTR root locus in Figure 6.3 provides insight to what happens in the s -plane as the design is being worked in the frequency domain. First, LQG/LTR inverts the plant as described above. For a stable, minimum phase system, it accomplishes this task almost totally. Then, the designer forms a desired Kalman filter loop shape in the frequency domain. If total recovery were allowed at this point by setting $q=\infty$, the resulting root locus would have the closed loop poles placed so that the closed loop system had gain and phase margins of [6]:

$$-1/2 < GM < \infty$$

$$-60^\circ < PM < 60^\circ$$

However, infinite control power would be required. Therefore, the recovery process, in effect, performs a trade-off between gain margin, phase margin, and control usage when selecting the final compensator pole locations and gains.

4. Notice that by placing a heavy penalty on control usage, the closed loop poles for the LQG/LTR system all have natural frequencies less than 6.5 rad/sec.
5. The complexity of the LQG/LTR methodology is readily apparent from the root locus. It is highly unlikely that a designer using classical techniques could arrive at such a pole/zero placement for the compensator. Inverting the plant may be obvious, but the remaining pole/zero placement would remain a mystery.

Figure 6.4 compares the loop shapes for the system transfer function, $G(s)K(s)$, for the two design approaches. From this figure, the following comments can be made:

1. The classical design's loop shape is not Type-1; the LQG loop shape is. If an integrator is added to the classical compensator, the resulting classical loop shape will be Type-1 and will look very similar to the LQG system in the frequency domain. However, adding the integrator to the classical root locus forces the short period roots unstable at a relatively low gain ($K_q \approx 1$).
2. The classical controller yields a system with a significantly higher bandwidth and only -20 db/decade roll-off at high frequency. Thus, the classical rate controller design will be more susceptible to the negative effects of high frequency noise. A high frequency pole could be augmented to this controller to provide the system with better high frequency roll-off.
3. The higher system gain at low frequency for the LQG system will result in better command tracking and better disturbance rejection.

The corresponding phase margins for these systems are as follows:

<u>Method</u>	<u>PM</u>
LQG/LTR	$\pm 31^\circ$
Classical	$\pm 11^\circ$

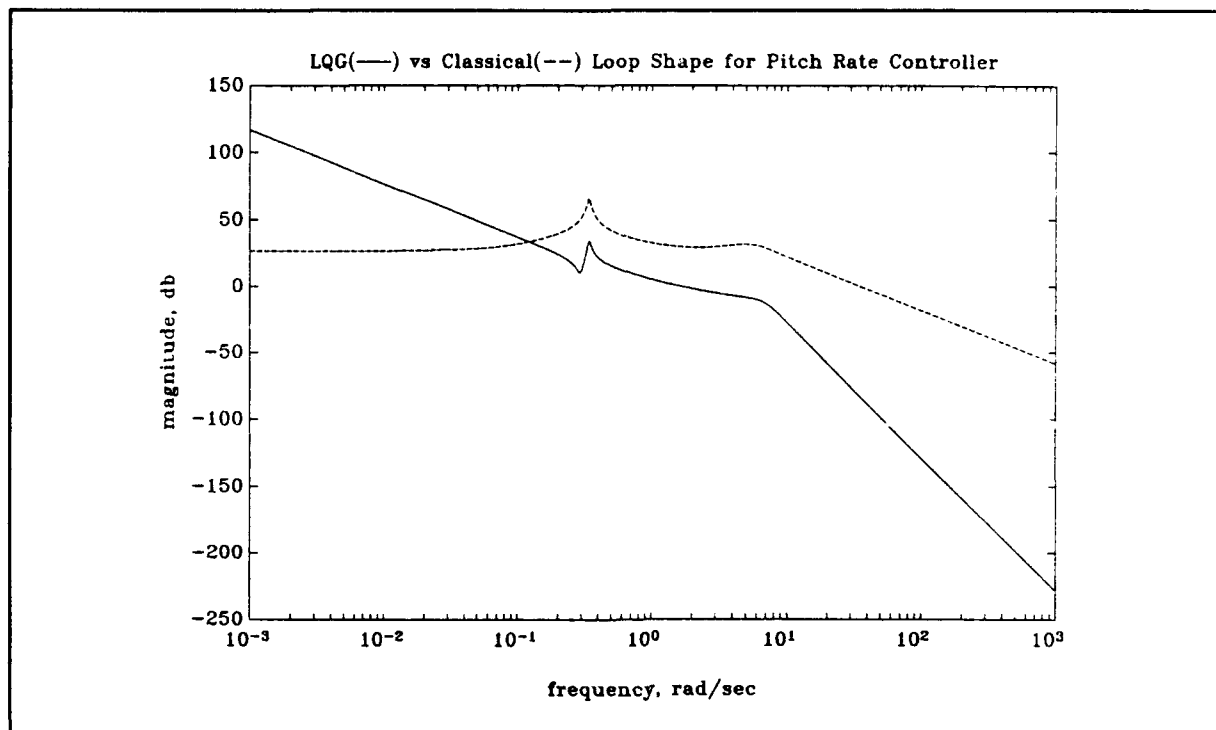


Figure 6.4. $G(s)K(s)$ Loop Shape Comparisons for the Pitch Rate Controllers.

Overall, the LQG/LTR approach for this controller produced a better design than did the classical approach. This was due mainly to the structure present in the LQG/LTR methodology. LQG/LTR allows the engineer the freedom to design a desired loop shape in the frequency domain and then force the overall closed loop system to recover those desired loop characteristics. The resulting system dynamics are a compromise between desired margins (performance and robustness) and control power usage. In retrospect, the performance of the classical compensator may be improved by adding another integrator to the system.

6.2.2. Roll Rate Controller Comparisons

The open loop system characteristics for the two design approaches are given in Table 6.3.

Table 6.3. Open Loop System Dynamics for the Roll Rate Controllers.

<u>Classical (p/δ_A):</u>		<u>LQG/LTR (CΦB):</u>	
Poles:	Zeros:	Poles:	Zeros:
-0.7275 \pm 2.7933i	-0.7089 \pm 2.7275i	-0.7275 \pm 2.7933i	-69.757
-5.1930	0	-5.1930	-1.225
0.0213		0.0213	0
-5.50 (servo)		-5.50 (servo)	
		-6.20 (servo)	
		-1.225 (wind)	

Note: $y=[\beta, p]^T$

Notice that the open loop plant is slightly unstable.

Figure 6.5 compares the closed loop roll rate time responses to a unit step roll rate command input for the two design approaches. The responses have the following characteristics:

<u>Response</u>	<u>M_p (%)</u>	<u>t_r (sec)</u>	<u>t_s (sec)</u>
LQG/LTR	40	0.50	3.50
Classical	0	0.25	0.50

The classical approach appears to have produced a much better roll rate controller. Its time response meets the desired performance listed in Table 6.1.

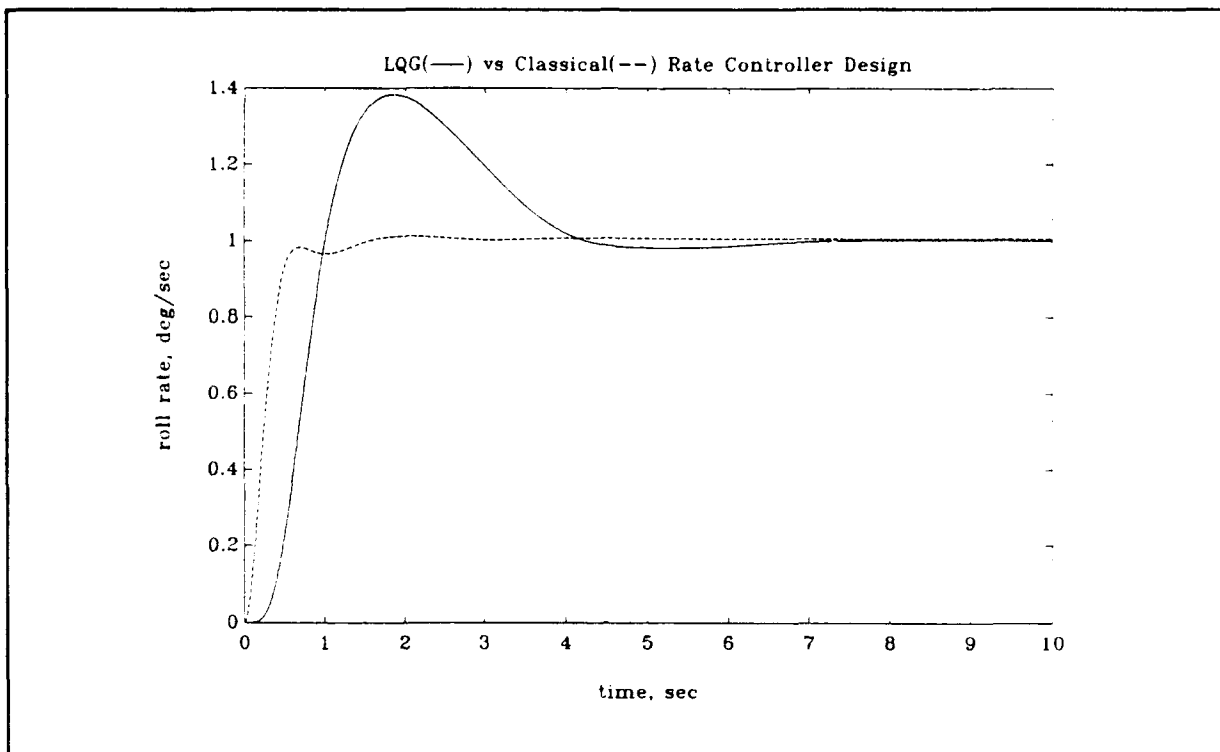


Figure 6.5. Closed Loop Roll Rate Time Response Comparisons.

The compensators for the two designs are vastly different. The compensator for the classical design is

$$K(s) = 0.15 (s+3)/s \quad (6.8)$$

This is a very simple compensator. The LQG/LTR compensator is a 2x2 matrix transfer function -- $(\beta - \beta_{com})$ and $(p - p_{com})$ are the inputs, δ_A and δ_R are the outputs. The compensator for the classical SISO system is easy to understand. The plant itself has zeros that nearly cancel the dutch roll roots. Thus, all the compensator needs to do is pull the unstable spiral into the left hand side of the s-plane while slowly trading-off system damping. Notice that one compensator works for the entire flight envelope; no gain scheduling is required. The LQG/LTR compensator,

however, inverts the plant and replaces the original dynamics with those selected through the recovery process. The transmission poles and zeros of the LQG/LTR compensator are as follows:

Poles(K_{LQG}):	Zeros(K_{LQG}):
$-8.7458 \pm 3.4275i$	$-0.7245 \pm 2.7928i$
$-2.5358 \pm 6.5506i$	-5.1700
$-0.7555 \pm 3.5167i$	-0.2714
$-2.9465 \pm 2.1609i$	-5.5164
-6.3376	-6.2000
-1.2204	-1.2253
0	0

The first four zeros are the compensator's attempt to cancel the poles of the plant. Notice that the LQG/LTR methodology does not produce an unstable compensator zero to cancel the spiral root. Instead it produces a compensator zero that is basically a mirror image of the unstable spiral root about the imaginary axis. This is due to the fact that the Kalman filter can never be monminimum phase [6]. The poles of the compensator are then left to set the performance of the closed loop system. The order of the LQG/LTR compensator is the same as the order of the doubly augmented open loop plant.

Figure 6.6 compares the loop shapes for the transfer function, $G(s)K(s)$, for the two roll rate controller designs. Notice that the classical system is not Type-1. The LQG approach appears to have produced a better loop shape. The LQG system should exhibit better low frequency performance (better tracking and disturbance rejection) and better high frequency noise rejection. However, if a high frequency pole were added to the

classical system, the two controller designs would have very similar high frequency loop shapes.

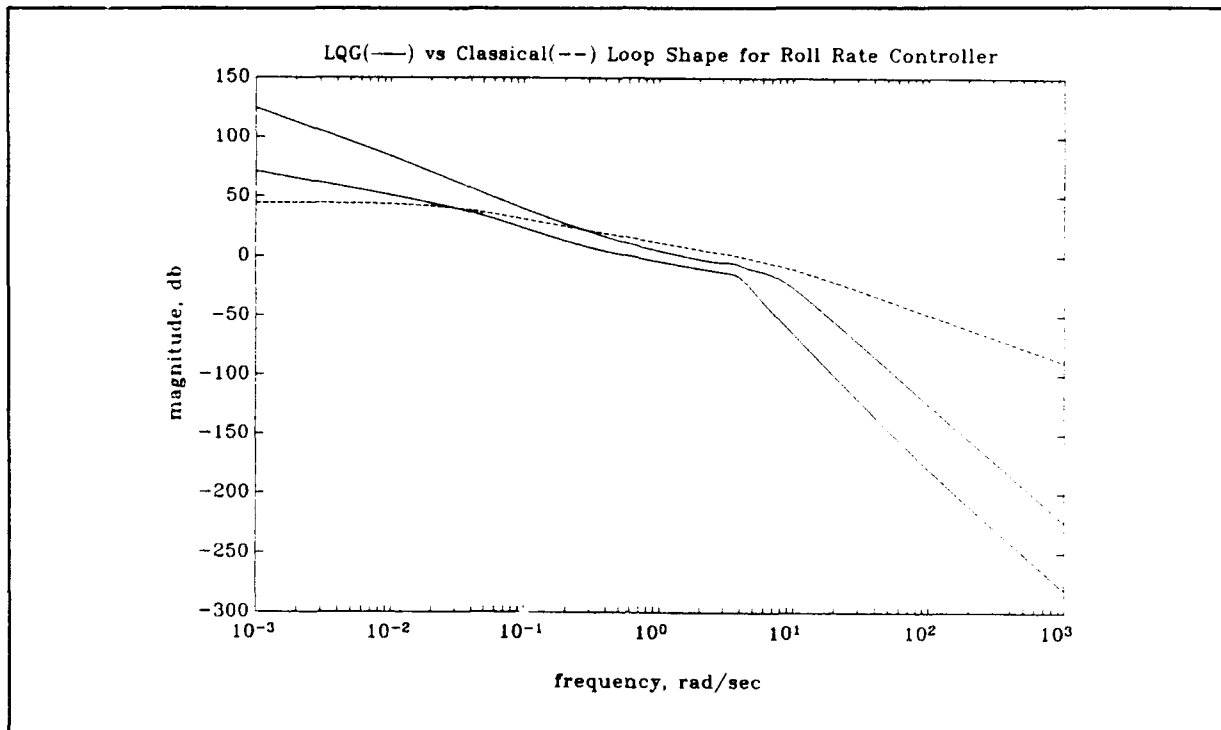


Figure 6.6. $G(s)K(s)$ Loop Shape Comparisons for the Roll Rate Controllers.

The phase margins for these two designs were:

Method	PM
LQG/LTR	$\pm 32^\circ$
Classical	$\pm 71^\circ$

There is quite a disparity in phase margin for the two closed loop systems. However, it must be realized that the LQG/LTR approach guarantees a phase margin of $\pm 60^\circ$ for $q=\infty$ (full recovery) if the transmission zeros of the open loop plant are all in the left-half of the s-plane. However, for this design $q=15$ which is much less than infinity. Thus, the phase margin is expected to be much less than 60° .

The main limitations to the LQG/LTR approach, in this case, were as follows:

1. Both roll rate and sideslip were being regulated. The classical approach only focused on roll rate.
2. If the ratio ρ/q could be increased, the closed loop time response of the LQG/LTR controller would approach that of the classical controller. However, higher ratios of ρ/q drove the loop shape below the desired performance barriers for this design. Notice that the loop shape of the classical approach does, indeed, penetrate the LQG performance barriers.
3. The LQG/LTR approach attempts to invert the plant. The unstable spiral root, therefore, causes some degradation in overall system performance.

The LQG/LTR design does have an advantage in the fact that both sideslip and roll rate are regulated. If the low frequency performance barriers are relaxed, a closed loop time response similar to that of the classical controller could be approached by increasing the ρ/q ratio. The LQG design also provides a loop shape that has good roll-off characteristics at high frequency for good noise rejection. However, if maintaining zero sideslip is not a priority, then the classical design is far superior.

Figure 6.7 compares the closed loop sideslip response to a unit step roll rate command for the two controllers. From this figure, it appears that the added complexity of regulating sideslip is probably not justified. For example, Λ would travel through less than 5 degrees of sideslip after 10 seconds

for a 10 deg/sec roll rate command input; however, it would have rolled through 100 degrees of bank angle in the same amount of time. By just adding a high frequency pole, the classical controller could have good low frequency tracking, good overall bandwidth, and adequate high frequency noise rejection. Therefore, the less complex, classical roll rate controller is probably the better overall design for Lambda.

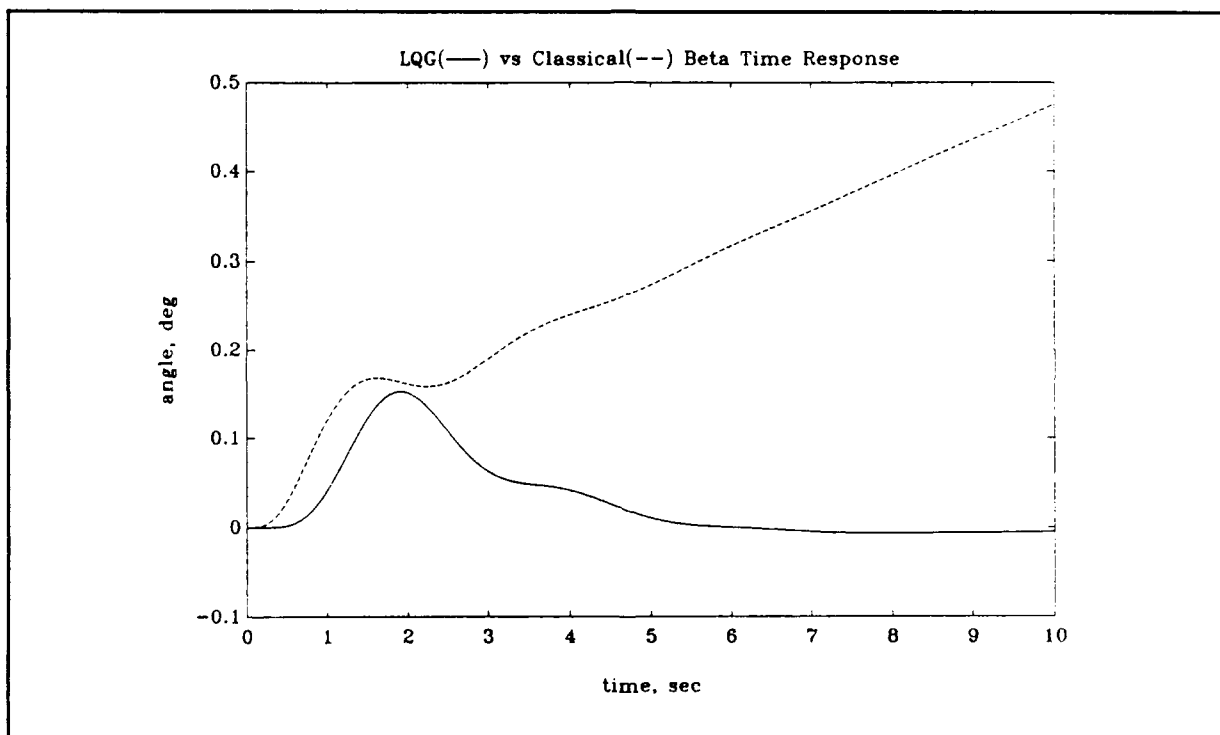


Figure 6.7. Comparison of Closed Loop Sideslip Response for the Roll Rate Controllers.

6.2.3. Yaw Rate Controller Comparisons

The following three yaw rate controller designs were developed in this thesis:

- #1: a classical, SISO yaw rate controller,
- #2: a LQG/LTR controller that regulated yaw rate and bank angle, and
- #3: a LQG/LTR controller that regulated yaw rate and sideslip.

The first and third controller designs above will be compared in this section. The open loop system for the second design was unstable and minimum phase. Therefore, the specifics of the LQG/LTR approach for this design are similar to that discussed in the last section. However, the open loop system for the third design is unstable and non-minimum phase. Therefore, further insight to the LQG/LTR methodology can be gained by examining this design.

The transmission poles and zeros of the open loop system for designs #1 and #3 are given in Table 6.4.

Table 6.4. Open Loop System Dynamics for the Yaw Rate Controllers.

<u>Classical (r/δ_r):</u>		<u>LQG/LTR ($C\Phi B$):</u>	
Poles:	Zeros:	Poles:	Zeros:
-0.7275 ± 2.7933i	-0.0403 ± 0.3216i	-0.7275 ± 2.7933i	-36.279
-5.1930	-5.2159	-5.1930	-1.225
0.0213		0.0213	18.384
-6.20 (servo)		-5.50 (servo)	
		-6.20 (servo)	
		-1.225 (wind)	

Note: $y=[\beta, r]^T$

The open loop plant for both systems is slightly unstable.

However, the open loop system for the LQG/LTR approach is also non-minimum phase.

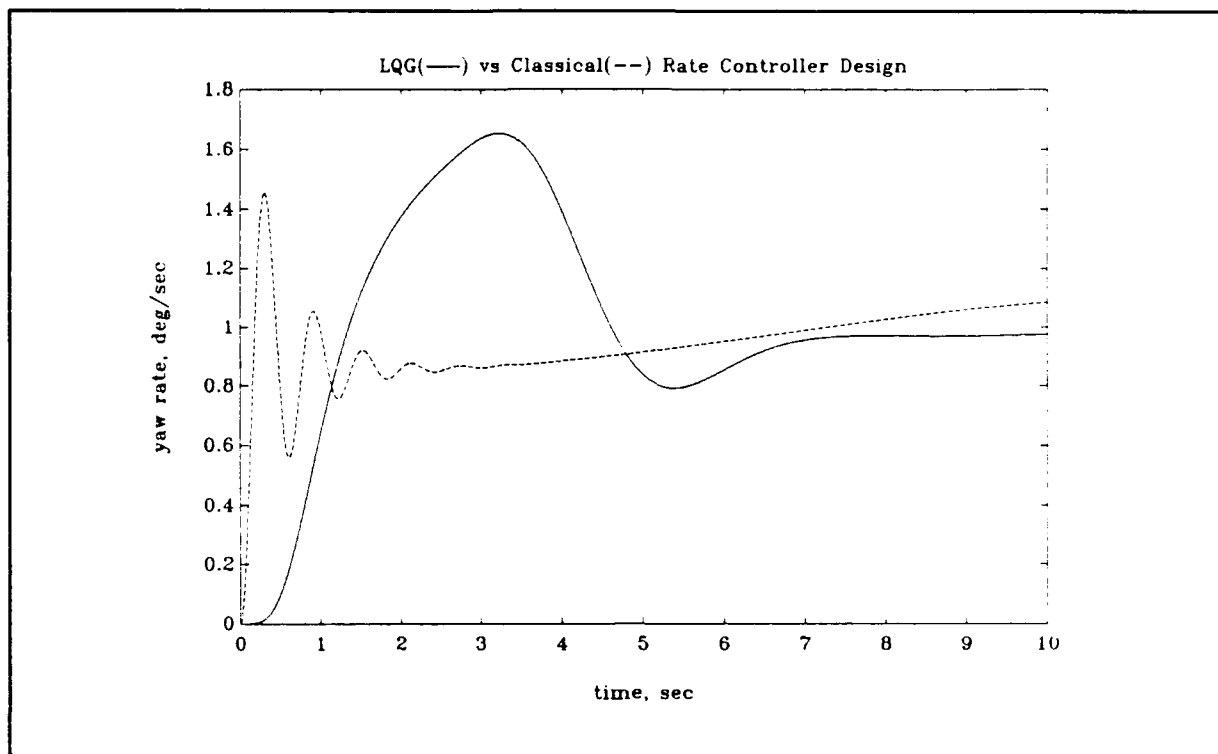


Figure 6.8. Closed Loop Yaw Rate Time Response Comparisons.

Figure 6.8 provides the closed loop yaw rate time responses to a unit step yaw rate command input for the two design approaches. The time responses have the following characteristics:

<u>Response</u>	<u>M_p (%)</u>	<u>t_r (sec)</u>	<u>t_s (sec)</u>
LQG/LTR	60	0.75	6.50
Classical	45	0.10	> 10

Notice that neither time response meets the performance objectives proposed in Table 6.1. The classical design exhibits a quick initial oscillatory response followed by a slowly dying, low frequency oscillation. In order to minimize the long period

oscillation in the classical controller, high gains had to be used which aggravated the initial oscillatory response. Both methodologies were plagued by the fact that the open loop system has zeros close to the origin which are very lightly damped, and the spiral mode is unstable.

In the classical design, the lightly damped zeros near the origin draw a pair of closed loop poles into them. These poles cause the long period oscillation in the closed loop time response. As compensator gain is increased, their effect is decreased due to near cancellation with the zeros; however, overall system damping is sacrificed. The transmission poles and zeros of the LQG/LTR compensator are as follows:

Poles(K_{LQG}):	Zeros(K_{LQG}):
-1.9338 ± 5.5903i	-0.6165 ± 2.6486i
-0.2024 ± 2.6727i	-0.1499 ± 0.1651i
-2.6975 ± 2.7526i	-6.2055
-6.7843 ± 2.3526i	-5.1943
-5.4210 ± 0.6805i	-5.5028
-1.2180	-1.2189
	-0.3585

Remember, the LQG/LTR compensator is a 2x2 transfer function matrix. Again, it is seen from the transmission zeros that the LQG/LTR compensator is attempting to invert the plant. The unstable spiral mode is, in effect, being mirrored by the zero at $s=-0.3585$. It can be seen from the closed loop time response that LQG/LTR was fairly successful in canceling unwanted system dynamics.

The loop shapes of the transfer function, $G(s)K(s)$, for both systems are given in Figure 6.9. Notice that the LQG approach

produces a much better loop shape. Both loop shapes, however, do not have smooth crossover transitions. The phase margins for the two designs are as follows:

Method	PM
LQG/LTR	$\pm 13^\circ$
Classical	$\pm 20^\circ$

Neither design has an adequate phase margin.

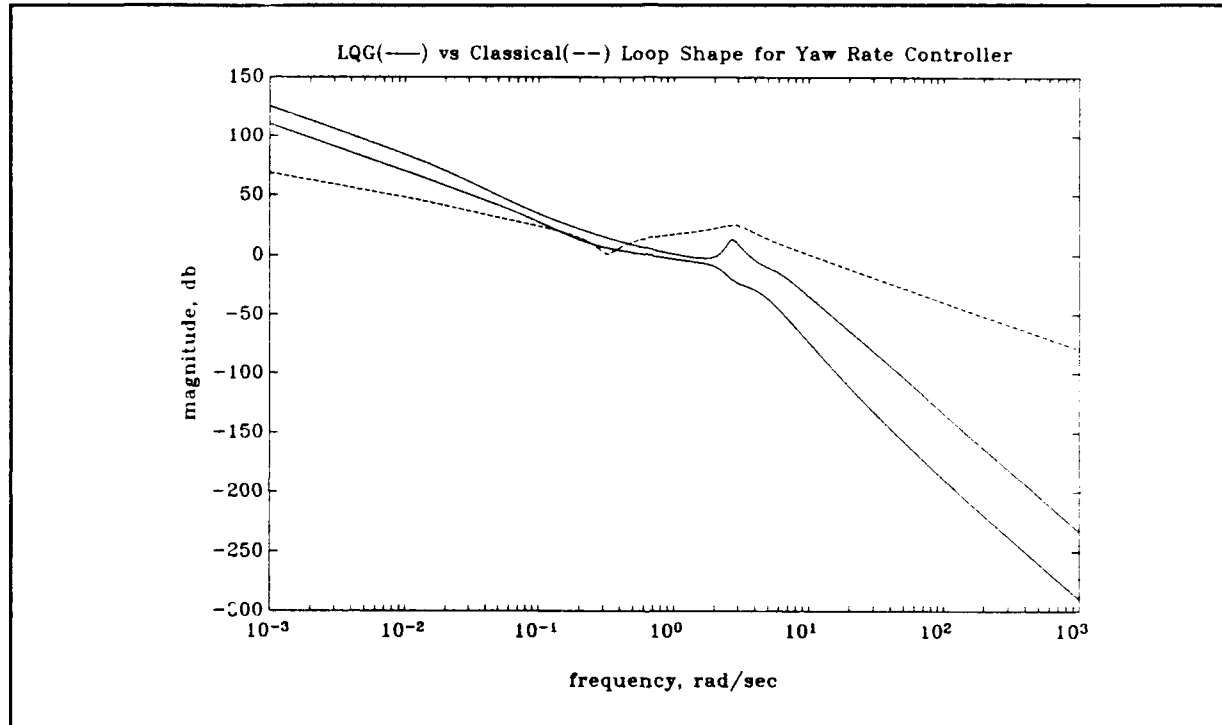


Figure 6.9. $G(s)K(s)$ Loop Shape Comparisons for the Roll Rate Controllers.

Since the strongpoint of the LQG/LTR controller is to provide a coordinated turn, the sideslip time responses to a unit step yaw rate command are compared in Figure 6.10 for both designs. For maintaining zero sideslip, the LQG/LTR compensator is a far superior yaw rate controller design.

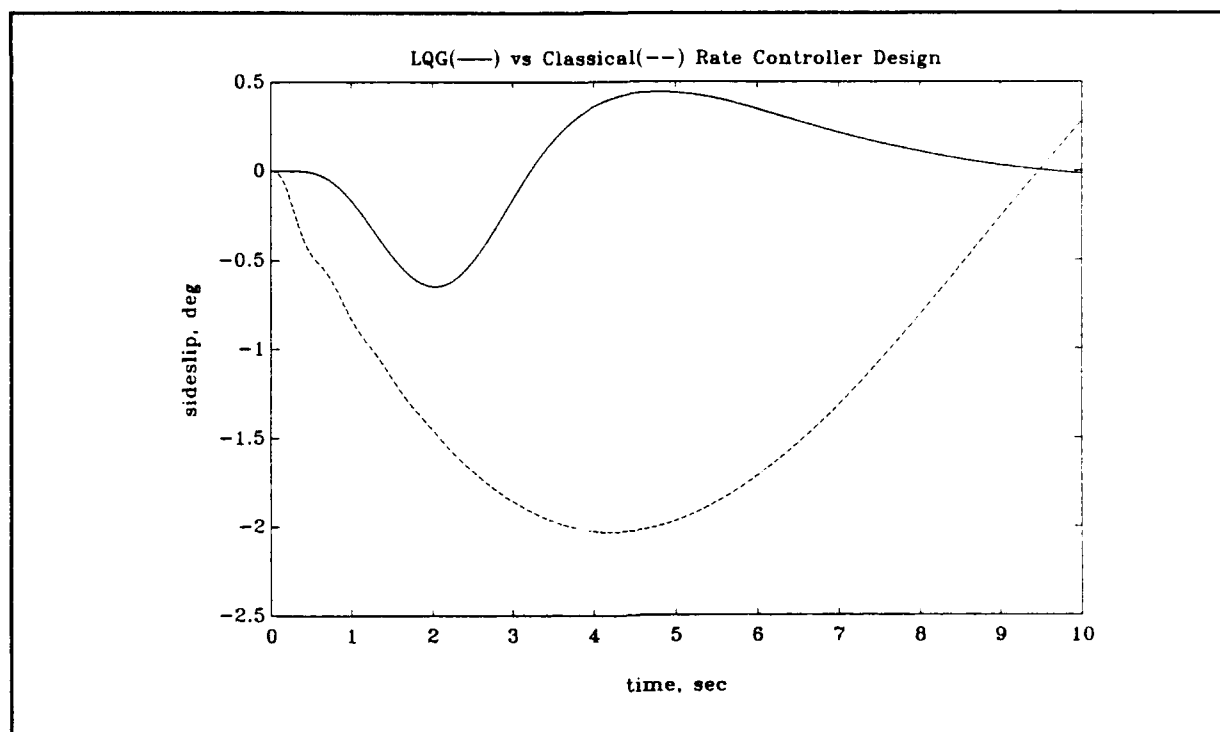


Figure 6.10. Comparison of Closed Loop Sideslip Response for the Yaw Rate Controllers.

The LQG/LTR approach produces the better system design. Both sideslip and yaw rate are regulated in this design, as opposed to only yaw rate in the classical approach. The LQG/LTR approach produces better overall closed loop time responses. Also, the LQG/LTR approach has a better loop shape for both low frequency tracking and high frequency noise rejection. However, both designs had problems with the low frequency, lightly damped dynamics of the open loop system. This is caused by the basic layout of the Lambda vehicle. Good recovery was especially difficult with this LQG/LTR design due to the non-minimum phase of the open loop system.

6.3. Conclusions and Recommendations

This section summarizes the important conclusions that can be drawn from the rate controller designs. It also provides recommendations on how to proceed with the given designs.

6.3.1. Conclusions

The following conclusions should be noted:

1. The rate controller design problem for the Lambda URV offered an excellent opportunity for comparing classical and LQG/LTR design methodologies. The pitch rate controller comparison in Section 6.2.1 vividly illustrates the differences in the two approaches. Although the classical design approach offers more insight to the actual dynamics of the open loop plant and compensator through root locus techniques, the LQG/LTR approach offers a much more structured approach that allows the designer to directly address system performance, robustness, and control usage.
2. Compensator complexity is a key issue in any design. LQG/LTR will always produce a compensator that is of the same order as the open loop plant. By their nature, designs using classical techniques will be relatively simple. For systems whose open loop dynamics are well behaved, classical approaches to controller design should be thoroughly examined before more complicated methods are attempted. However, if undesirable open loop dynamics are the problem (lightly damped/low frequency /unstable poles or zeros), then the LQG/LTR approach of plant

inversion and structured placement of closed loop dynamics will provide the engineer an effective design tool.

3. Although Lambda's flight envelope is fairly benign, the performance of the final rate controller designs (except for the classical roll rate controller), was enhanced through gain scheduling. Since plant inversion is fundamental to the LQG/LTR approach, accurate state estimation by the Kalman filter is a necessity. Thus, scheduling the Kalman filter gains always improved compensator performance.

4. Most of the problems encountered in finding effective controller designs stemmed from the basic design and layout of the Lambda URV. The performance of the pitch rate controllers were severely degraded by the slow elevator actuators used on Lambda. The yaw rate controller designs were plagued by the lightly damped, very low frequency zeros of the open loop plant. The open loop dynamics for the roll rate controller were well behaved (an unstable spiral mode is not uncommon).

5. From the comparisons presented in this chapter, the following significant features of the LQG/LTR design methodology are highlighted:

- LQG/LTR allows the designer to specify system performance and uncertainty information in the frequency domain.

- LQG/LTR offers a structured approach that allows the designer to trade between system performance, robustness, and control usage concurrently.

- Lightly damped/low frequency poles or zeros in the open

loop system cause problems in trying to obtain good closed loop time response performance.

- LQG/LTR will always produce a compensator of the same order as the open loop plant. Simpler compensators could be obtained through model reduction techniques.

- Since plant inversion is fundamental to LQG/LTR, good Kalman filter performance is essential. Gain scheduling is one method to obtain good Kalman filter performance. Other techniques such as parameter estimation and multiple model adaptive estimation are discussed in Reference 6.4.

6.3.2. Recommendations

The following recommendations are noted:

1. The implementation of faster control actuators on the Lambda URV should be strongly considered. The slow servo dynamics significantly degrade the performance of all rate controller designs no matter what methodology is used.
2. For a remotely piloted vehicle, attitude control is a more solid choice for the flight control system. Rate controller designs are better suited for conditions in which the pilot feels the rates acting upon the airplane and can provide command inputs accordingly. The pilot of a remotely piloted vehicle is much more comfortable providing attitude command inputs to the flight control system than he is in trying to anticipate appropriate rate commands. Also, closed loop performance of attitude controllers can be directly related to levels of flying quality

through MIL-STD-1797A.

3. All the LQG/LTR rate controllers, as well as the classical roll rate controller, are solid starting points for designs to be actually implemented into the Lambda URV. Before proceeding, improvements to the performance of the Kalman filter designs, by feeding back all available state measurements, should be investigated. Also, model order reduction of the compensators should be considered. A brief investigation into reducing the order of the LQG/LTR pitch rate compensator revealed that removing 3 states from the compensator did not significantly affect overall closed loop performance. Similar analysis for the LQG/LTR roll rate and yaw rate controllers showed that 4 states in each of these compensators could be removed without significant closed loop performance degradation.

4. The LQG/LTR controllers developed in this thesis were all regulator designs. Figure 6.11, adapted from Reference 21, depicts a command generator tracker (CGT) with a regulator. This set-up seeks a feedback control law that drives perturbations from the ideal plant trajectory to zero. Thus for Lambda, the set of desired closed loop time responses given in Figure 6.1 could be used to define ideal trajectories for the command generator tracker. This approach, however, was not pursued any further. It was felt that the slow servo dynamics would significantly degrade the performance of a command generator tracker just as they degraded the performance of the regulator designs. Thus, the increase in controller complexity using a

command generator tracker approach could not be justified.

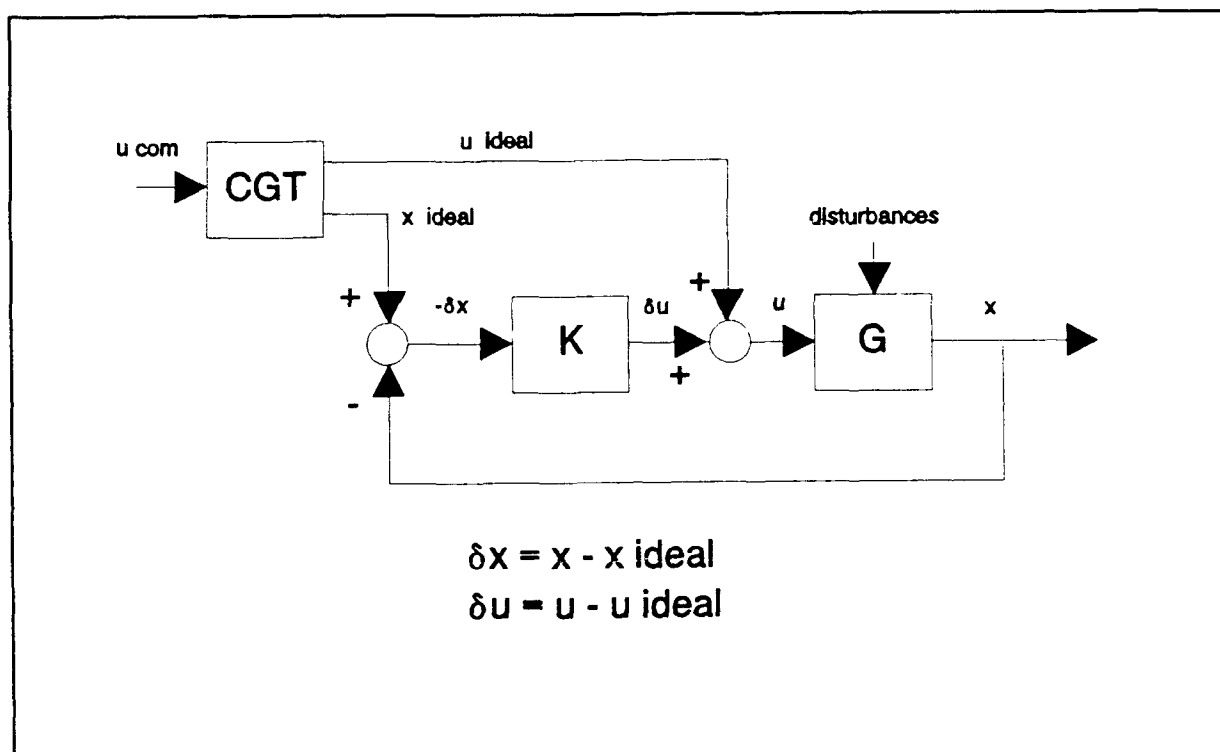


Figure 6.11. Command Generator Tracker (CGT) Block Diagram.

Appendix A:

Flight Test Data Example

This appendix presents the data measurements for the first pitch doublet maneuver (half flaps, full throttle) on the first day of flight testing.

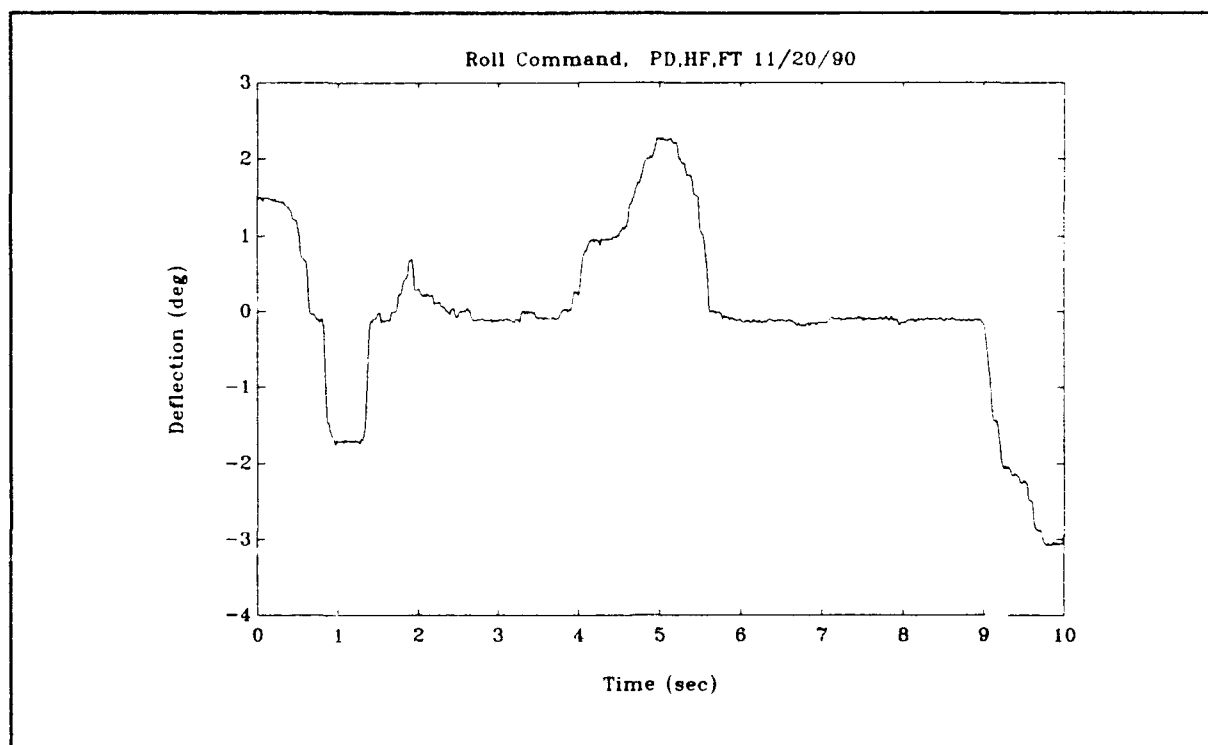


Figure A.1. Roll Command.

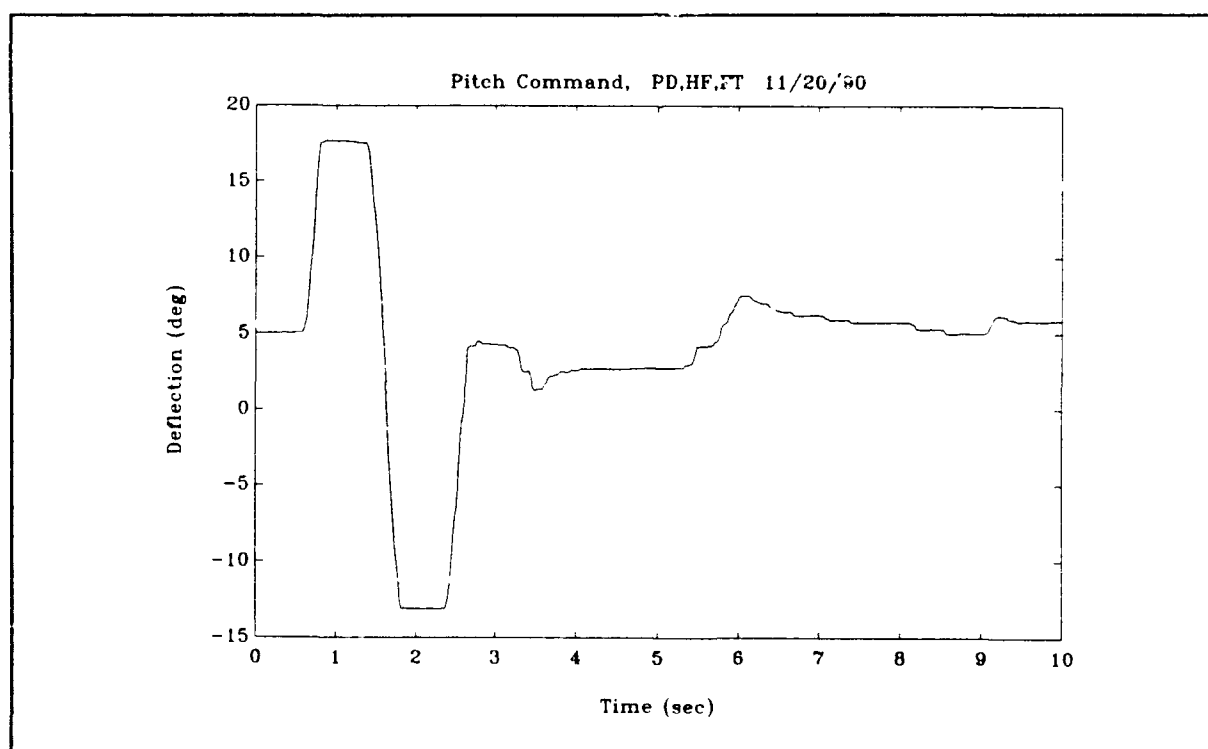


Figure A.2. Pitch Command.

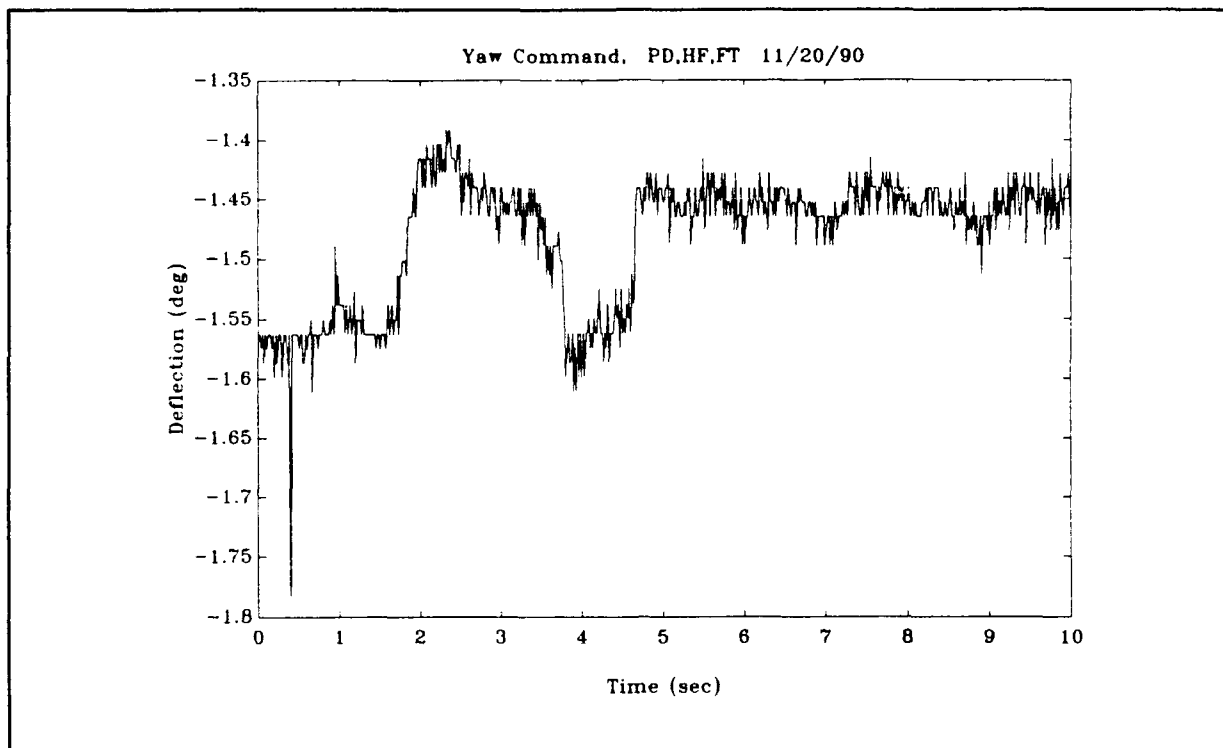


Figure A.3. Yaw Command.

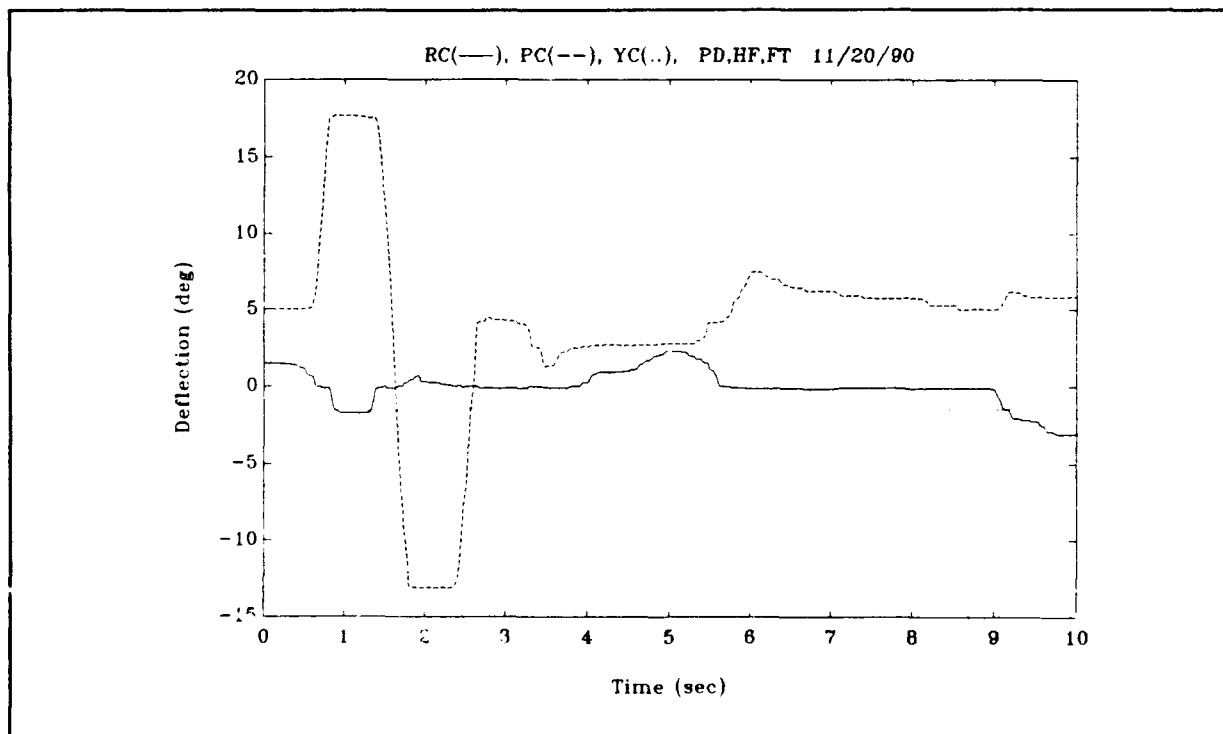


Figure A.4. Roll Command (RC), Pitch Command (PC), and Yaw Command (YC).

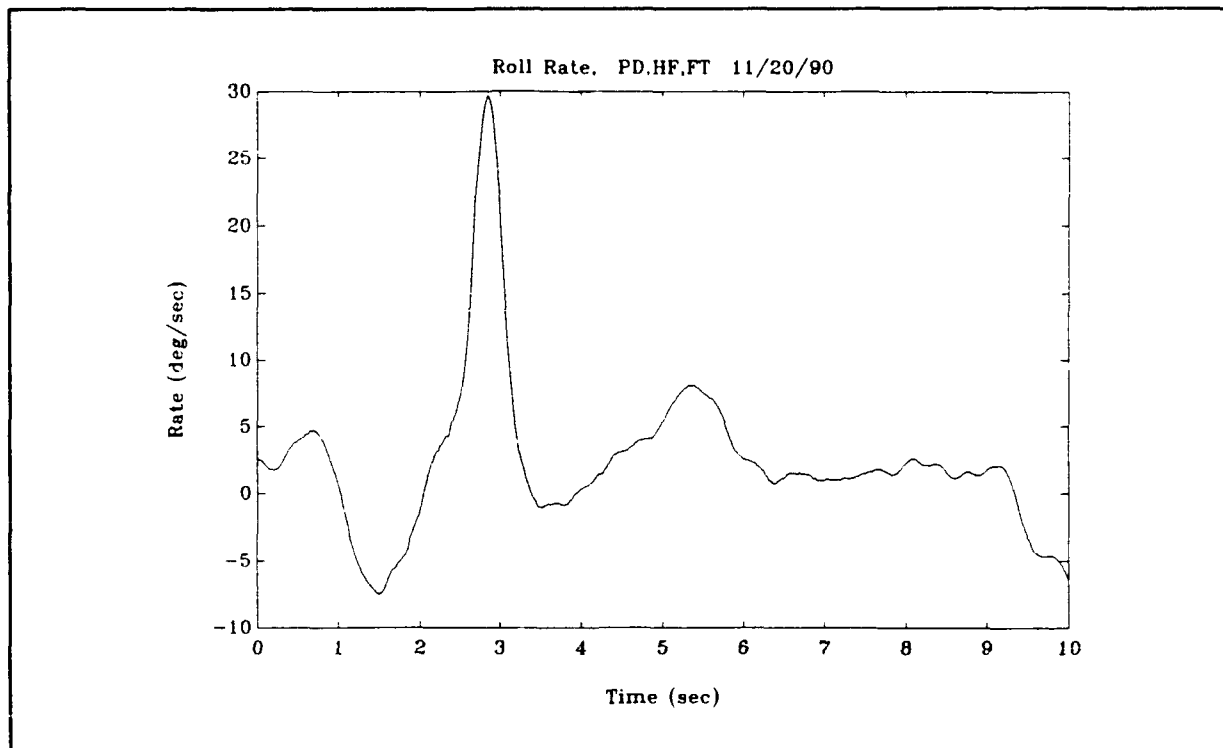


Figure A.5. Roll Rate.

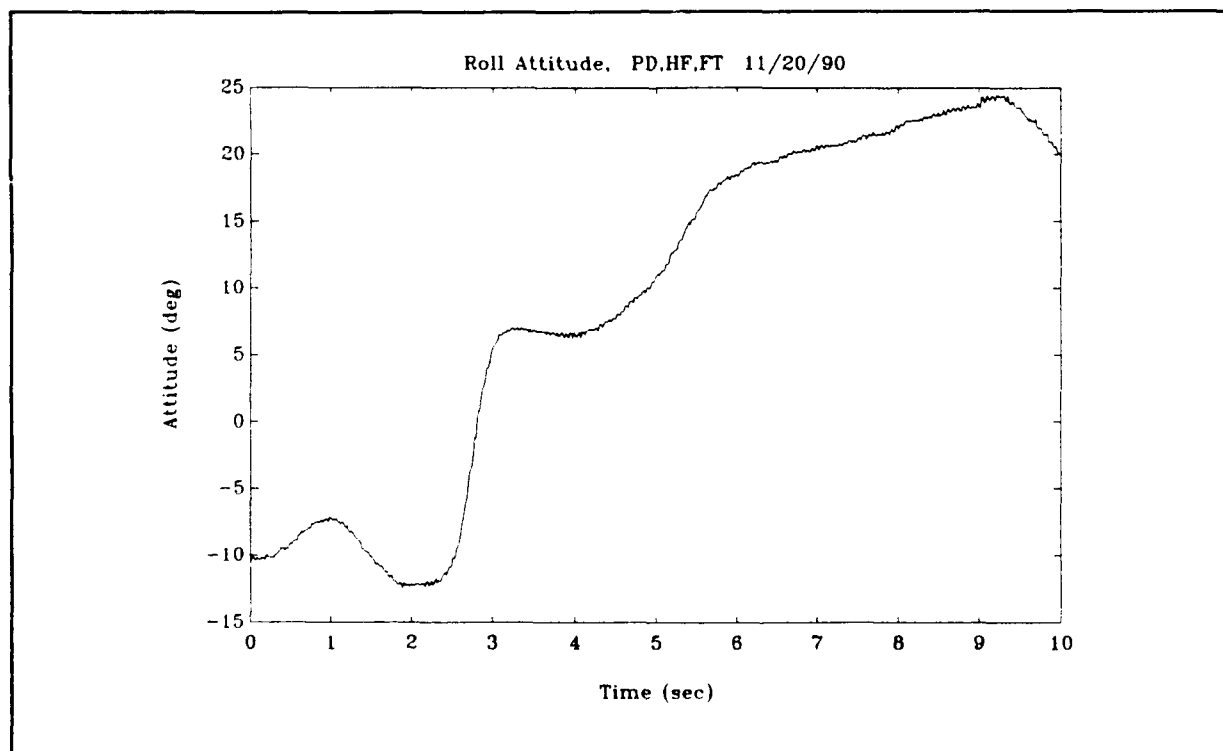


Figure A.6. Roll Attitude.

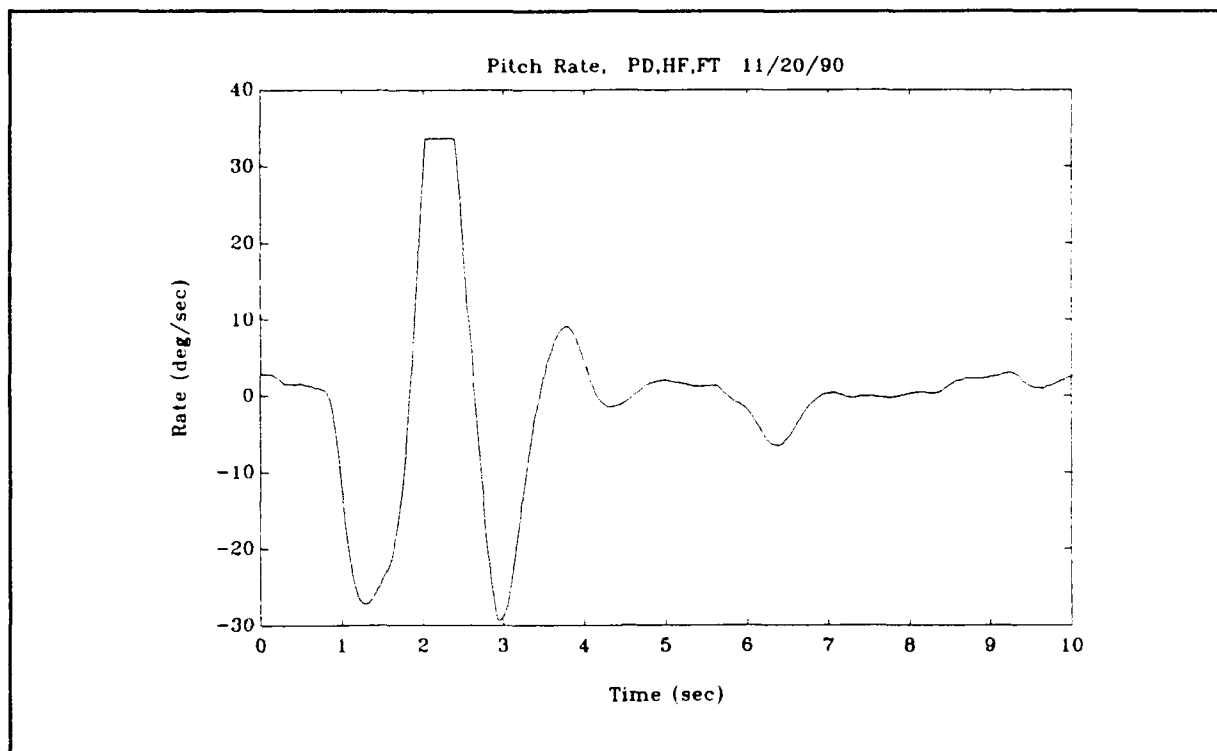


Figure A.7. Pitch Rate.

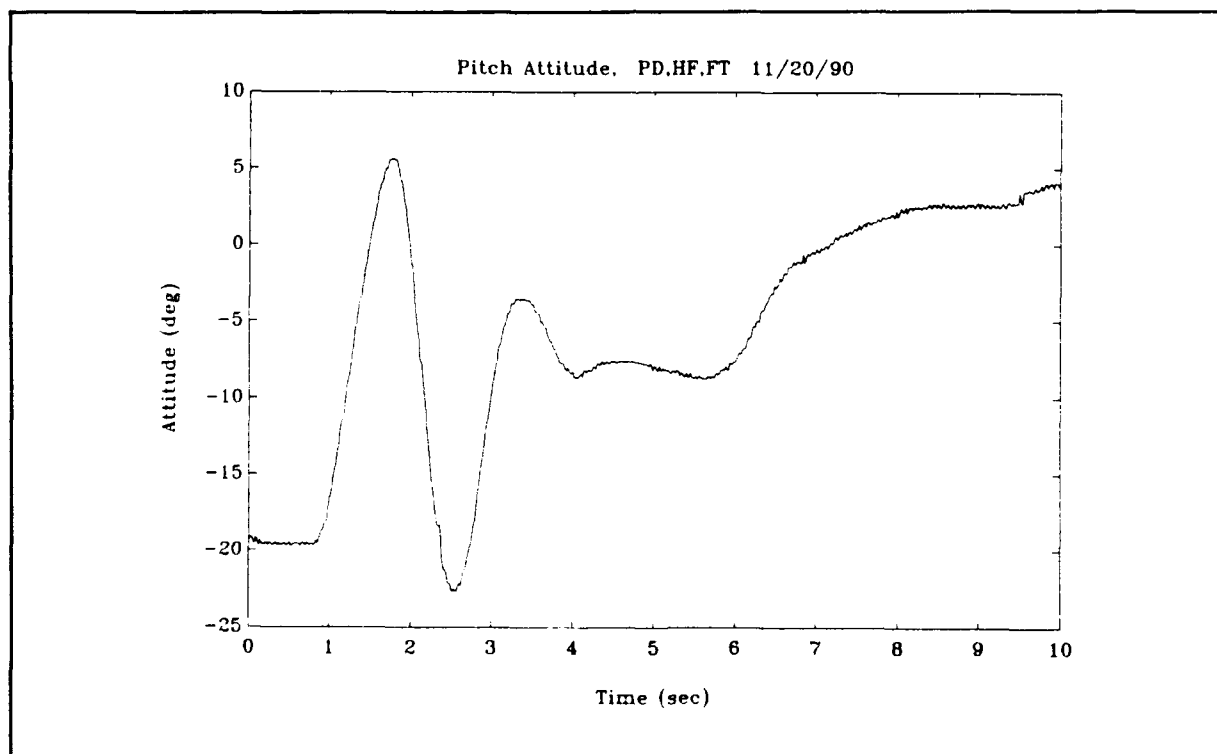


Figure A.8. Pitch Attitude.

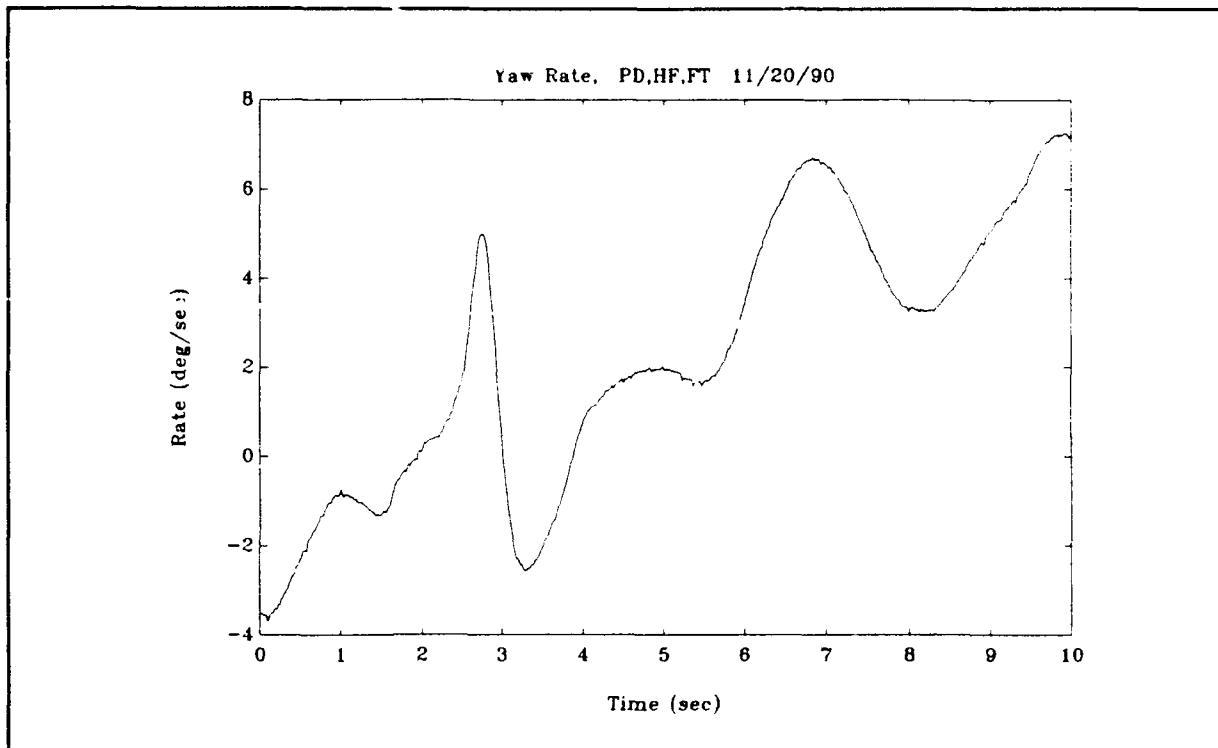


Figure A.9. Yaw Rate.

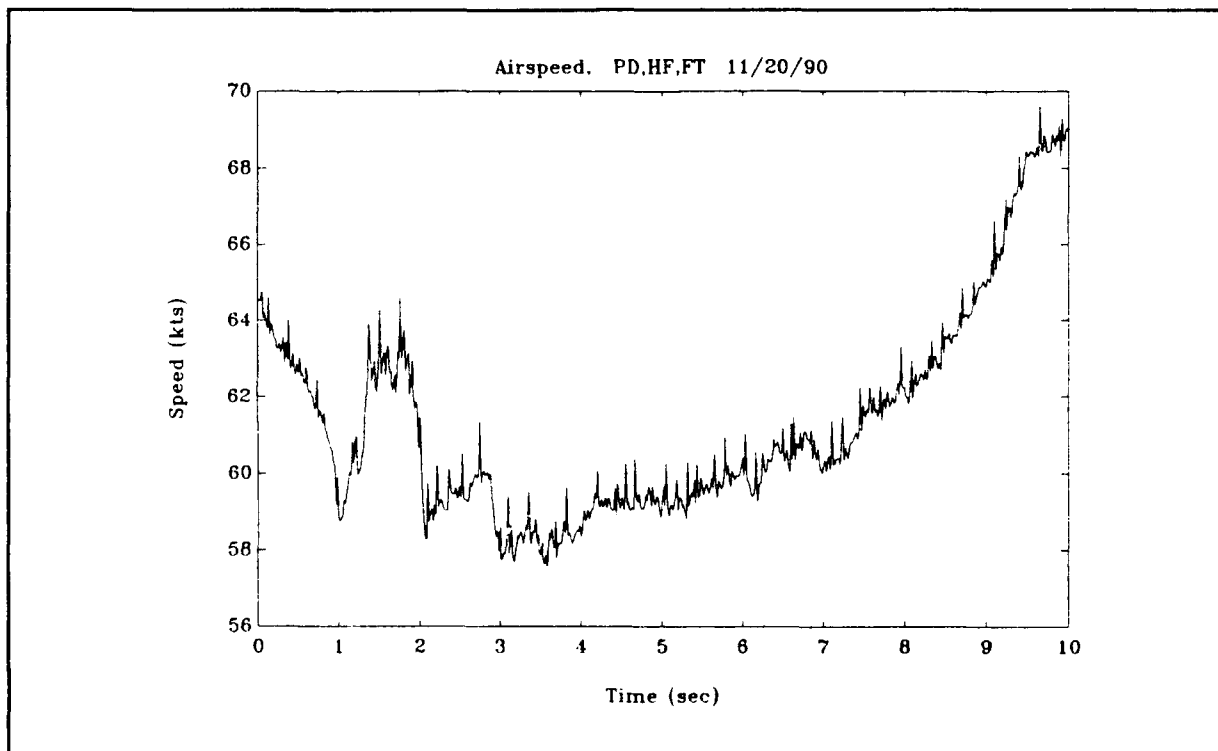


Figure A.10. Airspeed.

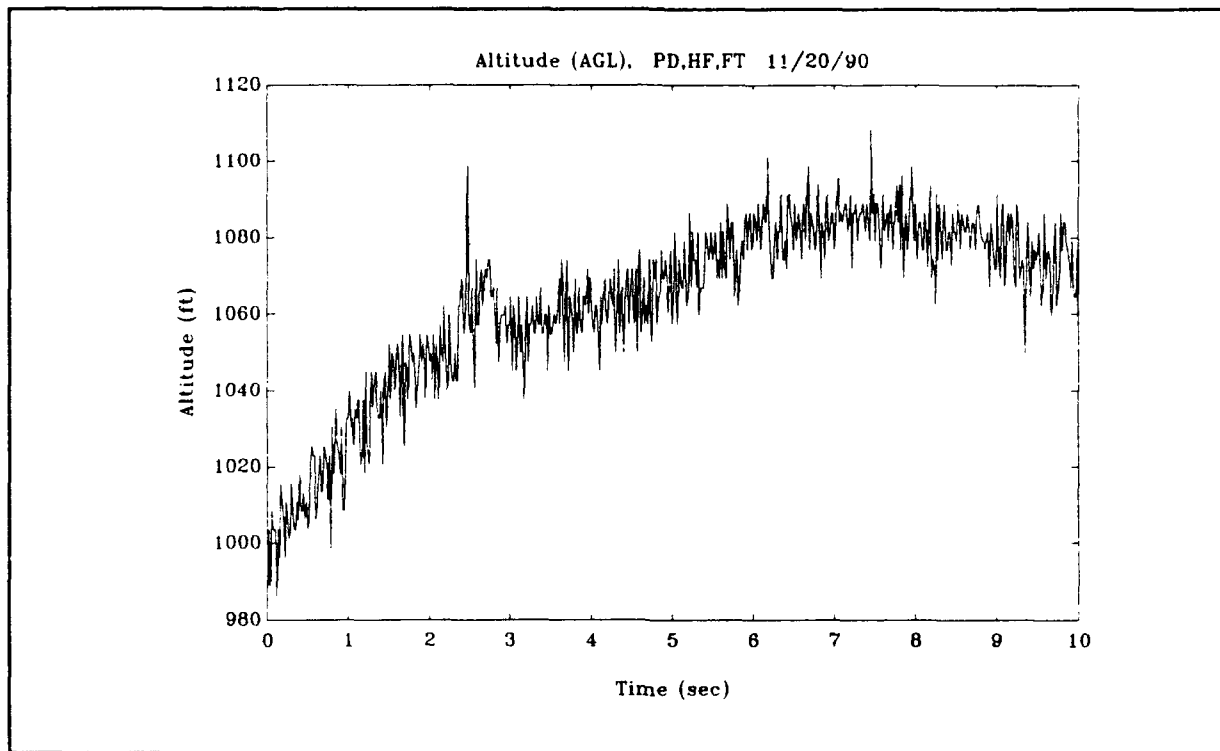


Figure A.11. Altitude.

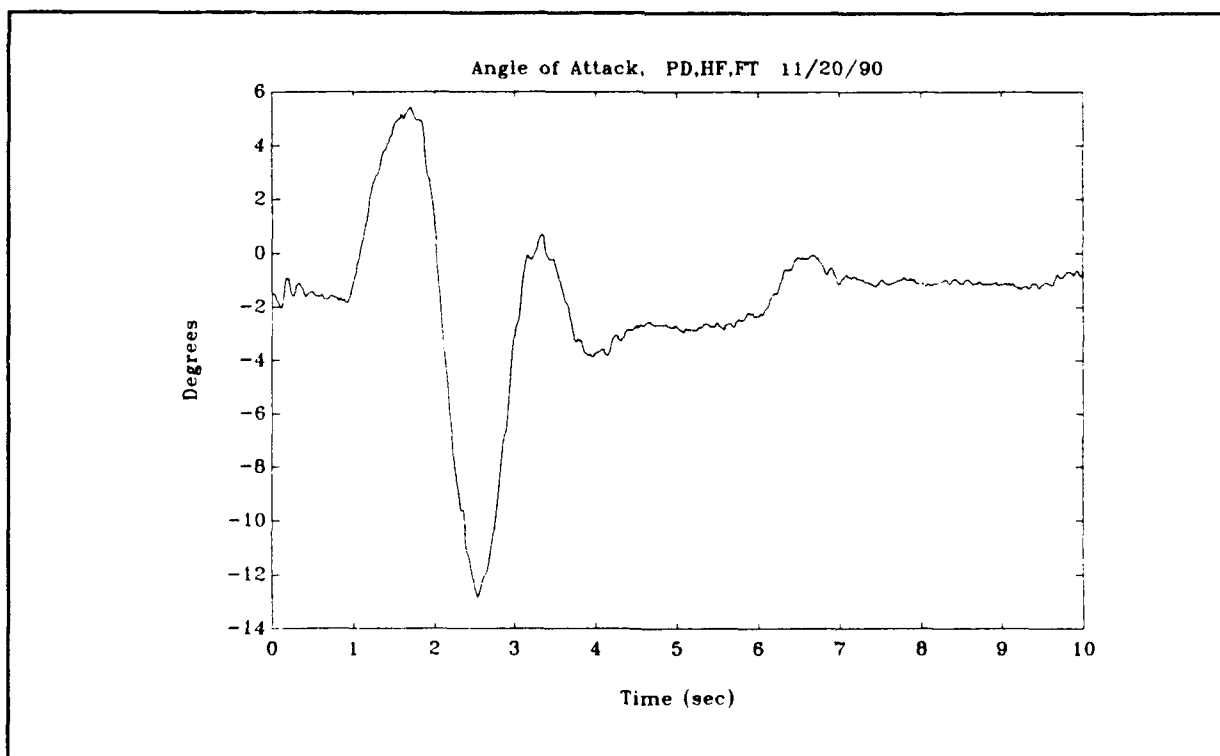


Figure A.12. Angle of Attack.

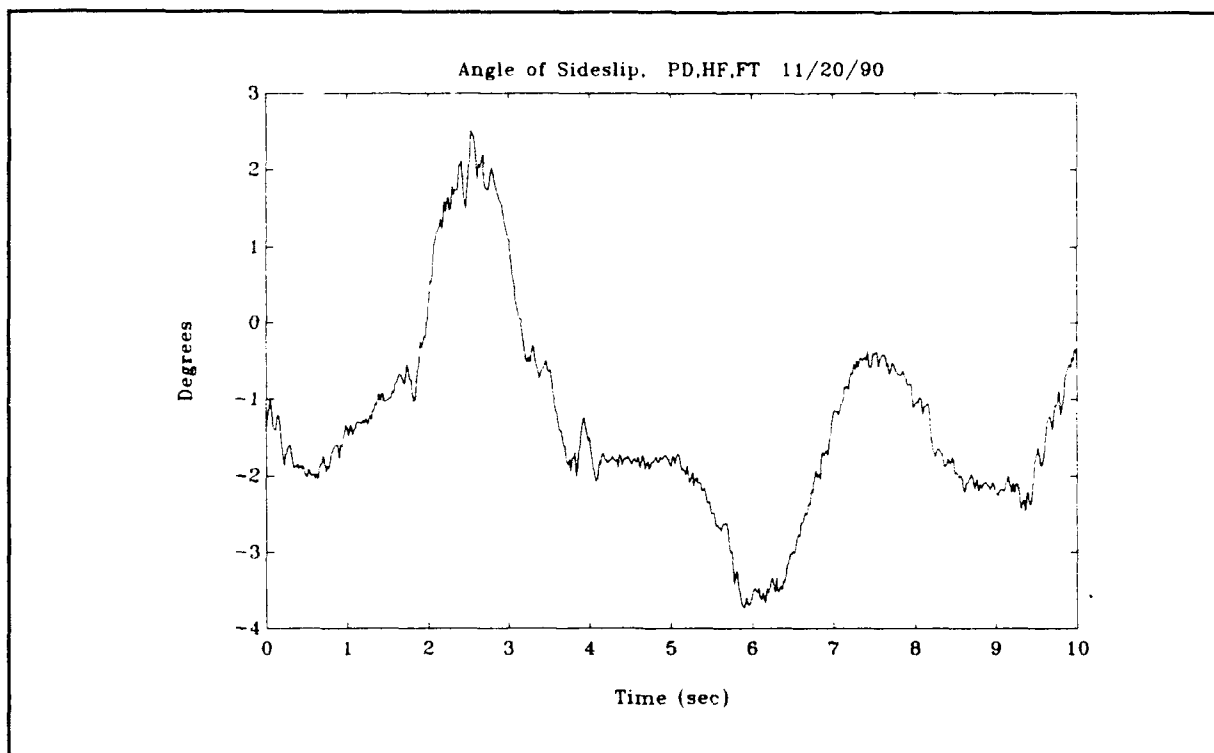


Figure A.13. Angle of Sideslip.

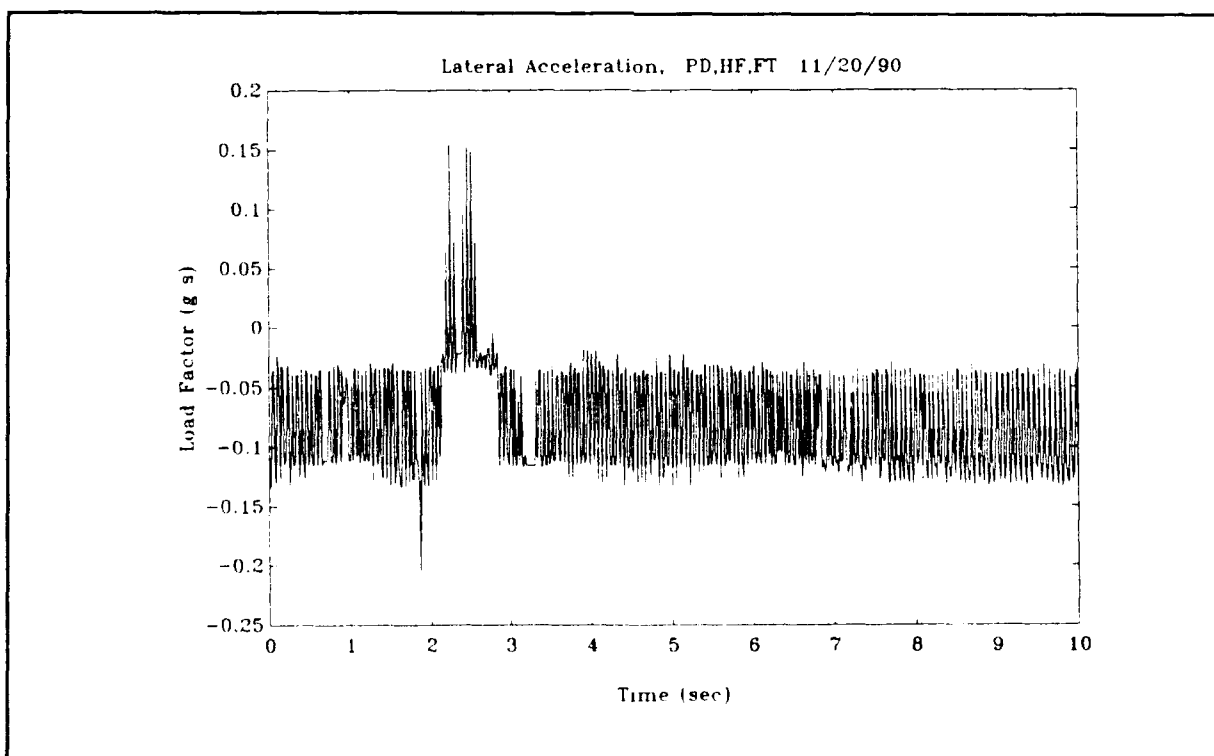


Figure A.14. Lateral Acceleration.

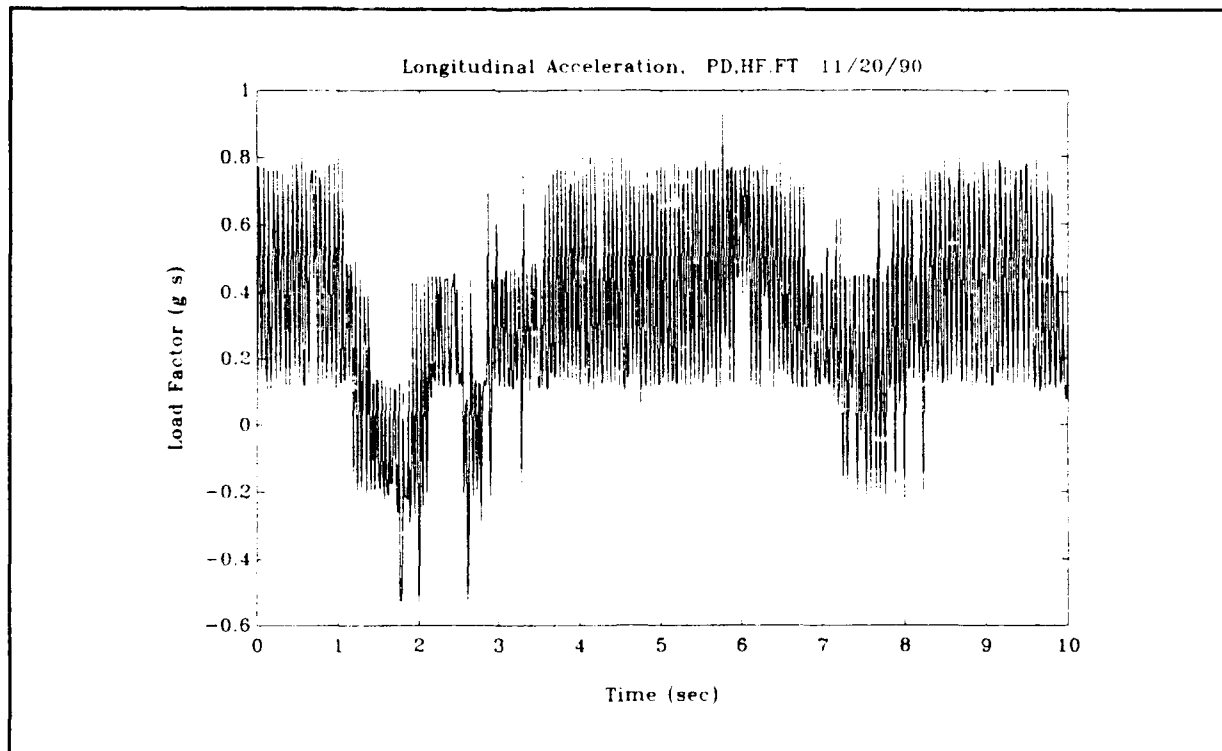


Figure A.15. Longitudinal Acceleration.

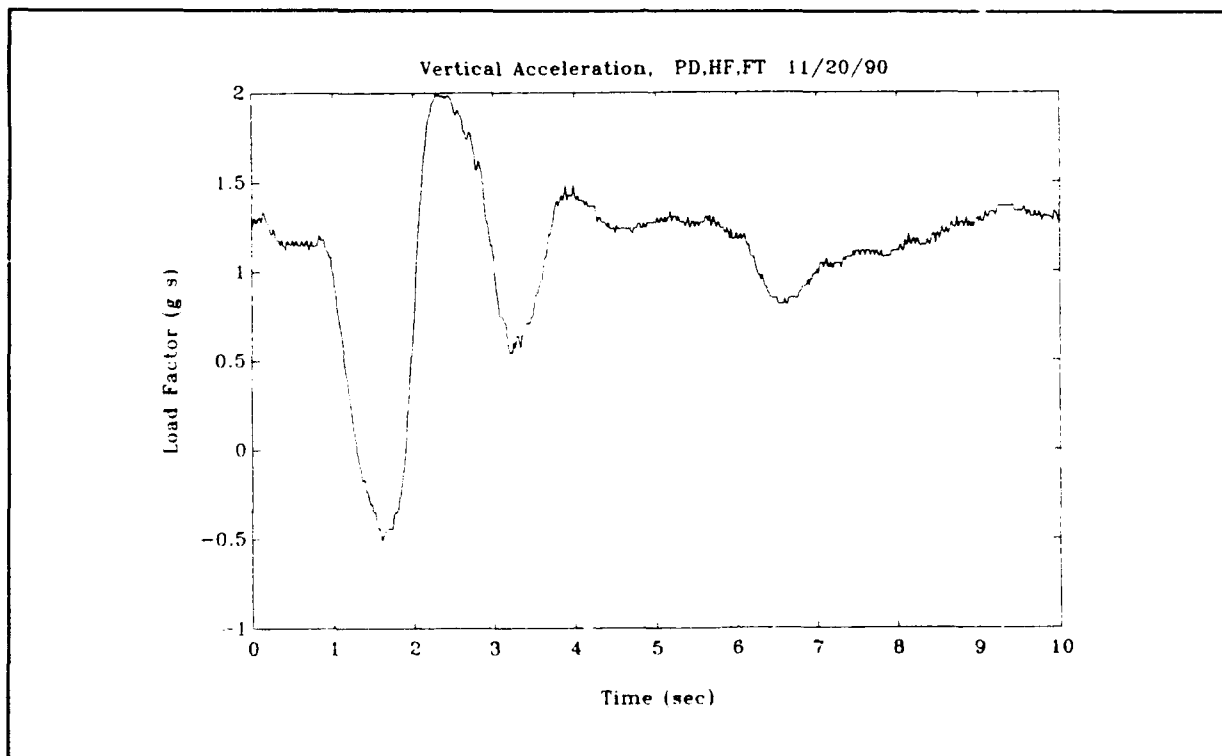


Figure A.16. Vertical Acceleration.

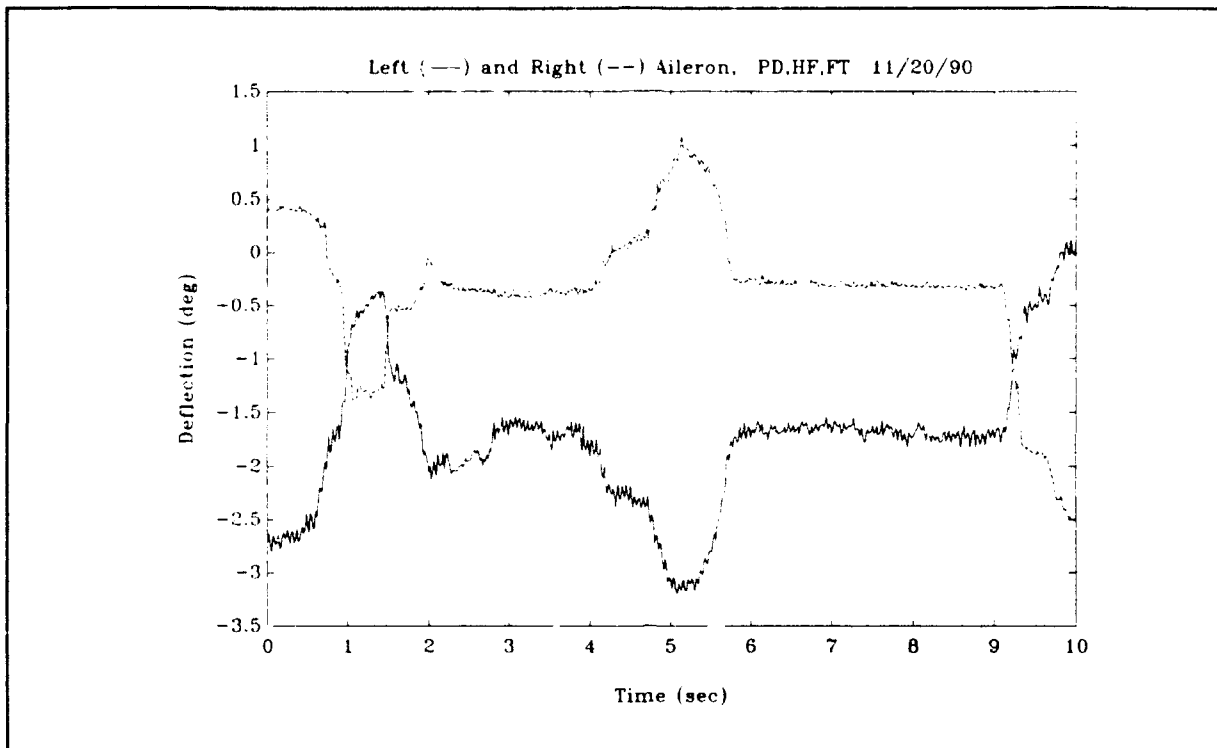


Figure A.17. Left and Right Aileron Deflection.

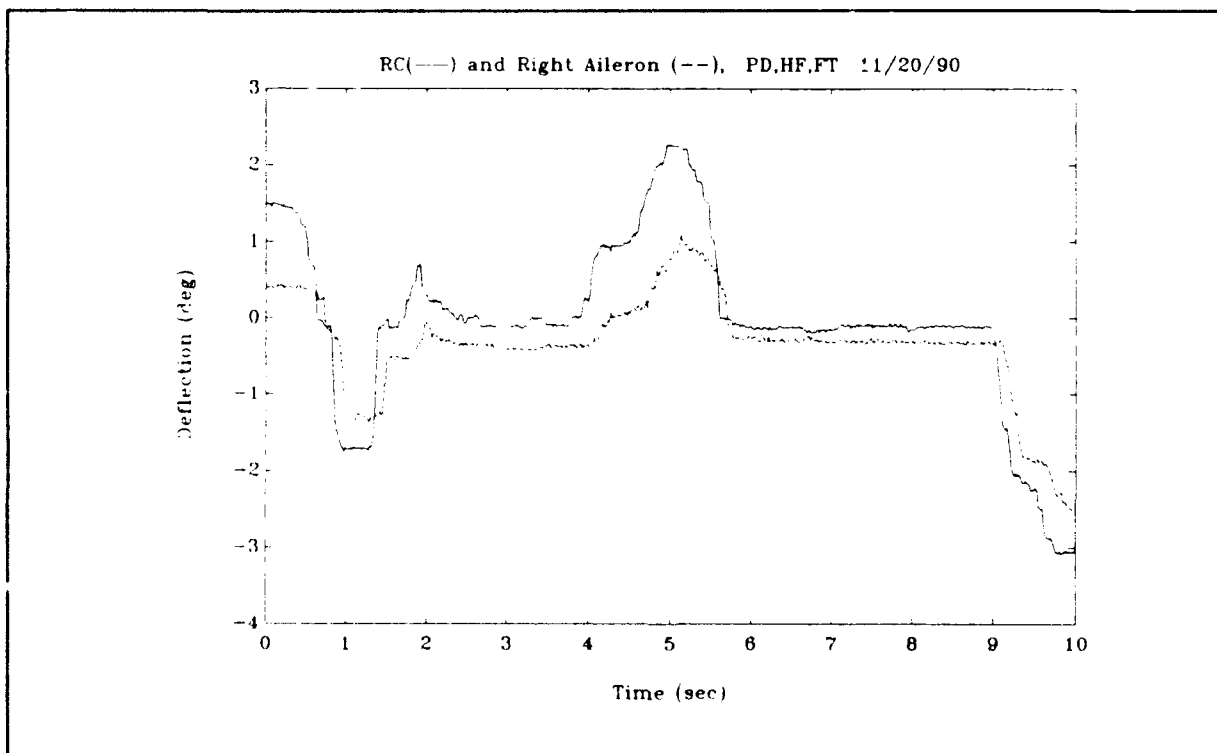


Figure A.18. Roll Command and Right Aileron Deflection.

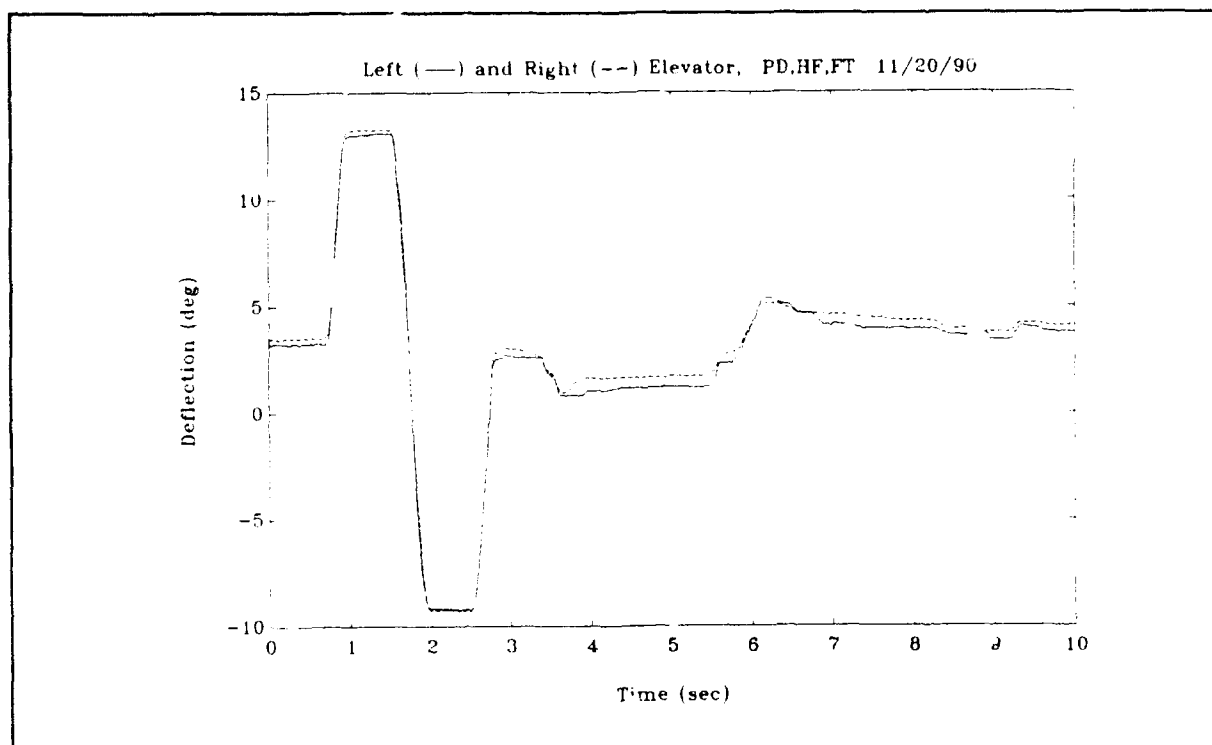


Figure A.19. Left and Right Elevator Deflection.

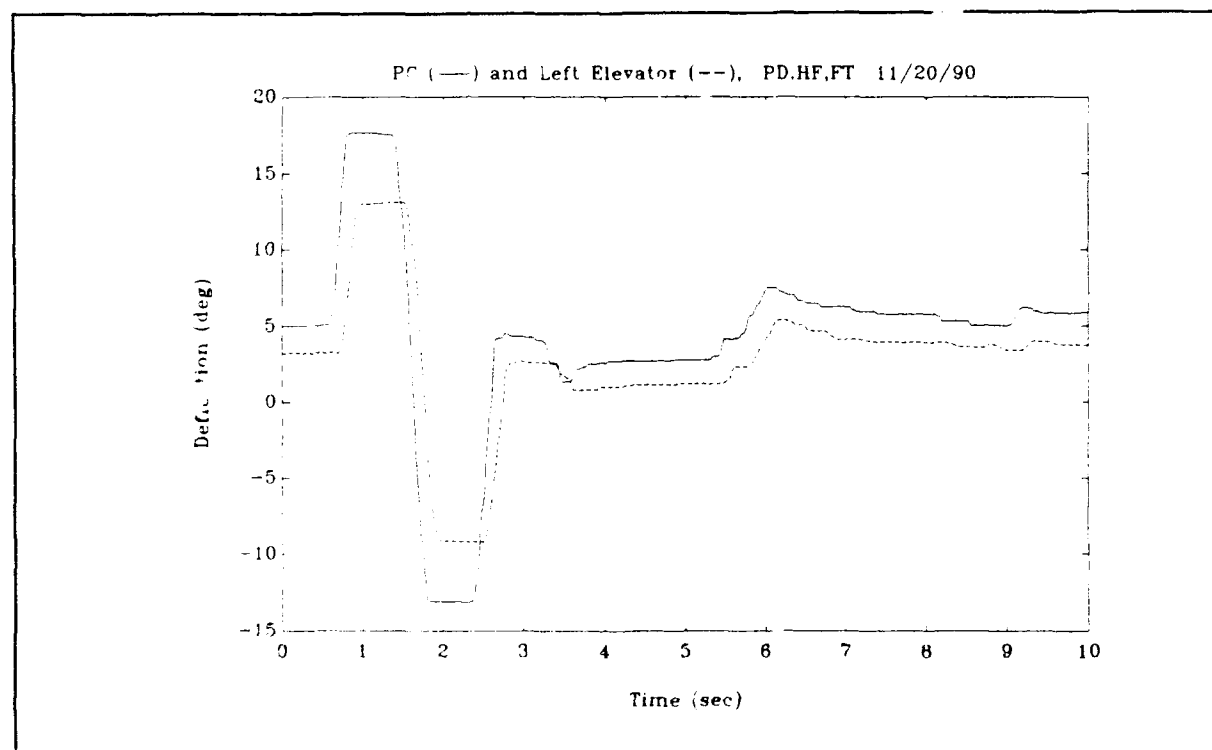


Figure A.20. Pitch Command and Left Elevator Deflection.

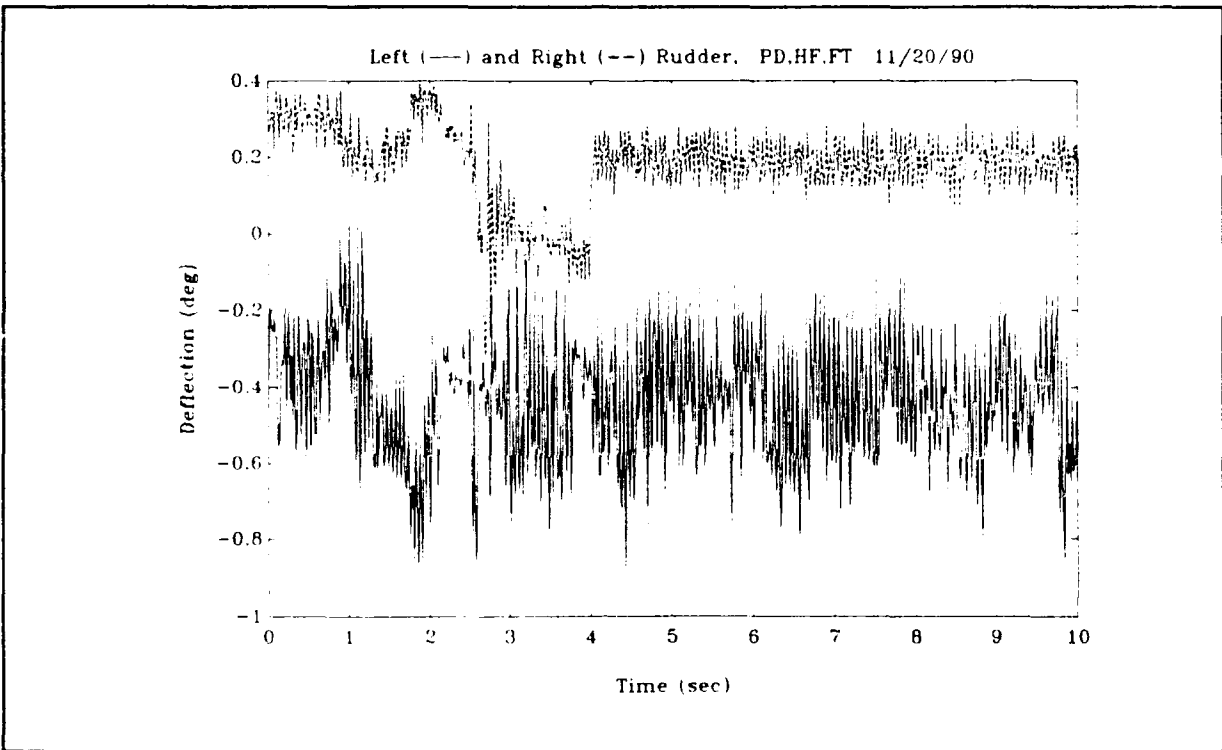


Figure A.21. Left and Right Rudder Deflection.

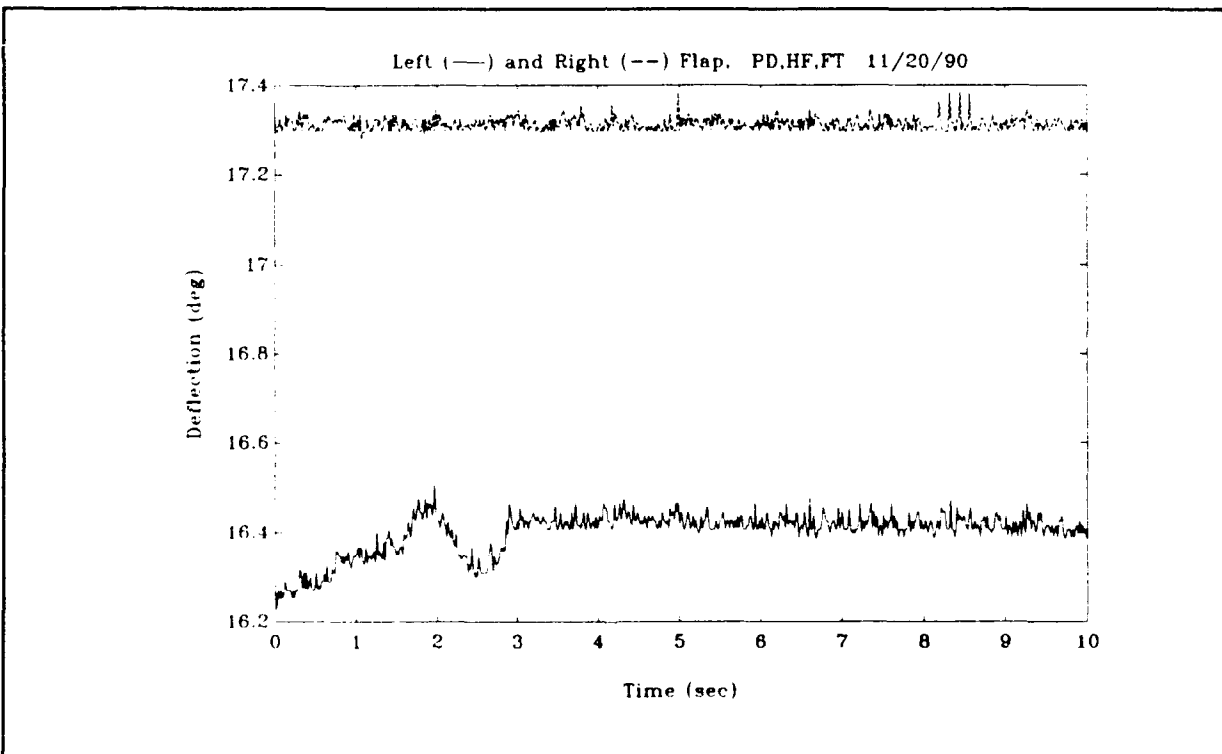


Figure A.22. Left and Right Flap Deflection.

Appendix B:

Maximum Likelihood Parameter Estimation Examples

This appendix presents examples of the data fit achieved from the maximum likelihood iterations for each type of flight test maneuver.

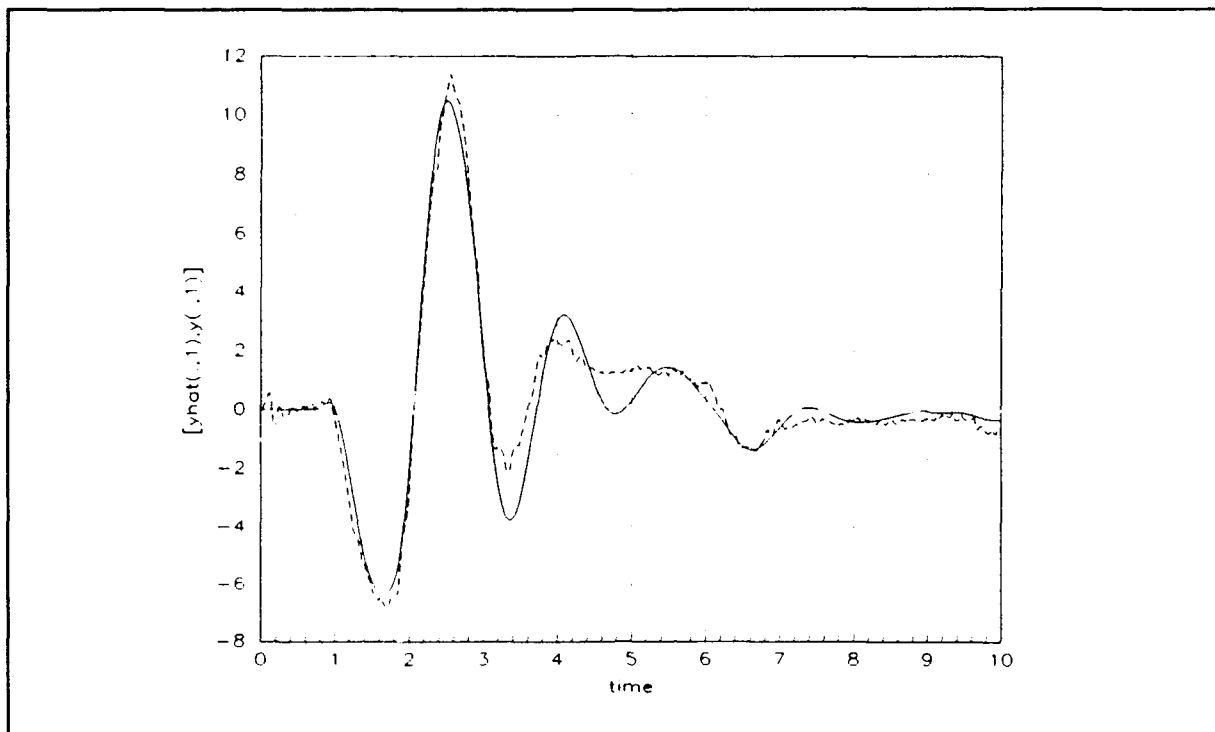


Figure B.1. Angle of Attack Data Fit for the First Pitch Doublet Maneuver (half flaps, full throttle) on the First Flight Test.

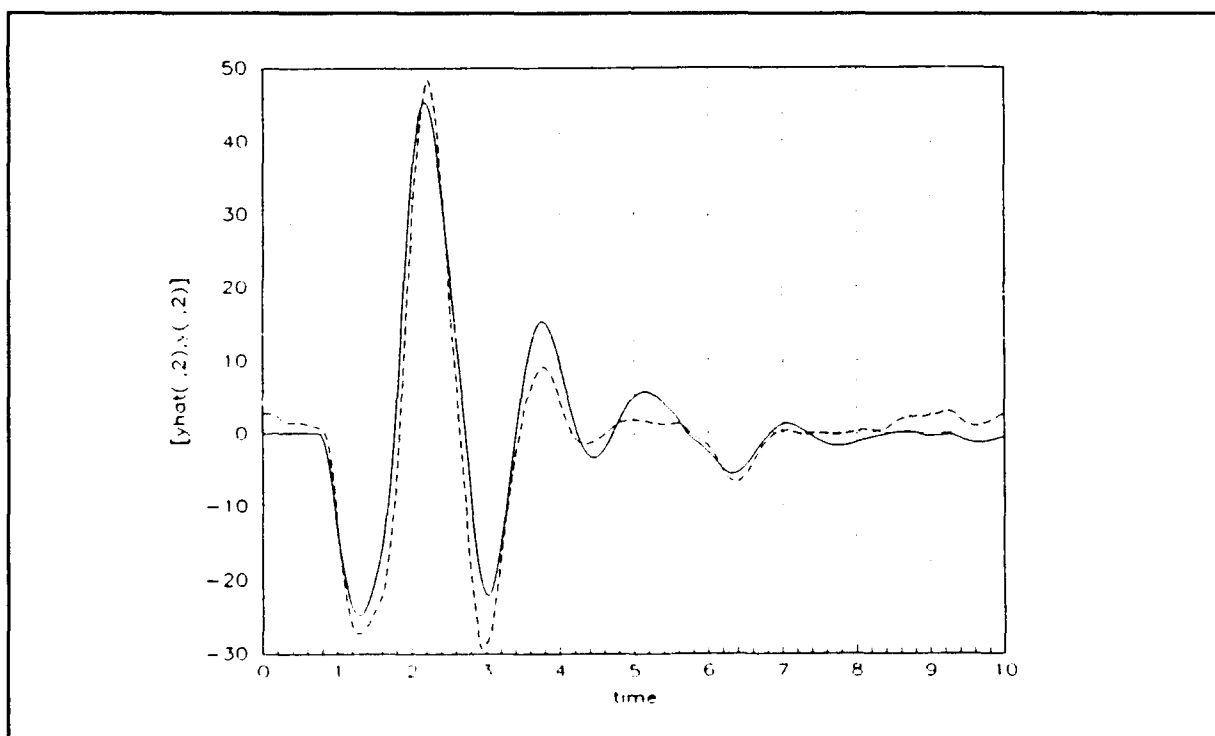


Figure B.2. Pitch Rate Data Fit for the First Pitch Doublet Maneuver (half flaps, full throttle) on the First Flight Test.

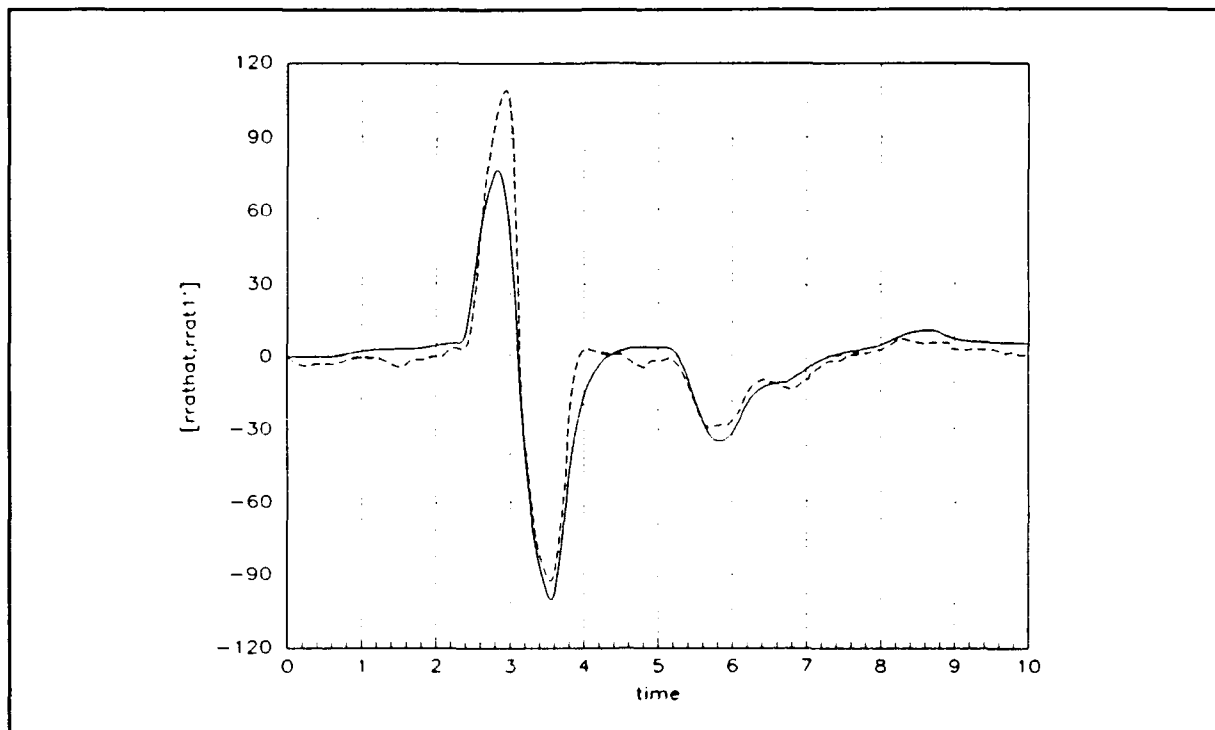


Figure B.3. Roll Rate Data Fit for the First Roll Doublet Maneuver (zero flaps, full throttle) on the First Flight Test.

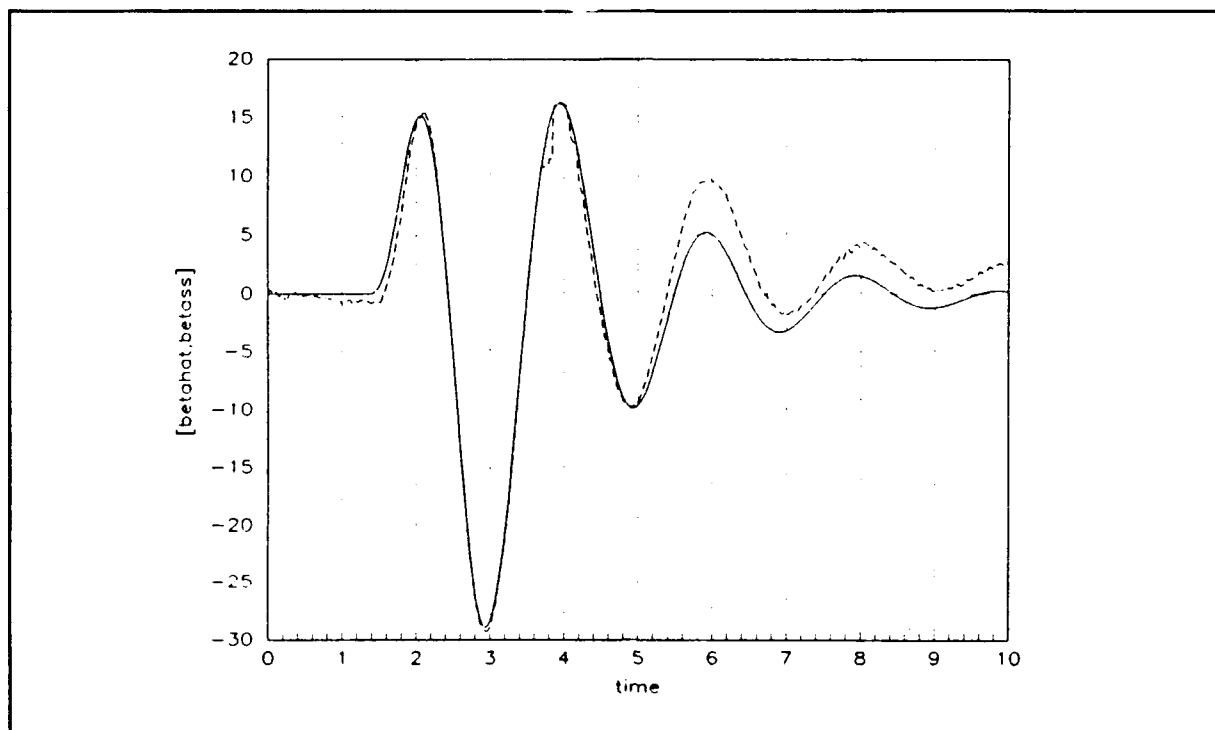


Figure B.4. Angle of Sideslip Data Fit for the First Yaw Doublet Maneuver (zero flaps, full throttle) on the First Flight Test.

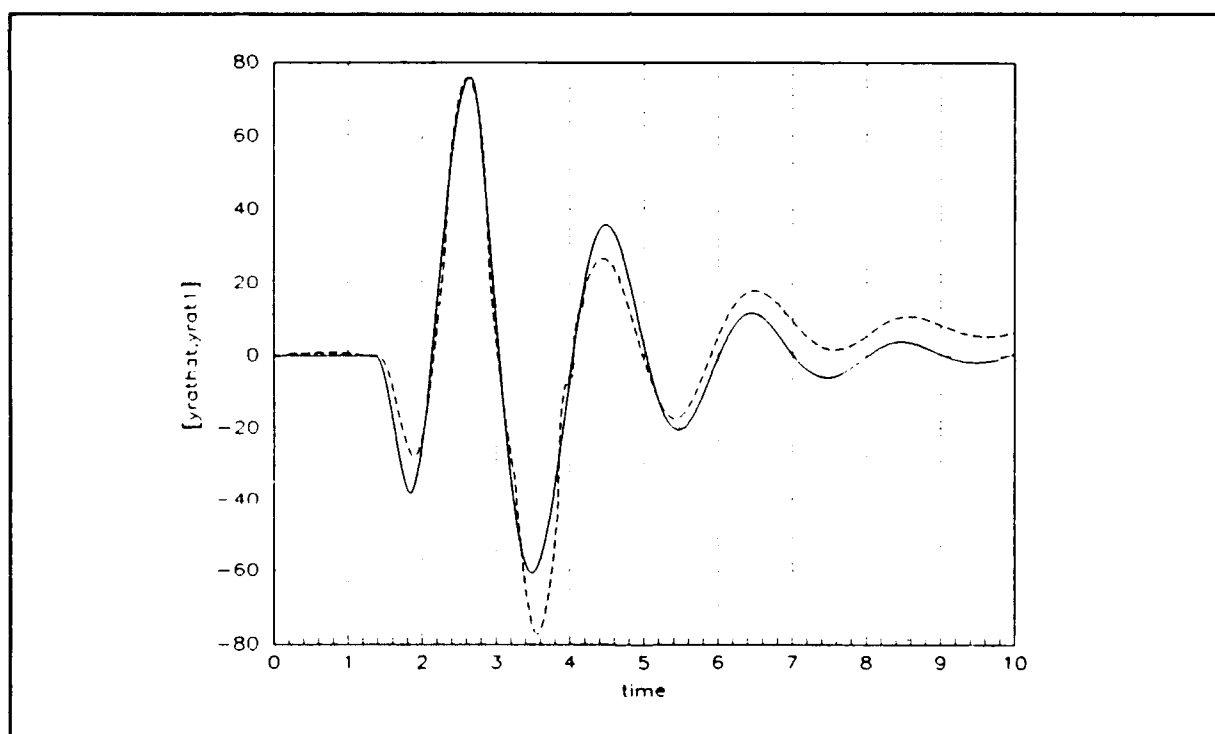


Figure B.5. Yaw Rate Data Fit for the First Yaw Doublet Maneuver (zeros flaps, full throttle) on the First Flight Test.

Appendix C:

Comparison of Actual Flight Test Data to the State Vector Time Responses Estimated by the Final Small Perturbation Model.

This appendix presents examples of the final small perturbation model's approximation of the state vector time responses compared to the actual flight test data for each type of flight test maneuver conducted. All data presented will be for the doublet maneuvers at zero flaps and full throttle from the first day of flight testing.

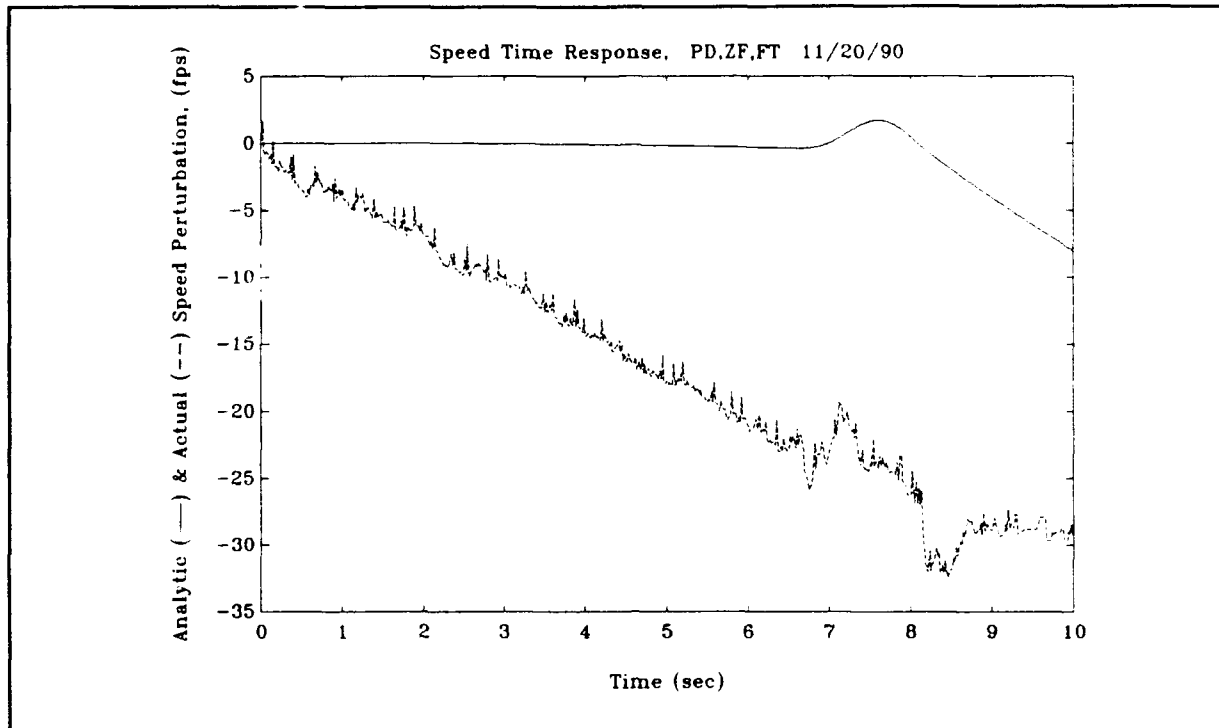


Figure C.1. Actual and Predicted Speed Time History for the Pitch Doublet Maneuver (zero flaps, full throttle).

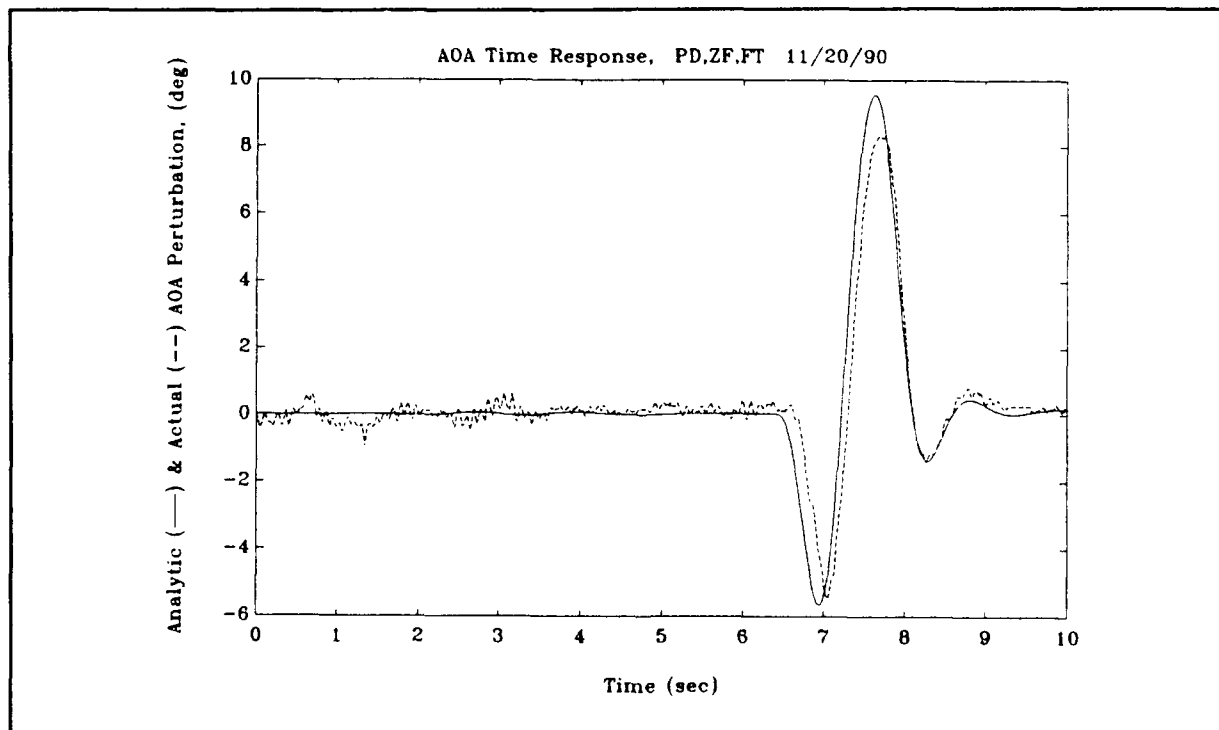


Figure C.2. Actual and Predicted Angle of Attack Time History for the Pitch Doublet Maneuver (zero flaps, full throttle).

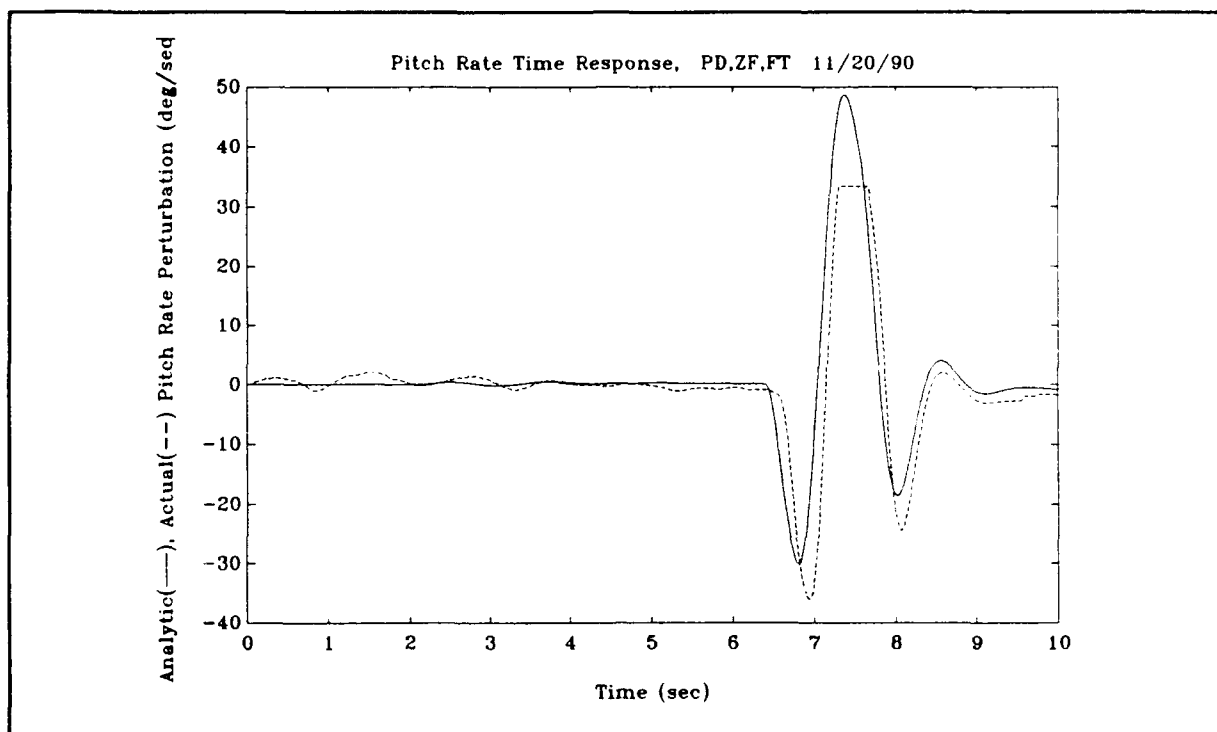


Figure C.3. Actual and Predicted Pitch Rate Time History for the Pitch Doublet Maneuver (zero flaps, full throttle).

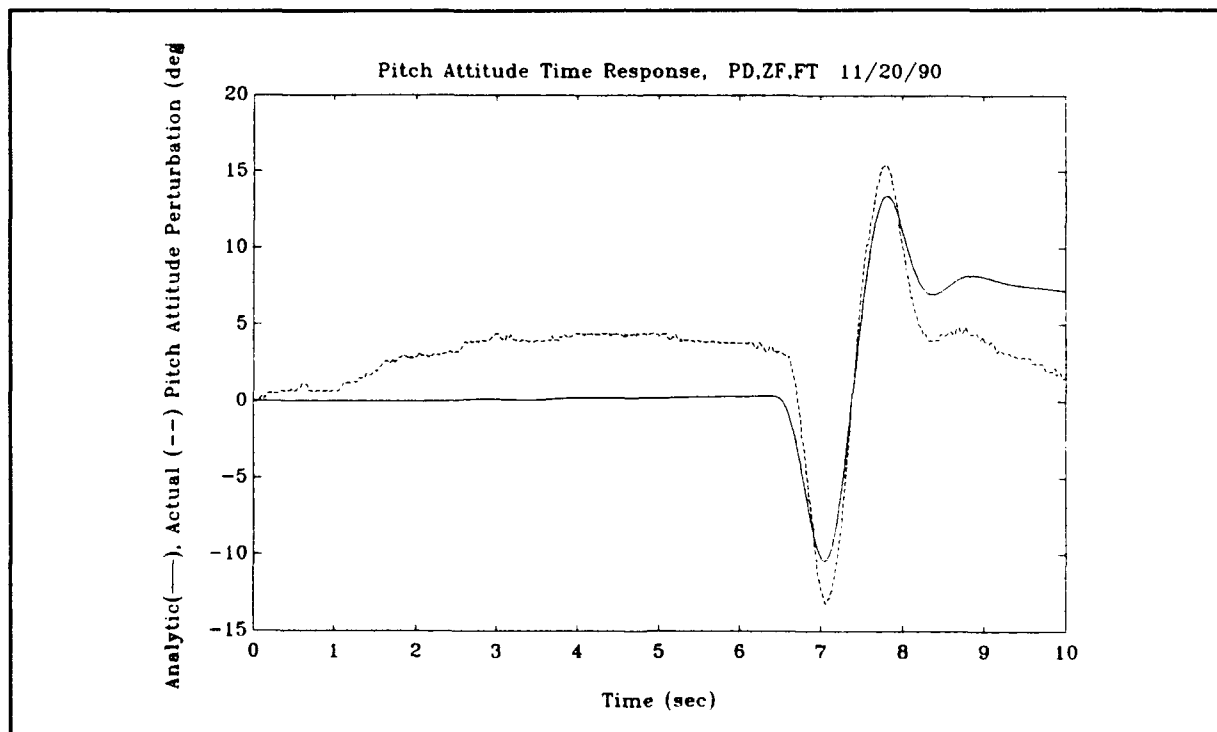


Figure C.4. Actual and Predicted Pitch Angle Time History for the Pitch Doublet Maneuver (zero flaps, full throttle).

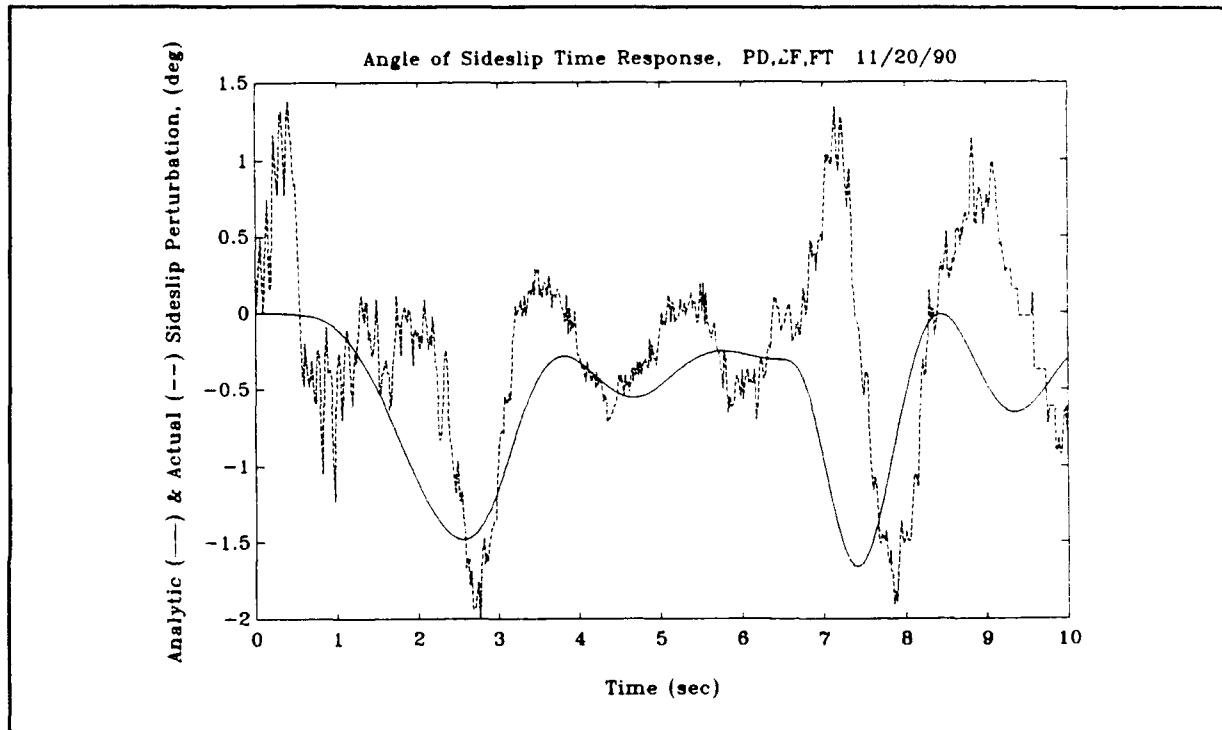


Figure C.5. Actual and Predicted Angle of Sideslip Time History for the Pitch Doublet Maneuver (zero flaps, full throttle).

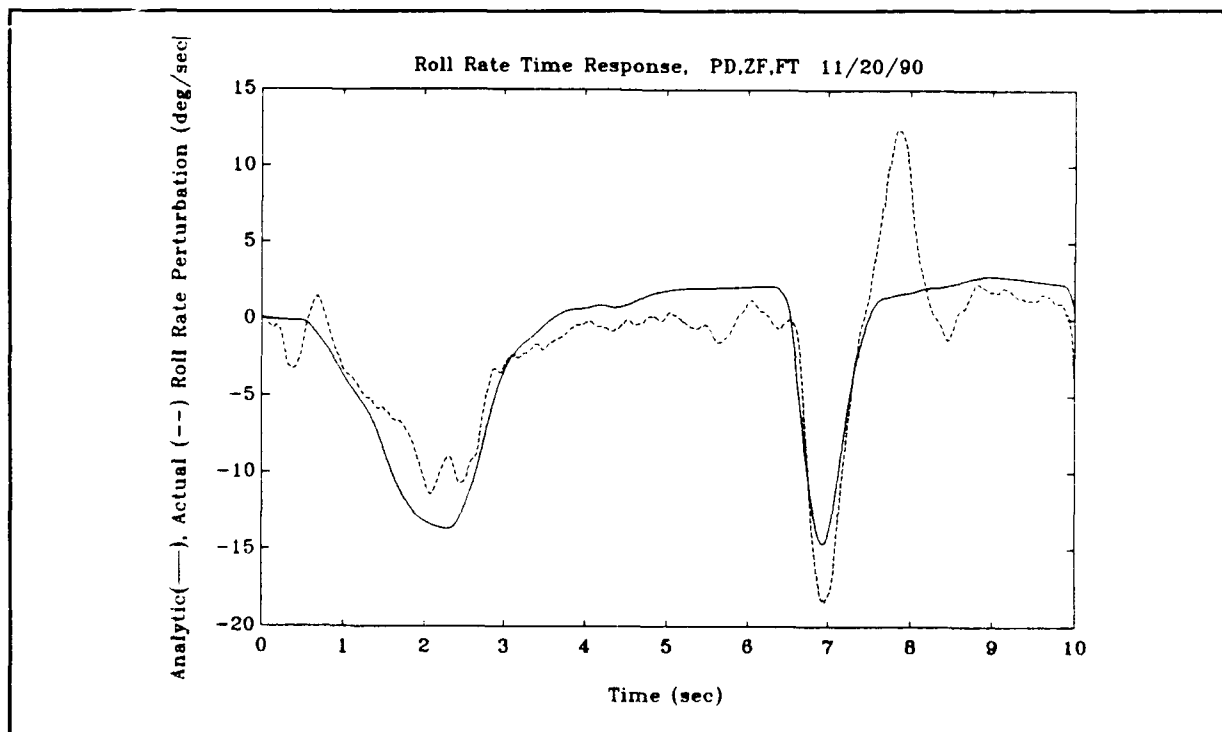


Figure C.6. Actual and Predicted Roll Rate Time History for the Pitch Doublet Maneuver (zero flaps, full throttle).

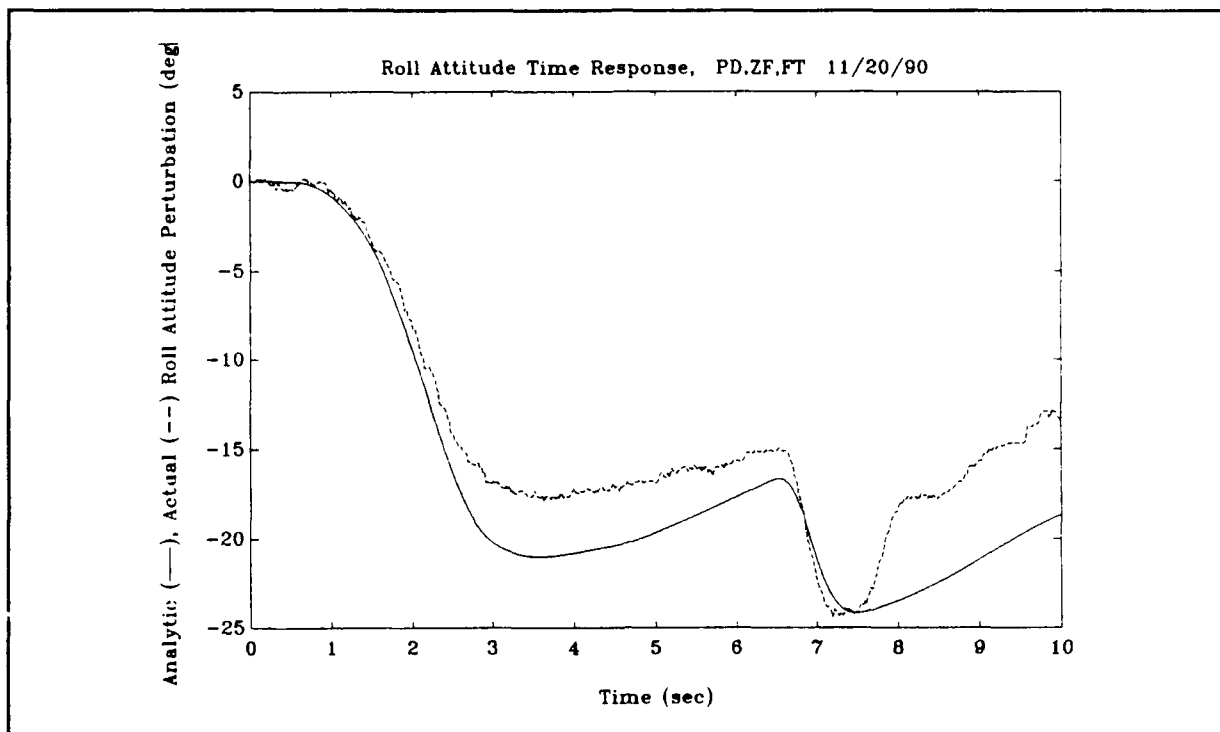


Figure C.7. Actual and Predicted Roll Attitude Time History for the Pitch Doublet Maneuver (zero flaps, full throttle).

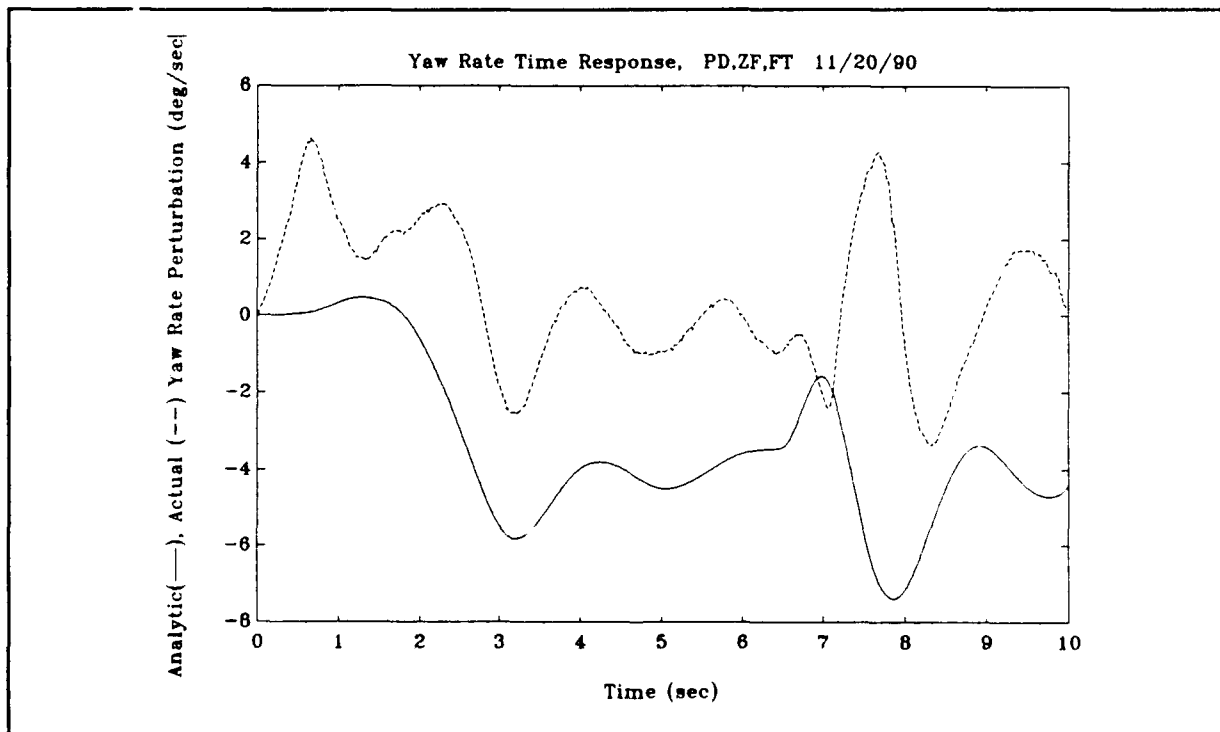


Figure C.8. Actual and Predicted Yaw Rate Time History for the Pitch Doublet Maneuver (zero flaps, full throttle).

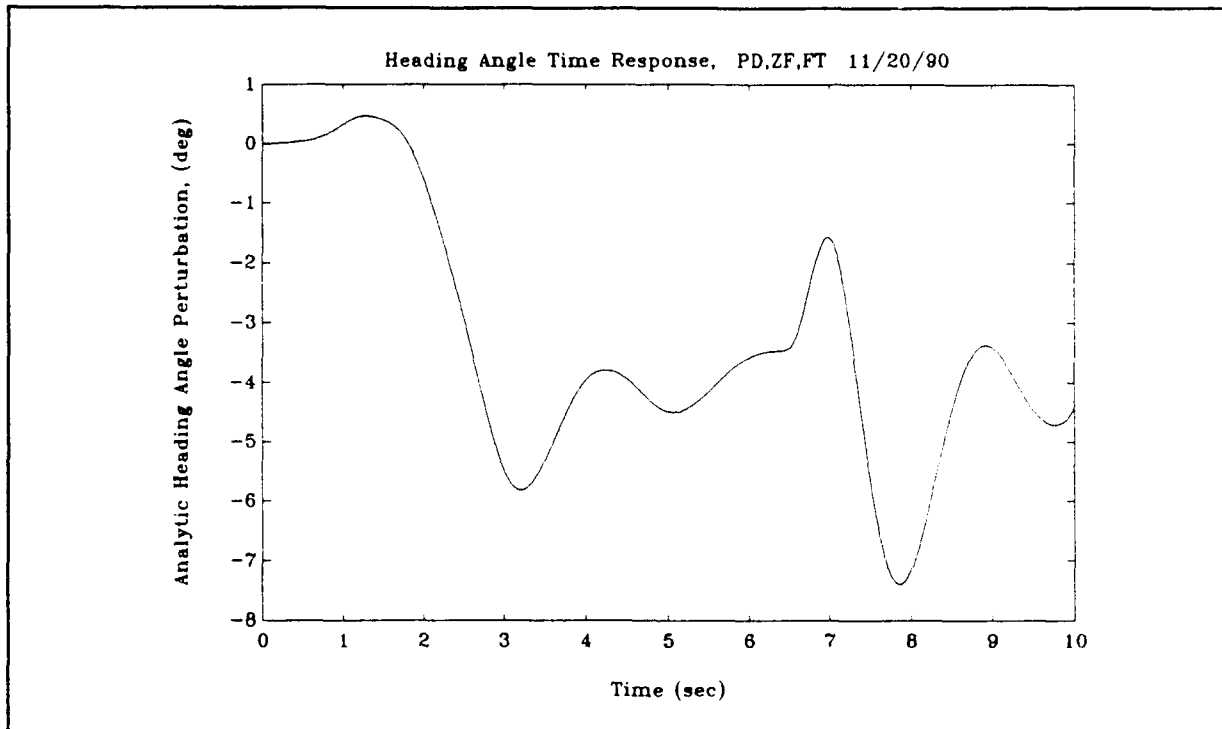


Figure C.9. Predicted Heading Angle Time History for the Pitch Doublet Maneuver (zero flaps, full throttle).

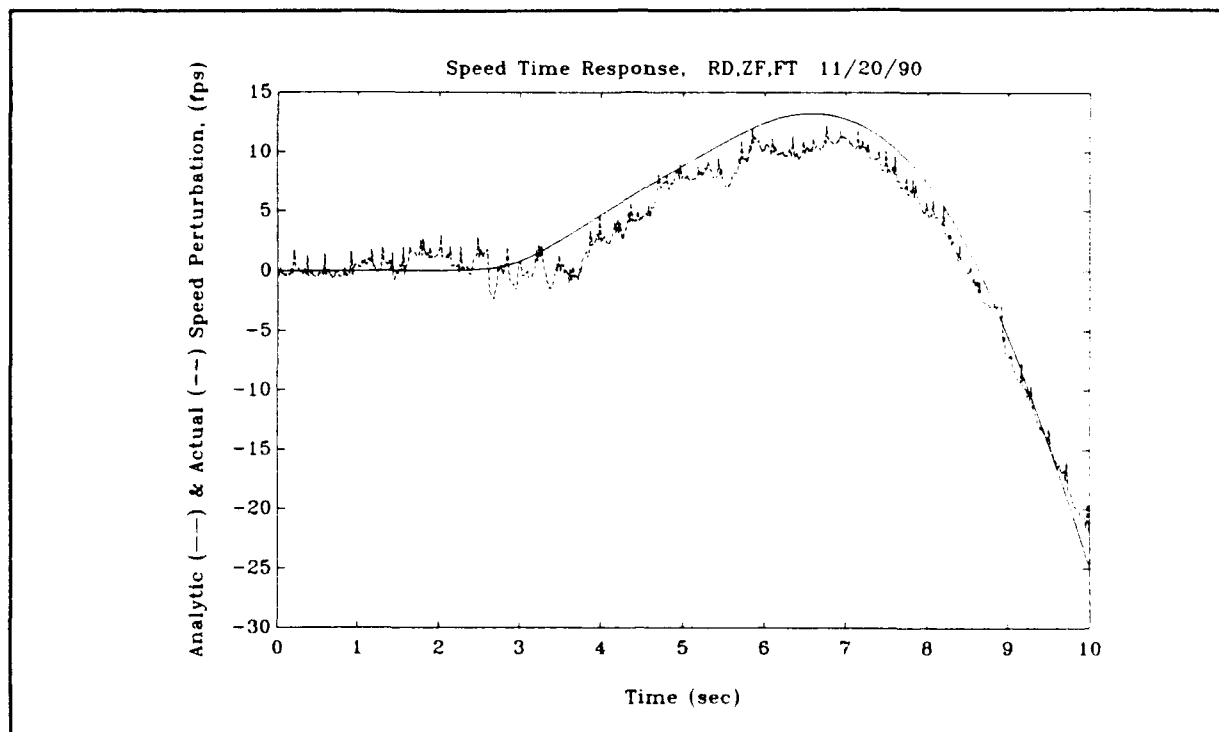


Figure C.10. Actual and Predicted Speed Time History for the Roll Doublet Maneuver (zero flaps, full throttle).

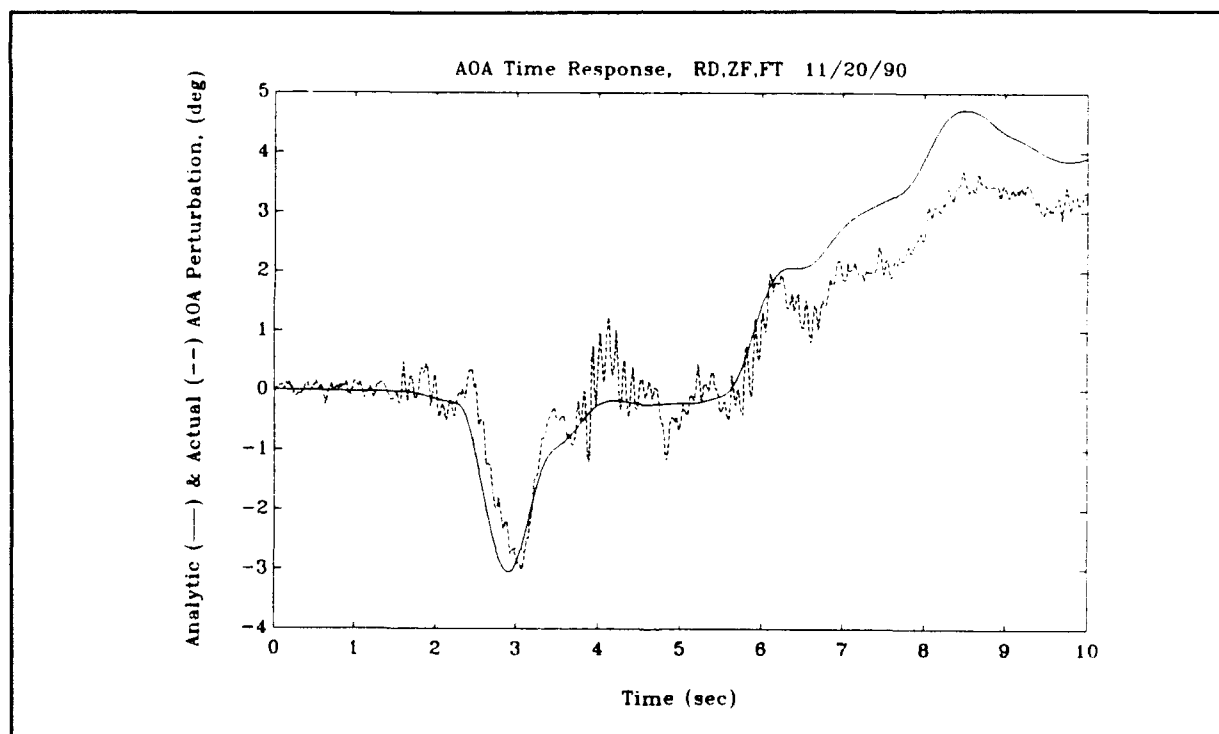


Figure C.11. Actual and Predicted Angle of Attack Time History for the Roll Doublet Maneuver (zero flaps, full throttle).

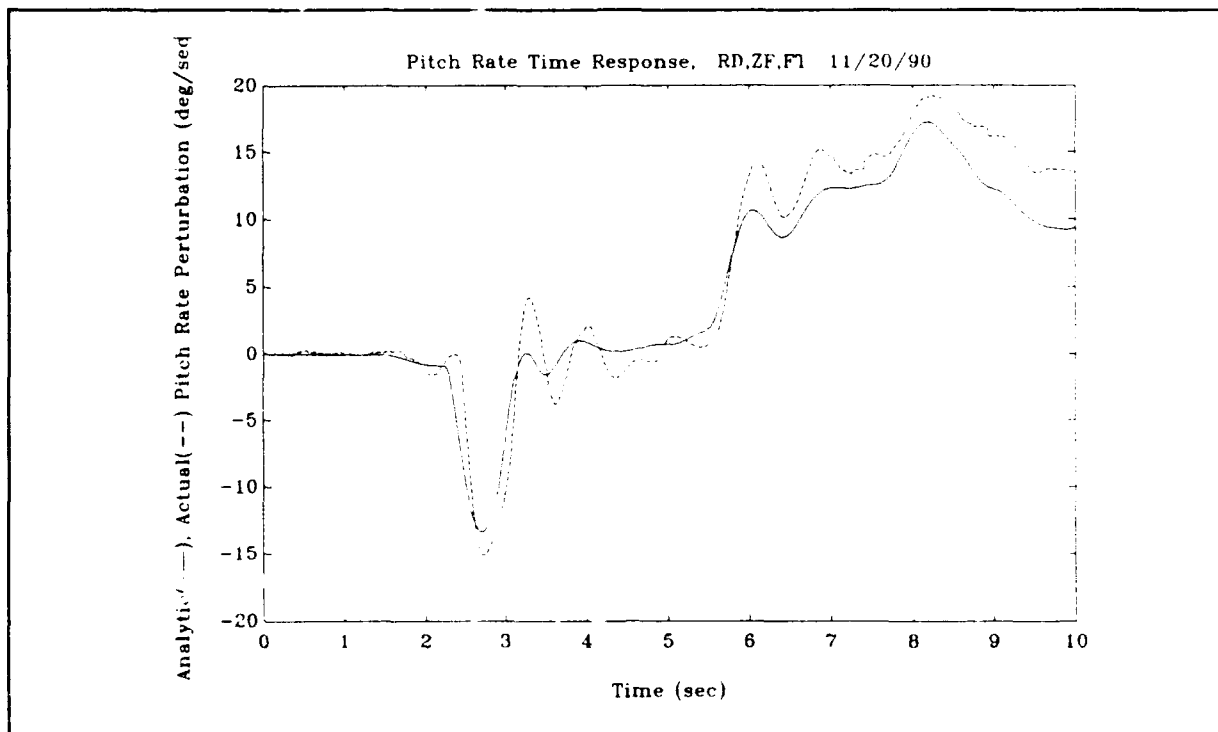


Figure C.12. Actual and Predicted Pitch Rate Time History for the Roll Doublet Maneuver (zero flaps, full throttle).

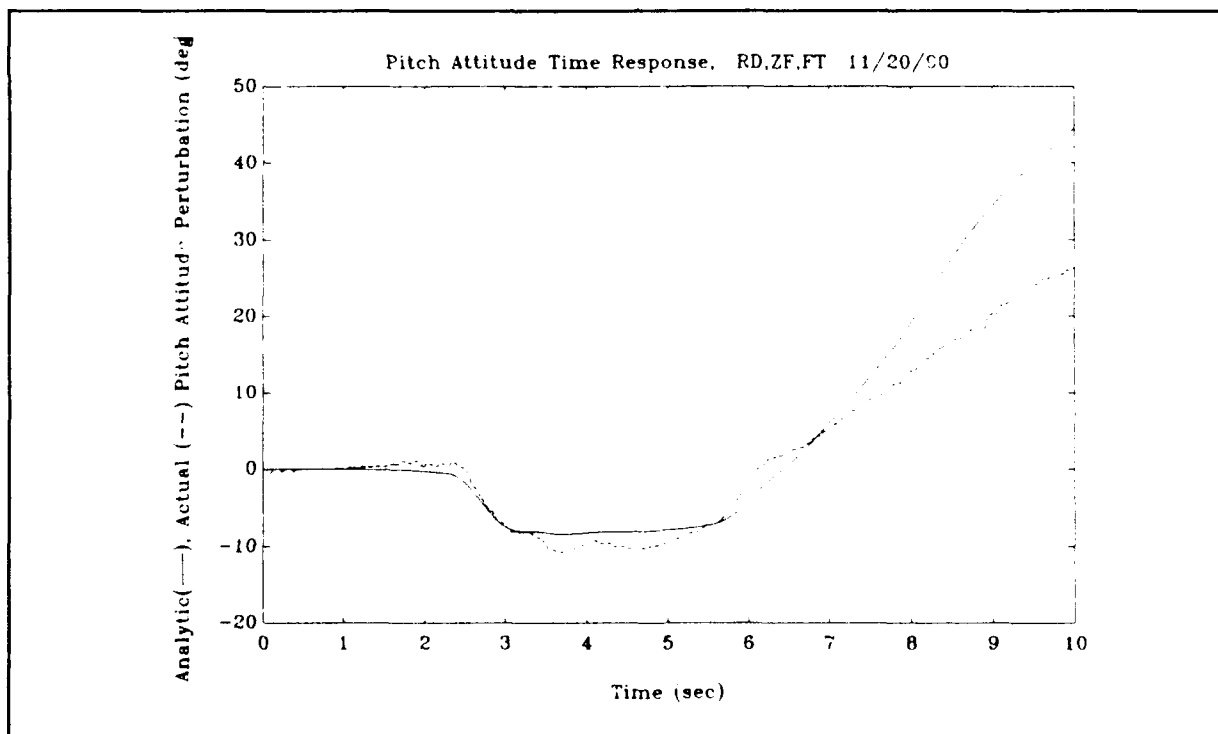


Figure C.13. Actual and Predicted Pitch Attitude Time History for the Roll Doublet Maneuver (zero flaps, full throttle).

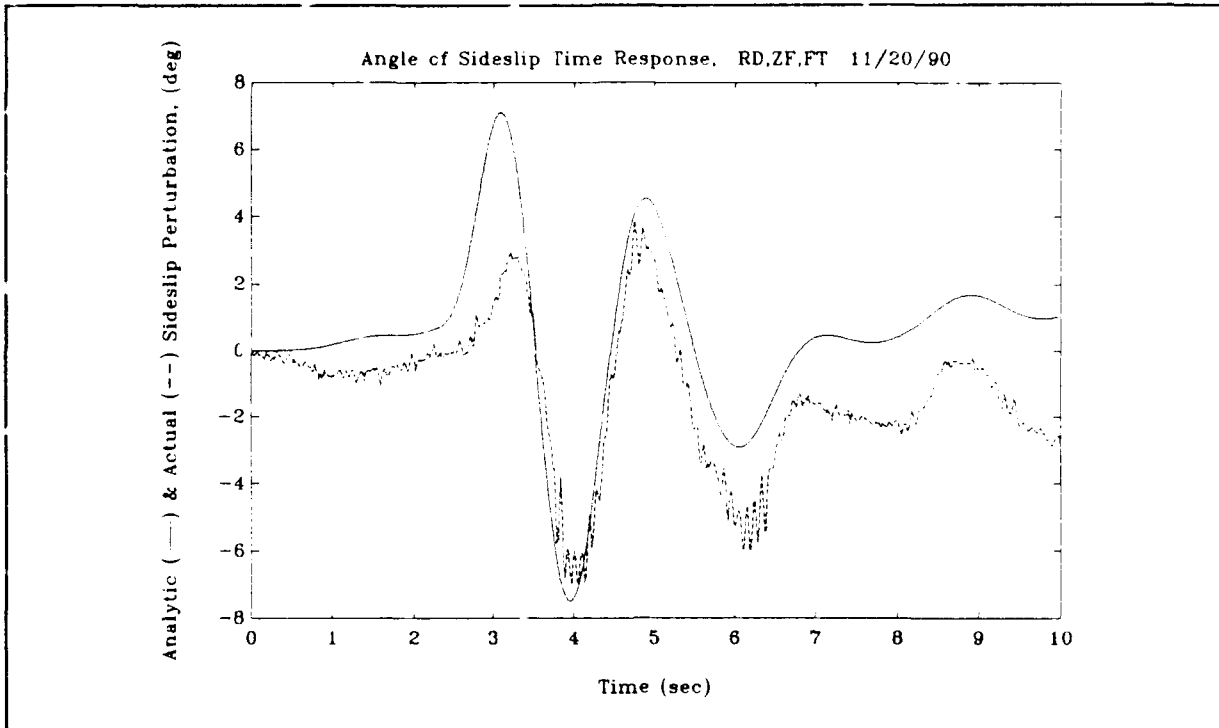


Figure C.14. Actual and Predicted Angle of Sideslip Time History for the Roll Doublet Maneuver (zero flaps, full throttle).

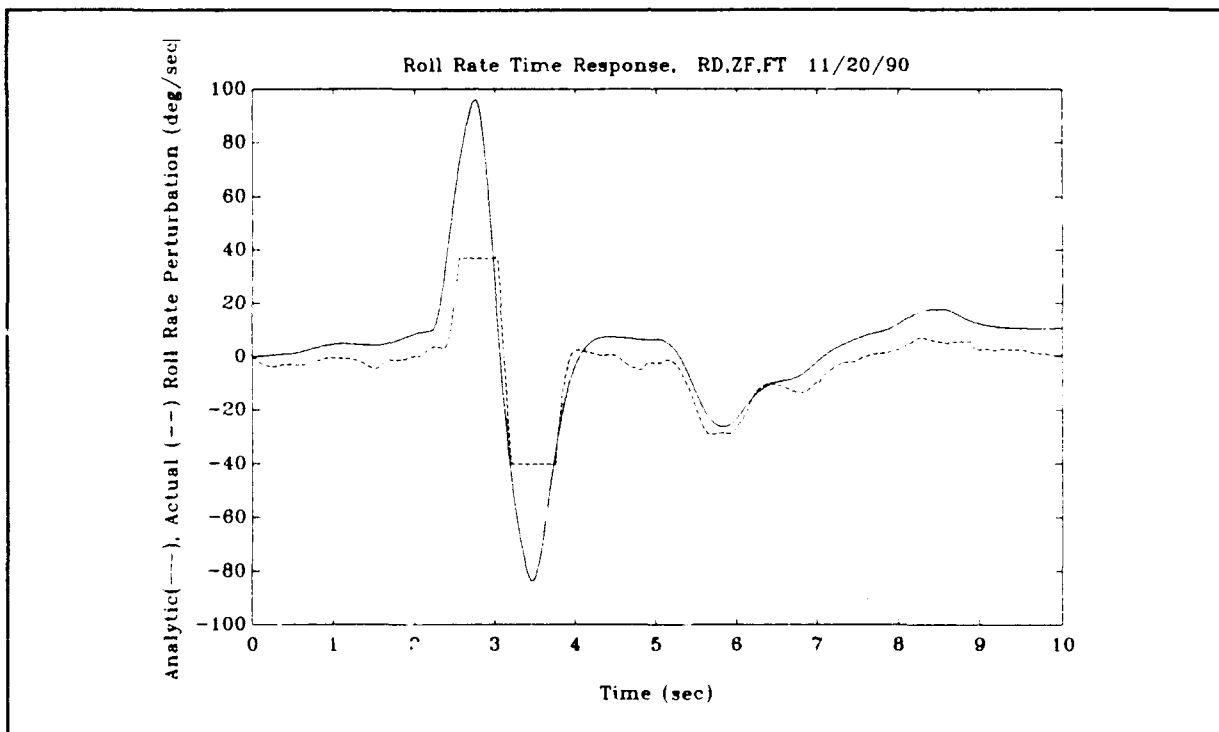


Figure C.15. Actual and Predicted Roll Rate Time History for the Roll Doublet Maneuver (zero flaps, full throttle).

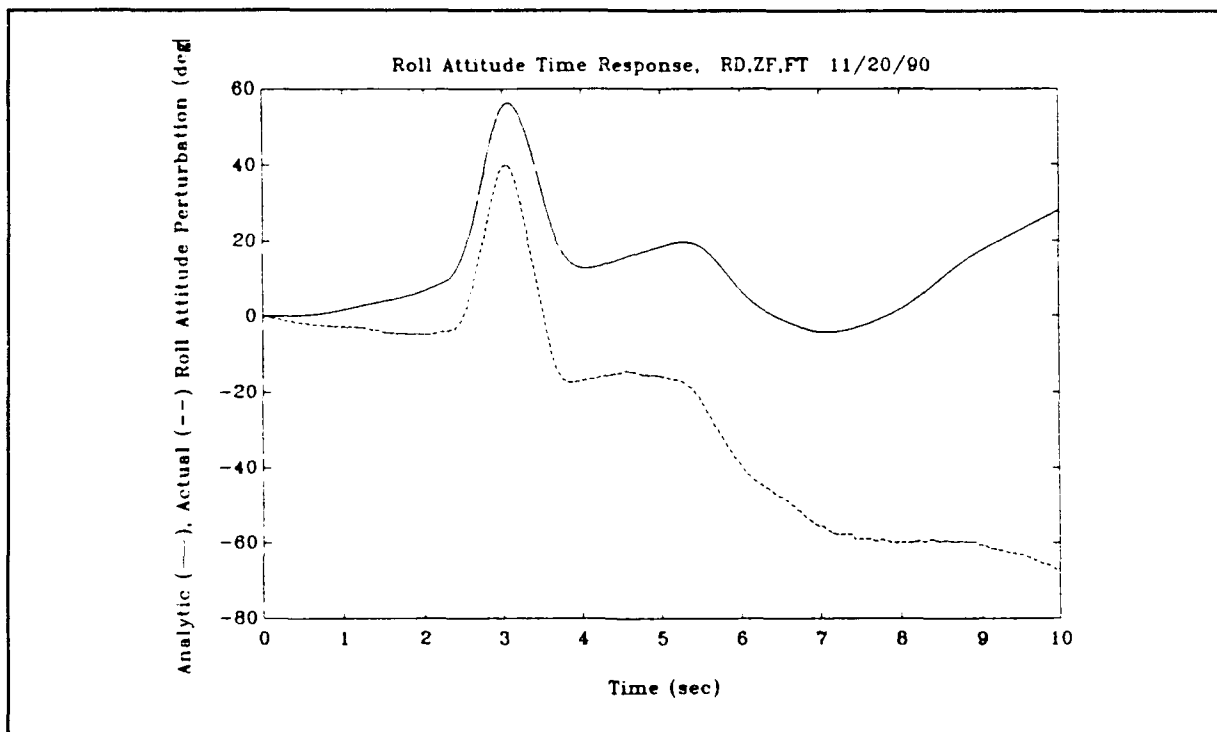


Figure C.16. Actual and Predicted Roll Attitude Time History for the Roll Doublet Maneuver (zero flaps, full throttle).

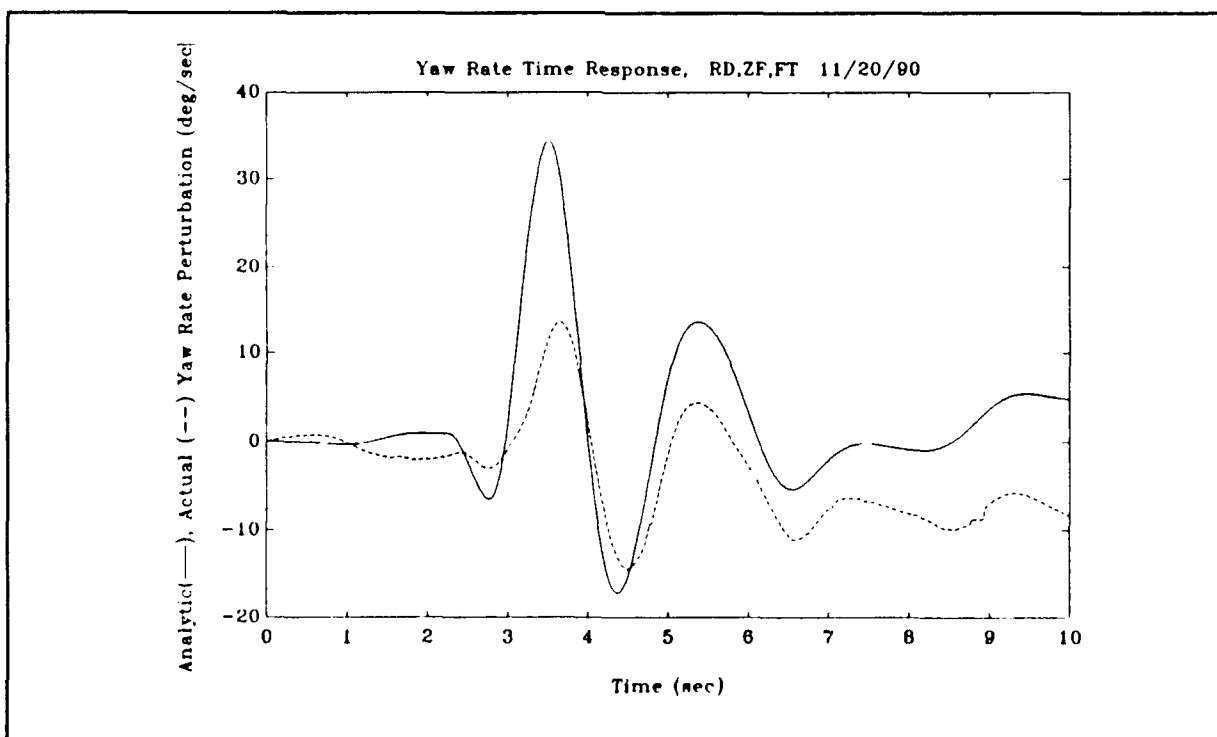


Figure C.17. Actual and Predicted Yaw Rate Time History for the Roll Doublet Maneuver (zero flaps, full throttle).

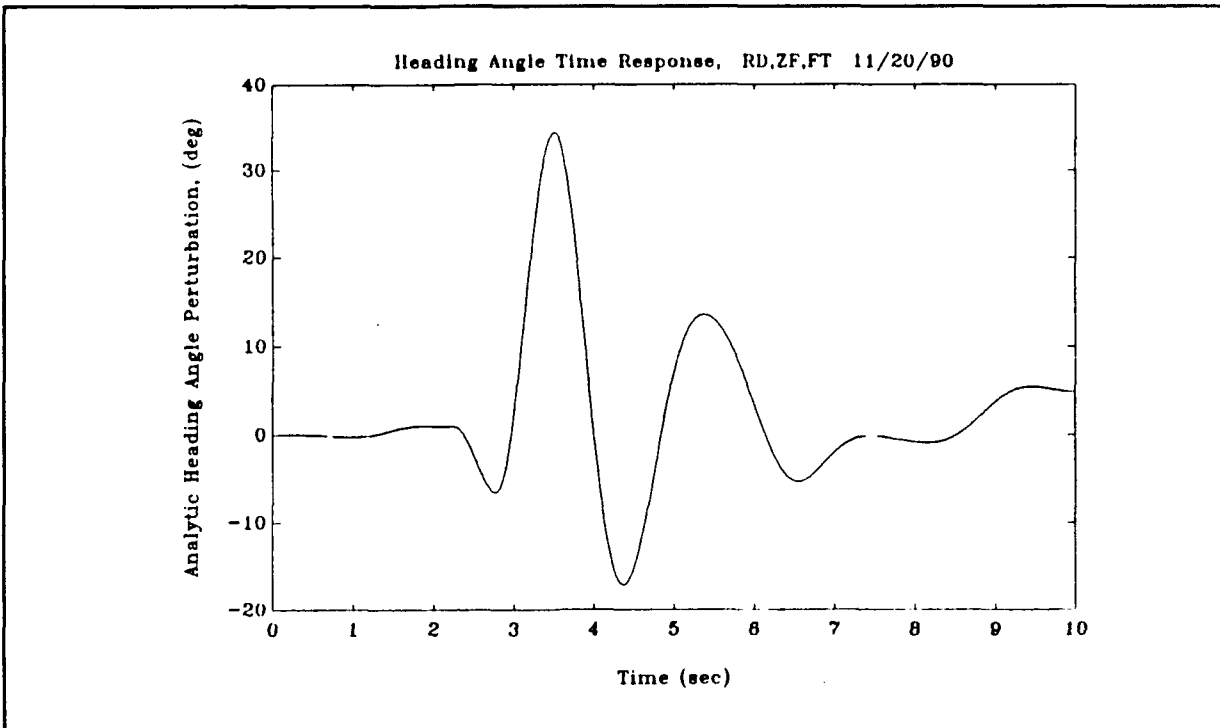


Figure C.18. Predicted Heading Angle Time History for the Roll Doublet Maneuver (zero flaps, full throttle).

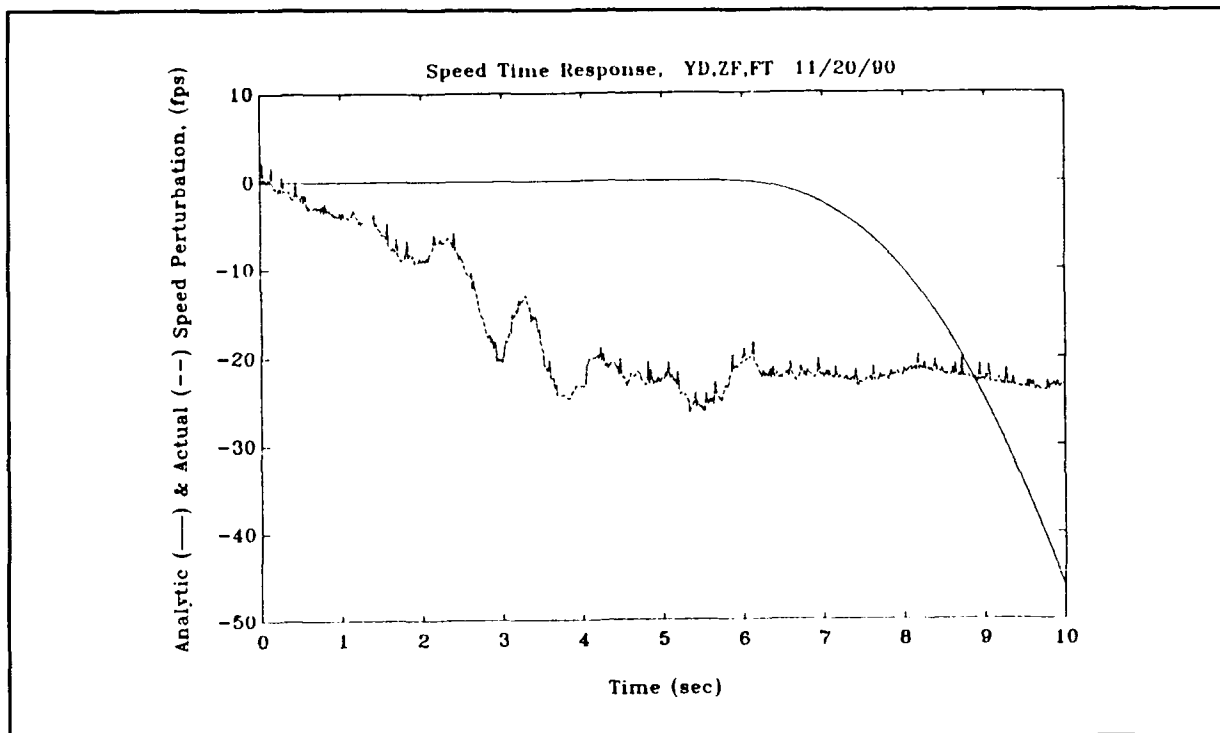


Figure C.19. Actual and Predicted Speed Time History for the Yaw Doublet Maneuver (zero flaps, full throttle).

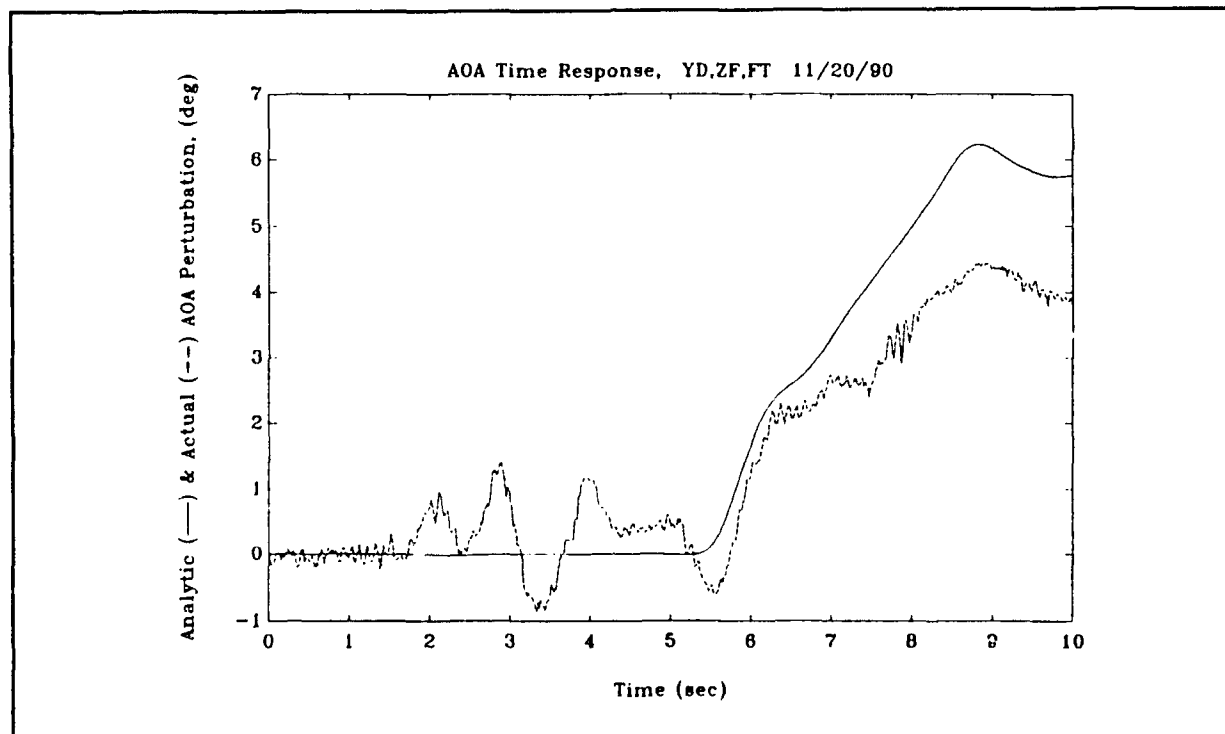


Figure C.20. Actual and Predicted Angle of Attack Time History for the Yaw Doublet Maneuver (zero flaps, full throttle).

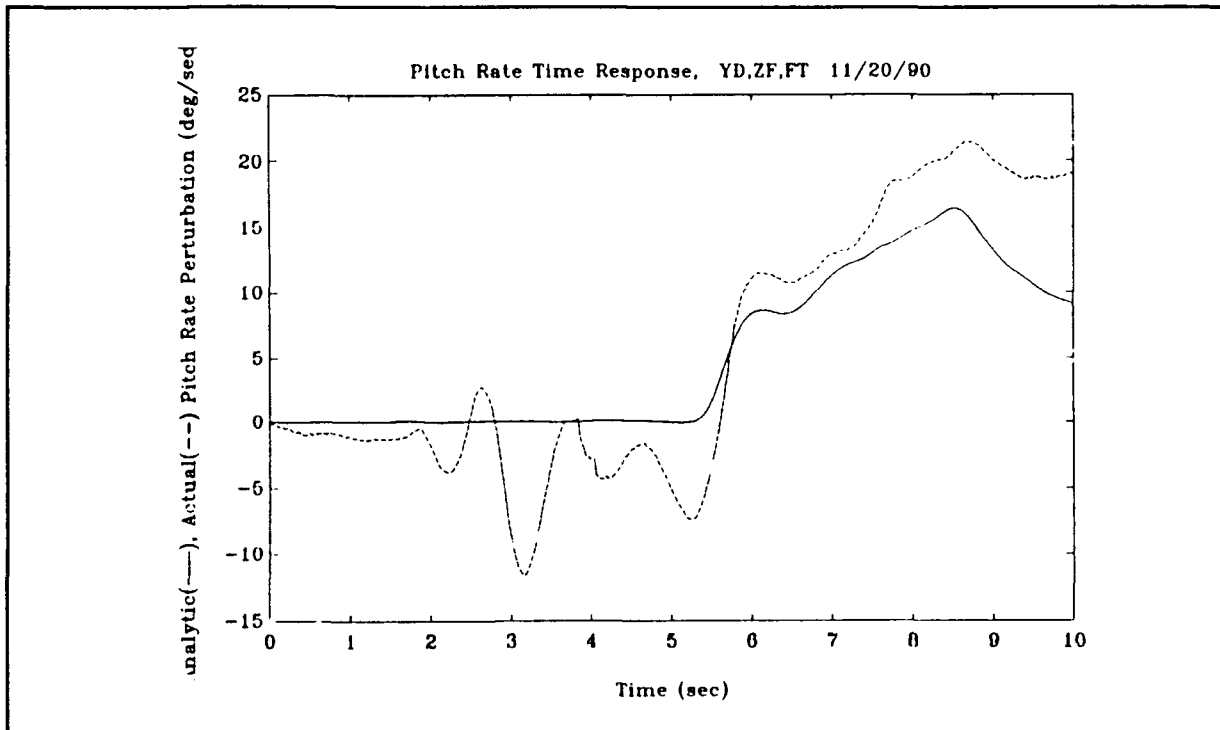


Figure C.21. Actual and Predicted Pitch Rate Time History for the Yaw Doublet Maneuver (zero flaps, full throttle).

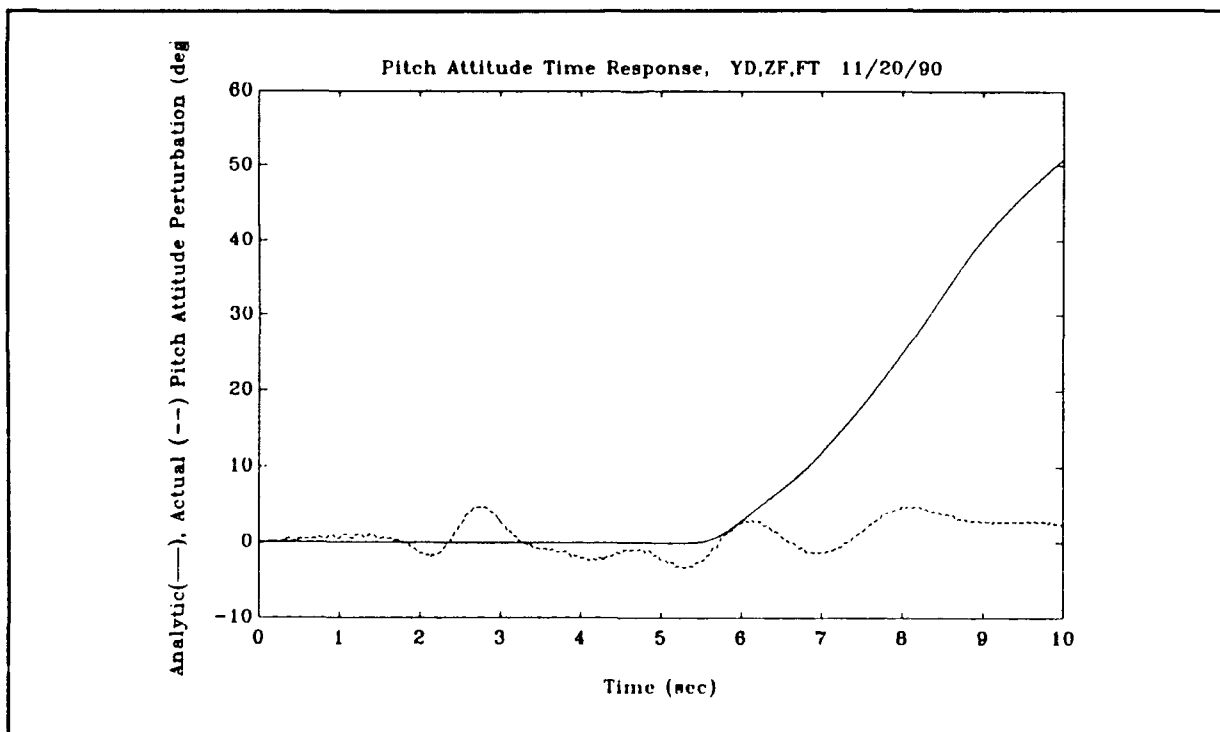


Figure C.22. Actual and Predicted Pitch Attitude Time History for the Yaw Doublet Maneuver (zero flaps, full throttle).

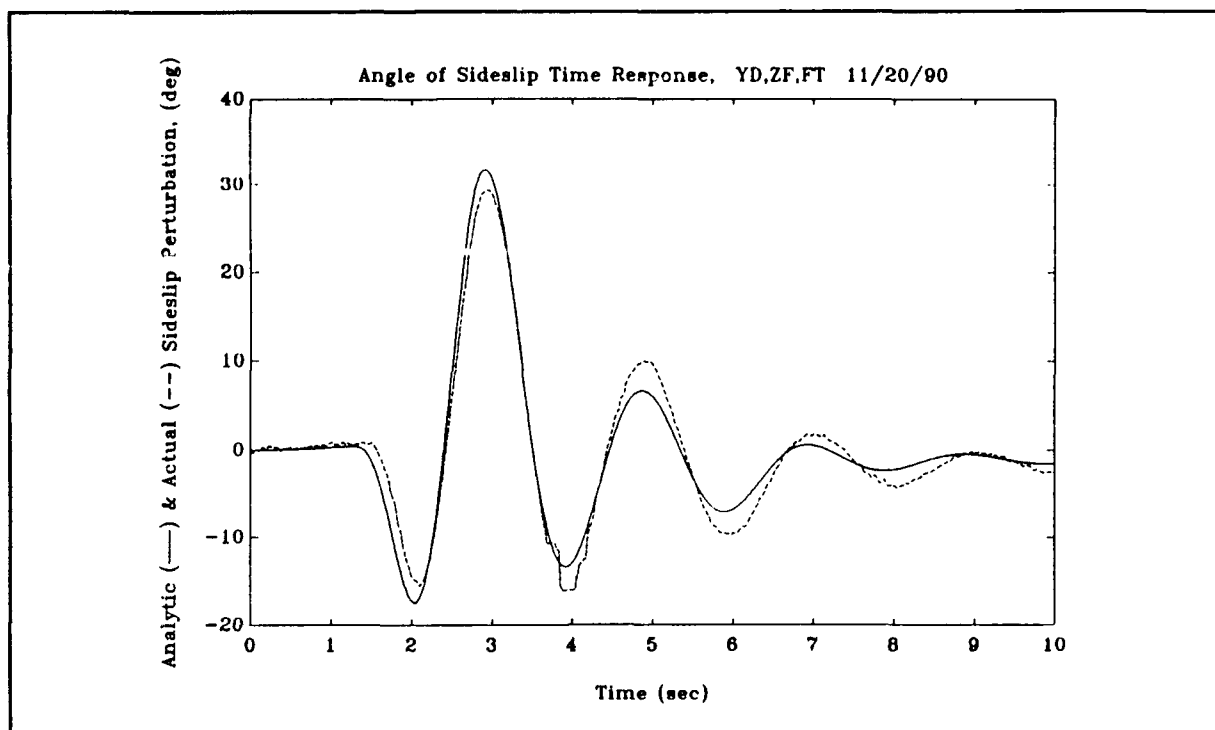


Figure C.23. Actual and Predicted Angle of Sideslip Time History for the Yaw Doublet Maneuver (zero flaps, full throttle).

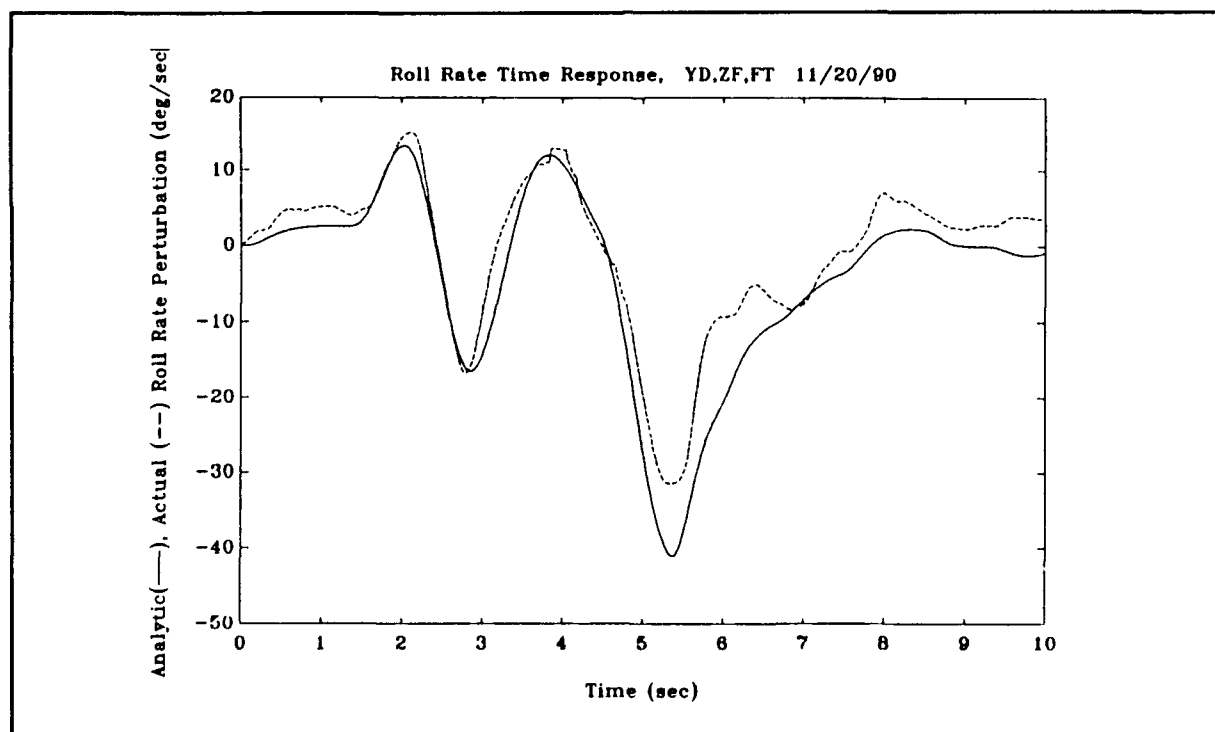


Figure C.24. Actual and Predicted Roll Rate Time History for the Yaw Doublet Maneuver (zero flaps, full throttle).

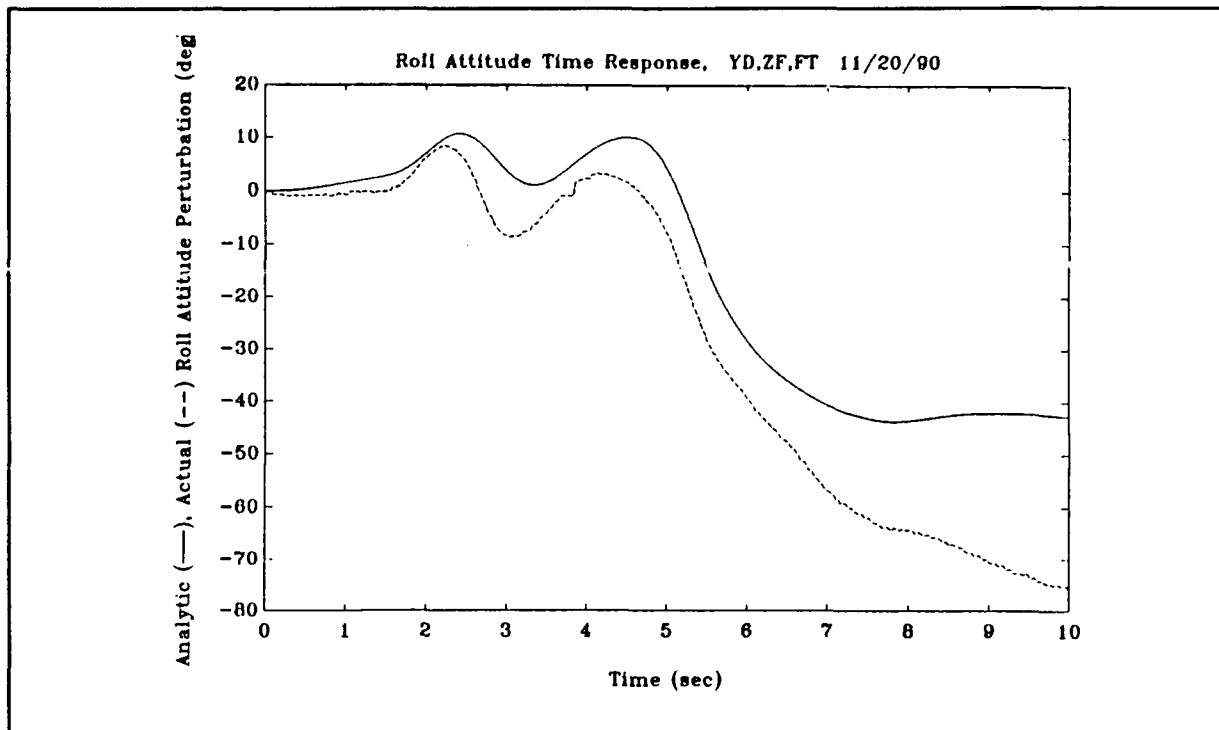


Figure C.25. Actual and Predicted Roll Attitude Time History for the Yaw Doublet Maneuver (zero flaps, full throttle).

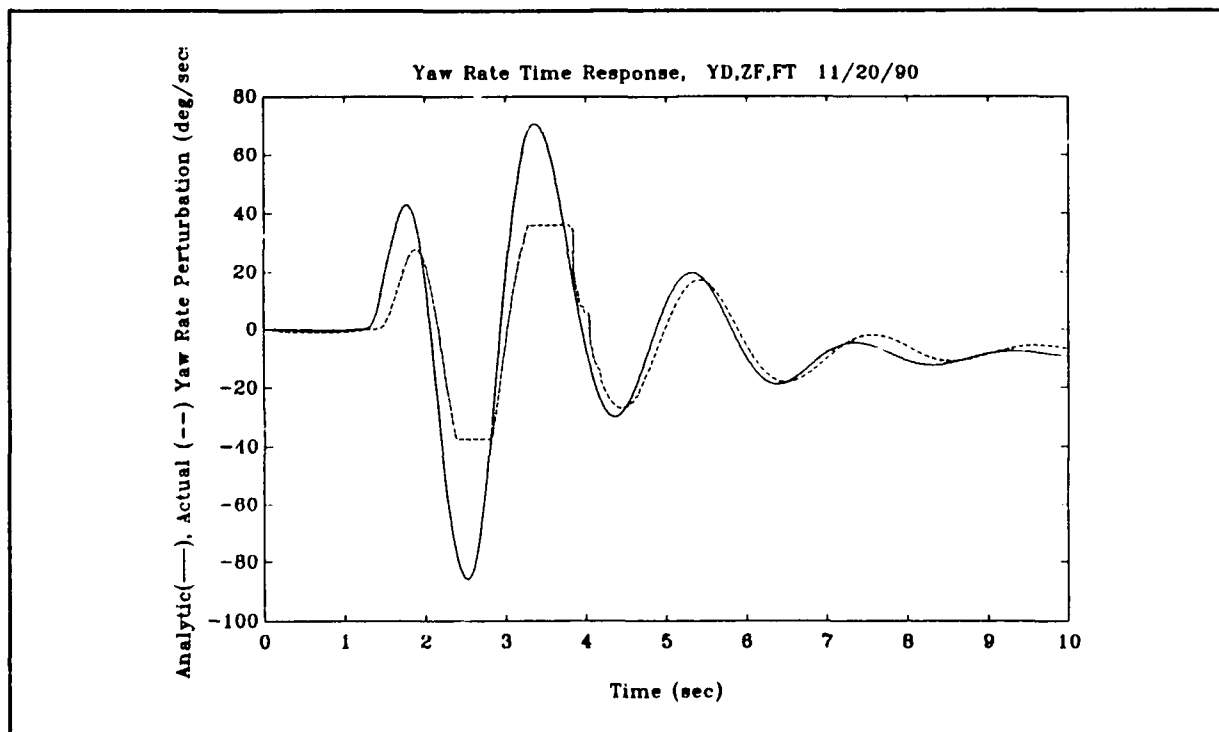


Figure C.26. Actual and Predicted Yaw Rate Time History for the Yaw Doublet Maneuver (zero flaps, full throttle).

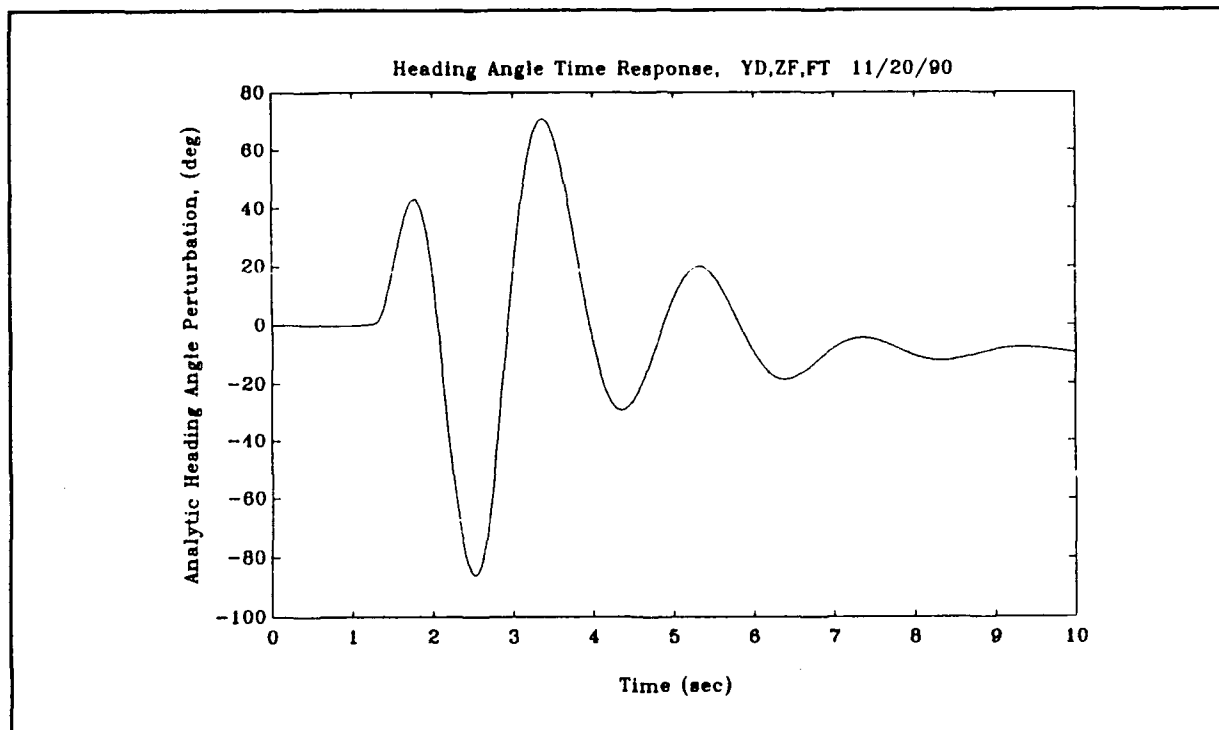


Figure C.27. Predicted Heading Angle Time History for the Yaw Doublet Maneuver (zero flaps, full throttle).

Appendix D:

Linear, State Space, Small Perturbation
Matlab Model: DERCALC.M.

This appendix presents the Matlab program, DERCALC.M, that calculates the linear, state space, small perturbation model (both longitudinal and lateral directional) for Lambda. Center of gravity location, trimmed flight speed, dynamic pressure, vehicle weight, and trimmed pitch angle are the only inputs required.

```

% This macro calculates the longitudinal and lateral-
% directional state space equations of motion for the
% Lambda URV given Xcg, U1, q1, W and theta.
%
% Input:  X=[Xcg,U1,q1,W,theta]
%
%   where, Xcg = inches
%           U1 = feet/second
%           q1 = pounds/sq foot
%           W = pounds
%           theta = degrees
%
% Outputs:
%
%   Clong=[CMu,CMa,CMad,CMq,CLu,CLa,CLad,CLq,CDa,CDu,
%           CLde,CDde,CMde,CLdf,CDdf,CMdf]'
%
%   Clat=[Clb,Clp,Clr,Clda,Cldr,Cnb,Cnp,Cnr,Cnda,Cndr,
%           Cyb,Cyp,Cyr,Cyda,Cydr]'
%
%   Dlong = corresponding vector of dimensional derivatives for
%           Clong
%
%   Dlat = corresponding vector of dimensional derivatives for
%           Clat
%
%   Along = A matrix for longitudinal equations of motion
%
%   Alat = A matrix for lateral-directional equations of motion
%
%   Blong = B matrix for longitudinal equations of motion
%
%   Blat = B matrix for lateral-directional equations of motion
%
CMu=0;
CMa=0.326643*X(1,1)-16.5189;
CMad=0.238235*X(1,1)-7.8977;
CMq=0.628420*X(1,1)-45.0582;
CLu=-0.0001719*X(1,1)+0.01518;
CLa=5.820;
CLad=-0.03838*X(1,1)+3.83508;
CLq=-0.65202*X(1,1)+37.8884;
CDa=0;
CDu=0;
CLde=0.2908;
CDde=0;
CMde=0.013464*X(1,1)-1.48039;
CLdf=1.419;
CDdf=0.08489;
CMdf=0.070932*X(1,1)-3.63838;

```

```

Clong1=[CMu,CMa,CMad,CMq,CLu,CLa,CLad,CLq,CDa,CDu];
Clong2=[CLde,CDde,CMde,CLdf,CDdf,CMdf];
Clong=[Clong1,Clong2]';
%
Clb=-0.01451;
Clp=-0.5538;
Clr=0.08763;
Clda=0.2608;
Cldr=0.000213*X(1,1)-0.00783;
Cnb=-0.00038*X(1,1)+0.07834;
Cnp=-0.03601;
Cnr=0.003087*X(1,1)-0.31072;
Cnda=-0.01368;
Cndr=0.001633*X(1,1)-0.15208;
Cyb=-0.4372;
Cyp=-0.001600;
Cyr=-0.00424*X(1,1)+0.46047;
Cyda=0;
Cydr=0.2865;
Clat=[Clb,Clp,Clr,Clda,Cldr,Cnb,Cnp,Cnr,Cnda,Cndr,Cyb,Cyp,Cyr,...
      Cyda,Cydr]';
%
% Calculation of Dimensional Derivatives
%
% Dlong=[Mu,Ma,Mad,Mq,Zu,Za,Zad,Zq,Xa,Xu,Zde,Xde,Mde,Zdf,...
%       Xdf,Mdf]';
%
% Dlat=[Lb,Lp,Lr,Lda,Ldr,Nb,Np,Nr,Nda,Ndr,Yb,Yp,Yr,Yda,Ydr]';
%
xcg=X(1,1);
u=X(1,2);
q=X(1,3);
m=X(1,4)/32.174;
s=21.1;
c=1.51;
b=14.07;
Ixx=32.502;
Iyy=26.666;
Izz=40.939;
Ixz=0.5922;
CL1=X(1,4)/(q*s);
CD1=0.027;
CM1=0.0;
A1=Ixz/Ixx;
B1=Ixz/Izz;
%

```

```

Mu=q*s*c*(CMu+2*CM1)/(Iyy*u);
Ma=q*s*c*CMA/Iyy;
Mad=q*s*c*c*CMad/(2*Iyy*u);
Mq=q*s*c*c*CMq/(2*Iyy*u);
Zu=-q*s*(CLu+2*CL1)/(m*u);
Za=-q*s*(CLa+CD1)/m;
Zad=-q*s*c*CLad/(2*m*u);
Zq=-q*s*c*CLq/(2*m*u);
Xu=-q*s*(CDu+2*CD1)/(m*u);
Xa=-q*s*(CDA-CL1)/m;
Zde=-q*s*CLde/m;
Xde=-q*s*CDde/m;
Mde=q*s*c*CMde/Iyy;
Zdf=-q*s*CLdf/m;
Xdf=-q*s*CDdf/m;
Mdf=q*s*c*CMdf/Iyy;
Dlong=[Mu, Ma, Mad, Mq, Zu, Za, Zad, Zq, Xa, Xu, Zde, Xde, Mde, Zdf, Xdf, Mdf]';
%
Lb=q*s*b*Clb/Ixx;
Lp=q*s*b*b*Clp/(2*Ixx*u);
Lr=q*s*b*b*Clr/(2*Ixx*u);
Lda=q*s*b*Cl da/Ixx;
Ldr=q*s*b*Cl dr/Ixx;
Nb=q*s*b*Cnb/Izz;
Np=q*s*b*b*Cnp/(2*Izz*u);
Nr=q*s*b*b*Cnr/(2*Izz*u);
Nda=q*s*b*Cnda/Izz;
Ndr=q*s*b*Cndr/Izz;
Yb=q*s*Cyb/m;
Yp=q*s*b*Cyp/(2*m*u);
Yr=q*s*b*Cyr/(2*m*u);
Yda=q*s*Cyda/m;
Ydr=q*s*Cydr/m;
Dlat=[Lb, Lp, Lr, Lda, Ldr, Nb, Np, Nr, Nda, Ndr, Yb, Yp, Yr, Yda, Ydr]';
%
% Calculation of the Longitudinal A and B matrices
%
theta=X(1,5)/57.29578;
Along=[Xu, Xa, 0, -32.174*cos(theta);
        Zu/(u-Zad), Za/(u-Zad), (u+Zq)/(u-Zad), -32.174*sin(theta);
        Mu+Mad*Zu/(u-Zad), Ma+Mad*Za/(u-Zad), ...
        Mq+Mad*(u+Zq)/(u-Zad), -Mad*32.174*sin(theta);
        0, 0, 1, 0];
Blong=[Xde, Xdf;
        Zde/(u-Zad), Zdf/(u-Zad);
        Mde+Mad*Zde/(u-Zad), Mdf+Mad*Zdf/(u-Zad);
        0, 0];

```

```

%
% Calculation of the Lateral-Directional A and B matrices
%
BA=1-B1*A1;
Alat=[Yb/u,Yp/u,32.174*cos(theta)/u,Yr/u-1,0;
      (Lb+A1*Nb)/BA,(Lp+A1*Np)/BA,0,(Lr+A1*Nr)/BA,0;
      0,1,0,0,0;
      (Nb+B1*Lb)/BA,(Np+B1*Lp)/BA,0,(Nr+B1*Lr)/BA,0;
      0,0,0,1,0];
Blat=[Yda/u,Ydr/u;
      (Lda+A1*Nda)/BA,(Ldr+A1*Ndr)/BA;
      0,0;
      (Nda+B1*Lda)/BA,(Ndr+B1*Ldr)/BA;
      0,0];

```

Appendix E:

Wind Dynamics Model

This appendix provides a brief summary of the wind dynamics model used for the controller designs developed in Chapter 5.

The wind model implemented into the controller models was taken from Appendix A of Reference E.1. This model is a reasonable approximation to the von Karman model and the Haines approximation.

The power Spectral density of the wind disturbance is given by:

$$\Phi_g = (\sigma^2/\pi) (L/V_o) [4/\{4+(L\omega/V_o)^2\}] \quad (E.1)$$

where, $L \equiv$ scale length, 200 ft at sea level

$V_o \equiv$ speed of the aircraft, ft/sec

$\omega \equiv$ frequency, rad/sec

$\sigma \equiv$ constant, 6 ft/sec

To obtain a state variable model, a normalized state variable, $w(t)$, is used as the wind state for both longitudinal and lateral-directional dynamics. The state variable $w(t)$ is the output of a first-order system driven by continuous white noise $\xi(t)$ with zero mean.

$$\dot{w}(t) = -2(V_o/L)w(t) + 2\sigma/(\pi LV_o)^{1/2}\xi(t) \quad (E.2)$$

$$\text{where, } E[\xi(t)] = 0 \quad (E.3)$$

$$E[\xi(t)\xi(\tau)] = \delta(t-\tau) \quad (E.4)$$

For the longitudinal dynamics, the wind state $w(t)$ influences the dynamics in the same manner as the angle of attack. Thus, in the longitudinal state equations, the wind state enters the equations as follows:

$$\dot{u}(t) = \dots + a_1 w(t)$$

$$\dot{q}(t) = \dots + a_2 w(t), \text{ etc.}$$

where a_1, a_2, \dots can be found from the open-loop longitudinal A matrix. For the lateral dynamics $w(t)$ influences the dynamics in

the same manner as sideslip angle. Thus, in the lateral-directional state equations, the wind state enters the equations as follows:

$$\dot{\beta}(t) = \dots + a_1 w(t)$$

$$\dot{p}(t) = \dots + a_2 w(t), \text{ etc.}$$

where a_1 , a_2 , ... can be found from the open-loop lateral-directional A matrix.

Given the above, the following was used as the baseline wind model for Lambda:

$$\Phi_g(\omega) = 9167/V_0 [4 + (200\omega/V_0)^2]^{-1} \quad (\text{E.5})$$

$$\dot{w}(t) = -(V_0/100)w(t) + 0.4787V_0^{-1/2}\xi(t) \quad (\text{E.6})$$

Reference:

E.1. Athans, Micheal; Castanon, David; Dunn, Keh-Ping; Green, Christopher; Lee, Wing; Sandell, Nils; Willsky, Alan; "The Stochastic Control of the F-8C Aircraft Using a Multiple Model Adaptive Control (MMAC) Method -- Part I: Equilibrium Flight". IEEE Transactions on Automatic Control, Volume AC-22, Number 5, October 1977.

Appendix F:

Rate Controller Matlab Models

This appendix presents the Matlab macros for the final rate controller designs presented in Chapter 5. Each macro calculates the closed loop rate and control surface time responses to a unit step rate command given the trimmed flight conditions as inputs.

Program: PRATCONV.M

```
function [pstep,destep,xstep,gml,gmh,pm]=pratconv(X)
%
% Pitch Rate Flight Controller Design For Lambda
%
% The only input required is flight condition vector, X:
%   X=[Xcg,U,q,W,theta]
%       in inches, fps, psf, lbs, and deg, respectively.
%
% The outputs are the pitch rate and elevator time responses to a
% unit step pitch rate command and the design's gain and phase
% margins. Gain scheduling is accomplished for the Kalman filter
% gains as a function of speed.
%

%
% Form the open loop, augmented, and doubly augmented systems
%
[Ap,Bp,Cp,Dp]=formq(X);
Aa=[Ap,Bp;zeros(Cp),0];Ba=[zeros(Bp);1];Ca=[Cp,0];Da=Dp;
A=[Aa,Ba;zeros(Ca),0];B=[zeros(Ba);1];C=[Ca,0];D=Da;
%
% Compensators designed for the following:
%
%   1/u=100, q=5500, rho=50,000,000, rho/q=9,090
%
% Kalman filter designed for FC#3:
Kfh=[-0.0024,0.9747,7.7262,1,-2.3130,-0.1562,-3.6393,-10]';
%
% Kalman filter designed for FC#4:
Kfl=[-0.0211,1.0498,5.7190,1,-4.2724,-0.0982,-5.7255,-10]';
%
% Gain schedule on the Kalman filter gains:
%
u=X(1,2);
delta=(u-76)/(168.9-76);
Kf=Kfl+delta*(Kfh-Kfl);
%
% Regulator designed for FC#3:
Kc=[-0.0781,0.0072,0.0251,0.0385,-0.0558,-0.2936,2.2065,2.1007];
%
% Calculate the required matrices:
%
Acl=[A,-B*Kc;Kf*C,A-B*Kc-Kf*C];
Bcl=[zeros(B);-Kf];
Ccl=[C,zeros(C)];
Ccl1=[zeros(C),-Kc];
Dcl=0;
```

```

Ao=[A,B*Kc;zeros(A),A-B*Kc-Kf*C];
Bo=[zeros(B);Kf];
Co=[C,zeros(C)];
Do=0;
As=Ao-Bo*Co;
Bs=Bo;
Cs=-Co;
Ds=1;
%
% Calculate the singular values of the sensitivity:
%
w=logspace(-3,3,1000);
sv=sigma(As,Bs,Cs,Ds,1,w);
infnm=max(max(sv));
infs=20*log10(infnm);
%
% Calculate the margins:
%
inf=10^(infs/20);
gml=-20*log10(1+1/inf);
gmh=-20*log10(1-1/inf);
pm=2*asin(1/(2*inf))*180/pi;
%
% Calculate the time responses:
%
T=[0:0.01:10];
[qstep,xstep]=step(Ac1,Bc1,Cc1,Dc1,1,T);
destep=step(Ac1,Bc1,Cc1,Dc1,1,T);
%
% Plot the time responses:
%
t1='time, sec';
t2='rate, deg/sec';
t3='deflection, deg';
plot(T,qstep),xlabel(t1),ylabel(t2),title('q to qstep')
pause
plot(T,destep),xlabel(t1),ylabel(t3),title('de to q step')

```

Program: RRATCONV.M

```
function [pcl,dclp,gml,gmh,pm]=rratconv(X)
%
% Roll Rate Flight Controller Design For Lambda
%
% The only input required is flight condition vector, X:
%   X=[Xcg,U,q,W,theta]
%       in inches, fps, psf, lbs, and deg, respectively.
%
% The outputs are roll rate, sideslip, aileron deflection and
% rudder deflection time responses to a unit step roll rate
% command. The design's gain and phase margins are also given.
% Gain scheduling is accomplished for the Kalman filter gains as
% a function of flight speed.
%
% Form: [pcl,dclp,gml,gmh,pm]=rratconv(X)
%
%
% Form the open loop, augmented, and doubly augmented systems
%
[Ap,Bp,Cp,Dp]=formp(X);
Aa=[Ap,Bp;zeros(2,9)];Ba=[zeros(7,2);eye(2)];Ca=[Cp,zeros(2,2)];
Da=Dp;
A=[Aa,Ba;zeros(2,11)];B=[zeros(9,2);eye(2)];C=[Ca,zeros(2,2)];D=Da;
%
% Compensators designed for the following:
%
%   1/u=100, q=100, rho=100,000, rho/q=1,000
%
% Kalman filter designed for FC#4:
Kf1=[4.8762,-3.3391e-2,8.5897e-8,-1.1771e1,5.1452e-1,9.9592,...
      1.2273e-1,6.3299e-1,1.1562e1,6.4546e-1,9.9791;...
      -3.3391e-2,7.8567,1,5.2452e-3,3.4439,-3.4389e-1,1.7581e-1,...
      5.1064,-4.4516e-1,9.9791,-6.4546e-1]';
%
% Kalman filter designed for FC#3:
Kfh=[5.4431,-2.5402e-2,1.0411e-8,-1.5306e1,4.5480e-1,6.4415,...
      5.2863e-2,6.0455e-1,8.0256,8.2724e-1,9.9657;...
      -2.5402e-2,1.1772e1,1,-6.9092e-2,1.9071,-2.2024e-1,...
      9.6412e-2,3.4052,-3.4430e-1,9.9657,-8.2724e-1]';
%
% Regulator design from the midpoint flight condition:
Kc=[1.2781e-2,3.2606e-3,5.6037e-3,8.4716e-4,5.2573e-2,-3.471e-3,...
      -7.5810e-4,1.6477,-6.7330e-2,1.8151,-2.9168e-2;...
      -4.1613e-3,1.4065e-3,7.8684e-3,2.2826e-3,1.0068e-2,...
      -2.4072e-3,-1.4163e-2,-6.8991e-3,2.6673e-1,-2.9168e-2,...
      7.2980e-1];
```

```

%
% Gain schedule on the Kalman filter gains:
%
u=X(1,2);delta=(u-76)/(168.9-76);
Kf=Kf1+delta*(Kfh-Kf1);
%
% Calculate the required matrices:
%
Acl=[A,-B*Kc;Kf*C,A-B*Kc-Kf*C];
Bcl=[zeros(B);-Kf];
Ccl=[C,zeros(C)];
CclK=[zeros(C),Kc];
Dcl=zeros(2,2);
Ao=[A,B*Kc;zeros(A),A-B*Kc-Kf*C];
Bo=[zeros(B);Kf];
Co=[C,zeros(C)];
Do=D;
As=Ao-Bo*Co;
Bs=Bo;
Cs=-Co;
Ds=eye(2);
%
% Calculate the singular values of the sensitivity:
%
w=logspace(-3,3,1000);
sv=sigma(As,Bs,Cs,Ds,1,w);
infnm=max(max(sv));
infs=20*log10(infnm);
%
% Calculate the margins:
%
inf=10^(infs/20);
gml=-20*log10(1+1/inf);
gmh=-20*log10(1-1/inf);
pm=2*asin(1/(2*inf))*180/pi;
%
% Calculate the time responses:
%
T=[0:0.01:10];
[pc1,xclp]=step(Acl,Bcl,Ccl,Dcl,2,T);
[bcl,xclb]=step(Acl,Bcl,Ccl,Dcl,1,T);
dclp=step(Acl,Bcl,CclK,Dcl,2,T);
dclb=step(Acl,Bcl,CclK,Dcl,1,T);
%
% Plot the time responses:
%
t1='time, sec';t3='deflection, deg';
t4='rate, deg/sec and deflection, deg';
plot(T,pc1),xlabel(t1),ylabel(t4),title('Response to p Command')
pause
plot(T,dclp),xlabel(t1),ylabel(t3)
title('Control Response to p Command')

```

Program: YRATCONV.M

```
function [rcl,dclr,gml,gmh,pm]=yratconv(X)
%
% Yaw Rate Flight Controller Design For Lambda
%
% The only input required is flight condition vector, X:
%   X=[Xcg,U,q,W,theta]
%       in inches, fps, psf, lbs, and deg, respectively.
%
% The outputs are yaw rate, roll angle, aileron deflection and
% rudder deflection time responses to a unit step yaw rate
% command. The design's gain and phase margins are also given.
% Gain scheduling is accomplished for the Kalman filter gains as
% a function of flight speed.
%
% Form: [rcl,dclr,gml,gmh,pm]=yratconv(X)
%
%
% Form the open loop, augmented, and doubly augmented systems
%
[Ap,Bp,Cp,Dp]=formr(X);
Aa=[Ap,Bp;zeros(2,9)];Ba=[zeros(7,2);eye(2)];Ca=[Cp,zeros(2,2)];
Da=Dp;
A=[Aa,Ba;zeros(2,11)];B=[zeros(9,2);eye(2)];C=[Ca,zeros(2,2)];D=Da;
%
% Compensators designed for the following:
%
%   1/u=1000, q=1000, rho=250,000, rho/q=250
%
% Kalman filter designed for FC#4:
Kf1=[3.1335e-1,4.5364e1,9.5159,-4.1854e-1,1.6280e1,-3.1173,...
      4.0555e-1,2.1724e1,-4.0642,3.1052e1,-5.9806;...
      -1.1759,-4.6276,-4.1854e-1,8.5273,-2.3618,-1.2541e1,...
      -6.6314e-1,-3.4566,-1.7325e1,-5.9806,-3.1052e1]';
%
% Kalman filter designed for FC#3:
Kfh=[6.5706e-2,7.9729e1,1.2614e1,-5.8438e-1,1.0510e1,-2.7698,...
      1.7557e-1,1.5634e1,-4.0222,3.0550e1,-8.1682;...
      -1.1145,-9.3266,-5.8438e-1,1.3195e1,-1.7524,-6.7477,...
      -3.8257e-1,-3.1244,-1.1095e1,-8.1682,-3.0550e1]';
%
% Regulator design from the FC#3:
Kc=[-3.5338e-1,2.6232e-1,1.9493,2.3119e-1,3.7852,-4.3397e-1,...
      -4.0278e-2,1.5242e1,-2.3412e-1,5.5184,-1.7414e-1;...
      -1.3977,-1.0496e-1,-6.3275e-1,5.6180e-1,-1.1872,-1.1007,...
      6.5066e-1,-1.1797,3.3968,-1.7414e-1,2.6006];
```

```

%
% Gain schedule on the Kalman filter gains:
%
u=X(1,2);delta=(u-76)/(168.9-76);
Kf=Kf1+delta*(Kfh-Kf1);
%
% Calculate the required matrices:
%
Acl=[A,-B*Kc;Kf*C,A-B*Kc-Kf*C];
Bcl=[zeros(B);-Kf];
Ccl=[C,zeros(C)];
CclK=[zeros(C),Kc];
Dcl=zeros(2,2);
Ao=[A,B*Kc;zeros(A),A-B*Kc-Kf*C];
Bo=[zeros(B);Kf];
Co=[C,zeros(C)];
Do=D;
As=Ao-Bo*Co;
Bs=Bo;
Cs=-Co;
Ds=eye(2);
%
% Calculate the singular values of the sensitivity:
%
w=logspace(-3,3,1000);
sv=sigma(As,Bs,Cs,Ds,1,w);
infnm=max(max(sv));
infs=20*log10(infnm);
%
% Calculate the margins:
%
inf=10^(infs/20);
gml=-20*log10(1+1/inf);
gmh=-20*log10(1-1/inf);
pm=2*asin(1/(2*inf))*180/pi;
%
% Calculate the time responses:
%
T=[0:0.01:10];
[rcl,xclr]=step(Acl,Bcl,Ccl,Dcl,2,T);
[pcl,xclp]=step(Acl,Bcl,Ccl,Dcl,1,T);
dclr=step(Acl,Bcl,CclK,Dcl,2,T);
dclp=step(Acl,Bcl,CclK,Dcl,1,T);
%
% Plot the time responses:
%
t1='time, sec';t3='deflection, deg';
t4='rate, deg/sec and deflection, deg';
plot(T,rcl),xlabel(t1),ylabel(t4),title('Response to r Command')
pause
plot(T,dclr),xlabel(t1),ylabel(t3)
title('Control Response to r Command')

```


Program: YRATCONVB.M

```
function [rcl,dclr,gml,gmh,pm]=yaratconvb(X)
%
%   Yaw Rate Flight Controller Design For Lambda
%
%   The only input required is flight condition vector, X:
%       X=[Xcg,U,q,W,theta]
%           in inches, fps, psf, lbs, and deg, respectively.
%
%   The outputs are yaw rate, roll angle, aileron deflection and
%   rudder deflection time responses to a unit step yaw rate
%   command. The design's gain and phase margins are also given.
%   Gain scheduling is accomplished for the Kalman filter gains as
%   a function of flight speed.
%
%   Form: [rcl,dclr,gml,gmh,pm]=yaratconvb(X)
%
%
%   Form the open loop, augmented, and doubly augmented systems
%
[Ap,Bp,Cp,Dp]=formr2(X);
Aa=[Ap,Bp;zeros(2,9)];Ba=[zeros(7,2);eye(2)];Ca=[Cp,zeros(2,2)];
Da=Dp;
A=[Aa,Ba;zeros(2,11)];B=[zeros(9,2);eye(2)];C=[Ca,zeros(2,2)];D=Da;
%
%   Compensators designed for the following:
%
%       1/u=100, q=10, rho=10,000, rho/q=1000
%
%   Kalman filter designed for FC#4:
Kfl=[5.1598,5.4167e1,3.3939e1,1.9237e-1,1.3799e1,-1.5537,...
      1.1773e-1,1.5606e1,-1.3997,9.9511,9.8782e-1;...
      1.9237e-1,1.6541e1,1.1064e1,5.7109,3.6141,-6.9404,...
      -1.5679e-1,3.7938,-8.5124,9.8782e-1,-9.9511]';
%
%   Kalman filter designed for FC#3:
Kfh=[4.9195,1.1671e2,7.4366e1,3.4749e-1,1.1855e1,-8.9428e-1,...
      4.8562e-2,1.3594e1,-4.6537e-1,9.6064,2.7779;...
      3.4749e-1,5.9179e1,3.3031e1,8.4798,5.6622,-4.7502,...
      -8.1501e-2,6.1893,-6.2006,2.7779,-9.6064]';
%
%   Regulator design from the FC#3:
Kc=[-3.3862e-2,3.7874e-3,5.4696e-2,7.5498e-2,7.9511e-2,...
      -1.9743e-1,1.5901e-1,2.3190,1.6244e-1,2.1511,-1.0286e-1;...
      -2.6598e-1,-3.6540e-2,-2.0581e-1,1.8715e-1,-4.5083e-1,...
      -4.4425e-1,4.4656e-1,-5.3354e-1,1.0663,-1.0286e-1,1.4567];
```

```

%
% Gain schedule on the Kalman filter gains:
%
u=X(1,2);delta=(u-76)/(168.9-76);
Kf=Kf1+delta*(Kfh-Kf1);
%
% Calculate the required matrices:
%
Acl=[A,-B*Kc;Kf*C,A-B*Kc-Kf*C];
Bcl=[zeros(B);-Kf];
Ccl=[C,zeros(C)];
CclK=[zeros(C),Kc];
Dcl=zeros(2,2);
Ao=[A,B*Kc;zeros(A),A-B*Kc-Kf*C];
Bo=[zeros(B);Kf];
Co=[C,zeros(C)];
Do=D;
As=Ao-Bo*Co;
Bs=Bo;
Cs=-Co;
Ds=eye(2);
%
% Calculate the singular values of the sensitivity:
%
w=logspace(-3,3,1000);
sv=sigma(As,Bs,Cs,Ds,1,w);
infnm=max(max(sv));
infs=20*log10(infnm);
%
% Calculate the margins:
%
inf=10^(infs/20);
gml=-20*log10(1+1/inf);
gmh=-20*log10(1-1/inf);
pm=2*asin(1/(2*inf))*180/pi;
%
% Calculate the time responses:
%
T=[0:0.01:10];
[rcl,xclr]=step(Acl,Bcl,Ccl,Dcl,2,T);
[bcl,xclb]=step(Acl,Bcl,Ccl,Dcl,1,T);
dclr=step(Acl,Bcl,CclK,Dcl,2,T);
dclb=step(Acl,Bcl,CclK,Dcl,1,T);
%
% Plot the time responses:
%
t1='time, sec';t3='deflection, deg';
t4='rate, deg/sec and deflection, deg';
plot(T,rcl),xlabel(t1),ylabel(t4),title('Response to r Command')
pause
plot(T,dclr),xlabel(t1),ylabel(t3)
title('Control Response to r Command')

```

Bibliography

1. Thompson, Dan B., A Multiprocessor Avionics System for an Unmanned Research Vehicle. Technical Report AFWAL-TR-88-3003. Air Force Wright Aeronautical Laboratories (ASD), Wright-Patterson AFB OH, March 1988.
2. Wheaton, Capt David G., Automatic Flight Control System Design for an Unmanned Research Vehicle Using Discrete Quantitative Feedback Theory. MS Thesis AFIT/GE/ENG/90D-66. School of Engineering, Air Force Institute of Technology (AU), Wright-Patterson AFB OH, December 1990.
3. McDonnell Douglas Corporation, USAF Stability and Control Datcom. Air Force Flight Dynamics Laboratory (ASD), Wright-Patterson AFB OH, October 1960. (Revised April 1976).
4. Roskam, Jan, Airplane Flight Dynamics and Automatic Flight Controls, Parts I and II. Roskam Aviation and Engineering Corporation, Ottawa KS, 1979.
5. McRuer, D., Irving, A., and Graham, D., Aircraft Dynamics and Automatic Control. New Jersey: Princeton University Press, 1973.
6. Ridgely, D. Brett, and Banda, Siva, Introduction to Robust Multivariable Control. Technical Report AFWAL-TR-3102. Air Force Wright Aeronautical Laboratories (ASD), Wright-Patterson AFB OH, February 1986.
7. Roskam, Jan, Airplane Design: Part V, Component Weight Estimation. Roskam Aviation and Engineering Corporation, Ottawa KS, 1987.
8. Roskam, Jan, Airplane Design, Part VI: Preliminary Calculation of Aerodynamic, Thrust, and Power Characteristics. Roskam Aviation and Engineering Corporation, Ottawa KS, 1987.
9. McDonnell Douglas Corporation, The USAF Stability and Control Digital Datcom, Volume 1, User's Manual. Technical Report AFFDL-TR-79-3032, Volume 1. Air Force Wright Aeronautical Laboratories (ASD), Wright-Patterson AFB OH, April 1979. (AD A086557)
10. Mehra, Raman, and Tyler, J., "Case Studies in Aircraft Parameter Identification", Identification and System Parameter Estimation; Proceedings of the Third Symposium. 117-144. Amsterdam: North-Holland Publishing Company, 1973.
11. Iliff, Kenneth, and Maine, Richard, "More Than You May Want to Know About Maximum Likelihood Estimation", Atmospheric Flight Mechanics Conference. 1-24. New York: American Institute of Aeronautics and Astronautics, 1984. (AIAA Paper 84-2070)

12. Iliff, Kenneth, and Maine, Richard, "Further Observations on Maximum Likelihood Estimates of Stability and Control Characteristics Obtained From Flight Test Data". New York: American Institute of Aeronautics and Astronautics, 1977. (AIAA Paper 77-1133)

13. Iliff, Kenneth, and Maine, Richard, Bibliography for Aircraft Parameter Estimation. NASA Technical Memorandum 86804. Ames Research Center, Dryden Flight Research Facility, Edwards CA, 1986.

14. Wolowicz, Chester, and Yancy, Roxannah, Experimental Determination of Airplane Mass and Inertial Characteristics. NASA Technical Report R-433. 1974.

15. Nelson, Robert, Flight Stability and Automatic Control. New York: McGraw-Hill Book Company, 1989.

16. Doyle, John, and Stein, Gunter, "Multivariable Feedback Design: Concepts for a Classical/Modern Synthesis". IEEE Transactions on Automatic Control, Volume AC-26, Number 1, February 1981.

17. Doyle, John, "Multivariable Design Techniques Based on Singular Value Generalizations of Classical Control".

18. Doyle, John, "Limitations on Achievable Performance of Multivariable Feedback Systems".

19. Stein, Gunter, "LQG-Based Multivariable Design: Frequency Domain Interpretation".

20. Stein, Gunter, and Pratt, Stephen, "LQG Multivariable Design Tools".

Note: References 17 through 20 were presented in Multivariable Control Theory Analysis and Design. Prepared by Honeywell Systems and Research Center for the AGARD GRP Lecture Series 117, "Multivariable Analysis and Design Techniques", R.E. Pope -- Editor, October 1981.

21. Maybeck, Peter, Stochastic Models, Estimation, and Control, Volumes I, II, and III. San Diego: Academic Press, 1976.

22. Franklin, Gene; Powell, J. David; and Emami-Naeini, Abbas; Feedback Control of Dynamic Systems. Reading MA: Addison-Wesley Publishing Company, 1986.